NARROW GAP PULSE CURRENT GAS METAL ARC WELDING OF THICK WALL 304LN STAINLESS STEEL PIPE

A THESIS

Submitted in partial fulfilment of the
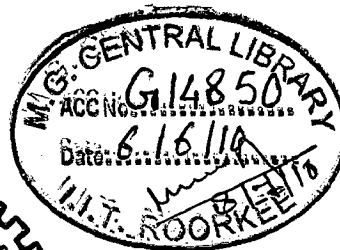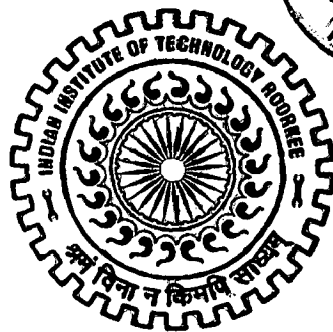*requirements for the award of the degree*
of
DOCTOR OF PHILOSOPHY
in
METALLURGICAL AND MATERIALS ENGINEERING

by

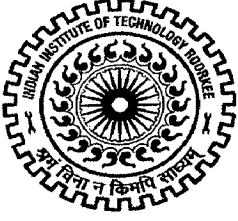## SHRIRANG GURUNATH KULKARNI

DEPARTMENT OF METALLURGICAL AND MATERIALS ENGINEERING
INDIAN INSTITUTE OF TECHNOLOGY ROORKEE
ROORKEE - 247 667 (INDIA)
JULY, 2008

INDIAN INSTITUTE OF TECHNOLOGY ROORKEE
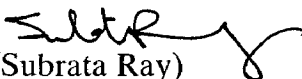# ROORKEE

CANDIDATE'S DECLARATION

I hereby certify that the work which is being presented in the thesis, entitled **NARROW GAP PULSE CURRENT GAS METAL ARC WELDING OF THICK WALL 304LN STAINLESS STEEL PIPE** in partial fulfilment of the requirements for the award of the degree of Doctor of Philosophy and submitted in the Department of Metallurgical and Materials Engineering, Indian Institute of Technology Roorkee, Roorkee is an authentic record of my own work carried out during a period from January 2003 to July 2008 under the supervision of Dr. P.K. Ghosh and Dr. Subrata Ray, Professors, Department of Metallurgical and Materials Engineering, Indian Institute of Technology Roorkee, Roorkee.

The matter embodied in this thesis has not been submitted by me for the award of any other degree of this or any other Institute.

(SHRIRANG GURUNATH KULKARNI)

This is to certify that the above statement made by the candidate is correct to the best of our knowledge.

(Subrata Ray)   (P.K. Ghosh)
Supervisor   Supervisor

Date: July 24, 2008

The Ph.D. Viva-Voice examination of **Mr. Shrirang Gurunath Kulkarni,** Research Scholar, has been held on _____.

Signature of Supervisors   Signature of External Examiner

ABSTRACT

The acceptability of weld joint is primarily governed by required fusion of base metal through formation of arc crater of sufficient extent in it, at an optimum thermal exposure giving rise to a minimum undesirable heat affected zone (HAZ) and residual stresses. The control of microstructure and residual stresses of weld joint becomes quite critical in case of joining of thick sections of austenitic stainless steel by multipass welding procedure due to its low thermal conductivity and high coefficient of thermal expansion. The arc welding of such steel is generally carried out by Shielded metal arc welding (SMAW), Gas tungsten arc welding (GTAW) and Gas metal arc welding (GMAW) processes, where they influence severity of weld thermal cycle in different manner depending upon amount of weld deposition, welding parameters and shielding environment. The severity of thermal and mechanical effects of welding can be considerably minimized by reducing the amount of weld metal in a joint by using narrow gap welding technique. The preparation of narrow groove weld joints by SMAW and GTAW processes generally requires welding at a lower angle of attack to groove wall by a skilled welder and the process automation is highly critical. SMAW has further limitation with respect to slag entrapment resulting in poor mechanical and fracture mechanics properties, while in GTAW process welding speed is significantly lower than SMAW and GMAW processes. The solution to these limitations of SMAW and GTAW processes can be satisfactorily addressed by the merits of GMAW process using spray mode of metal transfer which offers better ease of operation primarily due to dominating electromagnetic force resulting in projected transfer of the droplet. But, the convenient use of GMAW process in spray mode of metal transfer at high welding current increases heat input to the weld and consequently affects the size, temperature and solidification behaviour of weld pool resulting an adverse influence on grain coarsening of

heat affected zone (HAZ), residual stresses of weld joint and carbide precipitation along the grain boundaries. These undesirable conditions which are created by comparatively higher heat flow during welding can be controlled by two methods, first by reducing the amount of weld metal i.e. by narrow gap welding and secondly by modification of thermal and solidification behaviour of weld deposit, through control of welding process and parameters.

The difficulties in manipulation of relatively large conventional torch head of the order of 26mm O.D. in narrow weld groove deters the narrow gap GMA welding of thick section necessitating the development of a narrow torch head feasibly justified in order to have desired protection of metal deposition and groove wall fusion. In this context the possibility of using the merits of pulsed current GMAW (P-GMAW) process primarily with respect to its more efficient characteristic of metal deposition has been studied to facilitate the narrowing down of weld groove without compromising the acceptable weld quality. The ability of P-GMAW process to combine a comparatively low work-piece heating along with high arc stiffness and strong mechanism of metal transfer depending upon pulse parameters allowing improved fusion and penetration in groove wall has been explored for preparation of narrow gap GMA weld having atleast a comparable or improved weld quality than that of conventionally produced narrow gap SMA weld. In the context of criticality and complexity in selection of simultaneously interactive pulse parameters like peak current (I_p), base current (I_b), pulse duration (t_p) and pulse frequency (f), it is decided to consider the summarized influence of pulse parameters through hypothetically derived dimensionless factor ϕ = $[(I_b/I_p)ft_b]$, where t_b is expressed as $[(1/f)-t_p]$.

In P-GMAW process during metal transfer primarily occurring at the peak current (I_P), two heat sources of different natures act simultaneously on weld pool. One is continuous heat source (arc heat source) of double ellipsoidal nature acting at the surface of the base plate, which melts and produces an initial weld pool in the base metal. The other one is an interrupted

heat source supplying superheated filler metal, considered as a point heat source dictating the size and geometry of weld pool over that initially developed by the arc heating. Thus, depending upon variation of ϕ, total heat transferred to the weld pool (Q_T) is primarily attributed to the initial arc heating (Q_{AW}) followed by the deposition of superheated filler metal (Q_f) affecting the thermal behaviour of the weld metal deposited per pulse. Thus in addition to the hypothetical factor ϕ, the variation of heat input (Ω) to the system as a function of mean current (I_m), arc voltage (V), welding speed (S) and heat transferred to the weld pool (Q_T) also influences the weld characteristics. Hence the planning of appropriate use of ϕ, Ω and Q_T has been planned in light of its reported utility to control P-GMAW process.

In view of the above the present investigation on welding of thick wall 304LN stainless steel pipe has been carried out using pulse current gas metal arc welding (P-GMAW) in narrow weld groove. The studies have been systematically planned in order to gain sufficient knowledge to establish a welding technique superior to some conventionally used welding processes and weld groove design.

1.   To design and develop a narrow GMA torch nozzle device which facilitates the application of P-GMAW process in narrow gap welding of thick wall pipes.

2.   To study the efficient use of factor ϕ, Ω and Q_T, by analysing its influence on sensitization and other characteristics of weld through bead on plate deposition. This is in order to develop a systematic knowledge for selection of appropriate range of welding parameters and procedure which may be effectively used in pulse current narrow groove welding of thick section.

3.   Development of narrow gap welding procedure by P-GMAW process for joining of thick sections by appropriate reduction in number of weld passes and amount of weld metal.

4. To study the effect of variation in pulse parameters considered by their summarized influence through the dimensionless factor ϕ on metallurgical, mechanical and fracture mechanics properties as well as residual stresses of weld joint.

5. To study the acceptability of weld joint with respect to corrosion susceptibility of its heat affected zone.

6. To establish suitability of narrow gap P-GMA welding by comparing it's utility to improve the properties of weld joint with respect to those prepared by commonly used SMA welding with and without narrow weld groove.

The entire details of investigation carried out in this work to achieve these objectives have been reported in six chapters as outlined below.

Chapter-1 contains the introductory remarks about the thermal influence of welding process and procedure on weld joint characteristics of thick austenitic stainless steel sections. The importance of P-GMAW and narrow gap welding has been categorically addressed and the problems associated with respect to its practical implementation are also briefly discussed. Finally, the methodology which can be followed for practical implementation of narrow gap P-GMA welding in thick sections has been highlighted and justified to address in this work.

Chapter-2 begins with the survey of the existing literature outlining the evolution of arc welding process and procedures used for joining of thick austenitic stainless steel sections. In this chapter the existing knowledge on thermal influence of welding processes on various weld joint characteristics with respect to its metallurgical, mechanical, fracture mechanics and corrosion properties has been critically analysed. Further, the influence of welding procedure on residual stress distribution across the weld joints has been carefully examined. The deficiency of knowledge with respect to influence of various pulse parameters on weld joint properties in P-GMAW process,

limiting its practical applications, has been identified and the problem proposed to be investigated has been outlined in this context.

Chapter-3 presents the development of narrow torch nozzle device suitable for narrow gap GMA welding of thick pipes/plates along with proper consideration of the characteristics of shielding jacket at the outlet of torch head protecting the contamination of weld deposit from environmental reaction. The performance of newly developed torch with respect to arc stability and weld bead oxidation characteristics has been reported justifying the suitability of the narrow torch nozzle for use in narrow gap GMAW of thick section.

Chapter-4 describes the experimental procedures followed to prepare the conventional V-groove and narrow groove weld joints of austenitic stainless steel pipes using gas metal arc welding (GMAW), pulsed current GMAW with solid filler wire and Shielded metal arc welding (SMAW) for characterisation of the weld joints. The welding parameters and procedure used in this investigation with respect to the groove design and welding process have been thoroughly described, so that various aspects of weld characteristics of concern can be appropriately realised in the light of it.

The weld joints have been characterised primarily by studying the influence of heat input (Ω) on its residual stress distribution, susceptibility to intergrannular corrosion and initiation fracture toughness along with its conventional mechanical and metallurgical properties. In case of P-GMA welds the influence of different ϕ on weld joint properties has also been characterised to identify and analyse the causes behind its variation. The advantage of P-GMAW with due reference to Ω and ϕ, over the SMAW process with respect to various weld joint properties have been compared.

Chapter-5 presents the results of various experiments described in the preceding chapter and demonstrates the different facets of the present work, broadly classified into two

major features. Firstly, the influence of P-GMAW process on conventional groove weld joint characteristics have been analysed by varying ϕ, Ω and Q_T. Secondly, by using narrow gap welding procedure, the influence of groove design on weld joint characteristics have been established. In both the cases to establish the superiority of P-GMAW process, weld joints produced with SMAW process have also been analysed at almost similar groove design. For better understanding on influence of P-GMAW process on weld joint properties, pulse parameters have been correlated further with the amount of weld metal varied by changing groove design. Finally, by analysing the characteristics of weld joints with respect to their mechanical, metallurgical, corrosion and fracture mechanics properties along with residual stress distribution, the necessary control of welding parameters and narrow gap welding procedure in P-GMAW process has been established in order to improve the weld quality.

Chapter-6 concludes the investigation by several innovative knowledge and understandings over the influence of hypothetical factor ϕ on characteristics of weld joint produced by P-GMAW process. The advantage of narrow gap P-GMA welding of thick SS 304LN pipes with suitable modification in GMAW torch nozzle device have also been broadly realised.

ACKNOWLEDGEMENTS

CONTENTS

x

(a) 0.042 (b) 0.136 and (c) 0.224.

the top in P-GMA, GMA and SMA weld joints.

LIST OF TABLES

A_{arc}	mm^2	Surface area of arc
A_{wt}	mm^2	Cross sectional area of tube through which water is flowing
A	mm^2	Cross sectional area of the rectangular torch
C_p	J/Kg/K	Specific heat of argon plasma
C_{Pw}	J/Kg/K	Specific heat of water
D_W	%	Dilution of weld deposit
D_P	mm	Projected arc diameter
D_R	mm	Arc root diameter
I_{eff}	A	Effective current
I_m	A	Mean current
I_p	A	Peak current
I_b	A	Base current
f	Hz	Pulse frequency
K	$Js^{-1}m^{-1o}K^{-1}$	Thermal conductivity of argon (0.625)
k_p		Pulse duty cycle
L	m	Arc length
n		Strain hardening exponent
Q_{cov}	Js^{-1}	Convection heat transfer
Q_{cod}	Js^{-1}	Conduction heat transfer
Q_{rad}	Js^{-1}	Radiation heat transfer
t_{pul}	ms	Pulse on time

t_b	ms	Pulse off time
V	Volts	Arc voltage
V_{eff}	ms^{-1}	Effective velocity of plasma
S	cm/min	Welding speed
ε		Emissivity of argon plasma (0.012)
σ	Wm^2/K^4	Stefan Boltzmann constant (5.68×10^{-8})
σ_0	MPa	flow stress
v	$Kg\, m^{-1}s^{-1}$	Kinematic viscosity of ionized shielding gas (0.0044)
μ_0	NA^{-2}	Permeability of free space ($4\pi \times 10^{-7}$)
ρ_g	kgm^{-3}	Mass density of plasma in arc column (0.06)
η_a		Arc efficiency
Ω	kJ/cm	Heat input to the system
Q_T	kJ/cm	Total heat transferred to the weld pool
Q_f	kJ/s	Heat transferred to the weld pool by the superheated filler metal
Q_{AW}	kJ/s	Arc heat transferred to the weld pool per unit time
V_w	cm/s	Wire feed rate
W	mm	Bead width
P	mm	Bead penetration
H	mm	Bead height
A_R	mm^2	Area of reinforcement
B_F	mm^2	Area of base metal fusion

Z	mm	Width of coarse grain region
H_W	VHN	Hardness of weld deposit
H_{FL}	VHN	Micro-hardness along the fusion line
H_{HAZ}	VHN	Micro-hardness in coarse grain region
T_{arc}	K	Temperature of the arc chavern
T_{in}	K	Inlet Temperature of flowing water
T_{out}	K	Outlet Temperature of flowing water
m_W	kg/s	Mass flow rate of water

The development of different grades of austenitic stainless steel (ASS) by appropriate designing of chemical composition including minor alloying have explored its numerous applications in chemical, pharmaceutical, petrochemical and nuclear power industries [Padilha and Rios 2002, Basak et.al. 1995]. This has primarily happened due to its good mechanical and fracture mechanics properties over a long temperature range from -80^0 to 450^0 C and superior resistance to corrosion in variety of environments in comparison to that of structural steel [Covert and Tuthill 2000, Peckner and Bernstein 1977, Folkhard 1984]. These unique properties are primarily achieved by keeping the carbon content at a significantly lower level (0.03-0.08 wt %) and through substantial additions of chromium and nickel to iron, along with addition of other elements such as manganese, molybdenum and nitrogen [Padilha and Rios 2002, Hertzman 2001]. However, the acceptance of ASS in critical applications has been often questioned by its sensitivity to carbide precipitation ($M_{23}C_6$, M_{11} $(CN)_2$) and/or intermetallic precipitation (Sigma phase, Chi phase and Laves phase) under adverse condition of thermal exposure especially during welding fabrication as well as in service [Harris and Nag 1975, Gill and Gnanamoorthy 1982, Cieslak et.al. 1984, Vitek and David 1986, Padilha and Rios 2002].

Welding is one of the most commonly used fabrication process employed for joining of such material with varied section size in normal as well as in critical applications. Depending upon application, the integrity of weld joint is largely adjudged by its relevant properties. Weld deposit being a comparatively weaker region of weld joint due to its cast morphology, often requires a critical control on its several characteristics primarily starting from continuous and discontinuous defects to microstructure and residual stresses largely dictating the properties. In welding the acceptability of weld joint is thus governed by

1

required fusion of base metal through formation of arc crater of sufficient extent in it at an optimum thermal exposure giving rise to a minimum heat affected zone (HAZ) of undesirable microstructure and low residual stresses in weld joint. The control of these aspects becomes comparatively more critical in case of joining of austenitic stainless steel due to its low thermal conductivity and high coefficient of thermal expansion especially when it is of thick section. The criticality primarily arises due to use of a welding process such as Shielded metal arc welding (SMAW), Gas tungsten arc welding (GTAW) and Gas metal arc welding (GMAW) with conventional procedure introducing significant impurities in weld deposit, large amount of metal deposition and cumulative effect of severity of weld thermal cycle. However, the severity of thermal and mechanical effects of welding can be considerably minimized by reducing the amount of weld metal in a joint by using narrow gap welding technique. The preparation of narrow groove weld joints by SMAW and GTAW processes generally requires welding at a lower angle of attack by a skilled welder and the process automation is highly critical. SMAW has further limitation with respect to slag entrapment resulting in poor mechanical and fracture mechanics properties, while in GTAW process welding speed is significantly lower than SMAW and GMAW processes. In the recent past the gas metal arc welding (GMAW) has emerged as a widely accepted welding process [Kim and Eagar 1993a, Liao and Chen 1999] due to its several advantages including ability to produce comparatively cleaner weld. It is also well established that the use of narrow groove in welding of thick sections [Malin 1983a and b, Kang and Na 2003] of≥25mm can significantly reduce adverse influence of welding including the severity of thermal cycle and residual stresses in weld joint. Thus, a combination of GMAW and narrow gap welding procedure can be considered as an interesting technique to weld thick section stainless steel having improved properties of weld joint than those observed in case of commonly available shielded metal arc (SMA) weld.

In GMAW process, spray transfer mode which offers better ease of operation primarily due to dominating electromagnetic force, resulting in projected transfer of the droplet is achieved only at considerably higher welding current above a transition level, which increases heat input to the weld. This, increase in heat input consequently affects the weld pool size and temperature along with grain coarsening in heat affected zone (HAZ). An increase in weld pool size and temperature affect its solidification behaviour and thus adversely influences the residual stresses of weld joint while grain coarsening in HAZ affects kinetics of carbide precipitation along the grain boundaries. These undesirable conditions which are created by comparatively higher heat flow during GMA welding can further be controlled by modification of thermal and solidification behaviour of weld deposit through P-GMAW process [Maruo and Hirata 1984, Praveen et.al. 2005, Palani and Murugan 2006]. Hence, the ability of P-GMAW process to combine a comparatively low work-piece heating along with high arc stiffness and strong mechanism of metal transfer depending upon pulse parameters allowing improved fusion and penetration in groove wall should be explored.

In this context it is realised that the use of P-GMAW effectively in narrow groove of at least 25mm thick section is practically impossible due to difficulties in manipulation of relatively large conventional torch head of the order of 24mm O.D. in weld groove. Thus designing of a narrow torch head is necessary for better manipulation in narrow groove satisfying the required characteristics of metal deposition giving rise to desired groove wall fusion. Here, it may also be noted that the selection of appropriate pulse parameters which can provide desired fusion and weld bead profile through controlled thermal and metal transfer behaviour of depositing droplet becomes further complicated due to simultaneous influence of the pulse or peak current (I_p), base current (I_b), pulse time (t_p) and pulse frequency (f) on each other at a given mean current (I_m) of P-GMAW process [Quintino and Alllum 1984, Subramaniam et.al. 1998, Randhawa et.al. 2000]. These difficulties of controlling the pulse parameters have been well addressed by considering summarized

3

influence of pulse parameters proposed earlier and defined [Ghosh 1996 and 1999] by a hypothetical factor $\phi = [(I_b / I_p) f.t_b]$ where, $t_b = [(1/f) - t_p]$, derived on the basis of energy balance concept of the system. However in addition to the hypothetical factor ϕ, the variation of heat input (Ω) to the system as a function of I_m, arc voltage (V), welding speed (S) and heat transferred to the weld pool (Q_T) also influences the weld characteristics [Goyal et.al. 2008]. In P-GMAW process during metal transfer primarily occurring at the peak current (I_P), two heat sources of different natures act simultaneously on weld pool. One is continuous heat source (arc heat source) of double ellipsoidal nature acting at the surface of the base plate, which melts the base plate and produces an initial weld pool in the base metal. The other one is an interrupted heat source supplying superheated filler metal, considered as a point heat source dictating the size and geometry of weld pool over that initially developed by the arc heating. Thus depending upon variation of ϕ, total heat transferred to the weld pool (Q_T) is primarily attributed to the initial arc heating (Q_{AW}) followed by the deposition of superheated filler metal (Q_f) affecting the thermal behaviour of the weld metal deposited per pulse [Goyal et.al. 2008, Ghosh et.al. 2007].

Thus, during welding of ASS a more critical selection of pulse parameters is required for efficient energy distribution by the arc leading to comparatively low heat built-up in weld pool. In this regard the knowledge of correlation of Ω, ϕ and Q_T with the characteristics of weld joint in due reference to the arc characteristics and metal transfer behaviour is very much useful for more precise and wide spread application of P-GMAW process in welding of ASS of improved weld quality. Hence, it is felt that a systematic work considering the influence of welding process and procedure on characteristics of weld joint of thick wall pipe of 304LN stainless steel requiring multipass weld deposition will provide sufficient knowledge to establish a superior welding technique in comparison to some conventionally used welding process and weld groove design.

2.1 AUSTENITIC STAINLESS STEEL (ASS)

Austenitic stainless steels were invented in Essen, Germany [Padilha and Rios 2002] in the beginning of the 20th century. Their continuous development with substantial and minor additions of various alloying elements have resulted in its numerous applications essentially in chemical, pharmaceutical, petrochemical, civil constructions, transportation, nuclear power industries. These steels primarily contain 16-26% Cr, 8-24% Ni + Mn, normally below 0.15% C and small amounts of a few other elements such as Mo, N, Ti, Nb (Cb) and Ta. The balance between the Cr and Ni + Mn is normally adjusted to suppress austenite/ferrite transition temperature such that a microstructure of 90-100% austenitic grains in the matrix can be obtained at ambient temperature [Covert and Tuthill 2000, Padilha and Rios, 2002, Folkhard 1984].

2.1.1 Classification and its Application

These alloys are grouped in the 300 and 200 series, respectively, in the older but commonly used American Iron and Steel Institute (AISI) system. These older nomenclatures are now being replaced by the, Unified Numbering System (UNS) developed by the Society for Automotive Engineers (SAE) and the American Society for Testing and Materials (ASTM). These groups have developed a six character notation that assigns a unique designator to metals and alloys in a way that consistently defines a material [Covert and Tuthill 2000]. Chemical compositions of austenitic stainless steels as per AISI and UNS method are as given in Table-2.1. In these steels along with iron the main components are Cr to improve corrosion resistance and Ni to stabilize austenite. Chromium contents range from 15 to 26 % and nickel contents from 5 to 37 %. The 200 series have a comparatively lower Ni content than the 300 series. But these steels have a relatively high Mn content up to about

15.5 % and also a high N content that partly replaces Ni as a strong austenite stabilizer. In few compositions 2 to 4 % of Mo is also introduced to promote solid solution hardening and improving the resistance against pitting corrosion [Folkhard 1984].

Table-2.1: The standard compositions of common austenitic stainless steels classified according to the American Iron and Steel Institute (AISI)

Type	UNS No.	Composition, %(a)							
		C	Mn	Si	Cr	Ni	P	S	Other
201	S20100	0.15	5.5-7.5	1.00	16.0-18.0	3.5-5.5	0.06	0.03	0.25N
202	S20200	0.15	7.5-10.0	1.00	17.0-19.0	4.0-6.0	0.06	0.03	0.25N
205	S20500	0.12-0.25	14.0-15.5	1.00	16.5-18.0	1.0-1.75	0.06	0.03	0.32-0.40N
301	S30100	0.15	2.0	1.00	16.0-18.0	6.0-8.0	0.045	0.03	...
302	S30200	0.15	2.0	1.00	17.0-19.0	8.0-10.0	0.045	0.03	...
302B	S30215	0.15	2.0	2.0-3.0	17.0-19.0	8.0-10.0	0.045	0.03	...
303	S30300	0.15	2.0	1.00	17.0-19.0	8.0-10.0	0.20	0.15 min	0.6 Mo(b)
303Se	S30323	0.15	2.0	1.00	17.0-19.0	8.0-10.0	0.20	0.06	0.15 min Se
304	S30400	0.08	2.0	1.00	18.0-10.0	8.0-10.5	0.045	0.03	...
304H	S30409	0.04-0.10	2.0	1.00	18.0-20.0	8.0-10.5	0.045	0.03	...
304L	S30403	0.03	2.0	1.00	18.0-20.0	8.0-12.0	0.045	0.03	...
304LN	S30453	0.03	2.0	1.00	18.0-20.0	8.0-12.0	0.045	0.03	0.10-0.16N
302Cu	S30430	0.08	2.0	1.00	17.0-19.0	8.0-10.0	0.045	0.03	3.0-4.0Cu
304N	S30451	0.08	2.0	1.00	18.0-20.0	8.0-10.5	0.045	0.03	0.10-0.16N
305	S30500	0.12	2.0	1.00	17.0-19.0	10.5-13.0	0.045	0.03	...
308	S30800	0.08	2.0	1.00	19.0-21.0	10.0-12.0	0.045	0.03	...
309	S30900	0.20	2.0	1.00	22.0-24.0	12.0-15.0	0.045	0.03	...
309S	S30908	0.08	2.0	1.00	22.0-24.0	12.0-15.0	0.045	0.03	...
310	S31000	0.25	2.0	1.50	24.0-26.0	19.0-22.0	0.045	0.03	...
310S	S31008	0.08	2.0	1.50	24.0-26.0	19.0-22.0	0.045	0.03	...
314	S31400	0.25	2.0	1.5-3.0	23.0-26.0	19.0-22.0	0.045	0.03	...
316	S31600	0.08	2.0	1.00	16.0-18.0	10.0-14.0	0.045	0.03	2.0-3.0 Mo
316F	S31620	0.08	2.0	1.00	16.0-18.0	10.0-14.0	0.20	0.10 min	1.75-2.5 Mo
316H	S31609	0.04-0.10	2.0	1.00	16.0-18.0	10.0-14.0	0.045	0.03	2.0-3.0 Mo
316L	S31603	0.03	2.0	1.00	16.0-18.0	10.0-14.0	0.045	0.03	2.0-3.0 Mo
316LN	S31653	0.03	2.0	1.00	16.0-18.0	10.0-14.0	0.045	0.03	2.0-3.0 Mo; 0.10-0.16 N
316N	S31651	0.08	2.0	1.00	16.0-18.0	10.0-14.0	0.045	0.03	2.0-3.0 Mo; 0.10-0.16 N
317	S31700	0.08	2.0	1.00	18.0-20.0	11.0-15.0	0.045	0.03	3.0-4.0 Mo
317L	S31703	0.03	2.0	1.00	18.0-20.0	11.0-15.0	0.045	0.03	3.0-4.0 Mo
321	S32100	0.08	2.0	1.00	17.0-19.0	9.0-12.0	0.045	0.03	5 x %C min Ti
321H	S32109	0.04-0.10	2.0	1.00	17.0-19.0	9.0-12.0	0.045	0.03	5 x %C min Ti
330	N08330	0.08	2.0	0.75-1.5	17.0-20.0	34.0-37.0	0.04	0.03	...
347	S34700	0.08	2.0	1.00	17.0-19.0	9.0-13.0	0.045	0.03	10 x %C min Nb
347H	S34709	0.04-0.10	2.0	1.00	17.0-19.0	9.0-13.0	0.045	0.03	8 x %C min-1.0 max Nb
348	S34800	0.08	2.0	1.00	17.0-19.0	9.0-13.0	0.045	0.03	0.2 Co; 10 x %C min Nb; 0.10 Ta
348H	S34809	0.04-0.10	2.0	1.00	17.0-19.0	9.0-13.0	0.045	0.03	0.2 Co; 10 x %C min-1.0 max Nb; 0.10 Ta
384	S38400	0.08	2.0	1.00	15.0-17.0	17.0-19.0	0.045	0.03	...

(a) Single values are maximum values unless otherwise indicated. (b) Optional

Austenitic stainless steels are the most important class of corrosion resistant metallic materials. These steels were primarily developed for low temperature services suitable for handling, storage, or transportation of liquefied gases, such as nitrogen, oxygen, hydrogen, and helium which boil at cryogenic temperatures (below about $-101^{0}C$). The danger at low temperatures is brittle fracture, which can result in catastrophic destruction of complex engineering structures and equipment. Hence in addition to yield and tensile strengths, toughness and thermal expansion characteristics of a material are important because a large change in service condition from cryogenic temperature to room temperature can impose rather high stresses on equipment. Many steels perform admirably in relatively

6

low temperature service. However, for cryogenic temperature applications, the austenitic stainless steels are an excellent choice because they are relatively easy to fabricate and weld, do not require heat treatment after fabrication, and exhibit relatively high strength with excellent stability and toughness at significantly low temperatures [Peckner and Bernstein 1977, Covert and Tuthill 2000].

The austenitic stainless steels, due to their good resistance to oxidation, are also used in various elevated temperature applications such as boilers, nuclear reactors etc, which require compatible strength at high temperatures. In these alloys creep resistance with increasing temperature and service life requirements is achieved by solid solution and particle strengthening mechanisms. The substantial addition of alloying elements such as titanium, vanadium, niobium, nitrogen, molybdenum etc in ASS result in solid solution strengthening by formation of finely dispersed MC type carbides which provide increased creep resistance [Folkhard 1984, Peckner and Bernstein 1977].

2.1.2   Heat Effect on ASS

Austenitic stainless steels are generally put to service in the solution-annealed condition as they are quenched in water or other fast cooling media depending on the section size and distortion considerations from the annealing temperature (1040^{0}C-1130^{0}C). Thus, annealing has a different meaning than it has for carbon and low alloy steels, which are generally slowly cooled from the annealing temperature. The purpose of the annealing in ASS is either to eliminate and effect of prior work or to dissolve any carbide that may be present or both. However specific time-temperature combinations required represents a compromise between achieving the primary purpose and avoiding excessive grain growth. Thus ASS prone to sensitisation when subjected to improper annealing may result in intergranular corrosion problems in the temperature range of 723-1123K because of carbide precipitation at grain boundaries of the microstructure resulting in premature failures of

fabricated components [Covert and Tuthill 2000, Peckner and Bernstein 1977]. The temperature range leading to formation of detrimental phases are also often encountered during isothermal heat treatment of the fabricated components for stress relieving purpose, prolonged service at elevated temperatures, slow cooling from higher temperatures, improper heat treatments in the heat affected zone (HAZ) of the weldments or hot working of the material. Hence in order to analyse the influence of heat effect, phase diagrams are used to predict the precipitation of phases in the austenitic stainless steels [Folkhard 1984].

Austenitic stainless steels attain their corrosion resistance essentially based on two influential factors: high chromium content that provides a protective oxide film layer and a high nickel content that retains austenite in the matrix. Thus the base composition is normally a Fe–Cr–Ni alloy. However, in practice the situation becomes more complex especially in presence of several other elements such as, Mo, Mn, C and N amongst others. In such a complex situation one can almost never have a single austenite phase but invariable existence of some other phases in the matrix occurs. These phases are, with few exceptions, undesirable and they can be detrimental to the corrosion and mechanical properties [Padilha and Rios 2002]. Hence in order to understand the metallurgical reactions occurring during solidification various binary phase diagrams such as Fe–Cr, Fe–Ni, Cr–Ni, Fe–Mo, Fe–Ti, Ni–Ti, Fe–Nb, Fe–Mn and Fe–Si showing formation of various phases having detrimental effect on austenitic stainless steel are consulted for prediction of microstructure. The Fe–Cr–Ni and Fe–Cr–Mo ternary diagrams and the quaternary Fe–Cr–Ni–Mo diagram are also discussed by the researchers considering its deleterious phase formations in ASS [Koseki and Flemings 1996, Padilha and Rios 2002]. However as most of the stainless steel compositions in wide use occur on the iron-rich side of the ternary around 70wt. % iron, the ternary phase diagram as shown in Fig. 2.1 is commonly used to identify the primary solidifying phases or solidification modes for various compositions.
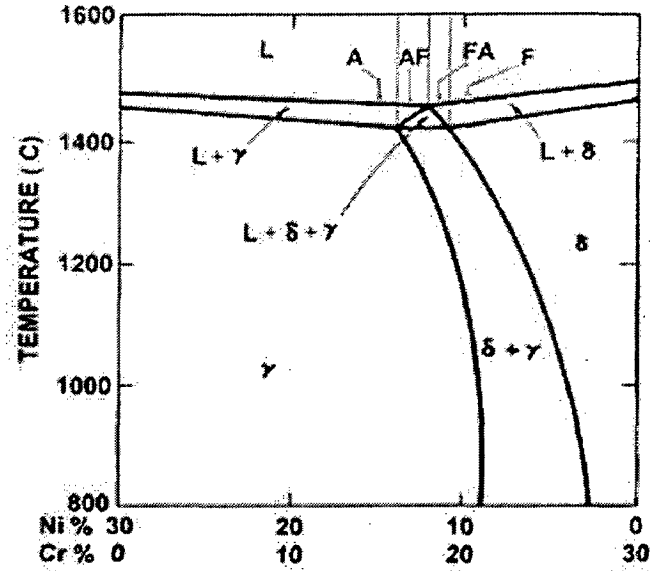
Fig. 2.1: Pseudobinary section of the Fe–Cr–Ni ternary diagram at 70% Fe, showing solidification modes; A - fully austenitic, AF - austenitic–ferritic, FA - ferritic–austenitic and F - fully ferritic. [Shankar et.al 2003b]

In ASS four distinct solidification modes exist as shown in Fig. 2.1 depending upon alloy composition viz., fully FCC solidification (A), primary FCC plus eutectic reaction (FCC + BCC) at the terminal stage (AF), primary BCC plus eutectic reaction (BCC + FCC) at the terminal stage (FA) and fully BCC solidification (F). [Folkhard 1984, Shankar et.al 2003b, Rajashekhar et al 1997]

$$L \rightarrow (L + \gamma) \rightarrow \gamma \qquad \text{(A mode)}$$

$$(Cr_{eq}/ Ni_{eq}) < 1.25 \qquad (2.1)$$

$$L \rightarrow (L + \gamma) \rightarrow (L + \gamma + \delta) \rightarrow \gamma + \delta \qquad \text{(AF mode)}$$

$$1.25 < (Cr_{eq}/ Ni_{eq}) < 1.48 \qquad (2.2)$$

$$L \rightarrow (L + \gamma) \rightarrow (L + \delta + \gamma) \rightarrow \delta + \gamma \qquad \text{(FA mode)}$$

$$1.48 < (Cr_{eq}/ Ni_{eq}) < 1.95 \qquad (2.3)$$

$$L \rightarrow (L + \delta) \rightarrow \delta \qquad \text{(F mode)}$$

$$(Cr_{eq}/ Ni_{eq}) > 1.95 \qquad (2.4)$$

Where,

$Cr_{eq} = [\%Cr] + 1.5[\%Si] + [\%Mo] + 0.5[\%Nb] + 2[\%Ti]$

$Ni_{eq} = [\%Ni] + 0.5[\%Mn] + 30[\%C]$

9

These equations show that higher ratio of Cr_{eq}/Ni_{eq} favours a transition to primary δ ferrite solidification, while at lower ratio of Cr_{eq}/Ni_{eq} primary austenite (γ) phase nucleates and solidifies. Elements such as Cr, Si, Mo, Nb and Ta increase the ratio of Cr_{eq}/Ni_{eq} whereas, Ni, Mn and C decrease the ratio of Cr_{eq}/Ni_{eq}. The critical value of the ratio of Cr_{eq}/Ni_{eq} corresponding to the transition from primary austenite to ferritic solidification increases from 1.43 to 1.55 with increasing growth rate [Inoue et al 1995, Suutala 1983].

2.1.3   Stress Effect

Stresses in any material can be introduced by an external loading, arising out of service conditions or mechanical working and fabrication process. Out of mechanical working or forming process, rolling and forging are largely known as the means to introduce significant amount of stresses during the process that may affect the phase transformation behaviour in the material [Parvathavarthini and Dayal 2002]. Similarly during the fabrication process like arc welding or fusion welding, the differential of expansion and contraction behaviour of material also introduces stresses in the area of joining influencing the phase transformation behaviour in this region [Elmer et al 1982]. In all the above cases of mechanical working, hot forming as well as fabrication, the material may also have some locked in stresses in the matrix that may influence the properties of material subsequently under the service condition. However in contrast to hot rolling and forging wherein temperature of base metal does not cross its melting point, weld metal solidifies from the temperature much above its melting point at a comparatively higher solidification rate. This results in significant amount of thermal stress distribution depending on both the difference in coefficient of thermal expansion (CTE) between the weld and base metals and the temperature change from the stress free temperature [Elmer et al 1982]. When the tensile strained metal is welded, the cracks form in the heat affected zone because of a sufficiently high level of residual surface stresses and precipitation of brittle secondary phases [Erve et al 1997].

10

In ASS based on DeLong diagram the mean CTE plotted as a function of Cr and Ni equivalents have been shown in Fig. 2.2. The figure shows three different regions of interest: single phase austenite field (A), two phase austenite and ferrite field (A + F) and the three phase austenite, ferrite and martensite field (A+F+M). The CTE is influenced by the presence of these phases, wherein highest CTE of around 19μm/m/ ^{0}C has been marked in the austenite phase field at a composition of 14 Ni_{eq} and 18 Cr_{eq}. The presence of ferrite in a stainless steel at room temperature will reduce its CTE due to reduction in its transformation to denser austenite phase at elevated temperatures. A contractive strain of 4.5×10^{-5} has been measured and shown to accompany each percent ferrite that transforms to austenite. This strain is directly associated with this phase transformation and can have the effect of loading the weld joint in tension [Elmer et al 1982].

Fig. 2.2: Mean coefficient of thermal expansion plotted on the Delong diagram as a function of chromium and nickel equivalents [Elmer et al 1982].

In stabilized ASS inspite of sufficient addition of niobium, micro stress leading to tensile strain exists in the austenite matrix around the undissolved NbC particles. It primarily occurs due to the mismatch of thermal contraction between NbC and austenite leading to $M_{23}C_6$ nucleation at the interface between undissolved NbC particles and the austenite

matrix. It has been further observed that the morphologies of $M_{23}C_6$ grown around undissolved NbC particles are different from those of $M_{23}C_6$ grown at other sites. Hence the basic intention of addition of Nb to bind C and avoid harmful $M_{23}C_6$ precipitation could not be fulfilled due to micro stress generation [Sarafianos 1992, Sasmal 1997].

2.2 ARC WELDABILITY OF ASS

Many metallurgical reactions take place during welding which influence crystallization structure, segregations, phase transformations, precipitation and embrittlement [Folkhard 1984] depending primarily upon alloy composition. With proper understanding of phase diagrams it is possible to make satisfactory predictions of these complex metallurgical reactions to a certain extent. However the phase diagrams have limitations due to the complexity of multi-component thermodynamic calculations and also due to the transformation kinetics that may prevent the attainment of the equilibrium phases. Regarding the first limitation, the number of relevant components are often more than five and published diagrams are rarely found to contain more than four components [ASM Handbook (Vol.3),1992]. As to the second limitation, the diffusion of alloying elements in austenite can be very slow and the precipitation of certain intermetallic compounds can take thousands of hours [Folkhard 1984]. Hence in case of welding of austenitic stainless steel the equilibrium phase diagrams are often found insufficient to precisely predict the resulting microstructure of solidification. However the best known method in this regard is followed by consideration of the Schaeffler and Delong diagrams.

Schaeffler and Delong divided the alloying elements in two groups according to their basic characteristics as ferrite and austenite stabilizers. Depending upon the degree of influence of an element on ferrite or austenite formation and to retain their stability at room temperature the expressions in terms of equivalent to chromium content and as equivalent to

nickel content was developed [Folkhard 1984]. Schaeffler's diagram as shown in Fig. 2.3, therefore allowed an estimation of the microstructure primarily in terms of δ ferrite and austenite formation as a function of the steel composition in weld metal. In many applications, the ability to control the δ ferrite content of stainless steel weld metal becomes important in order to negotiate its hot cracking resistance, corrosion resistance, mechanical properties and fracture toughness. Although the "percent ferrite" has been used as an indicator of ferrite measurement for decades, it is often marked [Shanker et al 2003b] as unreliable with large error because of lack of reference standards or agreement to calibration procedure. As a result, the index of measurement is chosen as magnetic attraction scale expressing ferrite contents in weld metals as ferrite number (FN).
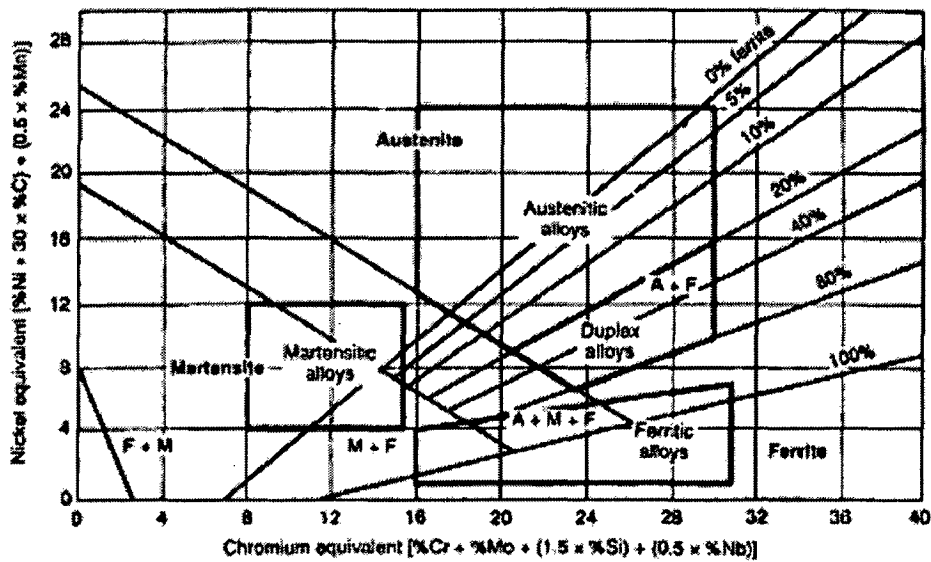
Fig. 2.3: Schaeffler's constitution diagram giving δ ferrite content in stainless steel. The compositional ranges of the ferritic, martensitic, austenitic, and duplex alloys have been superimposed on this diagram. [Shanker et al 2003b]

Schaeffer diagram however does not considers the powerful effect of N in promoting austenite at the expense of ferrite and is incorrect in its treatment of Mn. Manganese does not promote the high temperature formation of austenite at the expense of ferrite, as predicted by the diagram, although Mn does stabilize austenite in its low temperature transformation to

13

martensite [Vanderschaeve et al 1995]. Whereas, the DeLong diagram (Fig.2.4) which considers the effect of nitrogen is used as an important means for predicting the ferrite content of stainless steel weld metals as confirmed by its good agreement in case of shielded metal arc welds [Delong 1974]. However, the De Long diagram developed for low nitrogen containing austenitic stainless steels are not suitable for the higher manganese, higher nitrogen grades. For example, manganese content beyond 4 % is not potent as an austenite stabilizer, and may in fact act as a ferrite former [Shankar 2003b].
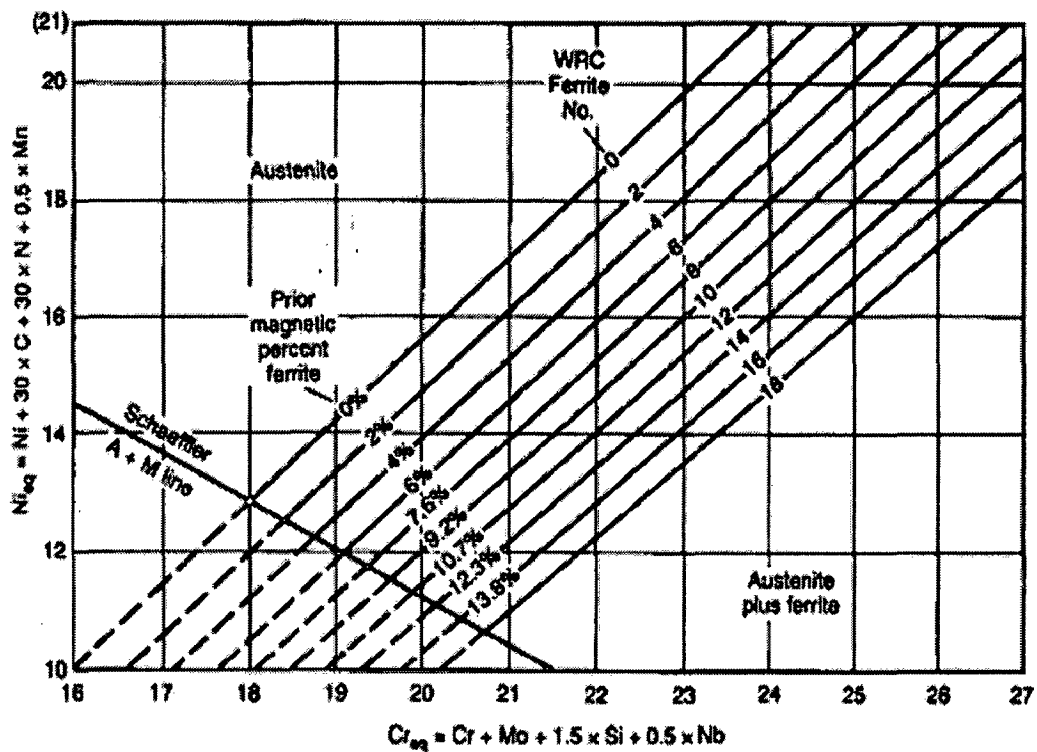
Fig. 2.4: DeLong constitution diagram for stainless steel weld metal [Delong 1974].

Siewert proposed a new ferrite diagram (Fig. 2.5) that predicted ferrite up to 100FN and thus covered the complete range of austenitic and duplex stainless steels. The accuracy of this diagram is superior to that of the DeLong diagram, since the bias due to a higher coefficient for N has been removed. More importantly from the point of view of cracking, the solidification mode boundaries have been included [Siewert et.al 1988, Shankar et al 2003b].
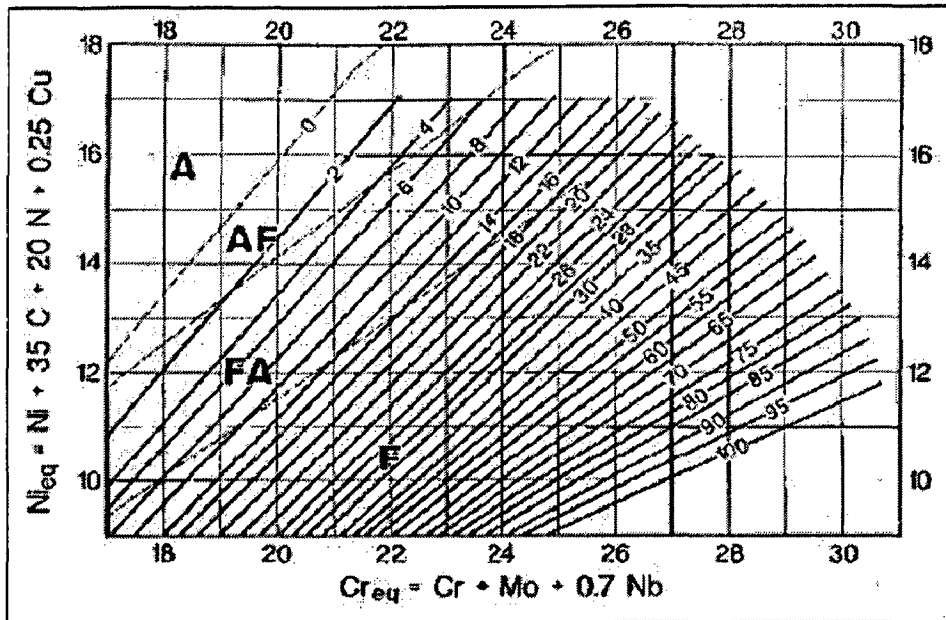
Fig. 2.5: The WRC-92 constitution diagram for weld metal ferrite, including solidification mode boundaries [Siewert et al 1988].

2.2.1 Conventional ASS

The presence of ferrite in an austenitic structure as it is resolved with the help of schaeffer, De Long or WRC-92 constitution diagram causes numerous other problems, such as lower toughness, deterioration of corrosion properties, brittle intermetallic phase formations at high service temperatures, and so forth. It is now well known that the sequence of solidification, rather than the retained ferrite content, is more relevant to cracking susceptibility of weld [Lundin et al 1993]. More significantly, the phase balance and evolution of the structure during solidification play a critical role. Hence mode of solidification which primarily depends on chemical composition along with weld pool cooling rate plays important role in determining the metallurgical characteristics of weld joint [Folkhard 1984, Cieslak and Ritter 1985,]. In short the cooling rate and chemical composition of the alloy influence (a) the primary mode of solidification (b) solute redistribution and second phase formation during solidification and (c) the nucleation and growth behaviour of the ferrite-to-austenite phase transformation during cooling [Hunter and Ferry 2002, Cieslak and Savage 1980].

15

2.2.1.1 Effect of chemical composition

All austenitic stainless steels depending upon alloy composition are susceptible to carbide precipitation and/or intermetallic phase precipitation under adverse condition of thermal exposure during welding and also in service.

Carbide precipitation

Carbon solubility in austenite decreases rapidly as nickel content increases and the alloy temperature decreases. As a consequence the commonly observed precipitation of $M_{23}C_6$ carbide takes place in austenitic stainless steel where, M represents Cr, Fe, Mo and Ni. The addition of "stabilizing elements" such as Ti, Nb and V reduces the carbon solubility even further invariably resulting in MC type carbides, where M represents Ti, Nb and/or V. The presence of molybdenum in certain alloys can cause the precipitation of η, a M_6C carbide, where M represents Fe, Mo and Cr [Gill and Gnanamoorthy 1982, Pujar et al 1998]. As all the three types of carbides primarily influence hardness, toughness and corrosion susceptibility of the matrix, their precipitation phenomena play an important role especially in multi-pass weld deposition affecting weldabilty of ASS joints [Andren et al 1980, Gill et al 1986, Ritter et al 1983].

Chromium rich carbides ($M_{23}C_6$) which contains two to four times the amount of chromium than the base material, precipitate along the grain boundaries followed by incoherent twin boundaries, coherent twin boundaries and finally at the dislocations within the grains. As they grow, carbon rapidly diffuses to the carbide-matrix interface and enters the growing carbide. Chromium diffuses much more slowly and is usually drawn from a volume of material around the grain boundary. This process leads to depletion of chromium content markedly below the resistance limit of approximately 11.5% chromium along the grain boundaries, and steel in this condition is often referred to as being sensitised [Folkhard 1984, Braint and Andresen1988, Briant 1987, Cui Phd. Thesis 2004, Hull 1952]

The MC (M = Ti, Zr, Hf, V, Nb and Ta) carbides are very stable and are invariably present in stabilized austenitic stainless steels such as AISI 321 (Ti stabilized), AISI 347 and 348 (Nb stabilized). The MC carbide precipitation is predominantly intragranular, on dislocations and stacking faults with fcc, NaCl type, structure [Folkhard 1984, Harris and Nag 1975]. However, MC precipitation at grain boundaries can also occur. The addition of stabilizing elements that form MC carbides, normally aims at hindering $M_{23}C_6$ precipitation and its associated undesirable consequences, particularly susceptibility to intergranular corrosion. However the addition of Ti, Zr or Hf results, unavoidably, in the formation of MN nitrides and $M_4C_2S_2$ carbosulfides that are even more stable than the MC carbide. Laves phase, Fe_2M (M = Ti, Zr, Hf, V, Nb and Ta), can also form. On the other hand NbC particles formed at extrinsic grain boundary dislocations and at grain boundary topographical defects [Harris and Nag 1975] gets dissolved again in the matrix closely below or besides the fusion line in the high heated part of the heat affected zone both in base material and in previously laid passes by deposition of further weld runs. The amount of carbon dissolved in this way can only partly precipitate again as niobium carbide during the rapid cooling after welding, with the residual carbon remaining in the matrix [Villafuerte 1990, Vitek et al 1983]. Hence it is worthy to note that the addition of stabilizing elements does not wholly suppress precipitation of $M_{23}C_6$, even if one adds a large amount of stabilizing elements. $M_{23}C_6$ carbides have been found in stabilized steels in which the Ti/C ratio was as high as 34 when the stoichiometric ratio is only 5. The precipitation of $M_{23}C_6$ becomes comparatively easier in relation to that of MC carbides as the temperature is decreased. For example at around 600°C, $M_{23}C_6$ precipitation occurs before the MC carbide precipitation. This type of carbide has a particularly large resistance to coarsening [Padilha and Rios 2002].

The carbides of this type M_6C (M=Fe, Cr, Mo, W, Nb and V), are also known as η-carbide, often found in austenitic stainless steels containing molybdenum, tungsten and

niobium. The M_6C carbide invariably contains more than one metallic element, requiring the presence of at least three types of atoms and is usually represented by the formulae A_3B_3C or A_4B_2C. The number of carbon atoms per unit cell is variable and there is evidence of this being carbon sub-stoichiometric carbide. This type of carbide has an fcc, diamond type, structure. Due to the size of their unit cells, M_6C and austenite might be expected to show a cube-on-cube orientation relationship [Folkhard 1984, Padilha and Rios 2002]

Intermetallic phases

Three intermetallic phases most frequently found in the austenitic stainless steels are sigma phase (σ), chi phase (χ) and Laves phase (η). Precipitation of these topologically close packed phases from delta ferrite during the thermo-mechanical processing of the alloy is normally associated with undesirable consequences like matrix impoverishment in alloying elements such as chromium, molybdenum, and niobium as well as loss of ductility, toughness and corrosion resistance [Folkhard 1984, Barcik 1983, Shaikh et al 1995].

Sigma-phase appears in several binary, tertiary, and quaternary systems such as Fe–Cr, Fe–Mo, Fe–V, Fe–Mn, Fe–Cr–Ni, Fe–Cr–Mo, Fe–Cr–Mn and Fe–Cr–Ni–Mo [Folkhard 1984]. The σ-phase occurs for an electron/atom ratio between 5, 6 and 7 and for an atomic radius ratio, in binary systems between 0.96 and 1.16. Sigma phase precipitation with equiaxed morphology in austenitic stainless steels occurs between 550 and 900°C at grain boundaries, especially on triple junctions, incoherent twin boundaries and intra granular inclusions [Iamboliev et.al, 2003, Song et al 1996a]. A typical σ-phase chemical composition found in AISI 316 or 316L austenitic stainless steels has the following (in %): 55 Fe; 29 Cr; 11 Mo and 5 Ni. The composition of sigma phase in austenitic stainless steels can be approximately written as: $(Fe, Ni)_3(Cr, Mo)_2$ [Song et al 1996a]. Alloying elements such as chromium, manganese, molybdenum, tungsten, vanadium, silicon, titanium, niobium, and

tantalum favour σ-phase formation, whereas nickel, cobalt, aluminum, carbon and nitrogen hinder its precipitation [Folkhard 1984]. In stabilized steels sigma phase precipitates via the ferrite (δ-phase) arising as a result of destabilizing of the austenite during precipitation of the Ti-C carbide. However in un-stabilized AISI 316 steel the σ-phase nucleates directly in the $M_{23}C_6$ carbide and chi-phase [Padilha and Rios 2002, Song et al 1996a, Sourmail et al 2003].

Sigma phase appears as an iron-chromium compound FeCr with a tetragonal crystal structure and a regular arrangement of one atom of iron and one atom of chromium. As observed in iron-chromium constitution diagram σ-phase starts to precipitate from temperatures below 820^0C, with the precipitation range being greatly expanded with the falling of temperatures [Malone 1967]. The formation of σ-phase in stainless steels is decisively influenced by the possibility of local chromium enrichment of about 20% in the steel, to about twice that amount in the phase. The chromium diffusion, which is necessary for this enrichment to take place, also seems to determine the lower temperature limit of sigma phase precipitation. This limit often overlaps the upper limit of the area of grain decay by intergranular corrosion attack that is governed by chromium diffusion [Vitek and David 1986]. In stainless steels, sigma phase rapidly precipitates in ferrite with chromium contents more than 16%. This also explains why in austenitic weld metal, which for reasons of improved crack resistance often shows ferrite contents of 5-12%, sigma phase predominantly precipitates in the dispersed ferrite crystals having higher diffusion potential of chromium. The area of sigma phase precipitations as well as the transformation kinetics are influenced by the structural requirements and alloying additions. The presence of carbon in austenite as a result of the solution annealing treatment will considerably slow down sigma phase formation until the precipitation of the carbide $M_{23}C_6$. With the precipitation of carbide, surrounding area of the matrix also becomes depleted of chromium and the chromium content of the carbon-free zones so created drops below the precipitation limit for sigma phase, which is

located at 16% chromium. This means a further slowdown in the precipitation of sigma phase. Precipitation can only start if the chromium depletion is equalized by chromium diffusion from the surrounding areas. In short sigma phase precipitation depends on following three factors: (i) higher chromium content, (ii) lower carbon content and (iii) presence of about 15% δ ferrite in the matrix [Vitek and David 1986].

On the other hand molybdenum exerts relatively strong influence on the precipitation of sigma phase. The sigma phase range is not only shifted to lower chromium and higher nickel contents, but also to higher temperatures. With higher molybdenum contents, freedom from precipitations can also be achieved by the addition of nitrogen. Molybdenum possesses good solubility in sigma phase and hence speeds up the precipitation of sigma phase. With an increase in molybdenum content beyond 2.5%, intermetallic phases containing molybdenum may also appear which influences or blocks the precipitation of sigma phase [Padilha and Rios 2002, Song et.all. 1996a]. It is established that the amount and morphology of sigma phase are the key factors in determining the strength, total elongation and extent of work hardening. The amount and morphology of sigma phase depends on the relative kinetics of various transformations, such as dissolution of delta-ferrite, growth of carbides, change of sigma phase, and the relative stability of the phases at the corresponding temperature of aging [Folkhard 1984, Gill et al 1989, Gill and Gnamoorthy 1982]. The minimum amount of ferrite required depends on alloy composition within a range of 0 to 6 FN [Vitek and David 1986].

Sigma phase transformation is governed by nucleation rate and not by speed of growth. Fine grain structure formed by recrystallization and deformation promotes nucleation by means of the large atomic movements involved. It is likely that ferrite in an austenite matrix accelerates sigma phase formation by providing more sites for the nucleation event. In

addition, the shrinkage of ferrite associated with its enrichment during aging provides a moving interface, with concurrent large scale atomic movements conducive to sigma phase formation [Gill and Gnanamoorthy 1982]. However, it can be concluded that σ-phase precipitation has a very slow kinetics and precipitate formation can take hundreds and sometimes thousands of hours primarily due to following reasons

(i)   Carbon and nitrogen are insoluble in σ phase; as a consequence, σ-phase normally appears only after the precipitation of carbide and nitride when the matrix is impoverished in carbon and nitrogen;

(ii)   Its nucleation is difficult on account of its crystal structure being complex and very different from the parent austenite as sigma grains contain numerous stacking faults; and (iii) it is very rich in substitutional elements thus requiring protracted diffusion times [Folkhard 1984, Song et al 1996a]

Chi (χ) phase is an intermetallic compound containing primarily Fe, Cr, and Mo. It is a body-centered-cubic phase (α-Mn structure) with a lattice parameter of $a_0 = 8.920A$. χ phase is often found in austenitic and ferritic stainless steels that contain molybdenum [Cieslak et.al 1984, Padilha and Rios 2002]. Molybdenum influences the process of carbide precipitation in stainless chromium-nickel austenitic steels, since this alloying element reduces the solubility of carbon in austenite. In molybdenum containing chromium-nickel austenitic steels the chromium-iron mixed carbide $M_{23}C_6$ is precipitated first at temperatures of 650-850^{0}C. With the prolonged annealing times this carbide picks up molybdenum, which is being a carbide forming element becomes increasingly dissolved in $M_{23}C_6$, with a simultaneous drop in carbon content. Iron–chromium-molybdenum mixed carbides formed are then converted to the chi phase $(Fe_{36}Cr_{12}Mo_{10})^6$ with about 1% carbon. For unstabilized

chromium-nickel-molybdenum austenitic stainless steels the precipitation scheme of carbon

containing phases are as follows [Folkhard 1984]:

$$(Fe, Cr)_{23}C_6$$
$$\downarrow$$
$$+ Mo$$
$$\downarrow$$
$$(Fe, Cr)_{21}Mo_2C_6$$
$$\downarrow$$
$$+ Mo$$
$$\downarrow$$
$$(Fe, Cr, Mo)_6C$$
$$\downarrow$$
$$+ Mo$$
$$\downarrow$$
$$(Fe_{36}Cr_{12}Mo_{10}) = \text{Chi-Phase}$$
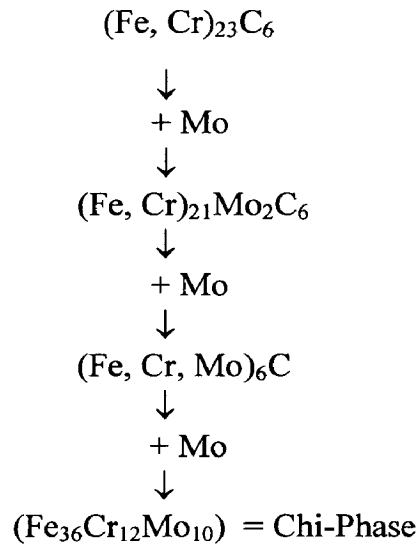
Carbon does not retard the precipitation of chi phase in austenitic stainless steels. χ-

phase can dissolve up to 0.24 % carbon, but only 0.007 % nitrogen addition delays the

precipitation. χ-phase formation in the solid state generally is enhanced by increasing

molybdenum and chromium content with decreasing nitrogen content. χ-phase has been

reported to form in the temperature range of 649-950^{0}C. In addition, chi has been found as a

eutectic constituent in alloys that had been processed with comparatively slow solidification

rate with lower melting point and surface tension causing hot cracking problems [Padilha and

Rios 2002,].

In general the χ-phase occurs for an electron/atom ratio between 6.3 and 7.8. The

precipitation range of the chi phase is somewhat narrower than that of sigma phase (550 to

900°C) and depends on Mo content of the steel. Its composition is similar to that of the σ -

phase, but in contrast to σ -phase, carbon can dissolve in the χ-phase. Owing to its ability to

dissolve carbon and relatively easier nucleation the χ-phase precipitation precedes σ -phase

formation. The χ-phase is found to form mainly on the grain boundaries, incoherent twin

boundaries, coherent twin boundaries, and on dislocations within the matrix [Cieslak et.al 1984, Padilha and Rios 2002].

Together with iron, molybdenum forms Laves phase (Fe_2Mo) with approximately 45% Mo [Folkhard 1984]. The Laves phases that occur more often in the austenitic stainless steels have a hexagonal close packed structure with stoichiometry A_2B. The major criterion for their formation is the tendency towards interstitial packing in the crystal lattice, which reaches a maximum at a ratio of atomic radii of B: A = 1.1225. The most common are Fe_2Mo, Fe_2Nb and Fe_2Ti, or a combination of all three, for example, $Fe_2(Mo, Nb, Ti)$. The Laves phases occur for electron/atom ratios between 6.33 and 8.0. The Laves phase is generally stable below 815°C, but it strongly depends on the Mo, Nb and Ti contents [Padilha and Rios 2002, Folkhard 1984].

In the iron-molybdenum constitution diagram, three phases appear between 45 and 55% molybdenum. The chi, sigma and Laves phase (Fe_2Mo) with approx. 45% molybdenum also known as η (eta) phase reaches down to relatively low molybdenum contents. The precipitation of these phases is additionally influenced by the constituent's carbon and nitrogen and precipitation kinetics. Regarding the influence of carbon and nitrogen, the precipitation kinetics of intermetallic phases is largely determined by the latters dissolution potential for these constituents [Folkhard 1984].

2.2.1.2 Effect of microstructure

In 308L weld metal δ ferrite is seen in both the dendritic and the interdendritic regions. Solidification in this case starts with the precipitation of ferrite and as the temperature is lowered the austenite becomes more stable and envelops the precipitated ferrite. As the austenite grows, micro segregations cause the liquid to become enriched with ferrite stabilizing

Cr upto a slightly greater extent than with nickel. As a result, the solidification changes back to the ferritic mode during the last stages. Another feature of this structure is that both the interdendritic ferrite and dendritic ferrite are connected at some places. This indicates that austenite does not envelop ferrite completely during the assumed peritectic reaction and perhaps liquid, austenite and ferrite were in equilibrium during the final stages of solidification. It has been observed by researchers that this structure provides the best resistance to solidification cracking [Gill et al 1989, Brooks et al 1983, Elmer et al 1989].

2.2.1.3 Effect of weld thermal cycle

While welding titanium stabilized austenitic stainless steel in order to avoid the excessive and uncontrollable burn off of titanium across the arc, particularly when welding with coated electrodes, niobium stabilized filler metals are used during welding [Harris and Nag 1975, Folkhard 1984]. However, both the Ti and Nb stabilized austenitic stainless steels are susceptible to hot cracking [Shanker et.al 2000, 2003b]. Hot cracking in stainless steels can occur in the fusion zone, in the base metal heat affected zone (BMHAZ), or in the heat-affected zone lying in previously deposited weld metal (WMHAZ) [Lundin and Savage 1980]. The cracking in the fusion zone has been attributed to the segregation of low melting constituents based on Nb or Ti, in association with S, P, and Si [Mandiang and Cizeron 1996, Shankar et al 2003b]. The formation of NbC-austenitic eutectic can further increase susceptibility to hot cracks. In the HAZ, the segregation takes place through solid-state mechanisms, and the extent of the cracking depends on metallurgical factors such as grain size and the presence of secondary phases where the formation of precipitates depends upon heat intensity of welding process in addition to bulk composition [Farrar 1987].

During solidification of unstabilized ASS with primary austenite (γ_p), the chromium, silicon, sulfur and phosphorus are rejected to the melt between the growing dendrites.

Depending upon weld thermal cycle it becomes sufficiently concentrated for "cellular" δ to form in this region. Conversely in FA mode, Ni along with considerably lower amount of sulphur and phosphorus is rejected ahead of the advancing interface during solidification until the concentration in the melt is sufficient for γ to form and this phase continues to grow. During further cooling diffusion controlled reaction with partitioning of Ni to the austenite and Cr to the ferrite, leaving only a Cr rich Ni lean ferrite core along the dendrite centre, results in the retention of stable "skeletal or vermicular ferrite" δ_p within the austenite at room temperature under normal arc welding conditions [Varin 1979, Vitek and David 1984].

Under more moderate solidification conditions, the primary ferrite transforms to austenite by either a peritectic reaction or a solid-state transformation. With the highest cooling rate, region of duplex $\gamma + \delta$ structure in Fe–Cr–Ni ternary diagram at 70% Fe shrinks resulting in change of solidification mode. The weld structures of type 308 and 312 steels are most sensitive to such rapid solidification. With highest cooling rates, the solidification mode of type 308 and 312 structure changes from duplex ferrite plus austenite to fully austenitic and fully ferritic respectively [Vitek et al 1983]. With the shift in solidification mode of duplex structure, eutectic ferrite enriched with Cr, Mo and Ni and depleted in Fe is formed during the terminal transient stage of solidification at the ferrite/austenite interface in comparison with primary δ-ferrite [Nage et al 2006].

2.2.1.4 *Effect of section size*

The increase in thickness of plate/pipe enhances the number of passes required to complete their weld joint. Hence in ASS low temperature sensitization (LTS) occurs in HAZ largely due to combination of the nucleation and subsequent low temperature heat treatments caused by multi-pass deposition [Herbsleb 1980, Krishnan and Rao 1991]. Therefore most of the studies concerning LTS in weldments of stainless steels have been carried out for HAZ.

However the weld metals of ASS are also in principle more easily sensitized than HAZ, because the weld metal of austenitic stainless steels have generally $\delta - \gamma$ duplex structure and the precipitation of chromium carbides at $\delta - \gamma$ grain boundaries occurs at much shorter time than that at γ grain boundaries [Mozhi et al 1987, Nishimoto et al 1995]. The integrated volume of chromium depleted region has been found out in type 308 stainless steel by estimating chromium content distribution in the matrix as a weighing function given by parameter ΔS. Estimation of ΔS as a function of time was carried out for the sensitizing process at the delta/gamma and gamma/gamma boundaries at the temperatures of 573, 673 and 773 K and the result obtained is as shown in Fig. 2.6 [Nishimoto et al 1995].
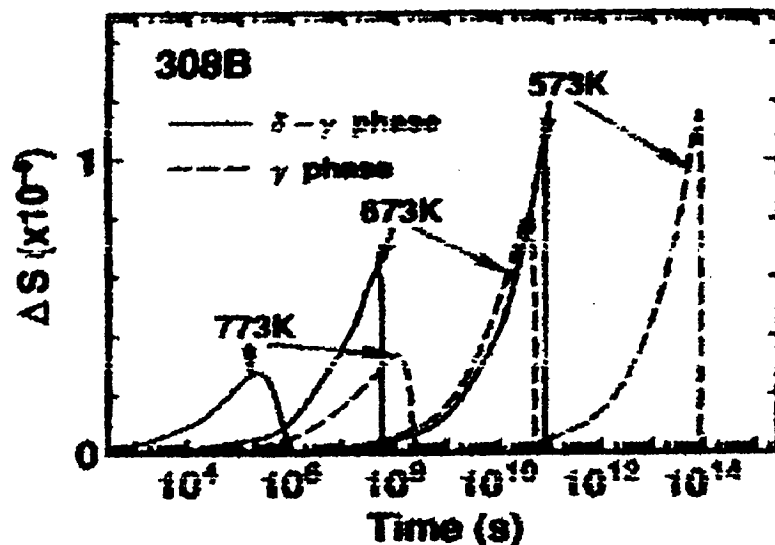
Fig. 2.6: Comparison of sensitizing behaviour of δ-γ phase and γ phase with calculated ΔS [Nishimoto et.al 1995].

The figure shows that ΔS first increases and then steeply decreases with increase in time. It further indicates that sensitization in the alloy with the delta-gamma duplex structure takes place in much shorter time than in that with the gamma single phase. At lower temperature, the difference in sensitization behaviours in both the cases is more pronounced. This result suggests that LTS would occur faster in weld metal than in HAZ.

2.2.2 Nitrogen Added ASS

Nitrogen-added stainless steels exhibit several unique characteristics such as superior strength at ambient as well as high temperatures, excellent corrosion resistance in various media and are candidate materials to replace other more expensive materials [Basak et al 1995, Baldev Raj et al 2002]. Alloying with nitrogen beyond the solubility limit markedly increases mechanism of strengthening due to lowering of the stacking fault energy and thus increases the yield strength of austenitic stainless steels, without any substantial loss of toughness [Vanderschaeve et al 1995]. Its addition partially substitutes carbon mainly by recovering the higher strength and elevated temperature properties associated with the lowering of carbon content. Moreover, precipitation kinetics of intermetallic compound formation in stainless steels is found be suppressed in stainless steels, when nitrogen is present at lower levels [Woo and Kikuchi 2002], though it can form nitrides, if its concentration exceeds certain level.

2.2.2.1 Effect of chemical composition

Nitrogen behaves as a strong austenite stabilizer in the weld metal. Its marked influence through modified Schaffler diagram on different phase formation is as shown in Fig. 2.7.

$$Cr_{eq} = Cr + 1.5Mo + 1.5W + 0.48Si + 2.3V + 1.75Nb + 2.5Al$$
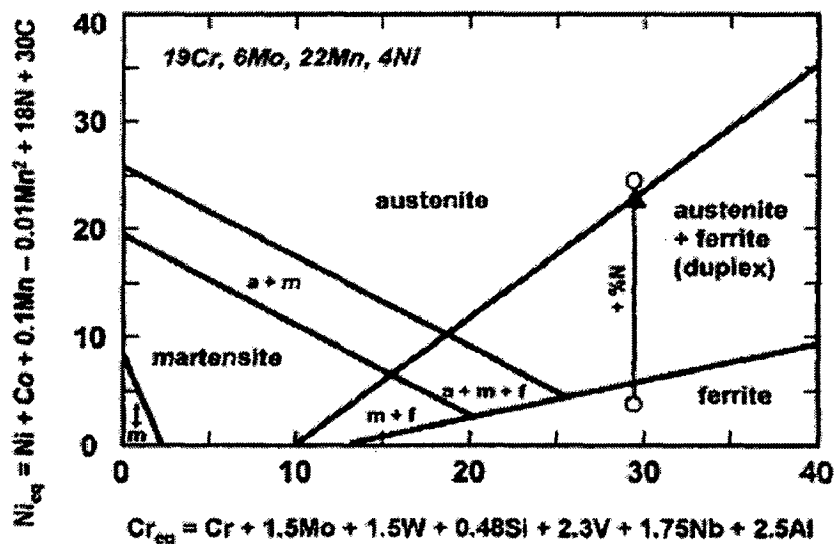
Fig. 2.7: Modified schaffler diagram for stainless steel weld metal [Woo and Kikuchi 2002].

Through the addition of 1% N, a purely ferritic stainless steel is rendered completely austenitic as marked by arrow in the Fig. 2.7. But, as to the weld metal containing a higher amount of nitrogen and or manganese, such description and prediction were found to be inaccurate. Thus the influence of nitrogen on weld metal was further evaluated by the researchers based on its influence on the δ ferrite content [Woo and Kikuchi 2002]. As a result various nitrogen coefficients where developed as shown in Table- 2.2 [Okagawa et al. 1983, Woo and Kikuchi 2002, Shankar et al 2003b].

Table-2.2: Various nitrogen coefficients determined in previous studies.

Researcher	Coefficient of N	N content (%)	Comment
DeLong	30	0.03-0.22	309, 310, 316, 410
Hull	18.4	0-0.15	309, 308L, 316, 316L
Espy	30(N-0.045) 22(N-0.045) 20(N-0.045)	0.13-0.33	4 nitronic series alloys
Hammer, Suutala	14.2	0.01-0.23	130 Austenitic SS
Mel'Kumor	20	0.05-0.46	Austenitic SS
Okagawa	13.4	0.04-0.29	GTA weld on 304L

Suutala stated that the solidification mode of austenitic stainless steel weld metal containing up to 0.23% nitrogen can be described by using Hammer's equivalents. On the contrary Okagawa reported that in nitrogen added type 304 welds, the nitrogen effect on ferrite content was smaller than that predicted by DeLong, and they estimated the nitrogen coefficient for nickel equivalent expression as 13.4, which was considerably lower than the coefficient of 30 determined by DeLong. Espy reported that the nitrogen effect as an austenite stabilizer decreased as nitrogen content increased, and proposed the modified Schaffler diagram, in which the nitrogen coefficient varied from 30 to 20 with nitrogen content. The discrepancies in the nitrogen effect results in a serious drawback in developing proper weld compositions to obtain the desired ferrite content and its distribution. Hence,

more systematic work is necessary to verify the nitrogen effect on solidification behaviours of stainless steel welds [Woo and Kikuchi 2002, Shankar et al 2003a]. Another drawback of non equilibrium diagram is it does not take into consideration the influence of the cooling rate and aging heat treatments [Padilha and Rios 2002].

In weld joints precipitation of all the phases not capable of dissolving nitrogen are shifted towards longer times. This means that nitrogen shifts the beginning of sigma phase formation to higher chromium contents and to longer time [Folkhard 1984]. Secondly precipitation of M_6C will be favoured to the detriment of $M_{23}C_6$, because the former is able to dissolve more nitrogen than the latter. Nitrogen addition also sometimes favours formation of nitrides. Nitrides that form in austenitic stainless steels can be grouped in two classes: (i) primary nitrides of type MN (M = Zr, Ti, Nb and V) formed in stabilized steels containing residual amounts of nitrogen (< 0.1 %); and (ii) secondary nitrides of the type M_2N (M = Cr, Fe), which precipitate in stainless steels containing high levels of nitrogen (0.1 to 0.9 %). Nitrogen is primarily added to stainless steel to improve its mechanical properties and corrosion resistance, and also because it is a strong austenite stabilizer. Due to the high stability and consequent low solubility of these nitrides, almost all nitrogen forms nitrides, particularly in Ti stabilized steels. These nitrides have a faceted morphology and their size is typically 10–15 μm [Padilha and Rios 2002]. If the solubility limit for nitrogen is exceeded in stainless steels, nitrogen precipitates as chromium nitride (Cr_2N) [Vanderschaeve et al 1995]. On the other hand, the maximum solubility of nitrogen in Fe–Cr–Ni or Fe–Cr–Mn–Ni austenite is about 0.9 %. This solubility decreases considerably with temperature below 1000°C. The $(Cr,Fe)_2N$ nitrides can precipitate continuously or discontinuously. The cellular precipitation of Cr_2N is a peculiar and complex phenomenon which involves two diffusion mechanisms: the diffusion of an interstitial element (nitrogen) and the diffusion of a substitutional one (chromium). The nucleation of the discontinuous precipitation arises from

a reduction of the surface energy of the precipitates. Furthermore, the precipitation growth is a non-steady state process, because the reaction is governed at first by the intergranular diffusion of chromium, and then tends to be controlled by its bulk diffusion [Woo and Kikuchi 2002]. In niobium stabilized ASS apart from niobium carbide and the mixed carbide Fe_3Nb_3C, the formation of carbo-nitride Nb(CN) and mixed nitride(CrNb)N also takes place. In general nitrogen depletion of the matrix due to precipitation of nitrides can make austenite unstable and it can make possible the formation of ferrite and sigma phase at aging temperatures [Padilha and Rios 2002]. On the other hand amount of δ ferrite in the weld metal is decreased by nitrogen addition in high nitrogen containing austenitic stainless steel resulting in increase in its susceptibility to solidification cracking [Shankar et al 2003b].

2.2.2.2 Effect of microstructure

The addition of nitrogen affects not only the composition of the weld but also the kinetics of solid-state transformation characteristics of delta ferrite. This is expected to help in obtaining weld with low residual delta ferrite content without encouraging solidification cracking incidences [Hertzman 2001, Okagawa et. al. 1983]. Thus the solidification mode in unstabilised ASS can be controlled by nitrogen addition. However its level in weld metal depends on welding parameters, compositions of filler metal and base metal, and other metallurgical factors.

Weld deposit

In weld metal the desired phase ratio is obtained by combination of nitrogen and increased nickel content. Nitrogen resides in weld metal in the following forms (i) interstitial nitrogen dissolved in the lattice structure – may collect around lattice defects, (ii) combined nitrogen present as nitrides, and (iii) occluded nitrogen in pores. It is the first two forms of nitrogen that affect the metallurgical behaviour of the weld metal [Ogawa et al 2002]. It has

been commonly observed that 18-8 type stainless steel weld metal which maintains the $\delta + \gamma$ dual phase at 0.16 % nitrogen content shows very good weldability with no porosity or loss of nitrogen along with increase in mechanical properties primarily caused by localized deformation through minimized segregation as well as reduction in secondary dendrite arm spacing making the microstructure finer [Ogawa et al 1984, Nage et al 2006]. However, with the increase in nitrogen content up to 0.24 %, pinholes and porosity due to nitrogen evolution are observed [Hertzman 2001, Padilha and Rios 2002, Kamiya et al 2002]. The maximum nitrogen content for porosity-free solidification rises from 0.2% at 17% chromium to 0.5% at 25% chromium in linear proportion with the chromium content [Woo and Kikuchi 2002, Shankar et al 2003b]. Furthermore, the nitrogen diffusion coefficient is temperature dependent and if austenite is formed at higher temperature the austenite growth rate will be enhanced. A secondary effect is that the decreased grain growth will increase the number of nucleation sites for austenite since austenite nucleates primarily on the ferrite grain boundaries. It has been demonstrated that the nitrogen diffusion rate in the ferrite governs the kinetics and, consequently, the transformation can be categorised as para-equilibrium controlled [Woo and Kikuchi 2002]. Hence it can be concluded that if nitrogen content is kept less than 0.16 % along with effective strengthening of austenitic steels it strongly enhances austenite reformation in complex grades i.e. nitrogen is essential in order to obtain good weldability in these steels.

Heat affected zone

As an austenite stabiliser, nitrogen has an equally strong influence on the transition phenomena in the ternary iron-chromium-nickel constitution diagram as does the carbon. But nitrogen possesses a much higher solubility in austenitic stainless steel alloys than carbon does, which results in a much lower susceptibility to form undesirable precipitations such as

carbides ($M_{23}C_6$, M_6C, MC) and/or intermetallic phases (Sigma, Laves, Chi) in austenitic steel grades [Ogawa et. al. 1995]. Sensitization behaviour of austenitic stainless steels is greatly influenced by nitrogen content in chromium equivalency parameter (Cr^{eff}) calculated as follows [Parvathavarthini and Dayal 2002]:

$$Cr^{eff} = Cr + 1.45Mo - 0.19Ni - 100C + 0.13Mn - 0.25Si - 0.51Al - 0.20Co + 0.01Cu + 0.61Ti + 0.34V - 0.22W + 9.2N \qquad (2.7)$$

With higher Cr^{eff}, the time to reach the resistance limit of chromium depletion at the grain boundaries is shifted to longer periods of time. The upper boundary temperature progressively decreases with increase in Cr^{eff}. This can be attributed to the fact that higher chromium content facilitates the diffusion of chromium into the depleted grain boundary areas. This produces a shift of the upper boundary of the area of sensitization towards lower temperatures. Increase in Cr^{eff} results in shifting of the onset of sensitization to longer durations and hence the area which is prone to sensitization is also narrowed [Parvathavarthini and Dayal 2002].

Nitrogen addition also considerably increases resistance to pitting corrosion. In the first step nitrogen dissolved during the corrosion reaction forms ammonia ion, $NH4^+$, at pit sites and results in the pit electrolyte less acidic by increasing the pH. Secondly the surface is enriched with nitrogen content while chromium diffusivity decreases thereby retarding the nucleation and growth of carbides and hence improves the passivity. In the third step nitrogen dissolved to form stable Cr–nitrides act as inhibitors locally at the pit sites [Woo and Kikuchi 2002, Vanderschaeve 1995].

2.2.2.3 Effect of weld thermal cycle

Nitrogen in weld metal arises from various sources such as prior content in the base metal, intentional addition through the shielding gas or as inadvertent pickup due to

inadequate shielding during welding. Its addition from any source significantly influences the mode of solidification as shown in Fig. 2.8 [Nage et al 2006].
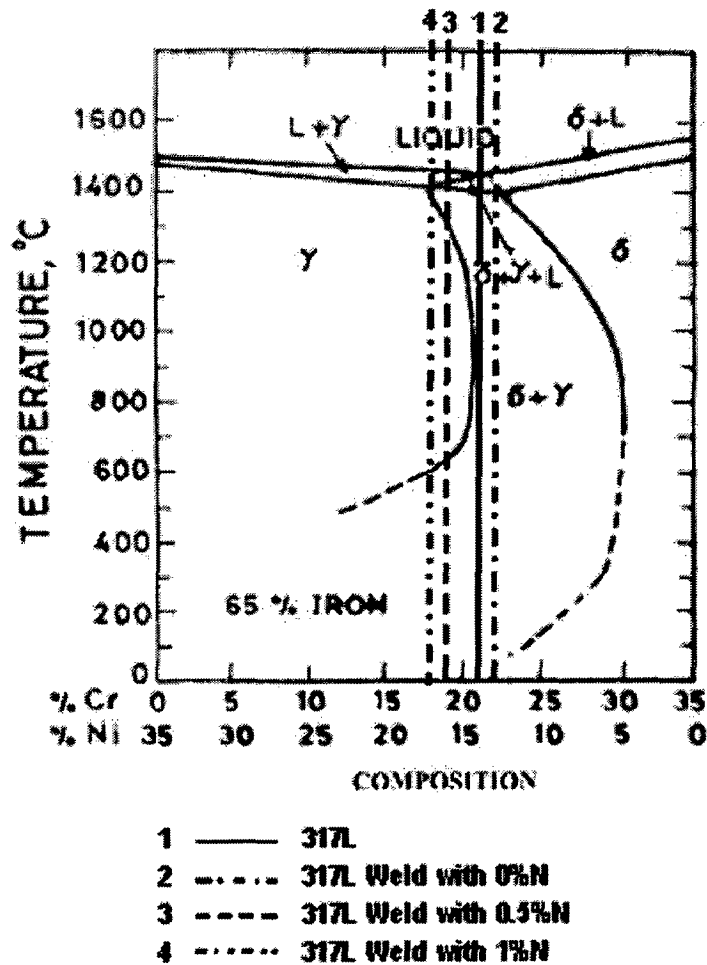
Fig. 2.8: Influence of nitrogen addition on weld solidification mode [Nage et al 2006].

Nitrogen as shown in Fig. 2.8 stabilizes γ phase by decreasing the occurrence of primary δ-ferrite, which results in reduced resistance to cracking. Several studies that focused on the possible role of nitrogen in influencing solidification cracking behaviour [Cieslak and Ritter 1985, Ogawa *et al* 1984] point to the fact that nitrogen changes the solidification mode from ferritic to austenitic, thus increases propensity to cracking. However solidification cracking susceptibility is dependent on the amount of residual liquid phases and thermal strain occurring in interdendritic regions. Among the elements whose effects on

cracking were investigated, molybdenum, manganese and nitrogen were found beneficial [Hull 1960] as they primarily increase the resistance of fully austenitic weld metal to cracking by retarding polygonisation [Kakhovskii et al 1971]. Presumably, these elements bind to the lattice defects during solidification and reduce the concentration of defects at the solidification subgrain boundaries, which decreases their wettability.

It has also been reported that dissolved nitrogen in the weld metal is significantly influenced by welding variables and, under certain conditions, can reduce the amount of δ-ferrite in a reheated weld metal microstructure below that adequate to prevent liquation cracking. In contrast higher nitrogen content suppresses grain growth in HAZ [Shankar et.al 2003] and considerably reduces secondary dendrite arm spacing [Ritter et al 1984] in weld. Hence liquation cracking susceptibility of austenitic stainless steel welds should improve considerably due to increase in boundary area/unit volume in both weld and HAZ [Shankar et al 2003a, b]. However secondary dendrite arm spacing is also a function of cooling rate and the mobility factor [Shankar et al 2003b]. This mobility factor in turn depends on the surface tension and partition coefficient. This is ultimately dependent on the composition of the weld. In summary, it appears that the effect of nitrogen in weld metal containing ferrite (or ferritic solidification mode) has better weld properties as well as susceptibility to liquation cracking.

2.2.2.4 Effect of section size

In thick sections, higher nitrogen content increases the kinetics by raising the lower temperature limit for single phase ferrite and thus both increases the driving force for austenite formation and decreases the temperature range where ferrite grain growth prevails. Hence higher amount of nitrogen content may enhance the occurrence of micro fissures in ferrite-free areas along the weld HAZ of a previous weld pass especially during multiple thermal cycling of the HAZ [Shankar et al 2003b]. In addition, a low ductility region exists in the weld metal of previously deposited weld pass from multipass deposits or from repair

welding. This region is usually the initial location for micro fissuring occurrence by following mechanisms when a weld exhibits a low ferrite number (FN), while under a high imposed strain that exceeds the strain tolerance of the microstructure [Cui et al 2005].

1. Enhanced segregation due to continued partitioning of harmful trace elements such as P, S, Si, etc to the dendrite boundaries in weld followed by liquation and rupture under strain.

2. Additional strengthening of the matrix by thermally-induced precipitate reaction as is the case for some ductility-dip incidences. The increased strength of the matrix may cause strain accumulation in the degraded grain boundary microstructure region thus leading to rupture.

3. Strain-induced precipitation leading to a strong matrix and the subsequent accumulation of strain in degraded micro structural region.

4. The simple accumulation of thermal and restrain strains over a range of temperatures produced by continued thermal cycling causing the strain tolerance of the grain boundary micro structural region to be exceeded.

2.3　CONVENTIONAL ARC WELDING OF THICK ASS SECTIONS

In last 30 years the most important contributions to welding technology have been through changes in the design of welding power sources [Ghosh et.al. 2001,] from generator set to inverter based digitally transistorized power source. It has achieved a significant improvement in volt-ampere characteristics, duty cycle, efficiency along with reduction in weight [Johnson et.al. 1995, Shanmugam 1997]. Performance of power source is of vital importance to the welding process with respect to arc ignition, stability of transfer of the melted electrode material and amount of spatter that is generated [Shanmugam 1997]. For this purpose, it is important that the two terms which are commonly used to define the V-A characteristics of a power source, static output and dynamic response are optimised to maintain a stable arc during the welding process [Johnson et.al. 1995].

Static output

Static output characteristics primarily indicates the achievable envelope of output limits, including the highest voltage the machine will support at a given current and the highest current that can be drawn at a given voltage [Johnson et.al. 1995]. It can be obtained by statically loading pure restive load from minimum or no load condition to the maximum or short circuit condition. These characteristics as shown in Fig. 2.9 are classified as steeply drooping, gradually drooping, flat, which are used for manual metal arc welding (MMAW), submerged arc welding (SAW) and gas metal arc welding (GMAW) processes respectively. Power sources with drooping and flat characteristics are known as constant current (CC) and constant voltage (CV) power source respectively.

(a)   Steeply drooping

The welding power source with steeply drooping V-I characteristics has a high open circuit voltage (OCV) and low short circuit current. In these power sources change in arc length does not affect welding current appreciably as depicted by Fig. **2.9**. With the change in arc length between $(I - \Delta I)$ and $(I + \Delta I)$, the change in welding current is small. This is best suited for SMAW process because a slight change in arc length due to intrinsic movement of human hand during welding does not affect the melting rate of the electrode significantly. Also high OCV ensures easy initiation and maintenance of welding arc.

(b)   Gradually drooping

The welding power source with gradually drooping V-I characteristics has comparatively lower OCV than steeply drooping characteristic power source. In this as the arc length changes from I to $(I \pm \Delta I)$, change in welding current is comparatively more and hence provides some sort of self-regulation of the arc length. This is best suited for SAW process.

(c)   Flat

In these power sources, for a small change in arc length, change in welding current is very high which makes it quite sensitive and helps in maintaining the constant arc length. This is generally referred to as self-regulation of the arc length and is essential requirement for GMAW process. However, flat characteristic is not truly flat but normally droops at 1-3V per 100 A. All welding power sources with flat V-I characteristics are almost invariably of the transformer cum rectifier type and electrode positive polarity is normally employed.
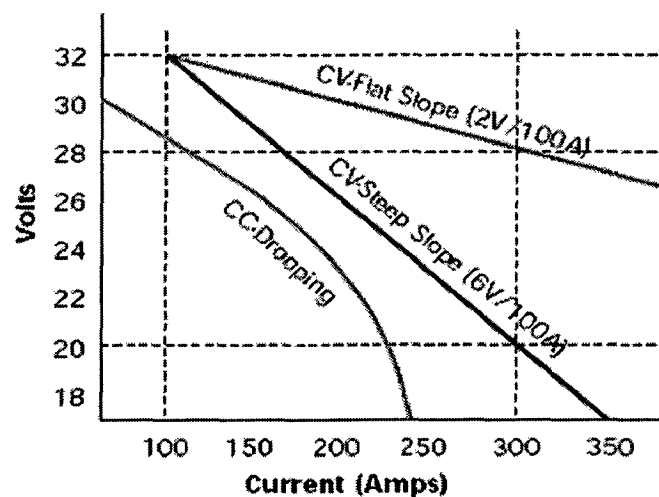
Fig. 2.9:   Power supply characteristic curves

Dynamic response

The dynamic characteristics of an arc welding power source is determined by recording the transient variations occurring over a short interval in welding current and the arc voltage [Johnson et.al. 1995]. In short, the dynamic characteristics is instantaneous response of power source to step changes in load voltage primarily associated with striking of arc, metal transfer from the electrode to the weld pool, and arc extinction and re-ignition during each half cycle of AC welding. The influence of these factors on the process stability is reflected in the current and voltage waveform of the welding arc [Shanmugam 1997].

These are obtained by recording the volt-ampere transients during actual welding operation. From dynamic characteristics it is possible to know the mode of metal transfer for a given set of welding parameters.

Depending upon power source characteristics, welding of thick pipelines is generally carried out by following processes, which are preferably used according to their specific process characteristics primarily in respect to working range of parameters and resulting weld quality.

(i)   Shielded metal arc welding (SMAW)

(ii)   Gas tungsten arc welding (GTAW)

(iii)   Gas metal arc welding (GMAW)

(iv)   Pulsed current gas metal arc welding (P-GMAW)

2.3.1   SMAW Process

The shielded metal arc welding has maximum flexibility and can weld many metals in all positions. There is definite relationship amongst the welding current, size of welding electrode and welding position. The molten weld metal can be retained in position by lowering the heat input to reduce the fluidity of molten weld metal and to give a small size of weld pool which solidifies before it has time to spill out of the joint. The heat input can be reduced by using a smaller diameter electrode (2.5-4mm) at about 90-140A of welding current [Kearns 1978]. The arc length can be varied to control the heat input and amount of molten metal in position [ASM handbook 1994]. The heat input can also be distributed and side wall fusion can be achieved by adapting an appropriate weaving technique. The sagging and spilling of weld metal can also be prevented by reducing the welding current and increasing the number of passes. However SMAW process has following disadvantages.

1.   Lower heat transfer efficiency of 0.55-0.70 [Radaij 1992] as comparable amount of energy is lost in resistance heating and flux melting resulting in comparatively lower metal deposition rate [Lancaster 1984].

2. Interruption in metal deposition due to limitation of electrode length enhances probability of defect formation.

3. Entrapment of slag occurs if it does not have 30-40% higher coefficient of thermal expansion (CTE) than that of parent metal.

4. Process automation is practically not viable.

Life of a weldment gets considerably affected by entrapment of slag primarily due to poor tensile and fracture mechanics properties [S´anchez-Cabrera 2007]. Thus SMAW process even though largely used in joining of thick sections, its use in welding especially in critical applications such as pressure vessels, piping etc. is on the verge of extension.

2.3.2 GTAW Process

In this process, an arc is established in between a tungsten electrode (non-consumable) and base metal. The arc gap is kept constant and current is controlled by the power source. The heat of the arc thus produced is utilized to achieve coalescence of metals with and without use of filler metal. Filler metal, usually available in 1 meter length of wire, is added to the leading edge of the pool as required. The arcing electrode and molten weld pool are generally shielded by inert gas or gas mixture of argon and/or helium. The current and heat input range of the process are followed of the order of 10-300A and 0.2 to 8 kJ/s respectively [ASM handbook 1994]. The most popular variation of this process is known as pulsed current GTAW. Both low frequency pulsation typically (0.1-20Hz) and high frequency pulsation (>100Hz) are often used in this process [Tujsek 2000]. The heat input depends on the mean current which is a function of the pulse height, pulse frequency and pulse duration. The pulsed current mode of this process offers a better control over the size of weld pool and its fluidity to manage the pool in position as well as over the penetration behaviour of the weld. The process has all positional welding capacity and lends itself to

produce high quality welds of metals such as aluminium, stainless steel, nimonic alloy and copper in chemical plants, sheet work in aircraft engines and structures. However GTAW process has following limitations.

1. Low process economy due to its considerably poor heat transfer efficiency of 0.20-0.50 [Radaij 1992].

2. Contamination due to both the transfer of molten tungsten from the electrode to the weld pool and exposure of the hot filler rod to air occurs during welding with comparable welding currents used in other processes.

3. Higher cost of operation due to relatively expensive shielding gases required during its comparatively slow deposition rate [Lowke et.al. 1997, Lucus 1992].

In addition to above limitations, a major disadvantage of GTAW process is very low metal deposition rate at comparatively lower welding speeds resulting in considerably severe weld thermal cycle. This problem of especially lower metal deposition rates has been largely solved with the invention of hot wire GTAW process. In this process consumable filler wire provided to the arc region is heated to a temperature just below its melting point by a different power source. Thus the major arc energy is utilized in melting of groove wall for proper fusion at considerably higher weld metal deposition rates. However the considerably large amount of heat generated by the welding arc and hot filler metal results in significant increase in weld pool temperature due to heat accumulation especially in metals having comparatively lower thermal conductivity such as austenitic stainless steel. Hence hot wire GTAW even though found suitable for joining ASS must be critically considered before its practical application. For these limitations, GTAW is generally not commercially competitive with other welding processes such as SMAW, submerged arc welding (SAW) and GMAW processes.

2.3.3   GMAW Process

The growing need of quality, economy and automation in welding has been found, in number of cases, to replace the versatile SMAW by GMAW process. The process is also popular as it provides to a weld a high resistance to hydrogen induced cracking due to its low diffusible hydrogen level (1-2ml/100gm) achieved by using bare solid filler wires, less chances of slag entrapment and low creation of smoke levels [Redding 2002]. In GMAW process a low voltage electric arc is established between a consumable filler wire and base metal, which melts both of them by arc heating. The wire is fed at a preset speed, which governs the magnitude of welding current, through a welding torch wherein it provides electrical connections and the shielding gas. The process has two basic requirements for successful open arc operation.

1.   The wire feed speed must be balanced with its burn off rate to maintain constant arc length.

2.   Transfer of metal from the electrode tip to weld pool should be stable.

In this process arc length is self-adjusted because of the constant potential (CP) characteristics of the power source. The weld metal is protected with suitable shielding gas and metal is transferred to the weld pool by desired mode of metal transfer as critically described in the sections below. Welding current and heat input commonly used are of the order of 60-500A and 1-25kJ/s respectively. It is a very versatile process and can be used in almost all positions and for welding any of the metal for which compatible filler wire is available. It is extensively used in welding of steels, aluminium, magnesium, nickel, copper, titanium and their alloys. However the smooth functioning of process primarily depends upon proper control of process variables, behaviour of metal transfer and thermal behaviour of weld.

2.3.3.1   Process variables and their control

In GMAW process, filler metal is transferred in the form of molten metal droplets. The mode of metal transfer defined by size and rate of droplet transferred primarily

determines the stability of the process. The term "Process stability" primarily depending upon welding current, arc voltage and electrode extension employed [Shanmurgam 1997] refers to the dynamic behaviour of the welding arc. Thus the characteristics of the weld pool [ASM handbook 1994, Kearns 1978] including the penetration, solidification mechanism, heat flow and rate of metal deposition are significantly influenced by arc stability [Shanmurgam 1997].

Welding current

Welding current plays an important role in deciding the mode of metal transfer and subsequently the weld quality. At low current, the globular transfer occurs if the arc length is sufficient. The drops grow at the tip of the electrode with a classic pendant drop shape, due to the competition between gravity and surface tension in the presence of relatively small electromagnetic forces [Kim and Eagar 1993a, Liu and Siewert 1989]. The large drops with diameter much greater than the diameter of the electrode are detached primarily by the gravity. When the welding current increases, the electromagnetic force becomes the dominant droplet force so that small drops with diameter equal or less than the diameter of the electrode can be detached. This is referred to as the spray transfer mode. It is found that there is an abrupt transition in the current, which divides the globular and spray transfer modes. This current or current range marked by high irregularity in the drop detachment frequency and the drop size is referred to as the transition current. With the further rise in current above spray mode, a short column of molten metal comes off at the end of the electrode tip and small drops are formed as this column breaks [Ueguri et.al. 1985, Kim and Eagar 1993a]. At a very high value of current, asymmetric force becomes significant compared to the initial force in the streaming of metal and the column spirals about the electrode axis [Lancaster 1984].

Arc voltage

Arc voltage primarily governs the arc length and affects size and shape of the fusion zone. When the arc length is too short, electrode may touch or short weld pool resulting in low base metal melting, narrow weld deposit and lower heat input and hence enhances the

possibility of forming flat and shallow deposit, allowing the arc to wander, increases spattering and may also cause porosity in weld deposit due to air aspiration in the shielding gas jacket [Johnson et.al. 1995]. Hence, it is important to select the proper arc length to obtain maximum weld pool control. The use of long arc length increases the arc plasma perimeter resulting in a wider weld pool, reducing heat concentration directly below the welding electrode and makes the weld pool response to weave very sluggish [Mattews et.al. 1992]. Shorter arc length improves weld bead characteristics and weld pool control.

Electrode Extension

It has been observed that an increase of electrode extension reduces transition current i.e. it dominates the transition current region of the filler wire [Rhee and Kamnatey, 1992] depending on the contact tube to work distance (CTWD), and affects the mode of metal transfer by changing the extent of ohmic heating. It has been revealed that at a given arc voltage, wire feed rate should be increased with the increase in CTWD [Heald et.al. 1994]. Electrode extension governs the arc length [Quinnet et.al. 1994]. Longer extension results in enhanced resistive heating and consequently reduces the balance of energy available to melt the filler wire and base metal, which may result in lack of fusion [Ralph and Yeo 1983, Stenbacka and Person 1989]. It may also reduce the stability of metal and may increase the risk of porosity in weld metal [Stenbacka and Person 1989].

It has been established that in the operating range of process variables (5mm arc length, 10-20mm electrode extension, 5-20% CO_2 mixture in any shielding) the specific burn off rate of 1-1.2 mm diameter filler wire and V-I relationship is linear. Consequently, the generalized burn off relationship in the range of parameters may be represented by linear control equations and can be applied for synergic control. Burn off rate is directly proportional to the electrode extension and resistivity of filler wire [Amin and Ahmed 1987].

Shielding Gas

The role of shielding gas in arc welding process is to protect the electrode and the work piece from harmful atmospheric contaminants and act as a medium in which current can flow to sustain the arc [Kearns 1978]. In welding area where molten droplets are transferred across the arc into the weld pool, protection from atmospheric contaminants can be provided successfully by suitable shielding gas or gases [Suban and Tusek 2001, Jonsson et.al. 1995]. The selection of a gas or a mixture of gases is also primarily guided by the physical and chemical properties of the gas, the operating characteristics that each gas imparts to a particular process and the kind of metal or alloy that the gas is suppose to protect. The basic properties of a shielding gas that governs its right selection to improve weld quality at reduced overall cost of the welding operation are listed in Table 2.3. Argon and carbon dioxide due to their relatively higher gas density than air (Table-2.3) requires lower flow rates in use than do the lighter gases as they can easily displace air from the electrode region to ensure adequate protection of the weld puddle [ASM handbook 1994]. Whereas gases such as hydrogen and helium which are 7 and 14 times less dense than air are prone to turbulent flow at the exit from the blowpipe nozzle due to thermal buoyancy [Suban and Tusek 2001]. Ionization potential [ASM handbook 1994] is the amount of energy required to remove an electron from a gas atom and make it an ion or an electrically charged gas atom. The importance of ionization potential of a gas in welding process is from the welding arc, arc power and energy distribution point of view [Jonsson et.al. 1995].

Table 2.3:   Basic physical and chemical characteristics of the gases.

Gas	Atomic weight (Kg/ kmol)	Relative gas density with regard to air at 273K and 1.013 bar	Ionization potential (eV)	Reaction in arc
Argon (Ar)	39.948	1.380	15.7	Inert
Helium (He)	4.002	0.138	24.5	Inert
Carbon Dioxide (CO_2)	44.011	1.529	14.4	Oxidizing
Oxygen (O_2)	31.998	1.105	13.2	Oxidizing
Nitrogen (N_2)	28.013	0.968	14.5	Reactive
Hydrogen (H_2)	2.016	0.070	13.5	Reducing

Energy distribution in axial and radial direction in an arc is also affected by the thermal conductivity of a gas [ASM handbook 1994] which varies with temperature as shown in Fig. 2.10 [Tusek and Suban 2000]. But for welding, the radial energy distribution is much more important because the radial energy distribution affects the axial one. Energy flow in radial direction has lower path length than the axial one i.e. path of least resistance, hence gas with higher thermal conductivity will have energy distribution across the arc in radial direction resulting in comparatively lower energy availability in axial direction [ASM handbook 1994, Liao and Chen 1999, Tusek and Suban 2000]. Inert gas helium which has higher thermal conductivity than argon (Fig.2.10) will produce lanticular shape of penetration in comparison with wine glass shaped penetration in steel material. Fig. 2.10 further shows that thermal conductivity of multi atom gases such as carbon dioxide, hydrogen and oxygen in the temperature range between 3000 and 4500 K is much higher than that of argon and helium [Tusek and Suban 2000]. When heated to high temperatures within the arc plasma, these gases break down or dissociate into their component atoms which get partially ionized, producing free electrons and current flow. As the dissociated gas comes in contact with relatively cool work surface, the atoms recombine and release heat at that point. This heat of recombination causes multi atomic gases to behave as if they have a higher thermal conductivity [ASM handbook 1994].
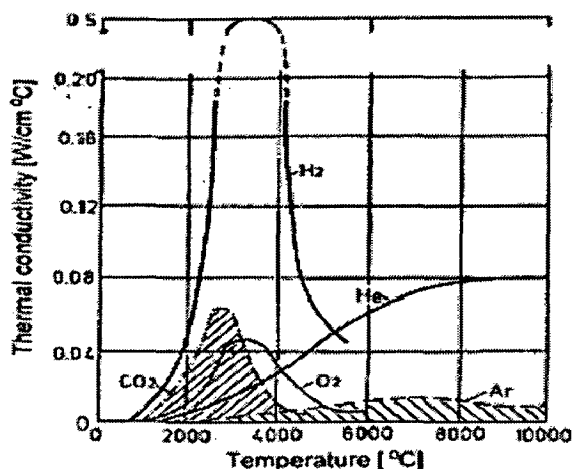
Fig. 2.10: Thermal conductivity of gases as a function of temperature

By far the gas blends developed can be roughly divided into three categories: pure gases, two gas blends and three part gas blends composed of argon, helium, oxygen, carbon dioxide, or hydrogen [ASM handbook 1994]. However there are number of other factors which influence the desirability of a gas for arc shielding. Some of these are the influence of the shielding gas on the arcing and metal transfer characteristics during welding, weld penetration, width of fusion and surface shape patterns, speed of welding and undercut tendency. Hence selection of pure or combination of gases will depend upon the function it has to perform in the desired application.

2.3.3.2 *Behaviour of metal transfer*

Metal transfer in gas metal arc welding (GMAW) refers to the process of transferring material of the welding wire in the form of molten liquid droplets to the workpiece. Metal transfer behaviour primarily depending upon the process parameters such as welding current, arc voltage, electrode extension, size and composition of filler wire and shielding atmosphere [Collard 1988, Kim and Eagar 1993a] are further influenced by a number of physical variables such as temperature, velocity, current density, electric potential, magnetic field, electromagnetic force, and pressure [Wang et.al. 2003]. Thus depending on the welding conditions, metal transfer can take place in three principally suitable modes: short-circuiting, globular and spray modes. Each of the modes have own characteristic arc length, weld penetration and weld pool shape [Heald et.al. 1994, Johnson et.al. 1995, Kim and Eagar 1993a].

Dip/Short circuit

Dip mode of metal transfer is primarily used for welding of steel with shielding atmosphere of CO_2, argon or their mixture in suitable proportion with electrode feed rate slightly higher than the melting rate, so that the tip of the electrode eventually dips into the

weld pool and extinguishes the arc. Consequently heavy flow of current occurs resulting in an increased heating of the molten bridge formed between the tip of the electrode and the weld pool. Due to the viscosity and surface tension, increased electromagnetic and hydrodynamic forces result in the transfer of molten metal [Wang et.al. 2003]. As the molten transfer takes place, bridge breaks and the voltage tend to jump to the OCV and thus arc re-ignites. It is used in welding of thin sheets, heat sensitive materials, bridging the gap of weld joint filling root passes and is also ideal for all positional welding [Maruo and Hirata 1984, Ralph and Yeo 1983] due to average current and arc voltage together with the intermittent arc resulting in small weld pool with low degree of superheat. However, lack of penetration along with excessive spatter and fast solidification are often reported [Alum and Quintino 1985a, David and Liu 1982, Mattews et.al. 1992].

Globular transfer

This mode of metal transfer is generally used to weld relatively thin work sheets only in flat position. In globular transfer, molten metal transfers in classic pendant droplet shape with 1.5 to 3 time's larger diameter than the filler wire at current below transition level due to the influence of physical variables as typically shown in Fig. 2.11 for 1.2mm mild steel filler wire. When the droplet detachment is about to occur, the temperature difference in the neck region rises by almost 2 times with the highest temperature generally located at the bottom of the neck and near the surface of the droplet. Whereas the liquid below the neck has high velocity away from the wire toward the work piece, and the liquid above the neck circulates upstream near the symmetry axis and downstream near the droplet surface. The centre of the neck is a velocity stagnation point. In the horizontal neighbourhood of this point, the liquid moves towards the centre and then goes either downward or upward. In the plot of current density, the current at the wire tip first converges towards the droplet neck and then diverges after passing through it. The current density in the centre of the neck is more than 50 times of that in the wire. Due to the

highly concentrated current density and greatly increased electrical resistance, the voltage drop on the neck is very large. Although physically connected, the voltage difference between the solid–liquid interface and the centre of the droplet can be as high as several volts at the moment before breakup. The high current density at the neck also generates higher magnetic field and a large electromagnetic force. The maximum value of the electromagnetic force is more than 10^4 times that of gravity. As a result of the large electromagnetic force and the surface tension due to the local curvature, the pressure reaches a peak value in the centre of the droplet neck. It causes the liquid to be squeezed out of the neck and thus accelerates the detachment process. Eventually the molten droplet falls down [Wang et.al. 2003, Choi et.al. 1998a].
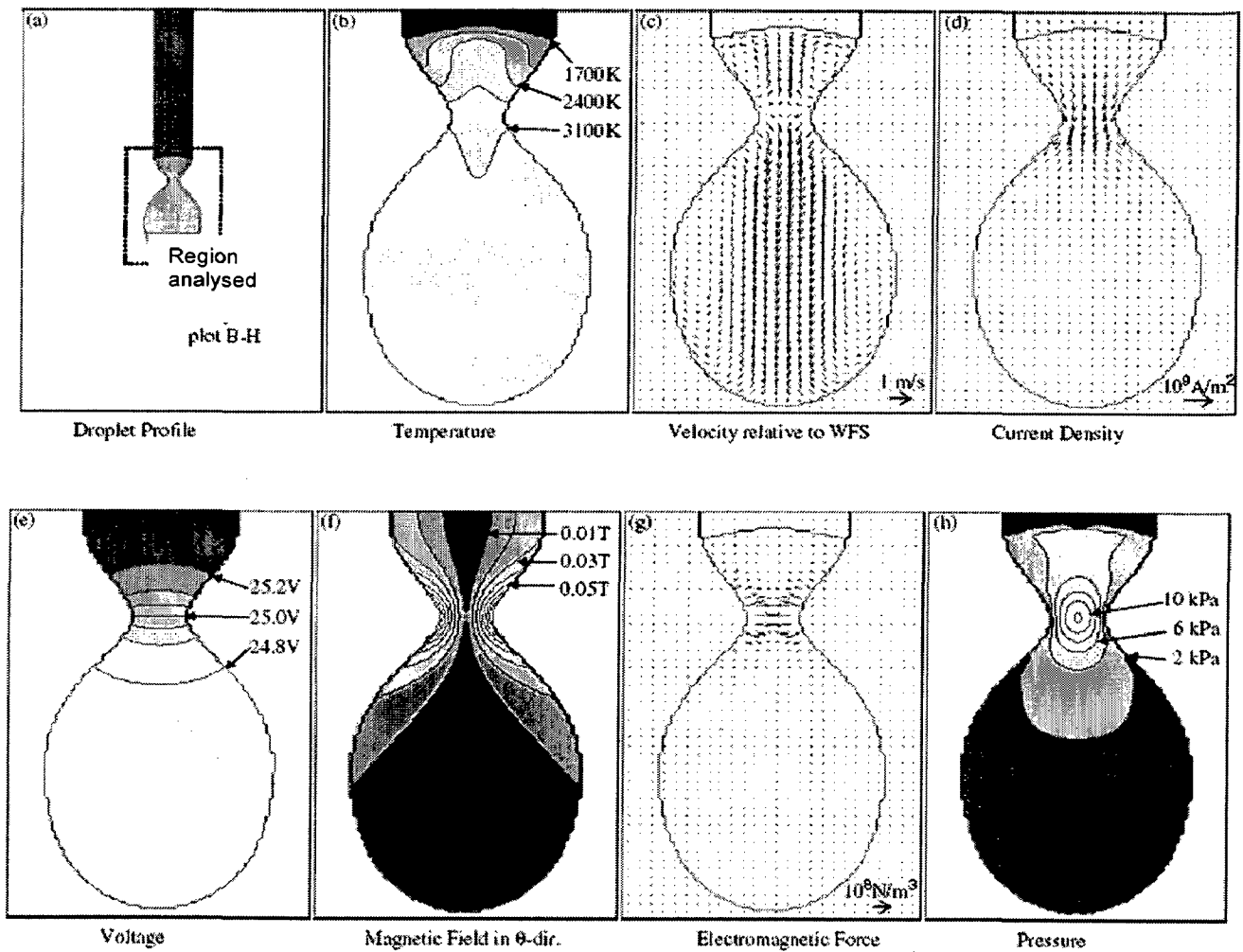
Fig. 2.11: Typical distributions of physical variables before droplet detachment (175 A) in globular transfer mode [Wang et.al. 2003]

Spray transfer

Spray transfer mode is a highly stable and efficient process widely used in welding of thick sections of ferrous and non ferrous materials. This mode occurs generally under argon shielding at medium and high current above a transition level when the series of droplets much smaller than the filler wire diameter are propelled axially from its tapered end at a considerably higher drop frequency [Wang et.al. 2003, Choi et.al. 1998a, Johnson et.al. 1995]. The tapering of wire at a given speed (WFS) occurs due to influence of distributions of temperature, velocity and electromagnetic force in the droplet as typically shown in Fig. 2.12 [Wang et.al. 2003]. The condensation of electrons on the side of the electrode [Jonsson et.al. 1995] generates heat on the unmelted portion of the wire resulting in preheating of the wire surface to an elevated temperature such that it tends to melt faster than the interior metal. When the current increases, the height of the convex melting interface also increases. The increased electromagnetic force pinches the molten fluid and drives it to move along the sloped surface to the bottom of the wire tip. Because of the liquid flow along the sloped surface, a thin liquid layer is formed on the surface. This thin liquid layer allows the arc heat to penetrate such that the melting proceeds in the direction perpendicular to the sloped wire surface. Figure 2.12 also shows that the taper formation is different from the necking (Fig.2.11) of a liquid column. For the necking of a liquid column, the diameter of the liquid shrinks due to external forces. But for taper formation, a solid wire first becomes tapered and the liquid moves along the tapered conical region and moves out of it in the form of small droplets. This conical region remains in quasi-stationary condition during the metal transfer process [Wang et.al. 2003].

| Temperature | Velocity relative to WFS | Electromagnetic force |
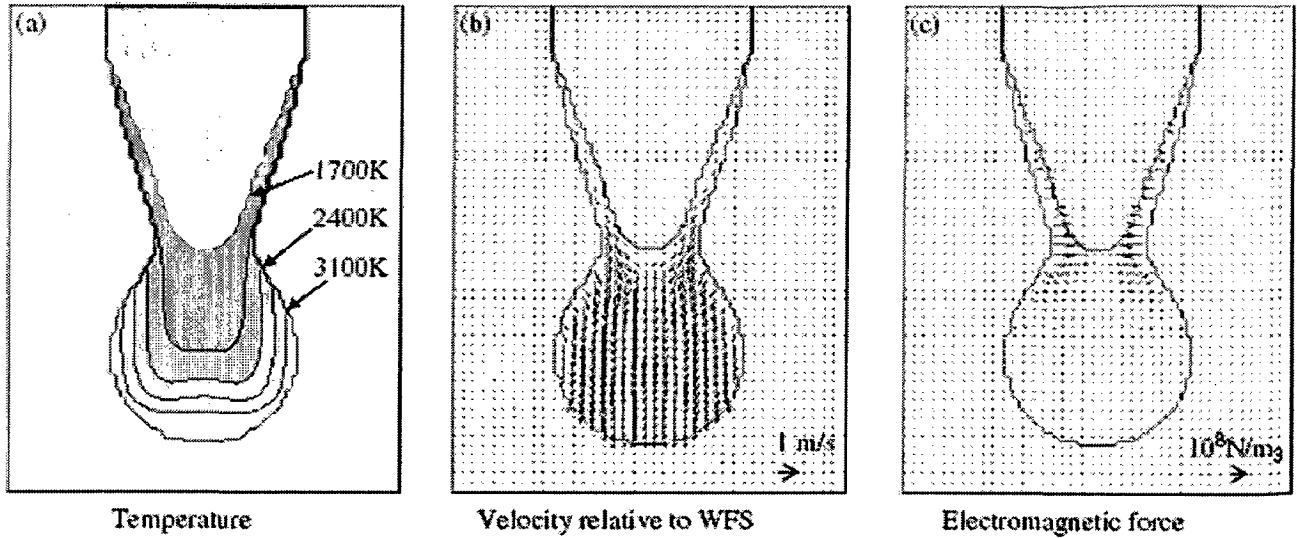
Fig. 2.12: Typical distributions of major physical variables before droplet detachment (350 A) in spray transfer mode [Wang et.al. 2003]

The use of higher welding current in spray mode increases the fluidity of the molten metal in the weld pool making it difficult to control in positional welding but it has been found ideal for flat and horizontal welds. However in high conducting materials such as aluminium which prevents the formation of too large weld pool, spray transfer mode can be efficiently used for welding in all positions [Subramaniam et.al. 1998].

2.3.3.3 Thermal behaviour of weld

Wire melting characteristics

For successful arc operation of GMAW process, the burn off rate must be equal to the wire feed rate to maintain constant arc length. Therefore, the following energy balance per unit time has been proposed [Lancaster 1984, Smati 1986].

$$A_w V_{w(cc)} \rho_w Q_m = \left[V_a + \xi + \frac{3kT}{2e} \right] I + \frac{R_0 E_w I^2}{A_w} \qquad (2.5)$$

Where A_w is the cross sectional area of the filler wire(m^2), $V_{w(cc)}$ is the wire feed rate (m/s^2) for continuous current welding, ρ_w is the density (kg/m^3) of the filler wire, Q_m is heat per unit mass (J/kg) required for melting the filler wire, V_a is anode fall voltage (V), ξ is work function of metal surface (V), $\frac{3kT}{2e}$ is thermal energy of electrons (V), R_0 is resistivity (Ωm)

50

of the filler wire, E_W is electrode extension(m) and I is welding current (A). Eq.(2.5) may be rewritten as,

$$V_{w(cc)} = \frac{\psi I}{A_w V_w Q_m} + \frac{R_0 E_w I^2}{A_w^2 \rho_w Q_m}$$ (2.6)
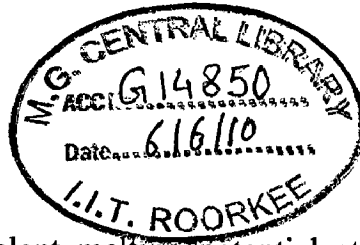
Where, $\psi = \left[V_a + \xi + \frac{3kT}{2e} \right]$ is the equivalent melting potential at anode (Work function + anode voltage fall + thermal energy of electrons) which can be estimated based on the expressions mentioned in the Fig.2.13 [Terumi and Kazuo 2002] depending upon filler wire size and shielding gas used for welding.
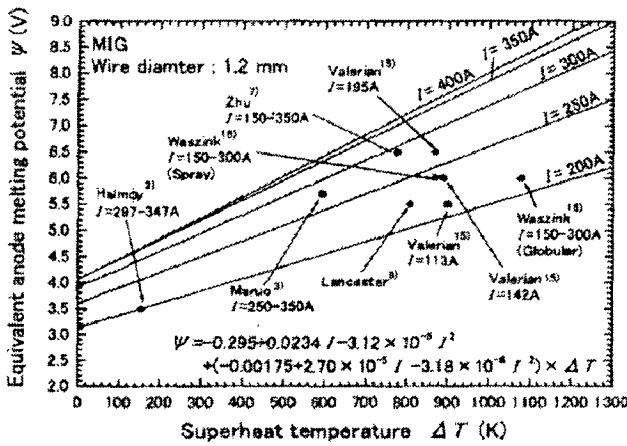
(a) MIG (1.2mm)
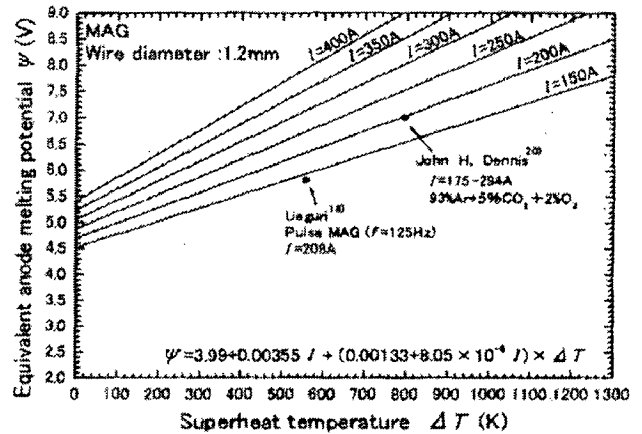
(b) MAG (1.2mm)
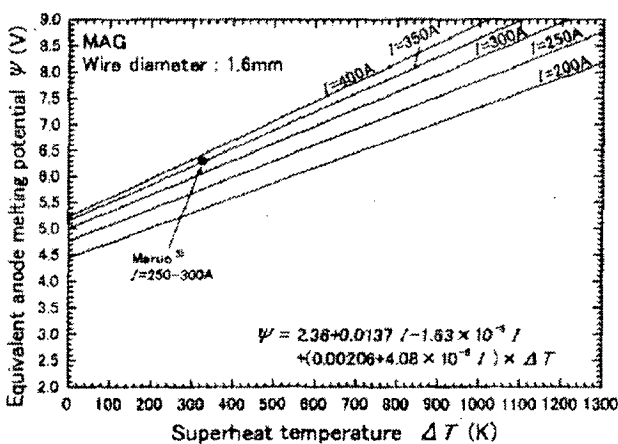
(c) MAG (1.6mm)
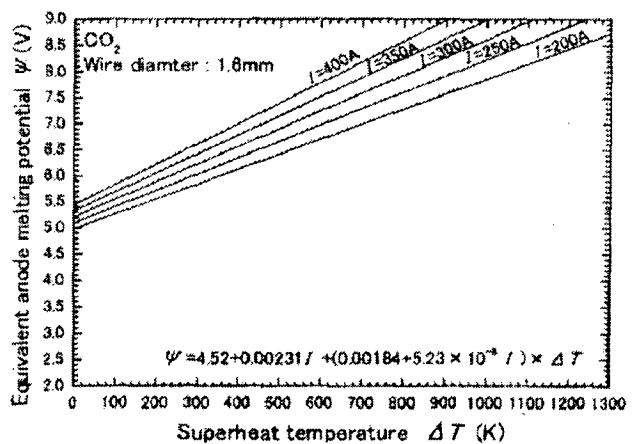
(d) CO_2 (1.6mm)

Fig.2.13: Correlation between super heat temperature and equivalent anode melting potential for filler wire and shielding gas combination of (a) 1.2mm, 100% Ar. , (b) 1.6mm, 100% Ar., (c) 1.2mm, 80% Ar+20%CO_2 and (d) 1.6mm, 100%CO_2 respectively [Terumi and Kazuo 2002].

Eq. 2.6 may also be expressed as,

$$V_{w(cc)} = AI + BE_w I^2 \qquad (2.7)$$

Where, A and B are constants representing wire melting due to arc heating and resistive heating respectively expressed as

$$A = \frac{\psi I}{A_w V_w Q_m} \qquad (2.8)$$

$$B = \frac{R_0 E_w I^2}{A_w^2 \rho_w Q_m} \qquad (2.9)$$

The reported values of physical constants for materials of the filler wire [Alum and Quintino 1985b, Colombieer, L. and Hochmann, L 1967, Metals Handbook 1979, Tekriwal and Mazmuder 1988, Waszink and Heuvel 1982] are given in Table-2.4.

Thermal behaviour of droplet

The thermo fluid behaviour of the electrode tip and droplet has significant effect on weld quality and production rate [Kim and Eagar 1993a]. It is reported [Waszink and Heuvel 1982] that resistive heating of the filler wire in general is not sufficient to melt the filler wire. Therefore certain amount of heat must flow from the arc through the anode surface. The resistive heating along with the heat flow through the anode surface governs the melting rate and remainder of heat generated at electrode surface affects the super heating of the droplet. The power supplied to the solid filler wire may be expressed as ($I^2 R_s + I\psi$), where R_s is the resistance of the electrode extension. The melting rate is then determined by the power supplied to the solid i.e., ($I^2 R_s + Q^*$) is the power transferred from the anode to solid part of the electrode. The temperature of the droplet is determined by the mass flow rate of the filler wire ($A_w V_w \rho_w$) and remainder of the power at the anode surface i.e., ($I\xi - Q^*$), if heat losses are neglected. The dependence of Q^* on the mechanism of heat transfer is essentially different for different modes of metal transfer, which in turn affects the temperature distribution in the electrode extension and its resistivity. It has been observed that during globular transfer, Q^* varies linearly with melting rate and slope of the lines at different mean current appear to be practically

independent of current. But, in the case of spray transfer, a non-linear correlation between Q^* and melting rate depicts initially a steep decrease in Q^* with the increase in melting rate and levelling off at higher values of melting rate. Thus, the heat balance at the wire tip is closely related to the mode of metal transfer. Spray transfer is characterised by continuous flow of liquid film surrounding a tapered end of electrode filler wire down to an emerging liquid tail just below it and final release in the form of series of droplets. This outer surface of the liquid film acts as an anode and the heat evolved at the surface is partly transferred to the un-melted filler wire by conduction; which contributes to the heating and subsequent melting of the filler wire. The remainder heat is carried away by convection and raises the temperature of the droplet. It has been reported [Jilong and Apps 1982] that resistance of electrode extension increases marginally with the current i.e. mode of metal transfer, but it falls markedly around 250A welding current (drop spray transfer) for 1.2mm steel wire under a shielding of argon+5% CO_2. During stream spray transfer, the resistance of electrode extension is again found to increase with welding current. The electrical resistance, thus depends on the mode of metal transfer because each mode gives rise to a different temperature distribution in the electrode extension [Waszink and Heuvel 1982].

It has been reported that the mean temperature of the droplets depend on the welding current and hence the mode of metal transfer [Jilong and Apps 1982]. In case of drop spray transfer, heat content of the droplet is found to be less than that with globular or stream spray transfer. Drop transfer endures less super heating of droplets resulting in higher melting rate than that of other transfer modes.

In case of globular transfer, it is reported [Lyttle 1983] that heat transferred from the droplet to the solid electrode tip is primarily due to convection within the drop caused by the Lorenz force if current diverges in the droplet. The liquid metal enters the droplet with certain initial velocity and is accelerated downwards by the electromagnetic force in the

region around the axis and reflected from the inner surface of the droplet. A boundary layer is formed at the drop surface above the anode, and heat is transferred through it to the circulating liquid. The power Q^* transferred to the solid part of the electrode and circulating velocity of the liquid metal within the droplet both are approximately proportional to the current therefore, droplet temperature is practically independent of current.

Table-2.4: Physical properties of different materials of filler wire [Alum and Quintino 1985b, Colombieer, L. and Hochmann, L 1967, Metals Handbook 1979, Tekriwal and Mazmuder 1988, Waszink and Heuvel 1982]

Property	Mild steel	Stainless steel
Melting Point, T_m, (K)	1750	1728
Specific heat, $C_{p(s)}$, (J/kg/K)	686	500
Specific heat, $C_{p(l)}$, (J/kg/K)	855	760
Latent heat of fusion, L, (J/kg)	2.76e5	2.84e5
Density of the solid metal, ρ_w, (kg/m^3)	7870	7750
Density of the molten metal, ρ_w, (kg/m^3)	6500	7507
Coefficient of surface tension, γ, (N/m)	1.03	1.35
Resistivity at melting point, R_0, (Ωm)	8.2E-7	1.3E-6
Emissivity of molten droplet, ε	025	0.25

2.3.4   P-GMAW Process

In spray mode of metal transfer in gas metal arc welding (GMAW) rate of droplet detachment considerably increases and droplet size decreases sharply giving a stiff arc and better control over metal transfer. However the major disadvantage of this mode is that it demands considerably higher welding current and therefore increases the heating of the work piece. During the 1960s an intermediate pulsed mode [Allum and Quintino 1985(b)] was invented and its use became widespread. In this mode, the current is well below the threshold current of the spray mode most of the time [Amin1983, Craig 1987(b), Ghosh and Gupta 1996], so the heat dissipated in the work piece is relatively small [Ghosh and Dorn 1993]. These

low-current periods are interrupted by high-current pulses above the threshold. During this pulse the arc transfers into spray mode. Since the pulse is short enough, it does not heat the work piece significantly. In other words in the pulsed regime arc current is maintained at a value high enough to permit spray transfer and long enough to initiate detachment of molten droplets [Jacobsen 1992]. Once the droplets are transferred, the current is reduced to a relatively low value, efficiently a pilot arc [Kim and Eagar 1993b]. These periods of low current allows the average arc current to be reduced into the range suitable for positional welding [Randhawa et.al. 1998], while periodic injection of high current pulses allows metal to be transferred in the spray mode [Ghosh and Rai 1998]. Thus, by repeated applications of current pulses as shown schematically in Fig. 2.14, synthetic spray transfer is produced at lower heat input. The process offers greater ease of operation for welding in any position for root passes without backing [Randhawa et.al. 1998] and the welding of heat sensitive materials and thin sheets [Trindade and Allum 1984, Ghosh etal. 2007b].
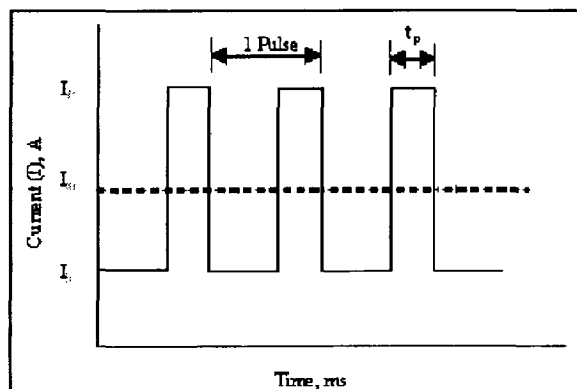
Fig. 2.14: Current waveform for pulsed current gas metal arc welding.

2.3.4.1 Process variables and their control

In the recent past the pulsed current GMAW has gathered considerable attention of welding technologists due to its number of unique merits in better control over metal transfer and heat input, resulting in improved weld quality and properties as compared to those observed in

case of conventional continuous current GMAW process [Praveen et.al. 2005, Collard 1988, Craig 1987a and b]. However, the exploitation of the merits of pulsed current GMAW process is largely dependent upon right selection of pulse parameters, like mean current (I_m), peak current (I_p), base current (I_b), pulse duration (t_p) and pulse frequency (f) as they affect the microstructure of weld and heat affected zone (HAZ) as well as chemistry and porosity content of the weld due to their influence on weld thermal cycle and arc characteristics [Ghosh and Dorn 1993, Ghosh and Rai 1998, Ghosh and Sharma1991, Lambentt 1989].

Peak current (I_p)

The peak current which must be maintained in spray transfer mode but/ not be too high, as it may lead to variation in arc pressure causing an air aspiration into the inert jacket resulting in instability of arc. Higher peak currents will result in greater axial force due to magnetic field generated by the current carried through the electrode and if numerous drops of relatively smaller diameter develop, the arc forces may cause them to be fragmented or propelled laterally [Palani and Murugan 2006, Praveen et.al. 2005, Quintino and Allum 1984, Rajasekaran et.al. 1998, Trindade and Allum 1984]. Hence in order to ensure appropriate amplitude and duration of peak current many researchers [Quintino and Allum 1984, Rajasekaran et.al. 1998, Trindade and Allum 1984, Wang et. al 2004] have used power law relations ($I_p^n t_P$ = constant, n=2), for determining the amplitude of peak current and duration. Minimum pulse amplitude has also been found out by using following expression for mild steel filler wire [Jacobsen 1992]

$$I_{p.min} = \frac{2.85 \times 10^4 \sigma^{0.5} d_e f^{0.245}}{I_{eff}^{0.465} t_p^{0.6}}$$

(2.10)

Here σ is the surface coefficient, in N/m, d_e is electrode diameter, in mm, f is pulse recurrence frequency, in pulses/sec, I_{eff} is effective current given as $I_{eff}^2 = \{k_p I_p^2 + (1-k_p) I_b^2\}^{1/2}$

wherein k_p is pulse duty cycle defined as t_p/t_{pul}, in A, t_p is pulse time, in sec. It has been further observed that depending upon filler wire size, the combination of the highest I_P and lowest t_P was found to be capable of providing both uniform arc length and uniform droplet detachment when compared to the combination of lowest I_P and highest t_P . In stainless steels slightly higher peaks and lower background currents are generally used in comparison with mild steel because of surface tension characteristics [Palani and Murugan 2006].

Base current (I_b)

The main function of the base current is to maintain the welding arc between pulses. By setting the base current to minimum value, heat flow in weld pool can be controlled and hence bead shape can get greatly influenced [Palani and Murugan 2006, Praveen et.al. 2005, Lenivkin1981]. Very low base current will produce a high crowned weld bead which may cause poor sidewall fusion. Hence base current levels can vary substantially depending upon material; for mild steel this will range from 30-50A, around 50A and 20A for austenitic stainless steel and aluminium alloys respectively. However base current level and its duration are primarily decided based on mean current employed [Palani and Murugan 2006].

Pulse frequency (f)

The pulse frequency is having significant effect on both the minimum base current and minimum electrode melting rate [Quintino and Alllum 1984, Smati 1986, Subramaniam et.al. 1998] to obtain a constant arc length. At a given base current the increase in frequency of sinusoidal pulse enhances the mean and effective currents and electrode melting rate. However in case of variation in pulse frequency by keeping the mean current constant the base current should remain free to vary by following the energy balance criteria to achieve constant arc length. It is in general reported that [Trindade and Allum 1984, Palani and Murugan 2006] at a low pulse frequency the metal transfers as large drops or lumps where the weld pool appears

viscous and the arc becomes erratic. Whereas with the increase in pulse frequency the metal transfer takes place as small axial droplets with size corresponding to the balance between detaching forces at the peak current and retaining surface tension force. Hence the appropriate frequency, which is primarily a function of average current, can be pre-selected at a given condition based on a theoretically calculated frequency obtained by dividing the electrode melting rate by the mass of one drop as given in Eq. 2.11 [Praveen et.al. 2005].

$$\text{Theoretical frequency} = \frac{m_{pulse}}{V_{drop}(I_p)\rho_d} \qquad (2.11)$$

Where m_{pulse} is the electrode melting rate with current pulsing, $V_{drop}(I_P)$ the volume of the drop at the peak current and ρ_d is the density of the drop. The average melting rate for the square wave current may be estimated as the weighed sum of the melting rate at the peak current and at the base current, as given in Eq. 2.12.

$$m_{pulse} = Dm(I_p) + (1\text{-}D)m(I_b) \qquad (2.12)$$

Where D is the load duty cycle, $m(I_p)$ and $m(I_b)$ are the melting rate at peak and base current respectively. At a high pulse frequency of the order of 100 Hz the metal transfer takes place as small axial droplets where, the arc remains stable due to higher arc pressure and the weld pool widens. A low pulse frequency of the order of 25 Hz enables to use a low mean current, when it is convenient for welding thin sheets [Praveen et.al. 2005, Palani and Murugan 2006]. However the mechanism of the influence of pulse frequency on welding process and weld characteristics is yet not fully understood.

Pulse duration (tₚ)

Pulse duration is variable which would be altered to achieve the ultimate reduction in power to the GMAW arc, while sustaining spray transfer mode of metal transfer. Power input to the arc is affected by changing the shape of pulse. A square wave, for example, has greater

effective width than that of sine wave or triangular wave [Palani and Murugan 2006, Lenivkin 1981]. The pulse duration is regarded as an important operating parameter as neck formation and elongation of the pendent drop occurs mostly during this period. If the pulse duration is kept too short, the elongated drop would recoil back to a spherical shape after the pulse and if the duration is too long, several drops might get detached during the period. Hence peak duration should be selected appropriately to detach one molten drop per pulse [Rajasekaran et.al. 1998, Subramaniam et.al. 1998, Wang 2004] or multiple droplet detachment per pulse [Ghosh et.al.1996, Ghosh et.al. 2007a]. The process of one drop transfer per pulse with relatively low rate of metal transfer is popularly used in joining of thin section, whereas the multiple droplet transfer per pulse with proper control of arc characteristics and the behaviour of metal transfer resulting in high deposition rate finds wide spread application of P-GMAW process in weld fabrication of different materials of varied section size. An empirical relationship for aluminium, relating the peak and background conditions by a combination of exponential and Lorentzian function can be used to define the minimum time at peak required for droplet detachment at a desired peak current level [Praveen et.al. 2005] as given by eq. 2.13, where value of t_p and t_b should be given in milliseconds. This threshold decreases slightly as the peak current is increased.

$$t_p = \left[\left(496.1 \times \left(1 - e^{-0.003 \times I_b t_b} \right) \right) + \frac{270.1}{\dfrac{\left(I_b t_b - 188.2 \right)^2}{8423.5}} \right] / I_p \qquad (2.13)$$

Peak duration was also determined by several researchers [Wang 2004, Palani and Murugan 2006] based on the concept that pulsation period (t_p) (Eq. 2.13) needed to have the cylinder changed into a spherical of diameter equal to the wire diameter (d_e) can be assumed as peak duration.

$$T = \frac{240V_{drop}}{\pi d_e^2 W_f}$$
(2.14)

Where $T = t_p + t_b$, V_{drop} is the droplet volume, $(\pi D_d^3)/6$ (mm^3), D_d the droplet diameter (mm) and W_f is the wire feed speed (m/min)

Ratio of peak current to base current (I_p / I_b)

During continuous current GMA welding the increase in welding current reduces the duration of presence of molten droplet in arc cavern. Thus, it reduces the absorption of gases and consequently the porosity content of weld deposit. Whereas in case of pulsed current welding, the variation in arc pressure, which is primarily governed by the ratio of peak current to base current, leads to formation of vortex in inert jacket resulting air aspiration into shielding atmosphere causing enhancement of porosity content in weld metal. However it is also observed that a combination of highest I_p and the lowest t_p provides more uniform arc length (stable arc) and droplet detachment when compared to the combination of the lowest I_p and the highest t_p. Thus the ratio of peak current to base current (I_p / I_b) should preferably be kept less than 10 in case of pulse current MIG welding [Ghosh 1996] by suitable adjustment of pulse frequency, pulse duration and wire feed speed to avoid difficulties such as rotating arc, heavy tapering of the liquid tip and disturbance in the shielding caused by the fluctuation in arc pressure. Earlier investigation [Ghosh and Sharma 1991, Ghosh and Gupta 1996] carried out on single pass pulsed current MIG of Al-Zn-Mg alloy have shown the influence of the ratio of I_p/I_b on the porosity content of weld deposit and suggested that the I_p/I_b ratio should be maintained in the range of 7.5 at a mean current of 150 A and around 4 at a mean current of 220 A to achieve a significant reduction in porosity content of the weld deposit. It has also been observed that by keeping the mean current in P-

GMAW process similar to the welding current of continuous current deposition, the porosity content of weld metal becomes comparatively lower than that observed in case of later one.

Superiority of P-GMAW however depends upon critical selection of pulse parameters by considering interaction amongst them during welding. This complicity in selection of pulse parameters for desired weld characteristics has been largely solved by using a hypothetical factor $\phi = [(I_b/I_p)ft_b]$ where, the t_b is expressed as $[(1/f) - t_p]$ which is having potentiality to analyse various basic characteristics of the weld and pulsed current GMAW process in reference to the pulse parameters [Ghosh 1999]. Utility of the factor ϕ has been amply justified by several investigators in various applications of pulsed current GMAW, such as welding of steel using solid and flux cored filler wires, positional welding of steel, stainless steel cladding of structural steel, single and multipass welding of high strength aluminium alloy [Ghosh and Dorn1993, Ghosh et.al. 1998, Ghosh et.al. 1999].

2.3.4.2 Behaviour of metal transfer

Mechanism of drop detachment

Total time for the detachment of a droplet in P-GMAW can be divided into four stages as time required for heating, drop growth, necking and detachment, while the current amplitude may be different during each stage [Jilong and Apps 1982]. Under the influence of peak current, a continuous spray of drops may transfer if the pulse duration is prolonged. Time required to form and detach a droplet is inversely proportional to the amplitude of peak current but is independent of its duration. Once the necking starts, it requires a certain period to detach the droplet, which primarily depends upon peak current and wire diameter, irrespective of the current level at the time of its detachment. Necking, a plastic deformation of the heated electrode is due to the Lorentz force and melting of filler wire occurs under the neck. The detachment of the drop is induced by the vaporisation of molten metal at the neck due to resistance heating. The speed of

droplet detachment is determined by the rate at which the fused metal is compressed into droplet [Cornu 1988]. Hence, it has been well established that in P-GMAW, the metal transfer characteristics and thermal behaviour of weld deposit are governed by the pulse parameters, which interact amongst themselves during welding and dictate the characteristics of weld deposit [Ghosh and Rai 1996, Ghosh 1996, Ghosh et.al.1991].

Mode of metal transfer

To achieve an acceptable metal transfer by P-GMAW at low level of mean current, a high lorentz force for short duration is regularly created by superimposing the pulses of very high current resulting in to drop detachment and its acceleration in axial direction. The amplitude and duration of these pulses are such that each pulse detached one or more droplets. It has been observed that at a given peak current and its duration; the mean current and base current and its duration has little influence on droplet transfer. It is also observed [Amin 1981, Jacobsen 1992, Smati 1986] that a droplet may be detached for a range of I_p and t_p combination according to $I_p^2 t_p$ = Constant (D_n), where constant depends on the filler wire properties. Although metal transfer primarily depends on the peak current and its duration the volume of metal detached per pulse is generally governed by the ratio of wire feed rate and pulse frequency. Therefore, it may be concluded that nature of the metal transfer such as diameter of droplet, its velocity and number of droplet transferred per pulse are largely governed by the combined influence of pulse parameters.

Mode of metal transfer in P-GMAW may be broadly classified into two categories as one drop per pulse and multi drop per pulse.

(a)   One drop per pulse

Required value of detachment parameter, D_n, can be obtained by selecting proper combination of peak current and its duration. The same value of detachment parameter may

be obtained using different combinations of peak current and its duration such as higher I_p with shorter duration or lower I_p with relatively longer duration. For getting one drop per pulse(ODPP), the droplet volume, $V_d = A_w.V_w/f$ [Allum 1983, Amin 1983] and wire feed rate (burn off rate), $V_w = m.I_m$ (m is slope) is combined to give V_d.

$$V_d = A_w.m.(I_p t_p + I_b t_b) \qquad (2.15)$$

Another approach to control the droplet transfer is through the prediction of theoretical pulse frequency, f', [Kim and Eagar 1993b] by using the following expression.

$$f' = \frac{A_w V_w'}{V_d'} \qquad (2.16)$$

Where, V_w' is estimated wire melting rate obtained from its weighted sum at I_p and I_b, and V_d' is estimated volume of a droplet obtained from the predicted droplet diameter using static balance theory at the peak current. When the ratio of applied pulse frequency to the theoretical pulse frequency is equal to unity, each pulse tends to produce one drop [Kim and Eagar 1993b].

(b)   Multi drop transfer per pulse

Based on pinch instability theory [Choi et.al. 1998a, Kim and Eagar 1993] metal transfer utilises instability condition to estimate a critical wavelength (λ_c) of a cylindrical current conductor liquid column, which tends to grow and cause the column to break up into droplets. This theory postulates that the pinch force on the liquid column due to self-induced electromagnetic force further enhances the break up. Electrode tip may develop a taper depending on its composition and welding current, which reduces the effective fluid cylinder diameter by a factor δ. The diameter of the droplet, D, may be estimated by considering the

electrode tapering coefficient, δ, using the concept of energy balance in detachment dynamics as follows,

$$D = \frac{4r}{[1 + \left(\frac{3\theta}{16}\right)}$$

(2.17)

Where,

$$r = R_w \, \delta$$

(2.18)

$$\theta = \frac{\mu_0 I_p^2}{\gamma \pi^2 r}$$

(2.19)

μ_0 and γ are the permeability of free space and coefficient of surface tension of liquid filler metal respectively and R_w is the radius of filler wire. The number of droplet transferred per pulse, N_D, may be assumed by mass transferred per pulse divided by mass of a droplet as follows:-

$$N_D = \left[\frac{(A_w V_w \rho_w)}{f}\right] \Big/ \left[\frac{\pi D^3 \rho_d}{6}\right]$$

(2.20)

Where, ρ_w and ρ_d are the density of the filler wire in solid and liquid phases respectively.

Eq. 2.20 implies that a given I_b and I_m, number of droplets transferred per pulse decreases with the increase in pulse frequency [Maruo and Hirata 1984]. As soon as the ratio of applied pulse frequency to the theoretical optimum pulse frequency becomes less than unity, it tends to promote a situation of multi drop transfer per pulse [Kim and Eagar 1993b]. In the case of multi drop transfer the detachment parameter, D_n, is significantly higher than that of one drop per pulse [Alum 1983]. It is also reported that if peak current

64

is set higher than critical transition level, the spray mode of metal transfer takes place during t_p [Maruo and Hirata 1984].

2.3.4.3 Thermal Behaviour of weld

Wire melting characteristics

The wire burn off rate/melting rate for P-GMAW is expressed [Craig 1987, Smati 1986] as

$$V_{w(pc)} = \int_0^{t_{pul}} V_w t_{pul} dt_{pul} \tag{2.21}$$

For a square pulsed current waveform it gives

$$V_{w(pc)} = (V_{wp}t_p + V_{wb}t_b)t_{pul}^{-1} \tag{2.22}$$

Where, $V_{w(pc)}$ is wire burn off rate and V_{wp} and V_{wb} are wire burn off rates during t_p and t_b respectively.

The V_{wp} and V_{wb} may be expressed as

$$V_{wp} = A.I_p + B.E_w.I_p{}^2 \tag{2.23}$$

$$V_{wb} = A.I_b + B.E_w.I_b{}^2 \tag{2.24}$$

Therefore, Eq.(2.22) may be rewritten as

$$V_{w(pc)} = \left[\frac{(A.I_p + B.E_w.I_p^2)t_p + (A.I_b + B.E_w.I_b^2)t_b)}{t_{pul}} \right] \tag{2.25}$$

Eq.(2.25) may be rewritten as

$$V_{w(pc)} = \left[\frac{A(I_p t_p + I_b t_b) + BE_w(I_p^2 t_p + I_b^2 t_b)}{t_{pul}} \right] \tag{2.26}$$

Using $I_m = [(I_p t_p + I_b t_b)/t]$ in eq. (2.26)

$$V_{w(pc)} = AI_m + BE_w(I_p^2 t_p + I_b^2 t_b)t_{pul}^{-1} \tag{2.27}$$

As $I_p^2 t_p \square I_b^2 t_b$ neglecting ohmic heating during base current period, Eq. (2.27) reduces to

$$V_{w(pc)} = AI_m + BE_w I_p^2 t_p t_{pul}^{-1} \tag{2.28}$$

Considering $f = 1/t_{pul}$ and $I_p^2 t_p = D_n$ Eq.(2.28) gives

$$V_{w(pc)} = AI_m + BE_w D_n f \tag{2.29}$$

By considering $V_d = A_w V_w/f$ in Eq.(2.29) a linear relationship has been obtained [Lambentt 1989] as follows,

$$\frac{f}{I_m} = \frac{AA_w}{V_d - BDA_w E_w} \tag{2.30}$$

Solving eq.(2.30) for droplet volume V_d,

$$V_d = AA_w \left(\frac{I_m}{f}\right) + A_w E_w BD \tag{2.31}$$

Eq.(2.31) shows that for any wire feed rate, by fixing (I_m/f), the droplet size can be held constant for a given wire diameter, electrode extension and detachment parameter.

It has been observed that for 1.2 mm diameter steel filler wire [Quintino and Alum 1984] for a desired combination of peak current and its duration, giving one drop per pulse, the base current and its duration may be evaluated using frequency value of 50Hz for 100A mean current. It gives satisfactory droplet transfer as well as volume of droplet remains insensitive to I_m. It can be expressed as

66

$$I_m/f = 2 \qquad (2.32)$$

By combining Eqs.(2.29) and (2.32)

$$V_{w(pc)} = AI_m + \frac{BE_w DI_m}{2} = I_m \left(A + \frac{BE_w D}{2} \right) = \overline{A}I_m \qquad (2.33)$$

Where, $\overline{A} = \left(A + \dfrac{BE_w D}{2} \right)$ is modified burn off factor

In P-GMAW process, by considering ohmic heating during base current duration, Eq. (2.31) reduces to

$$V_{w(pc)} = AI_m + BE_w I_{eff}^2 \qquad (2.34)$$

Where, $I_{eff}^2 = \left\{ k_p I_p^2 + (1 - k_p) I_b^2 \right\}^{1/2}$ and k_p is pulse duty cycle defined as t_p/t_{pul}

I_{eff} may also be expressed as,

$$I_{eff}^2 = I_m^2 + k_p (1 - k_p) I_e^2 \qquad (2.35)$$

By combining Eqs. (2.34) and (2.35),

$$V_{w(pc)} = AI_m + BE_w (I_m^2 + k_p (1 - k_p) I_e^2) \qquad (2.36)$$

In consideration of Eq.(2.7), Eq. (2.39) may be expressed as

$$V_{w(pc)} = V_{w(cc)equiv.} + BE_w k_p (1 - k_p) I_e^2 \qquad (2.37)$$

Eq. (2.37) reveals the following aspects of P-GMAW [Alum 1983].

1. The burn off rate of pulsed current welding is higher than continuous current welding under the same equivalent welding current.

2. Pulsed structure influences burn off rate for a given mean current and maximum burn off rate can be achieved when $k_p=1/2$ i.e., equal peak and base current time and at largest peak current in excess over the base current.

It has also been observed that melting rate under P-GMAW is practically greater than melting rate estimated using weighted sum of the melting rate (for DC currents) at the peak and base current [Kim and Eagar 1993b]. It is also pointed out that under certain circumstances, the power source dynamics i.e. rate of rise and fall of current pulse, may have a significant influence on the wire melting rate at given mean current [Joseph et.al. 2003].

Thermal behaviour of droplet

Recent developments in P-GMAW have led to a number of potential applications, where low heat input along with directional capability of metal transfer is required. Thermal analysis of metal transfer indicates that droplet temperature is comparatively lower [Waszink and Piena 1986] which is favourable to better control of weld pool. It is observed that the characteristics of metal transfer and thermal behaviour of weld deposit in the process are largely governed by pulse parameters [Ghosh and Dorn 1983] which simultaneously interact among themselves during welding and dictate the characteristics of weld deposit. It has been reported [Ghosh and Dorn 1983] that at a given mean current and pulse duration, heat content of the droplet at the time of detachment enhances significantly with the increase in pulse frequency. It has been identified [Ghosh et.al. 2006] that the variation in pulse parameters significantly affects the thermal and transferring nature of depositing metal, the control of which is imperative for desired weld characteristics. The heat content and temperature of the droplets at the time of deposition in the weld pool reduces with the increase of I_m significantly.

2.3.4.4 Concept of summarised influence of pulse parameters

The benefits of P-GMAW over GMAW in improving the weld characteristics and properties of various ferrous and non-ferrous metals, under different conditions of pulsation have been reported by many investigators [Weber1982, Allum and Quintino 1985(a), Amin 1983, Craig 1987b]. However, the wide acceptance of the process in fabrication is largely handicapped due to the criticality in the selection of pulse parameters. It is well established [Ghosh and Dorn 1983, Praveen et.al. 2005, Palani and Murugan 2006] that the variations in pulse parameters identified as I_m, I_p, I_b, t_p and f influence the weld characteristics to a great extent. It has been realized that a change in any one parameter affects the others also under the concept of energy balance. The variation in pulse parameter significantly influences the thermal behaviour and nature of metal transfer affecting the characteristics of weldment. Under these circumstances, the control of weld characteristics within a desired range is possible only by establishing a correlation amongst pulse parameters. It was also suggested that consideration of summarised influence of pulse parameters instead of individual one may be useful to study the different characteristics of the weldment.

A summarised influence of pulse parameters has been proposed by Ghosh [Ghosh 1999, Ghosh and Dorn 1983,], defined by a factor, $\left[\phi = \left(\frac{I_b}{I_p} ft_b \right) \right]$, where t_b is defind by $t_b = \frac{1}{f} - t_p$ and a good potentiality of the factor ϕ to analyse various basic characteristics of weld deposit has been reported. Many investigators [Praveen et.al. 2005, Hussain et.al 1996] have justified the applicability of ϕ in different conditions of pulsation by studying its effect on different weld characteristics using ferrous and non-ferrous materials.

2.4 NARROW GAP ARC WELDING OF THICK ASS SECTIONS

Narrow gap welding has generated great interest in the welding industry and has been the subject of much investigation in the last twenty years. But till to date there is some controversy around a proper definition for the technique. Most authors agree that narrow gap welding is applied to any welding process used for joining of heavy section (>25 mm) using an essentially square butt joint preparation with small gaps which will yield a weld with low volume weld metal [Shtrikman and Grinin 1977, Swada et al 1979, Vornovitskii et al 1977]. In broad terms narrow gap welding is a property –oriented bead-deposition technique associated with an arc welding process characterized by a constant number of beads per layer that are deposited one on top of the other in a deep, narrow square groove. Some of the advantages attributed to narrow gap welding processes, when compared with other welding processes for thick joints is listed below:

- Reduction in welding time due to less weld deposition with least number of beads

- Reduction in severity of weld thermal cycle producing less axial and radial shrinkage which may favourably affect the stresses at the root area compared to those observed in conventional groove welding

- A low dwell time in the critical sensitising temperature range due to less number of bead deposition and a favourable residual stress profile in the weld and heat affected zone which may improve the properties of the weld joint [Murugan et al 2001, Vornovitskii, L.V. et al 1977]

However in order to produce high-quality multipass narrow gap welds one of the most important parameters namely the width of the gap must be maintained constant during the welding of each pass. With the reduction in gap width the access to the welding zone becomes more and more difficult and the welding process may be disrupted as a result of short-

circuiting of the electrode with the edge. In addition to this a reduction in gap width increases the thickness of the layer of liquid metal (weld pool) underneath the arc and this may lead to lack of fusion between layers. The experimental results indicate that after welding 8-10 layers the gap may decrease by 25-40% [Shtrikman and Grinin 1979]. Hence this aspect should be considered while designing the narrow groove.

2.4.1 SMAW Process

2.4.1.1 Welding procedure

In SMAW process, the comparatively lower electrode size ranging from 2.4 mm up to 6 mm facilitates narrow gap welding procedure considering the ease in electrode manipulation in the groove. The selection of correct size of electrode for a weld is determined by the skill of the welder and the thickness of the base metal to be welded. Generally smaller diameter electrodes in which weld pool fluidity can be controlled are more suitable for narrow gap welding by using this process. However smaller diameter electrodes may not provide enough heat content to fuse the base metal and will also reduce the amount of weld metal deposition [Jeffus 1999]. Thus while narrow gap SMA welding a compromise between the electrode size and heat input plays a critical role in defining the characteristics of the weld joint.

2.4.1.2 Limitations

In narrow gap welding by using SMAW process the major problem which has been observed is detachability of slag with the reduction in gap width primarily due to an increase in magnitude of wedging effect. This primarily happens due to increase in strength of thick slag layer formed at the approaching edges of the weld groove due to specific cooling conditions provided by the narrow groove. Hence such a slag entrapment provides huge percentage of inclusions in the weld matrix and considerably reduces the tensile strength as well as fracture toughness properties of the weld joint [Shtrikman and Grinin 1979].

2.4.2 GTAW Process

2.4.2.1 Welding procedure

The conventional GTA welding can produce good quality welds, but it has its weak point as low deposition rate and very low process efficiency [Murugan et al 2001, Vornovitskii, L.V. et al 1977, Cook and Levick 1985]. With narrow groove advantages of conventional GTA can be combined with higher production rate due to reduction in volume of the groove as shown in Fig.2.15 [Vornovitskii, L.V. et al 1977]. However, the addition of hot wire filler metal to the pulsed current gas tungsten arc provides an attractive alternative that combines high deposition rate capability and independent control of heat input [Cook and Levick 1985] especially in the joining of very thick sections.
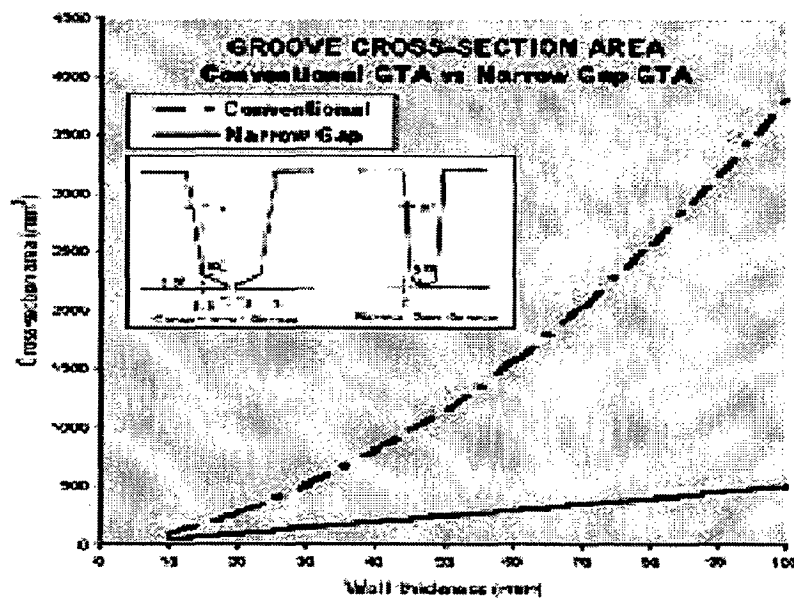
Fig. 2.15: Groove cross-section area when using the conventional and narrow gap welding [Cook and Levick 1985]

2.4.2.2 Limitations

The long standing problem with narrow gap GTA welding has been the control of sidewall fusion primarily due to shallow angle of attack. Hence during narrow gap welding the arc has to be precisely positioned with respect to side walls along with considerably higher energy input to achieve required penetration. The solution most suited to these applications is through-the-arc sensing, in which the arc voltage is monitored for both arc length control and cross-joint position [Cook and Levick 1985]. Thus along with increase in operating complexity, heat accumulation primarily due to large arc energy and considerably hot wire filler wire energy, may result in significantly higher weld pool temperature. This considerably elevated weld pool temperature will correspondingly increase residual stress formation in the weld.

2.4.3 GMAW Process

2.4.3.1 Welding procedure

GMAW was the first process to be used in narrow gap welding and it is still the one most commonly associated with the technique. This preference is related to the easily observable arc, relatively narrow groove, high welding quality, productivity and cost effectiveness [Malin 1983a and b]. However, narrow gap GMAW is rather prone to defect formation in the sidewalls, spattering and shielding gas deficiencies. These problems, which are associated with the difficulty in feeding the electrode and supplying a proper shielding gas coverage into a very narrow and deep groove, in obtaining well balanced arc heating between the side walls and the bottom of the joint, have been the major obstacles to a greater acceptance of narrow gap GMAW. In order to overcome these limitations, several wire deposition strategies and torch designs have been proposed and some of them used in industrial applications since the introduction of narrow gap welding.

- Ocillating the wire inside the groove using a straight long contact tube that is swung across or along the groove [Nakayama et al 1976, Futamura et al 1978].

- Rotating alternately a bent contact tip about its axis inside the groove [Innyi et al 1975].

- Plastically deforming the wire into some wavy shape before its entrance in the contact tube in order to oscillate the arc across the groove [Sawada et al 1979]

- Rotating the arc by feeding the wire through an eccentric contact tube that rotates [Nomura and Sugitani 1984]

- Rotating the arc by using a special "twist" electrode wire [Kimura et al 1979]

2.4.3.2 Limitations

Basic disadvantage of GMAW process is its comparatively larger torch nozzle which does not provide the required manipulation in the weld groove. Hence most of the researchers have carried out narrow gap welding by keeping torch nozzle perpendicular to the groove at the centre and with maximum electrode extension. Another major difficulty in GMAW-NG is to ensure effective shielding gas coverage for the arc and weld pool inside the gap. The geometric configuration of the joint can promote air being entrained by the shielding gas column inside the groove while the relatively long distance that sometimes separates the gas nozzles from the arc, renders the process very sensitive to draughts. As a result, porosity can be formed. Narrow gap welding by using GMAW process is generally carried out in spray transfer mode as explained earlier in the section 2.3. . Thus the considerably higher heat input employed further deteriorates the properties of the weld joint.

2.4.4 P-GMAW Process

The application of P-GMAW process for narrow gap welding has been rarely tried by the researchers primarily due to larger torch nozzle and complexity in selection of simultaneously interactive pulse parameters. However with proper control of pulse parameters, P-GMAW has numerous advantages over the conventional GMAW process [Praveen et al 2005, Collard 1988, Craig 1987a and b]. Such an advantage P-GMAW process has already been explained in section 2.3.4. Hence from the literature it appears that, if a narrow torch nozzle is developed with proper control of P-GMAW process parameters, the characteristics of the weld joint can be suitably improved by employing narrow gap welding procedure.

2.5 CHARACTERISTICS OF ASS WELD JOINT

2.5.1 Weld Chemistry

Chemistry of weld metal primarily depends upon proper selection of filler metal. The filler metal should not only provide good weldability, but also produce weldments having mechanical and corrosion properties equivalent to those of the base metal [Han and Sun1999]. Two principles are normally applied while selecting filler metals for producing corrosion-resistant weldments of stainless steels:

1) Use of additional alloying elements to obtain desirable corrosion properties, and

2) High level of purity in the steel should be maintained by reducing impurity contents (*i.e.*, carbon, sulphur and phosphorus) to achieve the enhanced corrosion properties.

To produce sound weld joints, microfissuring tendency should also be controlled by maintaining purity of consumable composition such that amounts of ferrite in the weld metal vary from 3 FN to 8 FN [Cui, 2004]. A higher nominal ferrite content does not ensure uniform distribution throughout the weld metal [Brooks et al 1983]. To achieve this filler metals for welding stainless steels are produced as coated electrodes (AWS A5.4), solid and metal core wire (AWS A5.9) and flux core wire (AWS A5.22). Mostly popular electrodes such as E308-16, E308L-16, E309-16, E310-16, E316-16, E316L-16 and E347-16 are used for welding of this class of steel. The electrodes are available with a lime coating (-15) (for use with DC only), a titania coating (-16) (for use with AC or DC) or a silica-titania coating (-17) (for use with AC or DC mainly in the downhand or horizontal positions) and in the standard or low carbon variety. These alloys which are mainly used in coated electrodes are also available as either solid wire, metal cored wire or flux cored wire. A few are available only as coated electrodes. These are 310H, 310Cb, 310Mo and 330H. Filler metals in general for austenitic stainless steels should either match or exceed the alloy content of the base metal. If a filler material of the correct match is not available, filler with higher alloy content normally should be used. There are several austenitic stainless types for

which no exact matching fillers are made. Examples are 201, 202, 205, 216, 301, 302, 304 and 305. The filler materials recommended for these base alloys are somewhat higher in Cr and Ni content. For example, 308 is used for 301, 302, 304 and 305 and may be used for 201, 202, 205 and 216 if 209, 219 or 240 are not available. The major recommended filler materials in the form of coated electrodes, solid and metal core wire and flux core wire are as listed in Table-2.5.

2.5.2 Microstructure

2.5.2.1 Weld

The solidification mechanism of weld metal during P-GMAW differs from that of GMAW and SMAW processes. In GMAW and SMAW process the solidification of weld metal takes place under a continuous supply of heat coming from the direction of heat source giving a coaxial dendritic structure [ASM handbook, 1994]. Whereas, heat transferred to the solidification front is of intermittent nature in P-GMAW process. During P-GMA welding the molten pool solidifies during the pulse off time being initiated from its front part and the same remelts during the subsequent pulsation wherein, the back part of the molten pool continues to solidify. Thus the solidification takes place primarily into two steps, one during the off time period and other during development of weld spot resulting from the next pulse. The peculiar form of heat balance caused by this phenomena has been [Hussain et al 1996] found to affect the micro structural characteristics of the weld pool. During the pulse off time the solidification of droplets starts from its circumference as a coaxial growth of dendrite under a condition of practically no heat gain from outside because of the existence of a low arc current at the off time where no metal transfer is available. This process is called the off time solidification process. The extent of solidification of the droplet primarily depends upon the super heating, size of the droplet and the extent of off-time [Ghosh 1996, Hussain et al 1996]. However when the subsequent pulsation sets in the deposition of later droplet on the earlier one, it causes a localized melting and produces a thermal shock to the adjacent regions below it. The local melting may cause necking and pinching off the dendrite arms, and the crystallites may be

Table-2.5: Filler Metals for welding austenitic stainless steels.

Base Stainless Steel		Recommended Filler Metal		
Wrought	Cast	Coated Electrode	Solid, Metal Core Wire	Flux Core Wire
201		E209, E219, E308	ER209, ER219, ER308, ER308Si	E308TX-X
202		E209, E219, E308	ER209, ER219, ER308, ER308Si	E308TX-X
205		E240	ER240	
216		E209	ER209	E316TX-X
301		E308	ER308, ER308Si	E308TX-X
302	CF-20	E308	ER308, ER308Si	E308TX-X
304	CF-8	E308, E309	ER308, ER308Si, ER309, ER309Si	E308TX-X, E309TX-X
304H		E308H	ER308H	
304L	CF-3	E308L, E347	ER308L, ER308LSi, ER347	E308LTX-X, E347TX-X
304LN		E308L, E347	ER308L, ER308LSi, ER347	E308LTX-X, E347TX-X
304N		E308, E309	ER308, ER308Si, ER309, ER309Si	E308TX-X, E309TX-X
304HN		E308H	ER308H	
305		E308, E309	ER308, ER308Si, ER309, ER309Si	E308TX-X, E309TX-X
308		E308, E309	ER308, ER308Si, ER309, ER309Si	E308TX-X, E309TX-X
308L		E308L, E347	ER308L, ER308LSi, ER347	E308LTX-X, E347TX-X
309	CH-20	E309, E310	ER309, ER309Si, ER310	E309TX-X, ER310TX-X
309S	CH-10	E309L, E309Cb	ER309L, ER309LSi	E309LTX-X, E309CbLTX-X
309SCb		E309Cb		E309CbLTX-X
309CbTa		E309Cb		E309CbLTX-X
310	CK-20	E310	ER310	E310TX-X
310S		E310Cb, E310	ER310	E310TX-X
312	CE-30	E312	ER312	E312T-3
314		E310	ER310	E310TX-X
316	CF-8M	E316, E308Mo	ER316, ER308Mo	E316TX-X, E308MoTX-X
316H	CF-12M	E316H, E16-8-2	ER316H, ER16-8-2	E316TX-X, E308MoTX-X
316L	CF-3M	E316L, E308MoL	ER316L, ER316LSi, ER308MoL	E316LTX-X, E308MoLTX-X
316LN		E316L	ER316L, ER316LSi	E316LTX-X
316N		E316	ER316	E316TX-X
317	CG-8M	E317, E317L	ER317	E317LTX-X
317L		E317L, E316L	ER317L	E317LTX-X
321		E308L, E347	ER321	E308LTX-X, E347TX-X
321H		E347	ER321	E347TX-X
329		E312	ER312	E312T-3
330	HT	E330	ER330	
330HC		E330H	ER330	
332		E330	ER330	
347	CF-8C	E347, E308L	ER347, ER347Si	E347TX-X, E308LTX-X
347H		E347	ER347, ER347Si	E347TX-X
348		E347	ER347, ER347Si	E347TX-X
348H		E347	ER347, ER347Si	E347TX-X
Nitronic 33		E240	ER240	
Nitronic 40		E219	ER219	
Nitronic 50		E209	ER209	
Nitronic 60			ER218	
254SMo		ENiCrMo-3	ERNiCrMo-3	
AL-6XN		ENiCrMo-10	ERNiCrMo-10	

From AWS Filler Metal specifications: A5.4, A5.9, A5.22

77

removed from the liquid caused by agitation resulting from a thermal gradient. Many of these crystallites remelt at the upper part of the bead due to high temperature while the others retain in some part of the bead at a comparatively low temperature. These crystallites grow to new randomly oriented crystals resulting into a fine grain cast structure of the weld by a grain multiplication process [Hussain et al 1996].

Pulsed current GMAW can refine the microstructure by controlling the inward growing columnar grains into smaller equiaxed grains. A detailed micrographic study of the welds has suggested that suitable nuclei for equiaxed solidification would be stable only at or shortly after the pulse duration because of considerable superheat in the weld pool. Thus, high frequency pulsing is supposed to be more effective but, this would be limited by thermal inertia effects at higher pulse frequencies. It is also observed that at a given comparatively higher mean current (200 A) and pulse frequency, the increase in pulse duration also found to coarsen the microstructure due to enhancement in superheating of a droplet at higher peak current for a longer duration. In aluminium weld [Ghosh and Sharma 1991, Ghosh and Dorn 1993] the refinement of microstructure improves with the increase in pulse frequency up to 50 Hz where the mean current is kept of the order of 210 A. However with the further increase in pulse frequency up to 100 Hz, the droplet transferred to the weld pool does not get sufficient period to solidify enough at the low pulse off period before receiving the successive one and consequently it re-melts to a greater extent. Thus the process of solidification tends to be similar to that of continuous current weld deposit and the microstructure shows considerable growth of dendrite [Ghosh and Gupta 1996].

2.5.2.2 Heat affected zone

The use of P-GMAW process has also been found [Ghosh et al 1989] beneficial in reducing recrystallized zone at HAZ in comparison to that observed in case of GMA welds in aluminium based alloys. In single pass P-GMA welds, it has been observed that at a given pulse duration of the order of 6.5 ms the use of pulse frequency of the order of 50 Hz reduces the width of recrystallization at HAZ significantly followed by an enhancement in it with further increase in pulse frequency to 100 Hz, when the mean current is kept about 15-20% above the transition level . Recrystallization of base metal is reported to occur primarily at HAZ close to the fusion line. HAZ resulted during pulsed current MIG welding is found to have comparatively finer grain microstructure than that observed in HAZ of conventional MIG (Hz) weld. Thus, a tendency of grain coarsening is marked during welding at high frequency of order of 100 Hz in comparison to that of observed during the use of pulse frequencies of 25 Hz and 50 Hz [Ghosh et al 1991a and b]. This is because at a high frequency the pulse-off time becomes so low that the heat flow characteristics approach to conventional continuous current MIG welding as discussed earlier. However there is paucity of knowledge on influence of P-GMAW process on HAZ microstructure of stainless steels.

2.5.3 Mechanical Properties

The design, prediction of performance, and safety analysis of austenitic stainless steel welded components generally require a complete knowledge of their physical and mechanical properties. In particular, it would be useful to have at one's disposal more information on the mechanical properties of the weld deposited metal as influenced by its material variability. This is characterized by microstructural variations between the parent metal (usually fully austenitic) and the weld metal (containing various amounts of δ-ferrite retained at room temperature). The presence of δ-ferrite in the austenite matrix is necessary to prevent cracking during welding according to a well-established practice [Piatti and Vedani 1990].

2.5.3.1 Tensile properties

Austenitic stainless steel welds generally contain delta ferrite content to avoid hot cracking. The weld thus obtained in comparison to base metal has relatively higher yield strength and ultimate tensile strength accompanied by reduction in elongation [Shaikh et al 1995]. During welding, the severe plastic deformation may occur in heat affected zone very near to the fusion line. Thus it has been observed the tensile properties depending upon crystallographic anisotropy may show considerable deviation in direction parallel and perpendicular to the direction of welding. The yield strength, and to a lesser extent the tensile strength are the properties most affected [Dieter 2001]. The yield strength in the direction perpendicular to the main direction of welding may be greater or less than the yield strength in the longitudinal direction, depending on the type of preferred orientation which exists. Such a anisotropy may play an important role in designing of thick wall tubes like pressure vessels which are subjected to high internal pressures [Dieter 2001]. Tensile properties are also greatly impaired by the presence of inclusion and porosity content in the matrix of weld metal. The typical ductile fracture behaviour showing cup and cone appearance on the macroscopic scale enlarges the cup or flat portion of the fracture surface and a strong diminution of the cone or shear portion depending upon presence of dimples associated with impurity particles which are generally round and have various different sizes [Patti and Vedani 1990, Çam et al 1999]. Thus void nucleation occurs at such impurity particle/matrix interface separation giving inferior tensile properties.

2.5.3.2 Charpy impact toughness

The chief engineering use of charphy test is in selecting materials which are resistant to brittle fracture by means of transition-temperature curves. Impact properties do not figure in the conventional design criteria for ductile materials, such as the austenitic stainless steels. However,

80

acceptance tests include specifications by keeping minimum values of 120 J in the as-received state for base metal and 70 J in the as-welded state for weld metal [Tavassoli 1995] of austenitic stainless steel at ambient temperature. However, impact properties of austenitic stainless steel welds varies depending upon its chemical composition. Increase in Mn:C ratio beyond 3 provides satisfactory notch toughness. The role of nitrogen is difficult to access because of its interaction with other elements. It is however generally considered detrimental to notch toughness. Whereas, increase in nickel content is generally accepted to be beneficial to notch toughness [Dieter 2001]. The presence of higher chromium content may drastically deteriorate the impact toughness by facilitating the formation of brittle sigma phase [Jahromi et al 2005].

2.5.3.3 Hardness

In welds metallurgical transformations takes place over very small areas. Thus mostly micro hardness measurements are carried to determine the formation of phases [Dieter,2001]. In austenitic stainless steel welds, ferrite content and the influence of weld thermal cycle on it causes precipitation of number of phases as already pointed out in section 2.2.1.1. Since ferrite in weld is similar in composition to ferritic steel, the cumulative effect of weld thermal cycles during multipass welding substantially increases the hardness in ferrite region. However due to very fine ferrite structure, it is likely that the austenite below the ferrite regions tested may contribute to the measured hardness and as the difference between hardness of ferrite and austenite increases, an increase in the scatter can also be expected due to partial contribution of austenite [David et al 1987]. Thus the increase in scattering magnitude primarily indicates that hard phases such as carbides and sigma are formed in the matrix.

2.5.4 Residual stresses

Residual stresses are those stresses remaining in a solid body under zero external force. During welding, the deposited metal fuses groove area and heats it up sharply relative to the

adjoining cooler area of base metal [Sarkani et al 2000]. As a result thermal expansion of the fused area is restrained by the surrounding colder area, giving rise to elastic thermal stresses. These thermal stresses which partly exceed the yield limit of weld metal at elevated temperature consequently plastically hot compress the weld area. Subsequently during cooling and solidification, the plastically hot compressed molten material will tend to shrink and pull adjoining parent material which will either follow the shrinking movement resulting in distortion or shrinkage or it will fully or partially resist distortion resulting in residual stresses. It thus displays tensile residual stresses and the surrounding area compressive residual stresses [Webster et al 2002, Basavaraju 2000]. These thermo mechanical treatments caused by complex multipass welding operations result in strain induced deformation which accelerates transformation reaction rates in materials through its effects on

1)   increasing the vacancy concentration leading to an increased diffusivity

2)   lowering the activation barrier to diffusion

3)   decreasing the free energy barrier to nucleation and

4)   increasing the effective driving force for nucleation .

The formation of residual stresses can be effectively controlled if the highest temperature reached at the weld centreline is just below the melting point of the material and that only elastic strains occur and no phase transformations whatsoever take place. However this practically impossible task can be optimized by reducing thermal strains accompanied by plastic upsetting to a lowest possible extent [Teng et al 2003, Lin and Chen, 2001]. This objective can be achieved by first understanding the stress distribution in thick sections and then with proper control of welding process and procedure.

2.5.4.1 Stress Distribution in thick sections

In a multipass welding operation, the number of thermal cycles that the material undergoes during welding is same as the number of passes, and with each pass, the residual stress pattern changes [Teng et al 2003]. The complex metallurgical process due to thermal cycles in welding, such as shrinkage, phase transformations produce both tensile or compressive residual stress in different zones of the welded structure. Residual stress, particularly tensile residual stress in the weldment, can be a very important factor in affecting the reliability and integrity of the weld [Yaghi 2005]. The formation of tensile residual stress may result in initiation of fatigue cracks, stress corrosion cracking, or other types of fracture. The development and distribution of such harmful residual stress in thick sections primarily depends on

1. Thermal expansion and contraction characteristics of weld metal resulting in plastic upsetting.

2. Welding direction as residual stresses near the weld interface on thick multi-pass weldments are more tensile in the direction normal to the weld than in the direction parallel to the weld [Brickstad and Josefson 1998].

3. Weld shrinkage which primarily depends on weld thermal cycle and groove design, affects the level and the distribution of residual stresses in the root area resulting in strain hardening in this area [Teng et al 2002].

4. Thicker pipes with lower diameter have less tensile or compressive residual stresses on the inside surface of the pipe [Brickstad and Josefson 1998].

5. In pipe structures, axial stress distribution is not rotationally symmetric, whilst the hoop stress may show a rotational symmetry [Chang and Teng 2004, Brickstad and Josefson 1998].

6.	The heat deposited during circumferential butt welding is high enough to result in a uniform temperature increase through the pipe thickness at the weld. The only deformation that will create thermal stresses is the circumferential strain due to the radial expansion and subsequent contraction. This radial decrease during cooling after welding together with symmetry condition at the centre section results in a almost linear through thickness axial stress variation with tensile axial stresses at the inner surface (sometimes of yield stress magnitude) and compressive axial stresses on the outer surface. The compressive hoop stresses are normally tensile all through the thickness and have about the same magnitude as the maximum axial stresses if the yield properties of the weld and base material are about the same [Brickstad and Josefson 1998]

### 2.5.4.2	Influence of Welding Process and Procedure

Welding process can be split into three stages: melting of the parent and filling materials, solidification of weld pool and transformation of phases. In each of these stages various phenomena dominate and they affect residual stress differently depending upon variations in the local composition of solid phases in the weld and heat affected zone (HAZ) [Deng et al 2008]. With multipass deposition, welding procedure gets further complicated depending upon the heat intensity of the localized heat source resulting in a nonuniform transient temperature field [Teng et al 2003]. This field initially causes a rapid thermal expansion followed by a thermal contraction of the affected material. Thus the resulting severity of induced temperature gradients and degree of restraint the joint imposes on the thermal deformations determine the residual state of the weldment when it has finally cooled. This residual state is characterized by a combination of internally balanced residual stresses and weld distortion [Sarkani et al 2001]. Thus it can be concluded that the residual stresses can be effectively controlled in thick sections by lowering the total amount of weld deposit with narrow gap

welding technique and secondly by reducing the severity of induced temperature gradients. Pulsed current instead of continuous current if applied efficiently reduces the severity of induced temperature gradients by controlling the thermal characteristics of metal transfer and weld bead geometry depending upon following parameters.

Pulse frequency, $F = 1/ (t_p + t_b)$

Pulse spacing, $S = V (t_p + t_b)$

Amplitude ratio, $A = I_b/I_p$

Where I_p is peak current, I_b is base current, t_p and t_b are peak and base time and V is travel speed.

The increase in pulse frequency produces greater concentration of energy density in the heat source and hence the weld depth-to-width ratio increases and considerably reduces the HAZ range of the weldment. Whereas, degree of double fusion of weld primarily caused by the amplitude of peak current considerably decreases with the increase in pulse spacing. Amplitude ratio also plays a critical role in reducing residual stress by minimizing temperature difference between the fusion zone and the unaffected base metal in the weldment i.e. temperature gradient. However the influence of pulse frequency, spacing and amplitude ratio by using P-GMAW process on ferrous and non ferrous material is not clearly justified in the literature [Tseng and Chou 2002].

2.5.5   Fracture Mechanics

Usually the design and analysis of any structure is based on the strength and toughness of the base metal. However, crack like defects initiate rapidly at non-metallic inclusions in the weld causing structural failure. Hence for components integrity, the identification of potentially dangerous defects and the condition under which these defects starts propagating has become the focus of research in fracture mechanics and this knowledge is being increasingly incorporated in our approach to design and quality control.

2.5.5.1 *Fracture toughness*

Fracture toughness has been defined as a "generic term for a measure of resistance to extension of a crack" [ASTM E1823-96, 1996]. The term fracture toughness is associated with the fracture mechanics method which deals with the effect of defects on the load-bearing capacity of structures and materials. The fracture toughness of a material is generally estimated by plain stress or strain intensity factor (K_{IC}), J-integral (J_{IC}) and crack tip opening displacement (δ_m). The greater the values of K_{IC}, J_{IC} and δ_m means higher the stress required for a rapid crack propagation indicating more resistance of a body to brittle fracture. Different standard test methods or test procedures have been developed by different organisations for fracture-toughness testing including American society for Testing and Materials (ASTM) in USA, British Standards Institution (BSI) in UK, European Society of Structural Integrity (ESSI) in Europe and Japenese Standards Association (JSA) in Japan.

Fracture toughness values are generated for a variety of reasons. The fracture mechanics method allows a quantitative assessment of the resistance of a material to fracture. As such, the fracture toughness value can determine a point of maximum load bearing capacity for a critical crack size in a structural element subjected to monotonically increasing load. Fracture toughness marks the onset of a stable extending defect indicating the end point of the useful life of a material or structure. As such it may be used as a parameter for determining the design conditions like allowable stresses in order to make material selection and also for determining the critical defect sizes to set inspection criteria in order to identify the conditions leading to failure during failure analysis. These parameters of fracture toughness are also used as design criterion for proper selection of material and evaluation of potential danger of a flaw present in a weld joint to improve its safety and reliability by preventing the catastrophic fracture. The use of a

new material or improvement in characteristics of existing material for higher critical stress intensity factor or plane-stress fracture toughness, K_C, reduces the factor of safety ($n = \sigma_u/\sigma_{max}$) on reliable operation.

In ductile materials such as austenitic stainless steel based on fracture mechanism being realised the process of operation should be divided in two classes. The first class includes materials of high ductility (plastically strained steels and their welded joints, produced with no flux), in which static loading at the level above the ultimate load produces unremarkable stable increment of initial defect but the formation of plastic collapse takes place. The second class is cast materials and welded joints obtained with the use of flux or manual arc welding with covered electrodes, i.e. materials of a lower toughness and characterized by crack increment under loading before the critical load achievement. The fracture resistance assessment of these materials should be carried out with the use of elastic-plastic fracture mechanics concepts [Timofeev et al 1999] determined experimentally through fracture test of a specimen or component by following ASTM standard E 813. Before carrying the fracture toughness test, specimens are precracked under cyclic load. During fatigue precracking a plastic zone is created and as long as precracking is performed in the linear elastic regime, the square-root of the plastic zone size, r_y, is proportional to the applied stress intensity factor K, under fatigue [Scibetta et al 2002, Cerjak et al 1999].

$$K = f\sigma_{y_s}\sqrt{\sigma\pi r_y} \qquad (2.38)$$

Where σ_{ys} is the yield strength, f is a function of the strain hardening exponent and the ratio of yield strength to young's modulus. Fracture toughness may artificially increase due to compressive residual stresses induced at the crack tip during pre-cracking. The residual stress affects fracture toughness and it is supported by experiments conducted in different studies

[Shihe and Ji-Liang, 1983]. Therefore, the plastic zone size during fracture must be larger than plastic zone size during fatigue.

2.5.5.2 Fatigue crack growth rate

Fatigue cracks in sound welded joints generally initiate along the toes of transverse welds. Various reasons for this include: (a) severity of the stress concentration at the weld toe: (b) presence of crack-like defects: and (c) welding residual stresses. Further, it is generally assumed that as a result of crack-like defects, the fatigue crack initiation life is negligible and the fatigue life of the joint is comprised mainly of the crack propagation phase [Bayley et al , 2000]. Hence in a welded joint, failure occurs with the initiation of small surface fatigue cracks at multiple sites along weld toes. These sites increase with the severity of cyclic stresses/strains along the weld toes, resulting in surface crack propagation through the thickness of the plate. Adjacent cracks coalesce into fewer cracks of lower aspect ratio and a dominant surface crack eventually forms [Bayley et al , 2000, Hafele 1994, Goswami 2003]. A small blow hole or inclusions observed in a weld matrix are the primary sites from where surface fatigue cracks initiates. However weld joints with higher toughness possesses better fatigue fracture resistance due to lower fatigue cracks propagation rate and secondly it can also tolerate more serious defects.

Fatigue crack growth behavior of welds can be characterized by the well-known Paris equation, which relates the fatigue crack growth rate, da/dN, to the stress intensity range, ΔK

$$\frac{da}{dN} = C(\Delta K)^n$$

(2.39)

Where a is the crack length, N is the number of cycles, and C and n are material constants. The stress intensity range, ΔK, is given by the difference between the maximum and minimum

88

applied stress intensity of the load cycle, $\Delta K = K_{max} - K_{min}$ [Anderson 2005]. While the stress intensity range is the main factor that governs the crack growth rate, the stress ratio, R, (ratio of minimum to maximum applied stress intensity) can also influence the crack growth rate. Generally, an increase in R results in an increase in da/dN for a given stress intensity range, ΔK. This influence of R can essentially come from two sources — a true material dependence of crack growth rate on R (i.e., an intrinsic material effect) and/or a crack closure effect. Crack closure refers to the condition in which the crack is not fully open during the entire loading cycle. In this condition, only a portion of the applied stress serves to drive crack propagation. Crack closure is most often attributed to residual stresses. For example, if the crack enters into a compressive stress field, the compressive stress will counteract the applied tensile stress. If the compressive stress is larger than the minimum applied stress, then the crack may remain closed during a portion of the load cycle. It has been observed that increase in crack growth rates as R is increased from 0.10 to 0.55 can generally be attributed to an extrinsic effect in which crack closure is overcome. In contrast, the increase in crack growth rate observed for an increase in R from 0.55 to 0.70 is a true intrinsic material response [Kusko et al 2004].

At a given ΔK, the fatigue crack growth rate of single and multipass pulsed current GMA weld has been found to be lower as compared to that observed in conventional continuous current (0 Hz) GMA weld. The estimation of fatigue life, of a tension and bending loaded engineering structure containing a semi-elliptical flaw, using both the material constants m and c of the Paris law under the fracture mechanics solutions of Newman and Raju [Newman and Raju 1980], show that the pulsed current GMA welding improves the fatigue life of weld deposit over that of continuous current GMA weld [Ghosh et al 1994].

2.6 FORMULATION OF THE PROBLEM

2.6.1 Motivation for the Present Study

Welding is one of the most commonly used fabrication process employed for joining of similar and dissimilar materials with varied section size in normal as well as in critical applications. Depending upon application, the integrity of weld joint is largely adjudged by its relevant properties. Weld deposit being a comparatively weaker region of weld joint due to its cast structure, often requires a critical control of its several characteristics primarily starting from defects to microstructure and residual stresses largely dictating the properties. Hence a suitable control of these aspects of weld often becomes a matter of great interest. However, the control of weld characteristics becomes comparatively critical in case of joining of heat sensitive material like austenitic stainless steel due to its low thermal conductivity and high coefficient of thermal expansion, especially when it is of thick section. The criticality primarily arises due to the use of a welding process and procedure introducing significant impurities in weld deposit, large amount of metal deposition and severity of weld thermal cycle. Such undesirable conditions may be avoided by selection of a comparatively cleaner welding process, reduction in amount of weld deposition using narrow gap welding procedure and modification of thermal and solidification behaviour of weld deposit through proper selection of welding parameters. In the recent past, pulse current gas metal arc welding (P-GMAW) has emerged as a widely accepted welding process due to its several advantages including ability to produce comparatively cleaner weld. It is also well established that the use of narrow groove in welding of thick sections of≥25 mm may significantly reduce a number of adverse influence of welding including the severity of thermal cycle and residual stresses in weld joint. Thus, a combination of P-GMAW and narrow gap welding procedure can be considered as an interesting technique to weld thick sections of stainless steel, having improved properties of weld joint than those observed in case of commonly available shielded metal arc (SMA) weld.

In this context it is realised that the use of P-GMAW effectively in narrow groove of at least 25 mm thick section is practically impossible due to difficulties in manipulation of relatively large conventional torch head of the order of 24 mm O.D. in weld groove. In order to successfully implement this technique, development of a narrow torch head giving desired protection to weld deposition, effective manipulation to achieve sufficient groove wall fusion and satisfactory arc stability is very much essential. Here it should also be noted that the critical selection of simultaneously interactive pulse parameters can only be made by developing a clear understanding of the influence of hypothetical factor ϕ, total heat transferred to the weld pool (Q_T) and the variation of heat input (Ω) on characteristics of the weld bead.

2.6.2 Objectives of the Work

In view of the above the present investigation on welding of thick wall 304LN stainless steel pipe has been carried out using pulse current gas metal arc welding in narrow weld groove. The studies have been systematically planned in order to gain sufficient knowledge to establish a welding technique superior to some conventionally used welding process and weld groove design.

1. To design and develop a narrow GMA torch nozzle device which facilitates the application of P-GMAW process in narrow gap welding of thick wall pipes.

2. To study the efficient use of factor ϕ, Ω and Q_T, by analysing its influence on sensitization and other characteristics of weld through bead on plate deposition. This is in order to develop a systematic knowledge for selection of appropriate range of welding parameters and procedure which may be effectively used in pulse current narrow groove welding of thick section.

3. Development of narrow gap welding procedure by P-GMAW process for joining of thick sections by appropriate reduction in number of weld passes and amount of weld metal.

4. To study the effect of variation in pulse parameters considered by their summarized influence as factor ϕ on metallurgical, mechanical and fracture mechanics properties as well as residual stresses of weld joint.

5. To study the acceptability of weld joint with respect to corrosion susceptibility of its heat affected zone.

6. To establish suitability of narrow gap P-GMA welding by comparing it's utility to improve the properties of weld joint with respect to those prepared by commonly used SMA welding with and without narrow weld groove.

DEVELOPMENT OF NARROW GMAW TORCH NOZZLE DEVICE

Gas metal arc welding (GMAW) process is not preferred in narrow gap welding of thick sections in spite of its numerous advantages over commonly used shielded metal arc welding (SMAW) and gas tungsten arc welding (GTAW) processes primarily due to its comparatively large diameter torch nozzle which poses difficulties in its required manipulation in weld groove. The research work so far carried out on development of GMA welding torch head has been primarily directed towards effective shielding of weld pool from air contamination [Tyagi 2000, Nosse 2001, Jones 2004] and improvement in current transfer efficiency of contact tip [Stuart 2005]. The removal of excess heat generated in weld groove especially during welding of comparatively thick sections with a groove width of 25mm was of considerable interest. However, the torch heads have not been developed for narrow gap GMA welding of thick pipes/plates along with proper consideration of the characteristics of shielding jacket at the outlet of torch head protecting the weld deposit from any types of contamination. This requires special attention while welding in narrow weld groove primarily due to significant constraints on dynamics of gas flow produced by the groove wall. The constraints on gas flow due to boundary conditions applied by groove design may induce turbulence in the shielding jacket resulting in porosity due to air aspiration in it at a given gas flow rate while using narrow torch head. Hence in the present study a narrow torch head addressing the above aspects upto certain extent has been designed and employed in narrow gap welding of thick wall (25mm) pipes.

3.1 DESIGN OF THE TORCH NOZZLE DEVICE

The commercially available torch nozzle for gas metal arc welding has been shown in Fig. 3.1 which is having an integrally formed copper tube with relatively large outlet diameter

(Fig. 3.2(a)). This is primarily suitable for shielding gas discharge in conventional V-groove butt welding of 10-12 mm thick sections when fitted to the forward end portion of a welding torch during use. Such large outlet diameter torch nozzle can seldom be used in conventional or narrow groove GMA welding of thick sections beyond about 15-20mm.
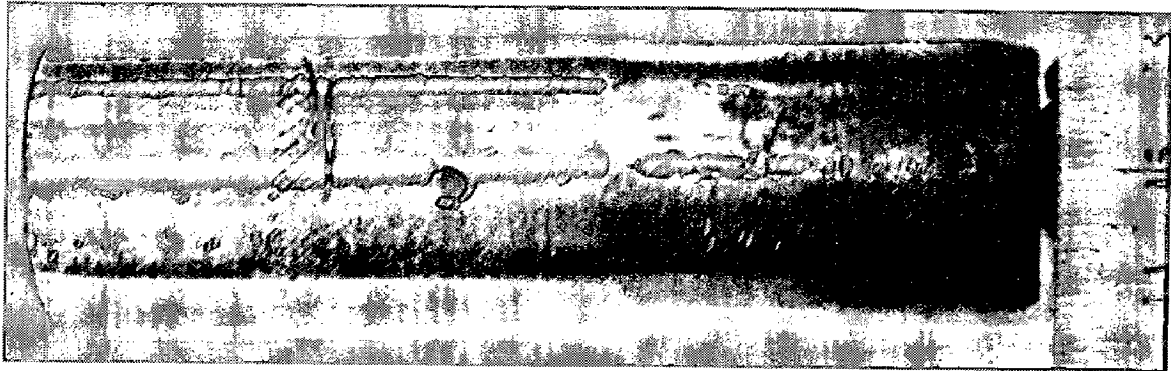
Fig. 3.1:   Photograph showing Conventional GMAW torch nozzle.

(a)

(b)

ALL DIMENSIONS IN mm
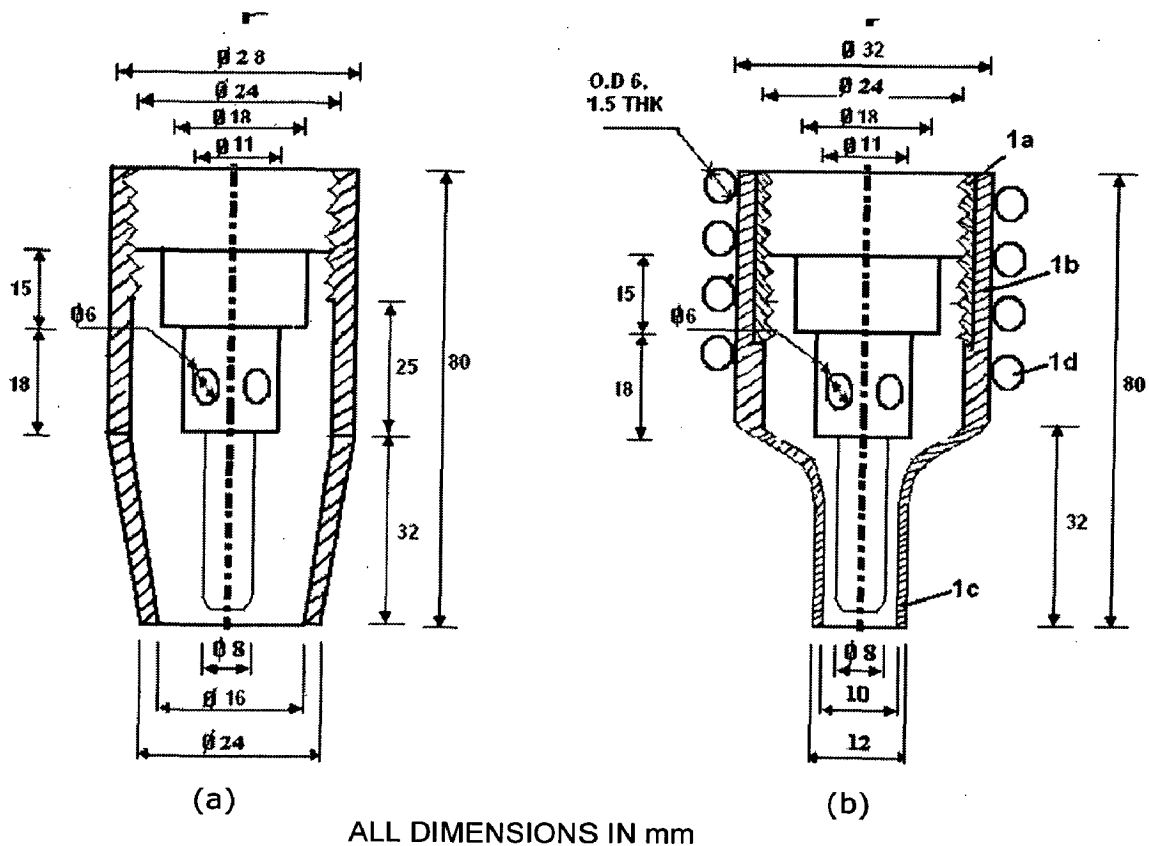
Fig.3.2:   Schematic diagram of (a) Conventional and (b) newly designed narrow GMA torch nozzle.

In this work a relatively easily attachable narrow torch nozzle device (1) as shown schematically in Fig. 3.2(b) has been prepared to introduce GMAW and especially P-GMAW process in narrow gap welding of thick sections. The device could be easily attached to the commercially available GMA welding torch (2) (Fig. 3.3) in such a manner that the wire holder (3), contact tip adaptor (4) and contact tip (5) are totally hidden within the welding nozzle. The newly developed narrow torch nozzle (Fig. 3.2 (b)) with respect to its use as a cost effective easily attachable part to the conventional GMAW torch head consist of three members. The first one is the torch nozzle device having a tubular internally threaded member (1a) which is removable from the welding torch (2), usually through the use of a screw threading method. The second one is the round tubular body (1b) with a drawn rectangular end portion (1c) of suitable length which is press fitted on the internally threaded member (1a) and the third one is the coiled copper tubular section (1d) brazed on the round tubular body (1b) to carry cooling fluid. The rectangular hallow end portion (1c) of the second member is a relatively thin body to direct the flow of shielding gas on weld area. This end portion (1c) is one of the primary aspects of the present design as it provides the desired torch manipulation in narrow weld groove. An adequate cooling is provided by the high conductive water cooled copper tubes (1d) spirally brazed on the cylindrical portion of the narrow torch nozzle to prevent excessive heating and burning thereof. As a result the durability of the narrow torch nozzle is extended up to that of a conventional one.
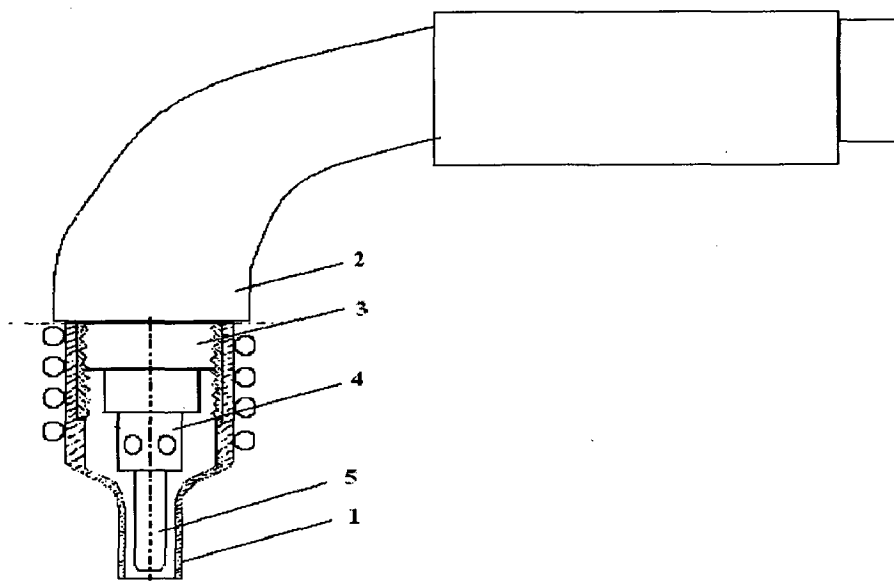
Fig. 3.3:   GMA torch head with newly developed narrow torch nozzle device

The photograph of the newly designed narrow torch nozzle is as shown in Fig.3.4. The nozzle has been designed and fabricated considering the following features.

- Narrow torch nozzle has a rectangular cross-section of enough depth at the gas flow outlet such that the torch manipulation required for setting optimum angle of attack in various narrow groove designs could be easily achieved.

- Internal cross-sectional area at the outlet of narrow torch nozzles has been kept same as that of conventional one such that gas shielding of the arc is least affected.

- Wall thickness at the gas flow outlet in narrow torch nozzle was reduced to 1mm by providing proper water cooling arrangement such that the heat accumulation at the thinner wall cross-section does not occur due to considerably higher arc energy and the entire torch nozzle body remains close to ambient temperature during welding operation.
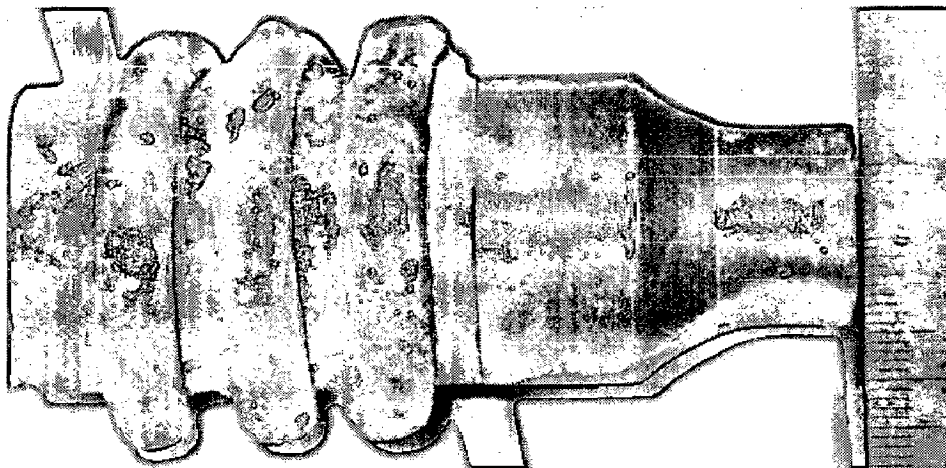
Fig.3.4: Photograph showing GMA narrow torch nozzle

The water cooling arrangement was so designed that the arc heat is transferred to the circulated water in three stages as shown schematically in Fig. 3.5. In the first stage maximum heat generated at the top surface of arc is dissipated through the argon gas flow to 1c (Fig.3.2(b)) of torch nozzle device by radiation. In the second stage the heat is transferred

from 1c to 1d through 1b by conduction. In the final stage heat is removed from 1d through flowing water by convection. The entire system is primarily designed for required water inlet temperature and flow rate through 1d such that heat accumulation amounting to melting of 1c does not occur. Thus to protect 1c the system was designed to maintain it at room temperature (303K) by proper extraction of heat.
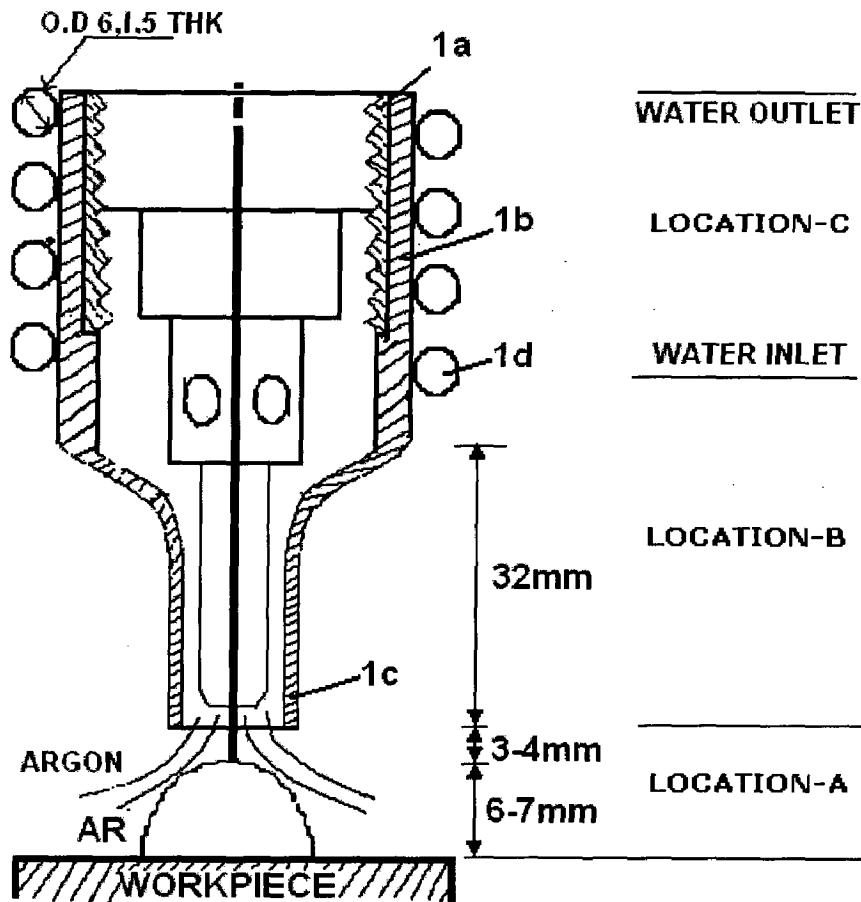
Fig. 3.5: Schematic diagram showing stages of arc heat transfer

LOCATION-A

Heat generated by arc is partially transported to surface of torch nozzle by conduction through ionised argon plasma, through flowing argon gas by convection and by radiation from arc chavern. Heat transferred by convection to nozzle surface may be assumed almost negligible considering the fact that argon gas is continuously flowing away from the surface (Fig.3.5) during welding. Thus the flow of charged ions towards nozzle surface will be

obstructed by the gas flow. However the temperature gradient across the argon plasma in the vicinity of nozzle surface may lead to continuous collision of these charged ions of argon and thus form a conductive medium for transfer of heat. Hence depending upon thermal conductivity of argon plasma, heat transferred to nozzle surface (Q_{con}) was estimated by following expression

$$Q_{arc} = KA \frac{dT}{dx} \qquad (3.1)$$

Here K is thermal conductivity of argon (0.625J/m/s/K), A is cross sectional area of the rectangular torch (75.2mm^2), dt is the temperature difference between arc charvern and torch nozzle surface and dx is the shortest distance between the arc root and nozzle surface. The temperature on the surface of the arc chavern (T_{arc}) generally lies in the range of 6000K for most of the ferrous metals [Wang et al 2003, Fan and Kovacevic 2004] whereas arc of root diameter (D_R), projected diameter (D_P) and length (L) of 7mm, 15.5mm and 7.5mm respectively were considered based on our observations published on stainless steel at an electrode extension of 12mm [Ghosh et al 2008].

Therefore by putting these values in eq. (3.1) by considering that torch is always maintained at room temperature (T) of 303K, heat conducted was estimated as

$$Q_{con} = 65.3J/s \qquad (3.2)$$

Heat generated at the surface of the arc chavern (Q_{rad}) transferred by radiation to the surface of the torch nozzle was estimated as follows.

$$Q_{rad} = \varepsilon \sigma A_{arc} (T_{arc} - T)^4 \qquad (3.3)$$

Here ε is emissivity of argon plasma taken as 0.012 [Redding 2002], σ is Stefan-Boltzman constant (5.67x10^{-8} W/m^2/K^4) [Lancaster 1993], A_{arc} is surface area of arc (m^2). A_{arc} was calculated by assuming arc as a conical cylinder as shown schematically in Fig. 3.6.
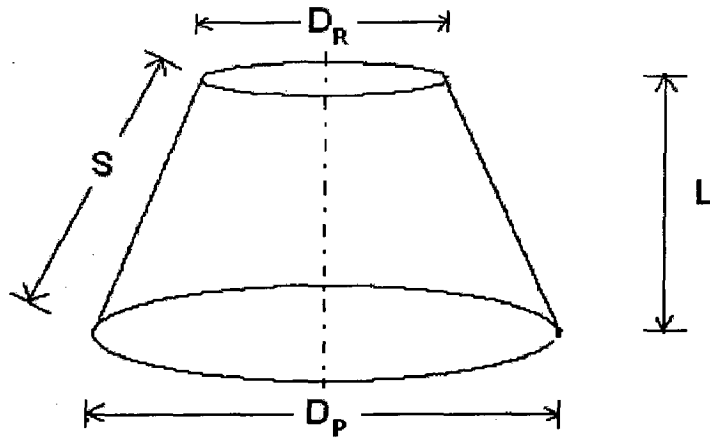
Fig. 3.6: Schematic diagram of arc

Hence surface area of arc has been calculated as

$$A_s = \pi \left[\left(\frac{D_P^2}{4} \right) + \left(\frac{D_R^2}{4} \right) + S \left(\frac{D_P + D_R}{2} \right) \right] = 532 \ \text{mm}^2$$

Therefore by putting the value of A_S in eq. 3.3 we get

$$Q_{rad} = 380.8 \ \text{J/s} \tag{3.4}$$

Thus from eq. (3.2) and (3.4), total heat transferred to the nozzle surface was estimated as

$$Q_{1c} = 65.3 + 380.8 = 446.1 \ \text{J/s.} \tag{3.5}$$

LOCATION-B

The 32mm long hollow rectangular copper nozzle section (1c) extracts the heat transferred to the nozzle surface (Q_{1c}) by conduction (Fig. 3.5). Thus effective temperature at the end of hollow rectangular section (T_{s2}'), for which heat sink (1b and 1d) has to be designed was estimated as.

$$Q_{1c} = KA \frac{dT}{dx} \tag{3.6}$$

$$Q_{1c} = 446.1 = 401 \times 75.2 \times 10^{-6} \times \frac{T_{s2} - 303}{32 \times 10^{-3}}$$

Here thermal conductivity of copper was taken as 401 J/s/m/K and surface area of torch nozzle was estimated as 75.2mm^2. Hence

$$T'_{s2} = 776.4K \tag{3.7}$$

LOCATION-C

Heat sink (Fig. 3.5) which extracts the heat from thin hollow rectangular section has been designed in two parts. First one is comparatively thick round tubular body (1b) of copper and the other one is copper coil (1d) brazed on this tubular body. Function of 1b is only to transfer the heat extracted from 1c to the water flowing through 1d by convection. Hence design of heat sink has been carried out in two steps. In the first step by considering that 1b has been maintained at room temperature the heat extraction rate required through 1d has been estimated. Secondly based on this required heat extraction rate, temperature of water at the outlet (T_{out}) through 1d has been estimated for a given maximum contact area of copper coil and normal tap water flow rate.

The heat extraction rate (Q'_{1b}) required for maintaining 1b at room temperature was estimated by considering the area of 1b as 351.9mm^2.

$$Q'_{1b} = 401 \times 351.9 \times 10^{-6} \times \frac{776.4 - 303}{48 \times 10^{-3}} = 1391.7 J/s \tag{3.8}$$

The heat extracted (Q'_{1b}) is transferred to the flowing water through the coiled copper tubular section (1d) having a contact area (length of copper tube in contact x thickness of tube) of 452.4mm^2 with 1b. Thus, the temperature of the flowing water at the outlet (T_{out}) was estimated by equating the heat flow rate across the section.

$$\frac{Q'_{1b}}{A_t} = \frac{m_w \times C_{pw} \times (T_{out} - T_{in})}{A_{wt}} \tag{3.9}$$

In eq.3.7 m_w is mass flow rate of water (0.083 kg/s), C_{pw} is specific heat of water (4.185 J/kg/k), A_{wt} is the cross sectional area of tube through which water is flowing and T_{in} is inlet temperature (303K) of flowing water through 1d (Fig.3.5). Hence by putting these values in eq. 3.7 we get

$$\frac{1391.7}{452.4 \times 10^{-6}} = \frac{0.083 \times 4.185 \times 10^3 (T_{out} - 303)}{7.06 \times 10^{-6}}$$

$$T_{out} = 303.06K \qquad\qquad (3.10)$$

Thus negligible T_{out} primarily indicates that water flow at normal room temperature is suffice to extract heat at a rate of 1.4kJ/s. Secondly comparatively thin rectangular section (1c) of narrow torch will always remain at room temperature during entire welding operation.

The design of torch nozzle was further experimentally verified by measuring temperature rise of water flowing through copper coil by carrying out GMA and P-GMA weld bead on plate deposition at different welding and pulse parameters respectively. It was found that even with the increase in Ω from 8.2 to 12kJ/cm in both GMAW and P-GMAW processes the outlet temperature of water remains at room temperature. Thus the design of torch nozzle was considered appropriate for analysing the welding performance of the nozzle.

3.2 WELDING PERFORMANCE OF THE TORCH NOZZLE DEVICE

Functioning of the currently designed narrow torch nozzle was compared with the conventional torch head by considering primarily two basic factors such as arc stability and protection of weld metal from contamination defined by production of oxide free weld surface. It was also studied by carrying out bead on plate experimentation using the GMAW and P-GMAW processes. The welding arc can be considered stable when metal deposition takes place at almost constant welding current and arc voltage over a considerable period resulting in uniform bead appearance. The oxide free weld surface indicates negligible atmospheric contamination of arc environment jacket of gas shielding provided by the torch nozzle.

3.2.1 Arc Stability

The stability of welding arc was studied during bead on plate deposition using the narrow torch nozzle and conventional torch head under a commercial (99.98%) argon gas shielding at a flow rate of 18L/min. The weld deposition was made with the help of 1.2 mm diameter SFA-5.9-308L filler wire at direct current electrode positive (DCEP) where the electrode extension was kept as 12 mm. The studies were carried out under semiautomatic process with the welding torch mounted on a carriage trolley having a provision to regulate the travel speed, where the conventional and pulsed current welding parameters were varied as shown in Table-3.1 and Table-3.2 respectively at a comparatively higher heat input of the order of 9.8 ± 1.5 kJ/cm. The high heat input was chosen to check the extreme performance of the narrow torch nozzle to protect the weld under severe condition of contaminating (oxidation) state of affair with respect to arc stability. During welding all the parameters were recorded with the help of transient recorder (maximum resolution of 1 MHz) and WMS 4000 software installed in a computer connected to the circuit of the welding power source. The conventional behaviour of current and voltage during GMAW process captured by the WMS 4000 software while using narrow torch nozzle has been shown in Fig. 3.7. Similarly behaviour of mean current and voltage during P-GMAW process was also captured by same procedure. The pulse waveform of current and voltage characteristics of the P-GMAW process captured by the transient recorder while using narrow torch nozzle has been shown in Fig. 3.8.

Table-3.1: Welding parameters of conventional GMA weld bead deposition using narrow torch nozzle and conventional torch head at a gas flow rate of 18L/min.

Sr. No	Shielding device	Welding Parameters		Ω (kJ/cm)
		Arc voltage (V)	Current (A)	
1	Narrow torch	24.5	230	11.8
2	nozzle	23.5	211	10.4
3	Conventional	25	227	11.9
4	torch head	23.3	202	9.9

Table-3.2: Welding parameters of P-GMA weld bead deposition using narrow torch nozzle and conventional torch head at a gas flow rate of 18L/min.

Sr. No	Shielding device	ϕ	I_m (A)	I_p (A)	I_b (A)	[I_b/ I_p]	t_p (ms)	t_b (ms)	f (Hz)	Arc voltage (V)	Ω (kJ/cm)
1	Narrow torch nozzle	0.06	211	319	32	0.10	2.6	4.6	138	19	8.4
2		0.23	201	315	123	0.39	2.7	4.0	150	21	8.9
3	Conventional torch head	0.07	206	324	36	0.11	2.7	4.4	141	19	8.2
4		0.23	198	318	127	0.40	2.7	3.5	161	21	8.7
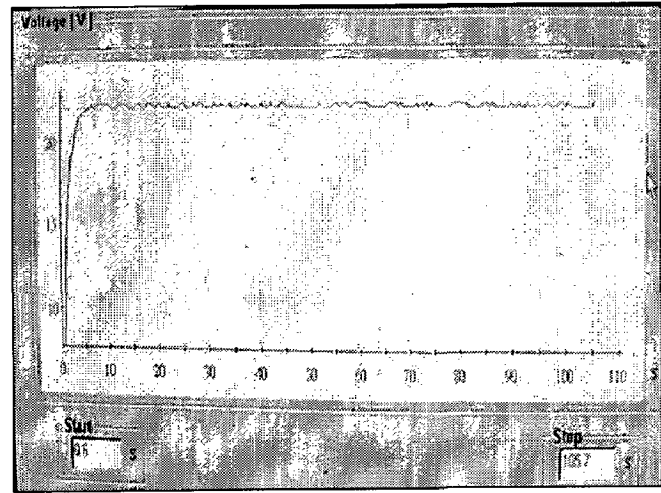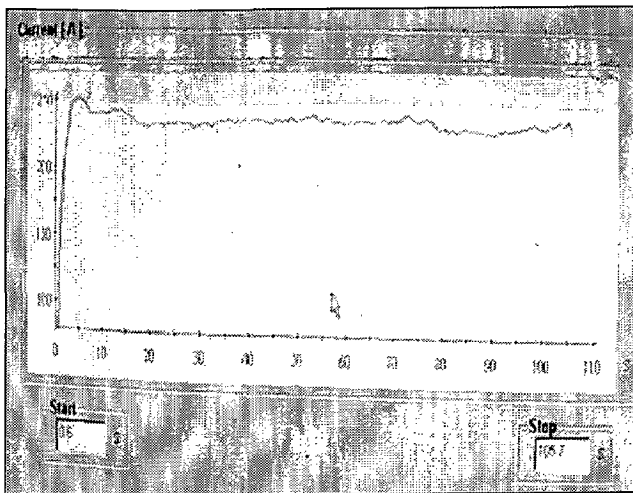
(a)
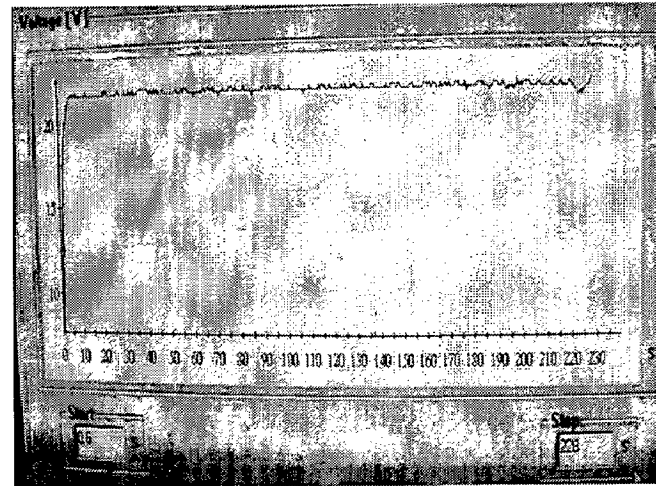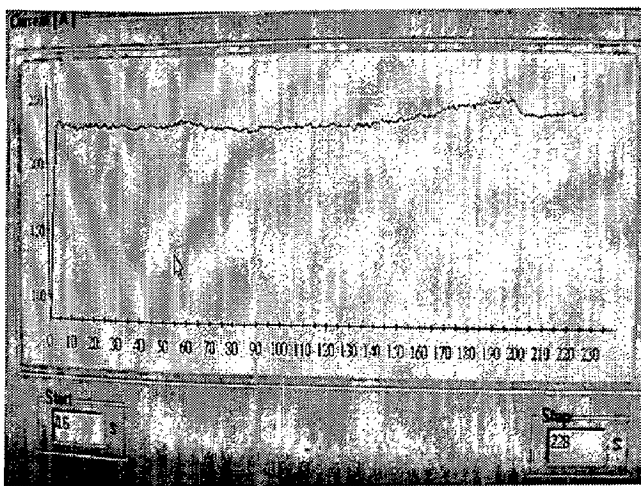
(b)

Fig. 3.7: Typical behaviour of conventional parameters observed during GMA welding by using (a) conventional torch head and (b) narrow torch nozzle device.
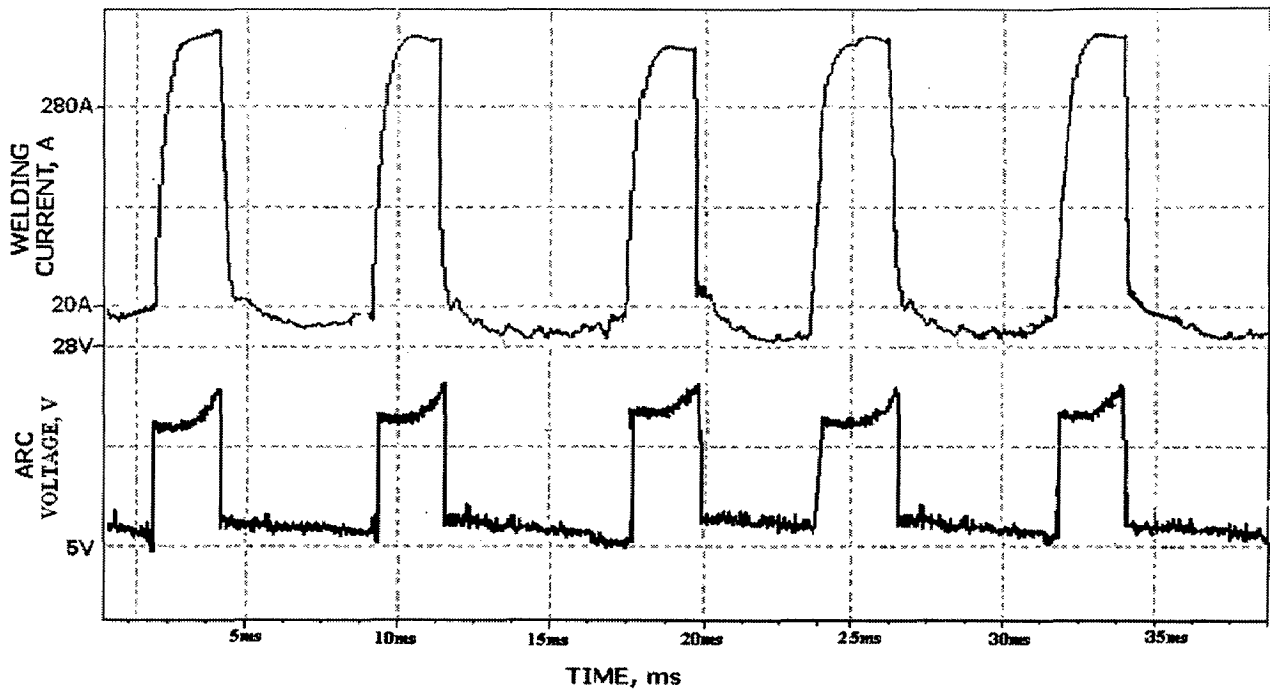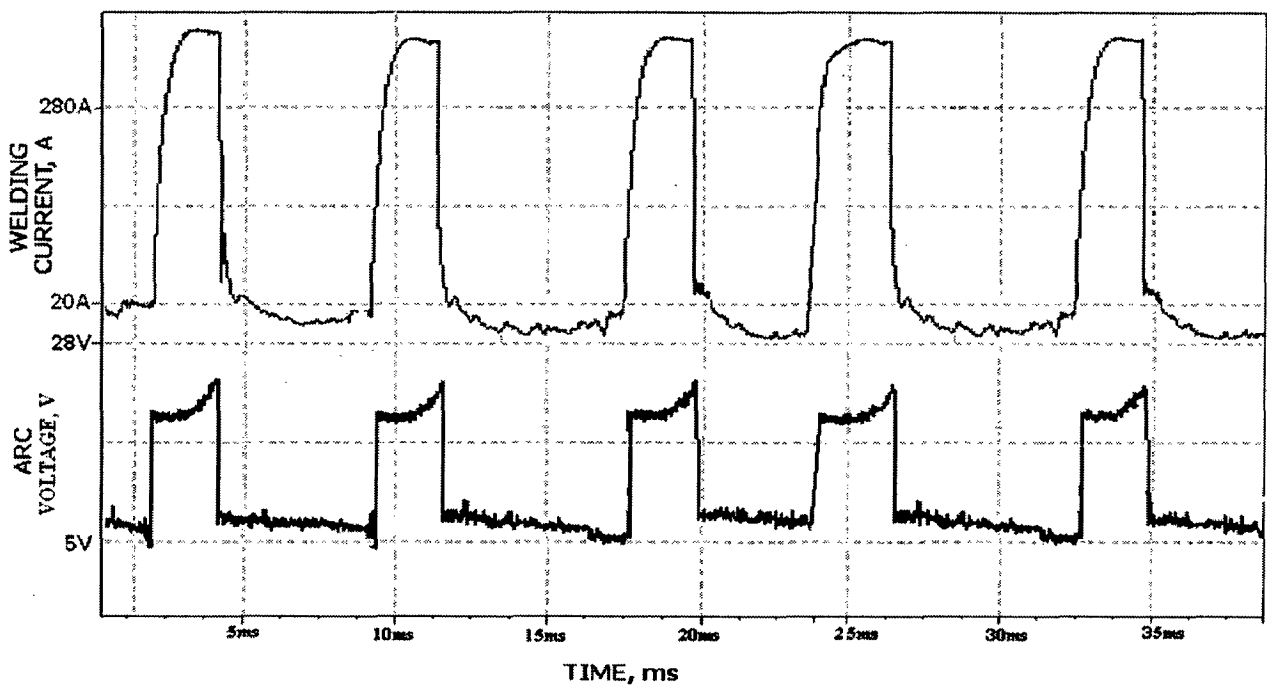
Fig. 3.8: Typical behaviour of the pulsed current and voltage observed during P-GMA welding by using (a) conventional torch head and (b) narrow torch nozzle device.

Figs. 3.7 and 3.8 primarily depicts that narrow torch nozzle device does not influence the controlled variation in conventional and pulse parameters while using both the GMAW and P-GMAW processes. Thus it confirms that narrow torch nozzle device does not affect arc

104

stability while using both the processes. However arc stability was further confirmed by visual appearance of weld bead and its porosity content estimated by following the procedures mentioned in section 4.6.4.2. It was observed that in both the GMA and P-GMA welds deposited under the argon gas shielding are having negligible porosity content of the order of 0.16±0.04 Vol.%. Thus, it may be assumed that the arc was practically stable enough to protect the shielding environment from appreciable contamination of weld deposit at a given range of welding parameters.

3.2.2 Oxidation of Weld

The effectiveness of shielding while using the narrow torch nozzle device was also studied with respect to the degree of oxidation of superheated weld bead immediately after its deposition in comparison to that observed on the weld bead deposited by using the conventional GMAW torch head. The matter was studied as a thickness of oxide layer present at the surface of the weld bead deposited under varying welding parameters of significantly high range of heat input (Table-3.1 and 3.2) at a given flow rate of shielding gas. The oxide layer thickness on weld bead was confirmed by measuring it as revealed under scanning electron microscope (SEM). The typical SEM photographs depicting the presence of oxide layer on GMA weld bead deposited by using the narrow torch nozzle and the conventional torch head at welding current of 230 ±5A have been shown in Fig. 3.9 (a) and (b) respectively. Similarly at a given ϕ of 0.23 and I_m of 200±6A, the SEM photographs depicting the presence of oxide layer on P-GMA weld bead deposited by using the narrow torch nozzle and the conventional torch head have been shown in Fig. 3.10 (a) and (b) respectively. The thickness of oxide layer observed in case of using the narrow torch nozzle and the conventional torch head on the weld deposited with GMAW and P-GMAW processes is given in Table-3.3.
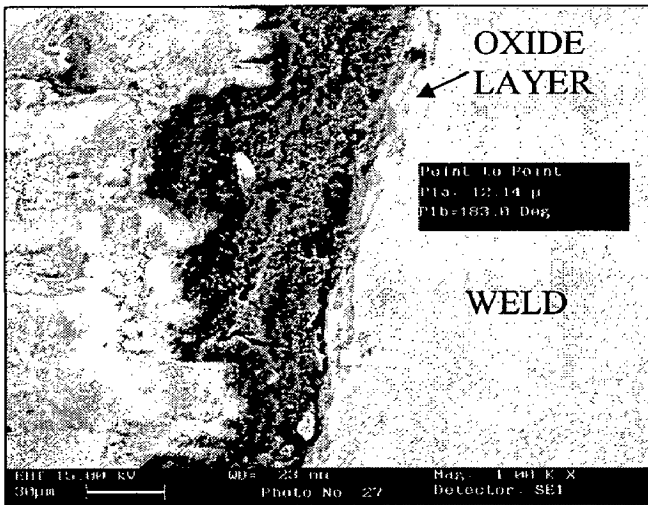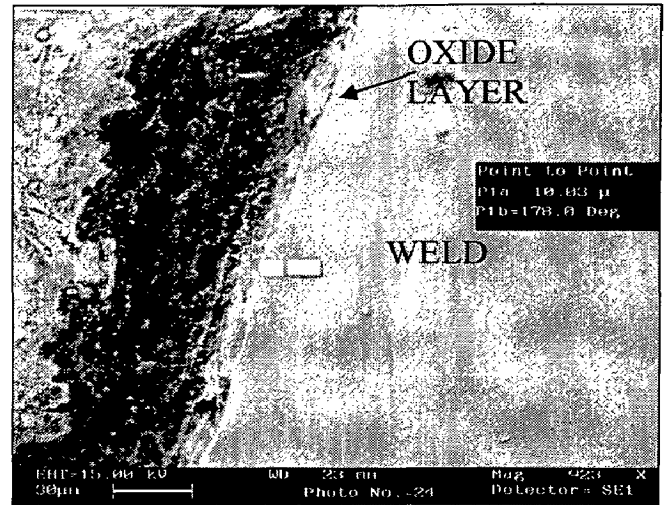
Fig.3.9 Typical SEM photograph depicting oxidation layer thickness on GMA weld bead deposited by using (a) Conventional GMAW torch nozzle and (b) Narrow GMAW torch nozzle at approximately 230A welding current.
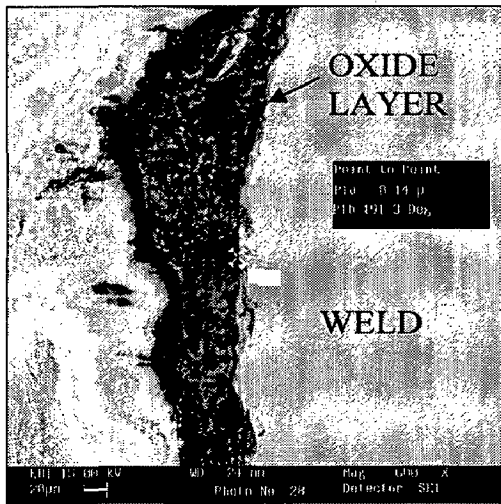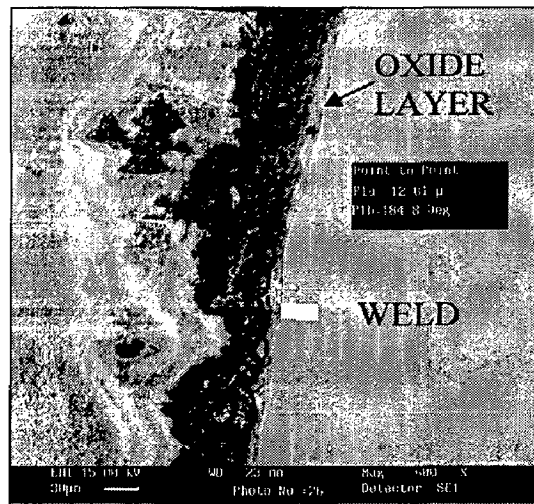
Fig.3.10 Typical SEM photograph depicting oxidation layer thickness on P-GMA weld bead deposited by using (a) Conventional GMAW torch nozzle and (b) Narrow GMAW torch nozzle at a given ϕ of 0.23 and I_m of 200±6A.

Table-3.3: Oxide layer thickness observed in GMA and P-GMA welds prepared by using narrow torch nozzle and conventional torch head

Sr. No	Shielding device	GMAW		P-GMAW	
		Ω (kJ/cm)	Oxide layer thickness (μm $\pm\sigma$)	Ω (kJ/cm)	Oxide layer thickness (μm $\pm\sigma$)
1	Narrow torch	11.8	11.04 ± 3.38	8.4	12.10± 3.43
2	nozzle	10.4	10.10 ± 2.19	8.9	15.10± 4.43
3	Conventional	11.9	10.70 ± 4.48	8.2	11.10± 2.31
4	torch head	9.9	09.88 ± 3.58	8.7	13.10± 3.13

The table primarily depicts insignificant variation in thickness of oxide layer on weld bead during using either of the narrow torch nozzle or conventional torch head with variation in welding parameters and process. However, the shielding characteristics by gas flow through the narrow torch nozzle in open atmosphere as observed in case of the bead on plate experimentation may vary while welding in weld groove primarily due to constraints on fluid dynamics of gas flow produced in presence of the groove wall. In any case the comparative studies on the performance of the newly designed narrow torch nozzle and conventional torch head justifies that it is largely comparable to govern the stability of welding process and quality of weld deposit with respect to its porosity content and oxidation. The observed extent of oxidation of weld deposit was assumed negligible when the multipass weld joints prepared by using normal interpass mechanical cleaning through wire brushing passed the X-ray radiography test as discussed later.

This chapter describes the experimental procedure followed in this investigation to examine the characteristics of weld joints of austenitic stainless steel pipes. The weld joints are prepared by different welding processes that include gas metal arc welding (GMAW) with conventional continuous current and pulsed current using solid filler wires and shielded metal arc welding (SMAW). The welding has been carried out using standard groove and narrow gap welding procedures. The weld joints have been primarily characterised by correlating the conventional mechanical properties and fracture mechanics properties of the weld and HAZ with their respective microstructures resulting from different welding processes, procedures and parameters.

4.1 BASE MATERIAL

The investigation has been carried out using 25mm thick extruded stainless steel pipes of AISI 304LN grade having NB of 300mm. The chemical composition of the base material has been given in Table 4.1.

Table 4.1: Chemical composition of base metal.

Material	Source	Chemical analysis (Wt.%)									
		C	Cr	Ni	Mn	N	Mo	Si	Cu	S	P
Base metal (304LN)	ASME Section IX	0.035	18-20	8-11	2.0	0.1-0.16	-	0.75	-	0.03	0.04
	Supplier test certificate	0.024	18.8	9.25	1.73	0.15	-	0.55	-	0.001	0.022
	*Laboratory test	0.023	19.02	9.14	1.82	0.16	0.19	0.57	0.30	0.002	0.021

* spark emission optical spectroscopy.

4.2 WELDING CONSUMABLES

The welding consumables have been primarily divided into two categories, filler wire/electrode and shielding gas. The gas metal arc welding with bare filler metal was carried out by using commercial argon of 99.98% purity as shielding gas. Depending upon welding processes, the filler wire/electrode was selected by generally matching the physical and chemical characteristics of base metal, such that the weld microstructure can have 4-8% δ-ferrite content as per WRC-92 Siewert diagram [Siewert et. al.,1988 and Shankar et. al., 2003(b)] to avoid hot cracking. The classified size and specification of filler metal used in different welding processes are given in Table 4.2.

Table 4.2: Consumables used for different welding processes

Welding process	Weld consumable specification		
	AWS/ASME classification	Size (mm)	Electrode flux (Class)
P-GMAW	SFA-5.9 ER308L	1.2	--
GMAW	SFA-5.9 ER308L	1.2	--
SMAW	SFA5.4 E 308L–15	3.15 and 4.0	Basic coated
GTAW	SFA 5.9 ER 308 L	2.0 and 2.5	--

4.3 BEAD ON PLATE EXPERIMENTATION BY P-GMAW PROCESS

4.3.1 Welding

Weld bead on plate deposition was carried out on 10mm thick AISI 304 austenitic stainless steel plate by employing direct current electrode positive (DCEP) pulsed current gas metal arc welding (P-GMAW) and conventional gas metal arc welding (GMAW) processes using 1.2mm diameter solid austenitic stainless steel filler wire of specification SFA-5.9-

ER308L. The chemical compositions of the base plate and filler wire are shown in Table-4.3. The P-GMA weld deposition was carried out at a given welding speed (S) and arc voltage of 20cm/min and 23.5 ± 1.2 V respectively where the heat input (Ω) was varied through a change of mean current (I_m) as a function of wire feed rate. However, during welding at a given wire feed rate the I_m was also varied with a change in pulse parameters (Table- 4.4) which has also been duly considered for estimation of heat input. The total heat transferred to the weld pool (Q_T) in terms of heat of the arc imposed on the weld pool surface (Q_{AW}) and transfer of heat inside the weld pool (Q_f) by the penetrating droplets [Goyal et.al. in press] depending upon variation of pulse parameters resulting at different ϕ has also been estimated as shown in Table- 4.4. These combinations of parameters facilitate to study and correlate the influence of pulse parameters and heat input on various characteristics of weld bead. Similarly for a comparative study some GMA weld bead deposition was also carried out at two moderate levels of heat input (Ω) by keeping the welding speed (S) at 20cm/min as shown in Table-4.5. During weld deposition the base plate was rigidly fixed in a fixture to avoid distortion and the torch was mounted on an automatic carriage trolley. The metal deposition was carried out in flat position by placing the welding torch perpendicular to the base plate and keeping an electrode extension of 12 mm. The weld deposition was performed by using the commercial (99.98%) argon gas shielding at a flow rate of 18L/min. A relatively lower grade of argon gas was chosen for shielding in order to leave a possibility of weld contamination, if appreciably happens at all, as a function of welding parameters under different welding procedures, which may provide an access to study the performance of welding parameters and procedure to produce sound weld. During welding the pulse characteristics, such as I_p, I_b, t_p and f were measured with the help of a transient recorder (maximum resolution of 1 MHz) fitted with the electrical circuit of the welding set up. The arc voltage (V) and the I_m were recorded with the help of WMS 4000 software installed in a

110

computer connected to the circuit of the welding power source. The heat input (Ω) of the P-GMA and GMA welding processes and total heat transferred to the weld pool (Q_T) during P-GMAW process was estimated as follows by assuming a process efficiency or thermal heat transfer efficiency (η_a) of the arc as 0.7 [Joseph et.al. 2003].

$$\Omega \text{ (kJ/cm)} = \eta_a \times \frac{\text{Mean current (A)} \times \text{Arc voltage (V)}}{\text{Welding Speed (cm/min)} \times 1000} \tag{4.1}$$

$$Q_T \text{(kJ / cm)} = \frac{(Q_{AW} + Q_f) \times 60}{\text{WeldingSpeed(cm / min)} \times 1000} \tag{4.2}$$

$$Q_{AW} \text{(J / s)} = \left(V.I_{eff} - \psi.I_{eff}\right)\eta_a \tag{4.3}$$

$$Q_f \text{(J / s)} = H_{fp}.f \tag{4.4}$$

$$H_{fp} \text{(J / pulse)} = H_{fpp} + H_{fpb} = H_{de}.m_t \tag{4.5}$$

Where, I_{eff} (A) is the effective current estimated by root mean square of the pulsed current wave form, ψ is the effective melting potential at anode (Work function + anode voltage fall + thermal energy of electrons), as 6.6 V [Terumi and Kazuo 2002]. H_{fp} is heat transferred to the weld pool by superheated filler metal per pulse, H_{fpp} and H_{fpb} are the heat transferred by the superheated filler metal within the duration of peak current and base current of a pulse respectively, H_{de} is the heat content per unit mass of the filler wire at the time of deposition and m_t is the mass of filler wire transferred per pulse.

Table 4.3:   Chemical composition of the base material

Material	Chemical composition (wt %)								
	C	**Cr**	**Ni**	**Mn**	**Mo**	**Si**	**Cu**	**S**	**P**
SS plate	0.087	21.1	7.5	1.42	0.35	0.54	0.20	0.015	0.012
SS filler wire	0.022	19.65	9.55	1.25	0.10	0.39	0.08	0.007	0.016

Table 4.4: Typical welding parameters used in P-GMA bead on plate experimentation

| Expt No | Wire feed rate, V_W (cm/s) | Heat Input, Ω (kJ/cm) | Q_{AW} kJ/cm | Q_f kJ/cm | Q_T kJ/cm | ϕ | Pulse Parameters | | | | | | Arc Voltage (V) |
							I_m (A)	I_P (A)	I_b (A)	t_P (ms)	t_b (ms)	f (Hz)	
1	14.2	9.3	8.2	4.8	13	0.047	183	464	30	1.98	5.32	137	24
2		9.9	8.0	4.7	12.7	0.069	191	435	40	1.87	5.38	138	24
3		10.2	7.9	4.7	12.6	0.091	194	420	53	1.99	5.20	139	25
4		10.9	7.8	4.6	12.4	0.141	203	385	76	2.01	5.03	142	25
5		11.1	7.6	4.6	12.2	0.185	206	357	93	2.02	4.92	144	25
6		11.4	7.5	4.6	12.1	0.225	211	331	106	2.07	4.83	145	25
7	12.5	8.1	7.1	4.0	11.1	0.044	166	460	26	2.00	6.47	118	23
8		8.6	7.1	4.0	11.1	0.061	175	437	35	1.95	6.45	119	23
9		8.9	7.1	3.9	11	0.100	178	412	55	2.00	5.87	127	24
10		9.5	7.0	3.9	10.9	0.153	182	378	78	2.01	5.80	128	24
11		9.9	6.9	3.8	10.7	0.193	189	357	94	2.03	5.55	132	25
12		10.2	6.8	3.8	10.6	0.237	190	318	104	2.06	5.46	133	25
13	10.8	6.9	6.3	3.3	9.6	0.042	145	448	24	1.96	7.47	106	22
14		7.2	6.1	3.3	9.4	0.058	151	419	31	1.97	7.55	105	22
15		7.6	6.1	3.3	9.4	0.080	156	400	41	2.02	7.15	109	23
16		8.3	5.9	3.2	9.1	0.147	165	359	69	2.04	6.66	115	24
17		8.6	5.9	3.2	9.1	0.197	171	327	85	2.04	6.43	118	24
18		8.8	5.9	3.2	9.1	0.218	172	300	87	2.05	6.28	120	24
19	9.2	5.7	5.7	2.7	8.4	0.041	125	434	22	1.96	8.24	98	22
20		6.2	5.6	2.7	8.3	0.064	133	409	34	2.03	6.90	112	22
21		6.6	5.3	2.7	8	0.093	140	383	44	2.00	8.00	100	22
22		6.8	4.9	2.7	7.6	0.136	145	343	59	2.01	7.89	101	22
23		7.2	4.9	2.6	7.5	0.189	153	311	74	2.06	7.74	102	22
24		7.6	4.8	2.6	7.4	0.224	156	285	82	2.07	7.36	106	23

Table 4.5: Typical welding parameters used in GMA bead on plate experimentation

Expt No	Wire feed rate, V_W (cm/s)	Heat Input, Ω (kJ/cm)	Welding Current (A)	Arc Voltage (V)
1	12.5	9.7	215	21.5
2	10.8	7.2	195	17.5

4.3.2 Studies on Characteristics of Weld Bead

The transverse section of weld bead, collected from central part of its length of deposition ensuring a stable welding, was polished by standard metallographic procedure using diamond paste of 0.25 µm size particles. The weld geometry revealed by electrolytic etching in 10% oxalic acid solution was studied under optical microscope. The weld bead geometry as shown schematically in Fig. 4.1 was estimated by measuring the bead width (W), the depth of penetration (P), bead height (H), area of bead penetration (A_P) and area of bead reinforcement (A_R) by graphical method with the help of an image analyzer software installed in the computer.
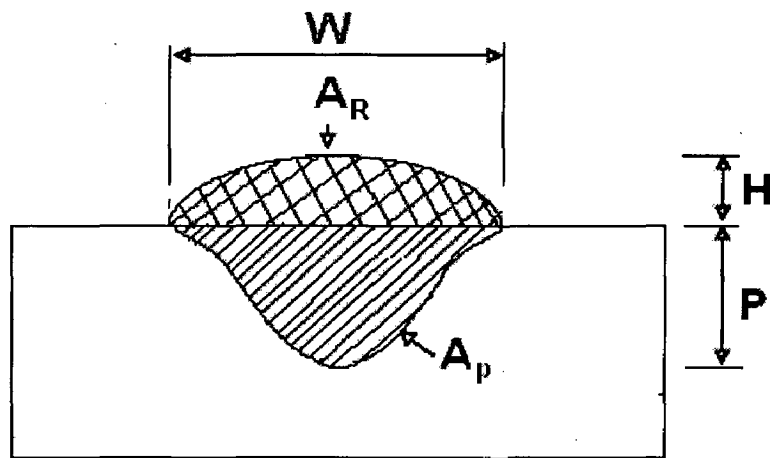
Fig. 4.1:   Schematic diagram of weld bead geometry

The dilution of weld deposit (D_W) was estimated as follows in terms of geometric solution of the graphic area.

$$\%D_W = \frac{A_P \times 100}{A_P + A_R} \tag{4.6}$$

4.3.3 Inter Granular Corrosion Studies

Acceptability of weld bead towards its susceptibility to inter-granular corrosion (IGC) was studied by carrying out a rapid oxalic acid electrolytic etch test as per ASTM E262 Practice A. The test was performed on the metallographic polished transverse section of weld joint by dipping it into a solution containing 100 g reagent grade oxalic acid ($H_2C_2O_4 . 2H_2O$) in

900 ml distilled water and using a current density of the order of 1 ± 0.1 A/cm^2. The susceptibility of HAZ to inter-granular corrosion (IGC) attack under the influence of varying ϕ and Ω in P-GMA welds was examined by measuring average grain boundary thickening (T) in the region within 0.02 mm adjacent to fusion line. Similarly the influence of Ω on IGC suceptibility, was also studied on the GMA welds. The measurements were carried out under an optical microscope. The distribution of chromium content at few locations of HAZ was studied by line mapping through EDAX under field emission scanning electron microscope (FE-SEM) having a resolution of 2nm for basic understanding about the susceptibility of matrix to IGC.

4.3.4 Microstructure Studies

The various features of microstructure of P-GMA and GMA weld bead and HAZ revealed under the rapid oxalic acid electrolytic etching were also studied under an optical microscope. The effect of ϕ and Ω on the morphology of P-GMA weld deposit has been studied primarily with respect to its co-axial growth of dendrite during solidification. The amount of practically round shape black spots considered as porosity content of weld deposit was estimated by measuring their area fraction in the matrix. The estimation was made with the help of image analyzer software used during optical microscopic studies on the metallographically polished unetched transverse section of weld bead. The analysis was carried out on at least 21 randomly captured images of different locations of the matrix viewed at a magnification of X100. The volume fraction of approximately round shape porosity in the matrix of weld bead deposited at different ϕ and Ω was estimated by assuming it as a linear function of its measured area fraction.

The width of HAZ defined as a zone having significant grain growth (Z) adjacent to fusion line was also measured with the help of Axio vision software based image analyser facility connected with the optical microscope. The grain size of the coarse grain region of HAZ adjacent to the fusion line as stated above in each weld bead was also measured by using the image analyzer software at 6-10 randomly selected spots as per ASTM E112. The

characteristics of HAZ were also studied as a function of ϕ and Ω in P-GMA welds and compared to those of the conventional GMA welds.

4.3.5 Hardness

The Vickers hardness (VHN) of P-GMA and GMA weld beads have been studied at different locations of its etched transverse section identified as weld deposit, fusion line and HAZ. The Vickers hardness (VHN) of base metal and weld deposit was measured by diamond indentation using a load of 5 kg. The hardness of weld deposit was randomly measured at least on five locations of its central region. However, the hardness along the fusion line and in coarse grain region of HAZ adjacent to fusion line was measured using micro hardness indentation at a load of 100g. The indentations on fusion line and in the coarse grain region of HAZ were randomly made to take care of true characteristics of hardness distribution. Finally by considering GMA (Table 4.5) weld bead data as a reference, the average micro hardness observed in weld, fusion line and HAZ for the given set of P-GMA (Table 4.4) parameters were further correlated with ϕ and Ω.

4.4 PREPARATION OF WELD JOINTS

4.4.1 Welding Power Source

A modern transistorised power source as shown in Fig. 4.2 of M/s ESAB make, ARISTO 2000- LUD 450 UW model along with MEK 44C wire feeder was used to carryout welding. The power source was capable to operate for different welding processes such as GTAW, SMAW, GMAW and P-GMAW with DC straight and reverse polarity in both the synergic and non-synergic modes at a given command on selection of material and diameter of electrode/filler wire as well as shielding gas. During using P-GMA welding in synergic mode at a given wire feed speed the power source was capable to self adjust the other parameters such as arc voltage, peak current, background current or base current, pulse frequency and peak duration, whereas in non-synergic mode it was possible to operate the power source with

manual setting of all the parameters by maintaining appropriate correlations amongst them. In the power source peak current, I_P and base current, I_b was capable to operate in steps of 4A, whereas the pulse frequency, f and peak duration, t_p in steps of 2Hz and 0.1ms respectively. The power source was fitted with a push type wire feed unit which consists of two sets of U-grooved wire drive rollers to accommodate required diameter of filler wire. The pressure on the wire drive rollers was suitably adjusted to avoid slippage of the filler wire.

The power source has inbuilt integrated gate bipolar transistor (IGBT) which absorbs fluctuation in power supply to the machine and provides stable energy supply to the welding process. The water-cooled torch provided with the power source for GTAW, GMAW and P-GMAW processes further ensured safe continuous working even at comparatively higher energy inputs. The filler wire was fed to the arc for GMAW and P-GMAW processes through the welding gun suitable to use up to 500A welding current for different diameters of filler wire in the range of 0.8 to 2.0mm.

Fig. 4.2:   Photograph of power source used in this investigation.

4.4.2　Fixture and Torch Manipulator.

Suitable fixtures for welding of pipes in 1GR position was designed and fabricated as shown in Fig. 4.3. The designed system has manipulator for rotation of pipe supported by a flexible torch holding and positioning facility fitted to a modern torch carriage trolley required for GMA and P-GMA welding of pipes. However SMA welding of pipes has been carried out manually by controlling the speed of manipulator.
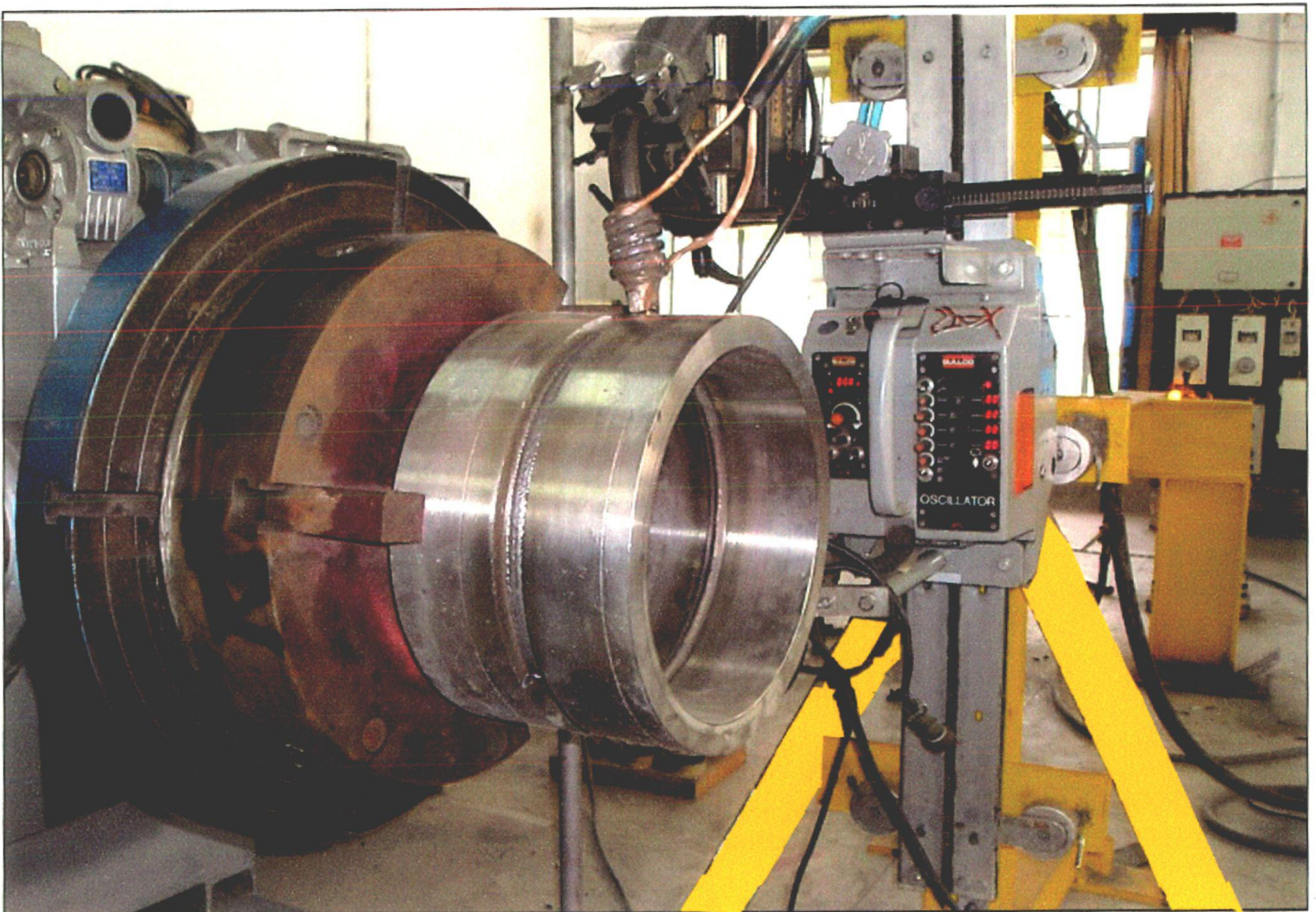
Fig. 4.3:　Photograph showing pipe holding fixture and torch manipulator used in welding of pipes.

The welding set-up consists of mechanised GMA welding gun travelling equipment and a "KAT" travel carriage capable to hold the welding torch rigidly in the rack and pinion arms and clamping pivots to adjust it at any desired position. The travelling equipment was having facility to vary the travel speed in the range of 2.6 -83.8 cm/min with a digital display. The torch carriage trolley which could also be locked at desired location helped further in positioning of torch especially inside the weld groove at a precisely maintained contact tip to workpiece distance during welding operation. The manipulator having a three-jaw chuck for firm holding and centring of pipes was used for its welding in 1GR position. The welding speed for the said dimension of pipe, depending upon requirement of the welding process, was controlled in the range of 1.4 - 27.4 cm/min by an electronically controlled mechanism (AC drive) which can control frequency input to the motor attached to the reduction gear box provided in the manipulator. Accuracy of travel speed of the carriage was verified before use by measuring the distance travelled at a given time using a stopwatch (0.01 second accuracy) at different speeds.

4.4.3 Welding Procedure

4.4.3.1 Conventional weld groove

The conventional V-groove used for preparation of weld confirms the ASME Section IX of Boiler and Pressure Vessel Code. The schematic diagram of the weld groove employed to P-GMA, GMA and SMA welding of pipes as well as the consumable insert used of matching composition with filler metal has been shown in Fig. 4.4 (a) and (b) respectively. The welding was carried out in 1GR position by holding the pipes in a rotating table with the help of three jaw clamping system. The weld joints were prepared by autogenous GTAW root pass followed by two GTAW filling passes and subsequent filling passes by either of the P-GMAW, GMAW or SMAW processes. The P-GMAW and GMAW passes were carried out

with fixture and torch manipulator arrangement as shown in Fig. 4.3. Whereas, GTAW and SMAW passes were manually carried out in synergic modes at a given command regarding the material and diameter of electrodes. During welding an interpass cleaning was carried out by stainless steel wire brushing primarily to remove slag along with oxide layer formed on the weld bead. Prior to carrying out the GMA welding of pipes, the welding procedure with respect to location of torch head, angle of attack and contact tip to work piece distance was established by simulated study on pipe sections. Finally the welding procedure was established by asserting repeatability on at least two full pipe weld joints. The SS308L consumable insert (Fig. 4.3(b)) was fused by GTAW autogenous root pass, whereas the remaining GTAW root passes were carried out by using 2 and 2.5mm electrodes respectively. The GTAW was carried out using water cooled torch with 7 mm diameter gas nozzle and 3.2 mm diameter 2% thoriated tungsten electrode having tip angle of 60^0 under the shielding of commercial argon at a flow rate of 12 L/min.
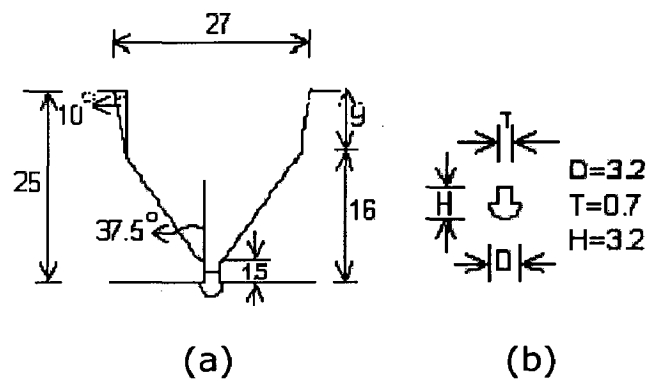
Fig. 4.4: Schematic diagram of (a) Conventional V-groove and (b) Insert used for SMA, GMA and P-GMA welding of pipes.

4.4.3.2 Narrow Weld Groove

In order to reduce the amount of weld deposition the designing of narrowest weld groove was approached in steps for P-GMAW and SMAW processes as schematically shown in Figs. 4.5 and 4.6 respectively by keeping in view the practical

difficulties of adopting the welding procedure to produce sound weld. The welding of narrow groove pipes was also carried out in 1GR position by following similar procedure as used in conventional groove with respect to the GTAW passes. Here also, welding procedure was established by asserting repeatability on at least two full pipe weld joints. However, filler passes were carried out at a much lower angle of attack to the groove wall, by semi-automation mode in P-GMAW and manually in SMAW processes, in comparison to that used in conventional groove welding procedure. In P-GMA weld joints all the passes were carried out with the help of 1.2mm diameter filler wire by using newly developed torch nozzle device with appropriate torch manipulation in the groove. Whereas, in SMA welds first two layers of filler passes were carried out by using 3.15mm diameter electrode while the remaining layers were carried out by 4mm diameter electrode.
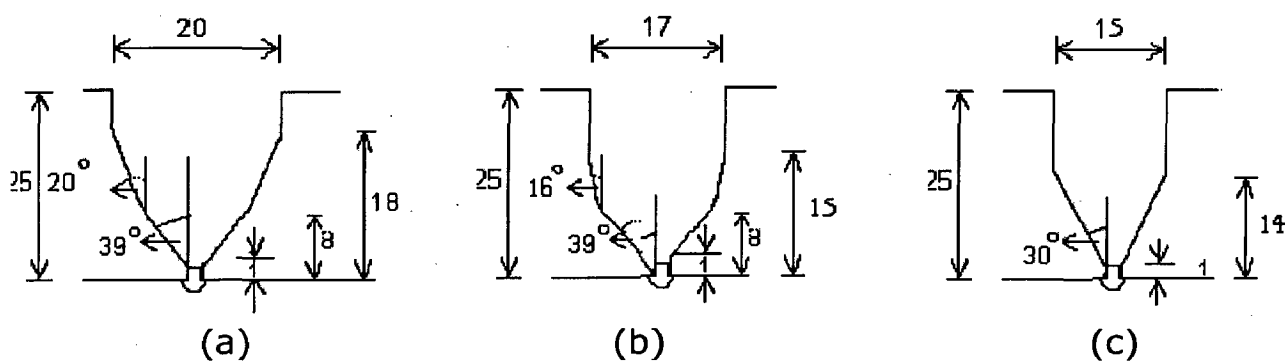
Fig. 4.5: Schematic diagram of, (a) Narrow U-groove with 20mm groove width (b) Narrow U-groove with 17mm groove width and (e) Narrow U-groove with 15mm groove width used for welding of pipes.
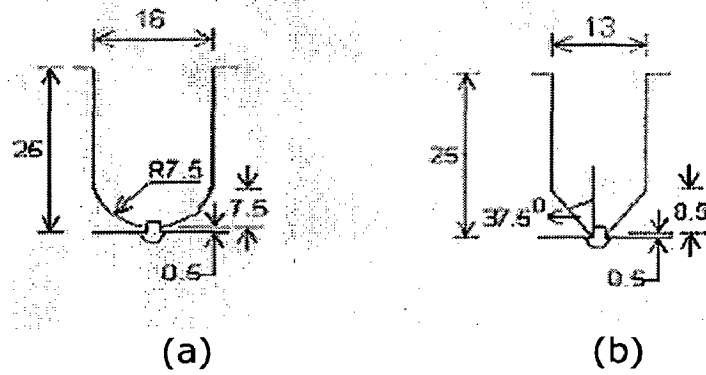
Fig. 4.6: Schematic diagram of (a) Narrow U-groove with 0^0 bevel and 16mm groove width and (b) Narrow U-groove with 0^0 bevel and 13mm groove width used for SMA welding of joints.

4.4.4 Welding Processes

4.4.4.1 Pulsed Current Gas Metal Arc Welding

The P-GMA weld joints were initially prepared with conventional V-groove by varying ϕ from 0.05 to 0.25 and at two different heat input levels of 9.2 ± 0.35 kJ/cm and 7.8 ± 0.35 kJ/cm. The narrow gap P-GMA welding of pipes was carried out at a constant heat input of 7.8 ± 0.5 kJ/cm at two different ϕ of 0.05 and 0.25. At eight equally divided quadrants of circumferential locations, the transverse axial shrinkage after each pass of multi-pass weld deposition was estimated by measuring the difference of distance between two axially located points at a known distance apart across the joint marked by centre punching (Fig. 4.7) prior to welding. The record sheet of each weld giving parameter details and overall transverse shrinkage has been presented in Annexure- I. Heat input per pass and heat transferred to the weld pool (Q_T) was estimated as per eq. (4.1) and (4.2) respectively by assuming a process efficiency or thermal heat transfer efficiency (η_a) of the arc as 0.7 [Joseph et.al. 2003] and finally the characteristics of the weld joints were correlated to the average heat input per pass estimated as mean value of heat input employed in its multiple filler passes.

121

$$\text{Heatinput(kJ / cm)} = \eta \times \frac{\text{Weldingcurrent(A)} \times \text{Arcvoltage(V)}}{1000 \times \text{Weldingspeed(cm / s)}} \qquad (4.7)$$
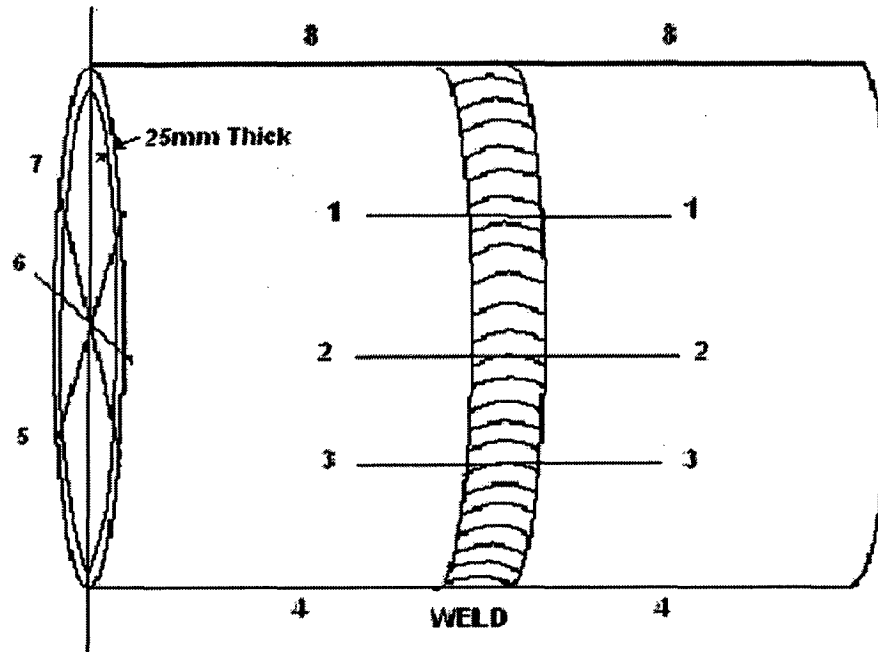
Fig. 4.7: Schematic diagram showing circumferential locations at which transverse axial shrinkage was measured across two axially located points.

4.4.4.2 Gas Metal Arc Welding

The GMA welding of pipes was carried out only in conventional groove with spray mode of metal transfer using newly developed narrow GMA welding torch nozzle. The GMA weld deposition was primarily carried out by using 1.2 mm diameter solid ASS filler wire under argon gas shielding at a flow rate of 18L/min with direct current electrode positive (DCEP) polarity at an electrode extension of 12-14 mm. The welding parameters and transverse shrinkage for multi-pass weld deposition were measured as mentioned in the record sheet presented in Annexure- I by following the same procedure as used in SMA welding of pipes. Heat input per pass was estimated also as per eq.(4.7) by considering process efficiency on an average as 0.7 [Radiaj, 1992] and the characteristics of the weld joints were correlated to the average heat input per pass estimated as mean value of heat input employed in its multiple filler passes.

4.4.4.3 *Shielded Metal Arc Welding*

The SMAW passes in conventional and narrow weld grooves were carried out with basic coated 3.15mm and 4.0 mm diameter SFA5.4 E308L–15 electrodes at electrode polarity of DCEP. The welding parameters and cumulative transverse axial shrinkage for multi-pass weld deposition was measured as shown in the record sheet presented in Annexure- I by following the same procedure as mentioned earlier. Heat input was estimated by considering the process efficiency, η, on an average as 0.7 [Radiaj 1992] and finally the characteristics of the weld joints were correlated to the average heat input per pass estimated as mean value of heat input employed in its multiple filler passes.

4.4.5 Recording of Welding Parameters

During welding the welding current or mean current, as applicable for GTAW, SMAW, GMAW and P-GMAW processes along with arc voltage were recorded with the help of WMS 4000 software installed in a personal computer. A transient recorder capable of recording welding current and arc voltage with a maximum resolution of 1MHz was also suitably connected to the welding circuit for simultaneous recording of their behaviour during welding. The potential drop across a standard shunt (75mV=600A) connected in series with the welding circuit was fed to the transient recorder for estimation of the welding current. The transient arc voltage was measured by connecting other channel of transient recorder parallel to the welding circuit. The transient arc voltage and welding current were simultaneously recorded and displayed on the screen of the recorder having time(s) as ordinate and potential (V) as abscissa. The electrical circuit diagram of welding and recording set up has been shown in Fig. 4.8. During pulsed current welding, values of the pulse parameters such as I_p, I_b, t_p and f were verified with their characteristics appeared in the transient recorder.

4.5 NON DESTRUCTIVE TESTING OF WELD JOINTS

NDT of welds was carried out in two steps, first by carrying out dye penetrant test intermittently between the passes and secondly after the completion of weld joint by 100% X-ray radiography. The methodology followed for carrying out these tests is explained in the following sections.

4.5.1 Dye Penetrant Test

The specifications for the dye penetrant test were prepared as per ASME section V, as given in Annexure-II. The test was conducted to detect and rectify the presence of any flaws at the weld groove surface after its machining as well as in autogenous GTA weld and in the filler passes carried out by P-GMA, GMA and SMA welding processes. The test was also conducted on root and top of the weld after the GTAW autogenous pass and on completion of the joint respectively.
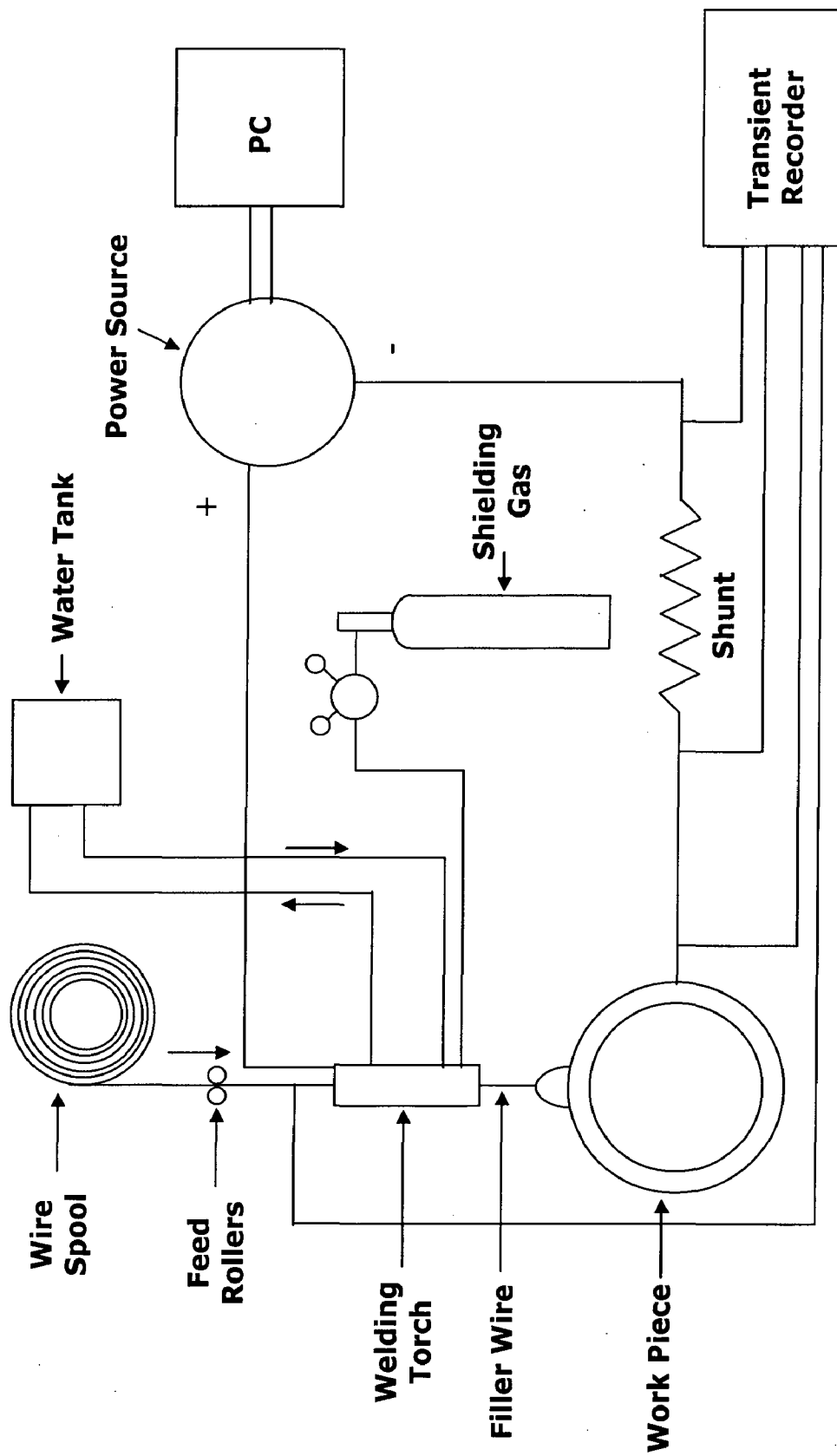
Fig. 4.8: Schematic circuit diagram of welding and recording set up.

4.5.2   X-Ray Radiography

The specifications for X-ray radiography were prepared as per ASME section V, as given in Annexure-III. The weld joints were fully (100%) tested by X-ray radiography. The total circular path of the weld was divided into eight quadrants (sectors) of film placement for X-ray radiography as shown in Fig. 4.9. The shooting and marking procedures of the X-ray radiography have been shown in Fig. 4.10 (a) and (b) respectively.
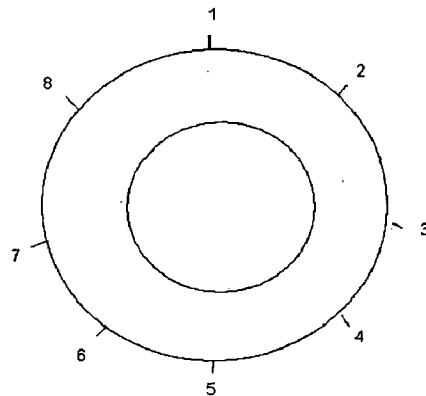
Fig. 4.9: Schematic diagram of film placement for X-ray radiography on total circular path of the weld divided in eight quadrants.
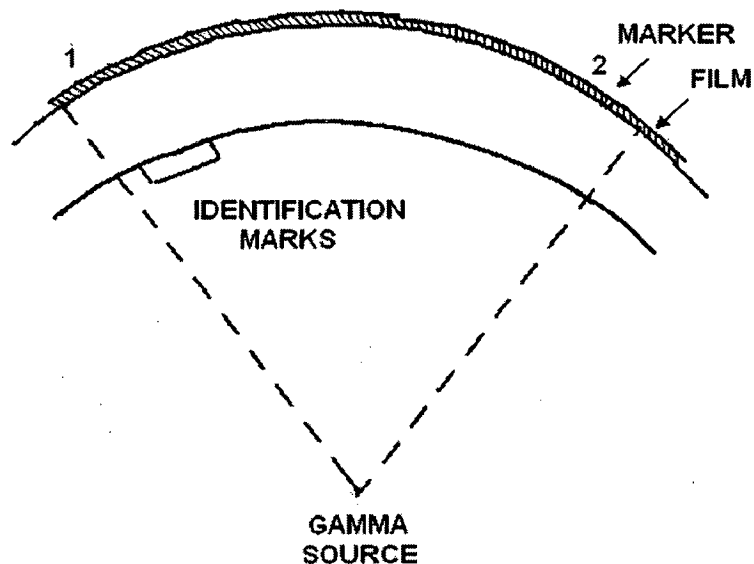
(a)
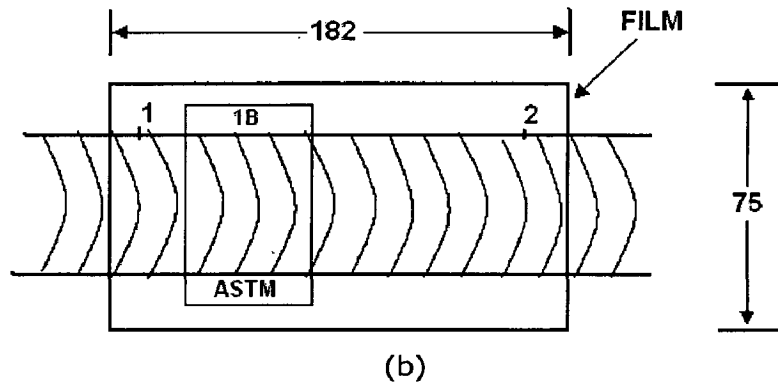
Fig. 4.10: Schematic diagram of (a) shooting and (b) marking procedures followed in the X-ray radiography of the weld joints.

4.6 Testing of Weld Joints

The weld joints prepared by varying welding process and procedure were characterized with respect to their metallurgical, mechanical and fracture mechanics properties by following the ASTM procedures. The residual stress distribution at the top and root of the weld joints were also measured by following the recommended ASTM standard. The methodology followed for collecting the specimen and carrying out the testing is described in the following sections.

4.6.1 Planning of specimen collection

Sectioning of the weld joints was made by power saw cut with due attention to remove any defective portion of the joint as identified by the X-ray radiography. The pieces were further suitably sectioned for machining out various test specimens. The orientation of the specimens for different mechanical testing, collected from the weld and base metal in reference to the weld joints, has been schematically shown in Fig. 4.11.

127
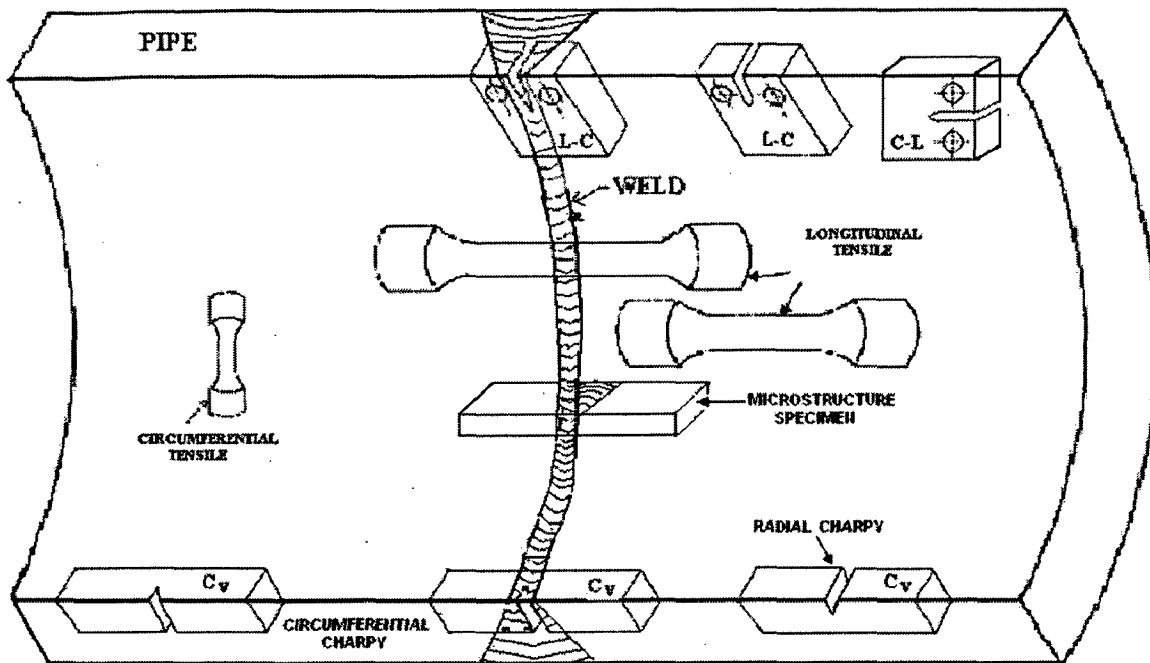
Fig. 4.11: Schematic diagram of collection of specimens from various locations in the weld and base metal for different mechanical testing.

4.6.2   Chemical Analysis

The chemical analysis of different samples was carried out under spark emission optical spectroscopy at a spot size of 3 mm diameter on solid specimens. The analysis was performed on weld metal at polished transverse section of the weld joint, base metal and mechanically flattened welding electrode to accommodate the test spot. However, nitrogen content of the base metal and weld deposit was analyzed under CHN infrared analyzer using a 10 mm long pin sample of 5mm diameter.

4.6.3   Measurement of Weld Size

The size of the weld as revealed on the metallographically polished and etched transverse section of all the weld joints have been graphically measured using image analyzer

software based on the macro photographs of the joints taken with digital camera. The influence of P-GMA, GMA and SMA welding processes and the conventional and narrow groove welding procedure on the measured weld size was further analysed.

4.6.4 Microstructure Studies

4.6.4.1 Morphology of weld

The transverse section of the base metal and P-GMA, GMA and SMA weld joints were polished by standard metallographic procedure and electrolytically etched in a 10% oxalic acid solution. Metallographic studies were carried out in multi-pass weld deposit under optical microscope (AXIOVERT 200 MAT) primarily at weld bead centre and at reheat refined region of weld passes. Microstructure of the multi-pass weld has also been analysed by measuring its columnar or coaxial dendrite content. Dendrite fraction measurement was carried out, with the help of Axio vision software based image analyser facility connected with the optical microscope as shown in Fig. 4.12. The image analysis was carried out at least on 21 randomly selected spots on the P-GMA, GMA and SMA welds.
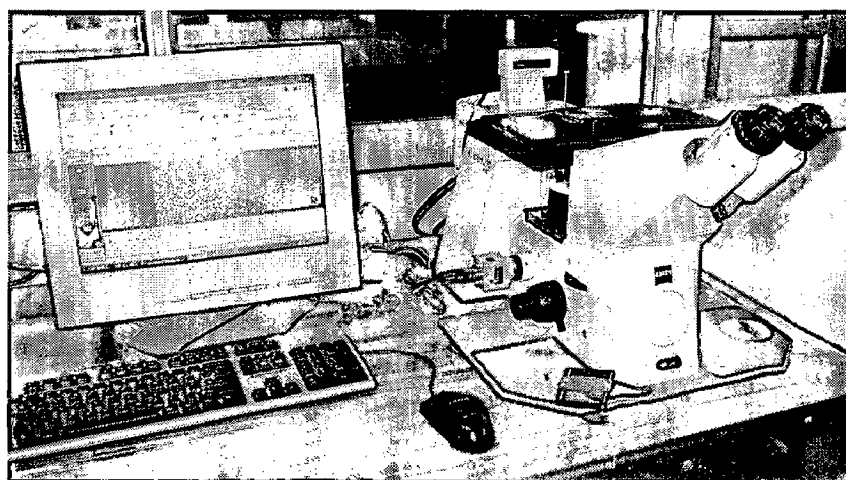
Fig. 4.12: Photograph of the AXIOVERT 200 MAT optical microscope used for recording microstructure.

129

4.6.4.2 Porosity/Inclusion content of weld

The inclusion and porosity content of base metal and weld deposit was measured with the help of image analyser software used in optical microscopic studies on the metallographically polished unetched transverse section of weld joint. The software analysis was carried out on at least 21 randomly captured images of different locations of the matrix viewed at a magnification of X100. The analysis was made considering the area fraction of practically round shape black spots observed on matrix of weld deposit as porosity or a void containing inclusions in it. The volume fraction of the spots present in the matrix was estimated by assuming it as a linear function of their measured area fraction.

4.6.4.3 Microstructure of HAZ

Metallographic studies were also carried out in HAZ especially in the region adjacent to the fusion line wherein grain coarsening takes place. The grain size of HAZ within 0.1mm from the fusion line (FL) on either side of weld joint was measured by using the image analyzer software at 6-10 randomly selected spots located at various parts of HAZ adjacent to the P-GMA, GMA and SMA weld deposits as per ASTM E112.

4.6.5 Mechanical Properties

4.6.5.1 Tensile testing

The tensile testing was carried out using round tensile specimen confirming to ASTM E8M specification and the properties are reported as an average of test results of at least three specimens. The tests were carried out at a strain rate of 0.003/s at an INSTRON universal testing machine. The tensile specimens of the base metal and weld joints of pipes were machined out from both of their longitudinal and circumferential directions. The longitudinal tensile specimens of the base metal and weld joint (axial weld) were having 50mm gauge length, whereas the circumferential (all weld) tensile specimens were having 25mm gauge length. The diameters of

the two types of specimens within their gauge lengths of 25 and 50 mm were 5 and 10 mm respectively. The yield strength was estimated at 0.2% offset strain.

4.6.5.2 Charpy impact toughness testing

The charpy V-notch (C_v) impact toughness test of the base material and weld centre was carried out at ambient temperature using specimens of square cross section (10X10mm) confirming the ASTM E23 specification. In the base material, the specimens where tested with notch location in circumferential and transverse direction as shown schematically in Fig. 4.11. Whereas, in weld metal the notch was located in the circumferential direction at the weld centre so that the cracking plane lies along the direction of welding.

4.6.5.3 Hardness measurement

The hardness of the base metal and weld joint across the weld and HAZ was measured by Vickers micro hardness testing at a load of 100 grams. Prior to carrying out testing, the machine was calibrated by measuring hardness of a standard sample at the same load. The relatively low load was used to get a small indentation, which may be more effective to study the characteristics of different locations of HAZ more precisely.

4.7.6   Measurement of Residual Stresses

The residual stresses at the top and root of the pipe weld joints were measured by placing three-element strain gauge rosette system in the desired locations and using blind centre hole drilling technique. The measurement of residual stresses has been carried out at different locations of the weld and HAZ adjacent to the fusion line (FL). The surface area of selected region for the measurement of residual stresses was mechanically smoothened and cleaned by acetone prior to fixing the strain gauge. The typical arrangement used for fixing of strain gauge and the experimental set up for the drilling operation at the top and root of weld joint has been shown in Fig. 4.13 (a) and (b) respectively.

131

(a)   (b)

Fig. 4.13:   Arrangement for fixing of stain gauge and the experimental set up for the drilling operation at (a) top and (b) root of the weld joint.

The measurement of residual stresses and their estimation was carried out in accordance to the procedure ASTM E-837. After the hole drilling operation the joint surface was metallographically polished and etched to reveal the location of drill with respect to weld fusion line at the top and root of the weld joint as shown in Fig. 4.14 (a) and (b) respectively.

(a)   (b)
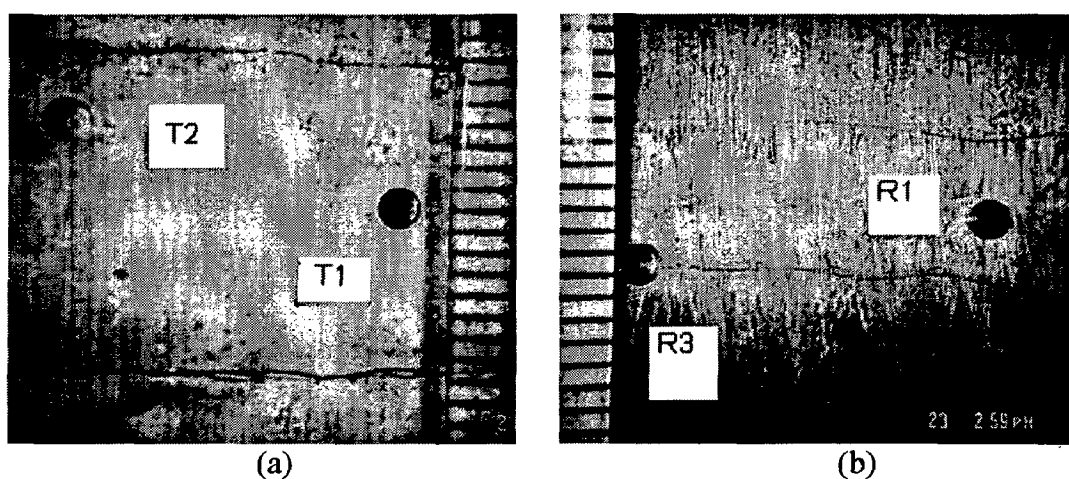
Fig. 4.14:   Typical etched surface revealing the location of drill after residual stress measurement at (a) top and (b) root of the weld joint.

132

4.7.7   Fracture Mechanics

4.7.7.1   Fracture toughness (J-Integral) test

The J-integral fracture toughness tests was carried out using the C(T) specimens (ASTM E-813-89 and E-1820-01) of the base metal as well as conventional and narrow groove weld joints. In base material orientation of notch was kept in L-C (Longitudinal-Circumferential) and C-L (Circumferential- Longitudinal) directions, whereas in weld joints orientation of notch was kept along the weld centre line in L-C direction as schematically shown in Fig. 4.11. The general proportions of the 20mm thick C(T) specimen configuration are shown in Fig. 4.15.

All DIMENSIONS IN mm.
ALL DIMENSIONS TO WITHIN ± 0.1mm
ROOT RADIUS OF NOTCH r ≤ 0.2mm
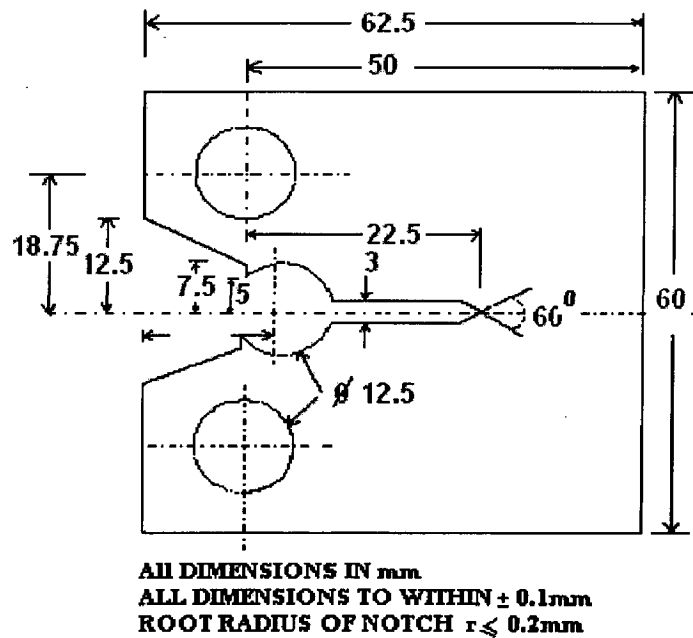
Fig. 4.15: Schematic diagram of C(T) specimen used in J_{1C} Fracture toughness test.

Prior to J_{1C} fracture toughness test, all specimens were pre-cracked by fatigue, upto about a length of 30mm, giving a crack aspect ratio of a/w = 0.6. The pre-cracking was carried out by decreasing ΔK method at a stress ratio (R) of 0.1 and cyclic frequency of 10Hz. The crack length was measured by compliance method using high-speed data acquisition and processing system connected to COD gauge. The loading criterion was kept in accordance with the ASTM specifications confirming the initial maximum load (P_{max}) in the range of 0.20-0.25 $P_{L(CT)}$, where the $P_{L(CT)}$ was estimated as given in equation (4.8).

$$P_{L(CT)} = \left[\left(Bb_0^2 \sigma_y\right)/(2W + a)\right] \qquad (4.8)$$

Where,

B   = Thickness of the specimen (mm)

W   = Width of the specimen (mm)

b_0 = Initial uncracked ligament (mm)

σ_y = Effective yield strength of the specimen (N/mm^2)

σ_y = (σ_{YS} + σ_{TS})/2

σ_{YS} = 0.2% offset yield strength (N/mm^2)

σ_{TS} = Ultimate tensile strength (N/mm^2)

During J_{1C} fracture toughness testing the specimen was statically loaded by bending under displacement control mode at a loading rate of 1mm/min. The test was carried out at the initiation of slow stable crack growth in accordance with ASTM E 813-89. The evaluation of elastic-plastic J-integral fracture toughness (J_{1C}) was carried out by using single specimen technique with the help of J_{1C} software installed in the computer connected with INSTRON universal testing machine as shown in Fig. 4.16. A plot of J-integral vs. crack extension (Δa_p) was obtained as the crack resistance J-R curve. The J_{1C} value was derived from the intersection

134

of the J-R curve with 0.2mm offset line parallel to the blunting line. After the J_{1C} test, post fatiguing was carried out at the same parameters as that of the pre-fatiguing so that the region of crack growth under the J_{1C} test can be clearly differentiated during fractography.

4.7.7.2 Fatigue crack growth rate (FCGR) test

Fatigue crack growth rate studies of base metal and weld deposit were carried out under cyclic loading at a stress ratio (R) of 0.1 and 0.5 in accordance with the ASTM E647-88a using an electro hydraulic universal testing machine. In base material the orientation of notch was varied to L-C (Longitudinal-Circumferential) and C-L (Circumferential- Longitudinal) directions, whereas in weld joints the orientation of notch was kept along the weld centre line in L-C direction as schematically shown in Fig. 4.10. The schematic diagram of the 20mm thick C(T) specimen used for the fatigue crack growth rate studies has been shown in Fig. 4.17.

Prior to the crack growth rate test the specimens were pre-cracked (prefatigue) under dynamic loading at ambient condition, where in the ratio of crack length (a) to width of the specimen (W) was kept in the range of 0.3-0.32. The crack length was measured by compliance method using high-speed data acquisition and processing system connected to COD gauge. The precracking was carried out by K-decreasing test procedure by shedding load with the crack growth started by cycling at a P_{max} of $0.20P_{L(CT)}$, where $P_{L(CT)}$ was estimated as given in Eq. (4.8). Subsequently the P_{max} was decreased (shedded) in a continuous manner by an automated technique controlled with digital computer. The rate of load shedding with increasing crack length was met by limiting the normalized K-gradient, $C = 1/K \cdot dK/da > -0.08$ mm^{-1} such that a P_{max} value of 10-12kN was achieved after prefatigueing. During prefatigueing the stress ratio (R) of 0.1 and cyclic frequency of 10Hz were kept constant.
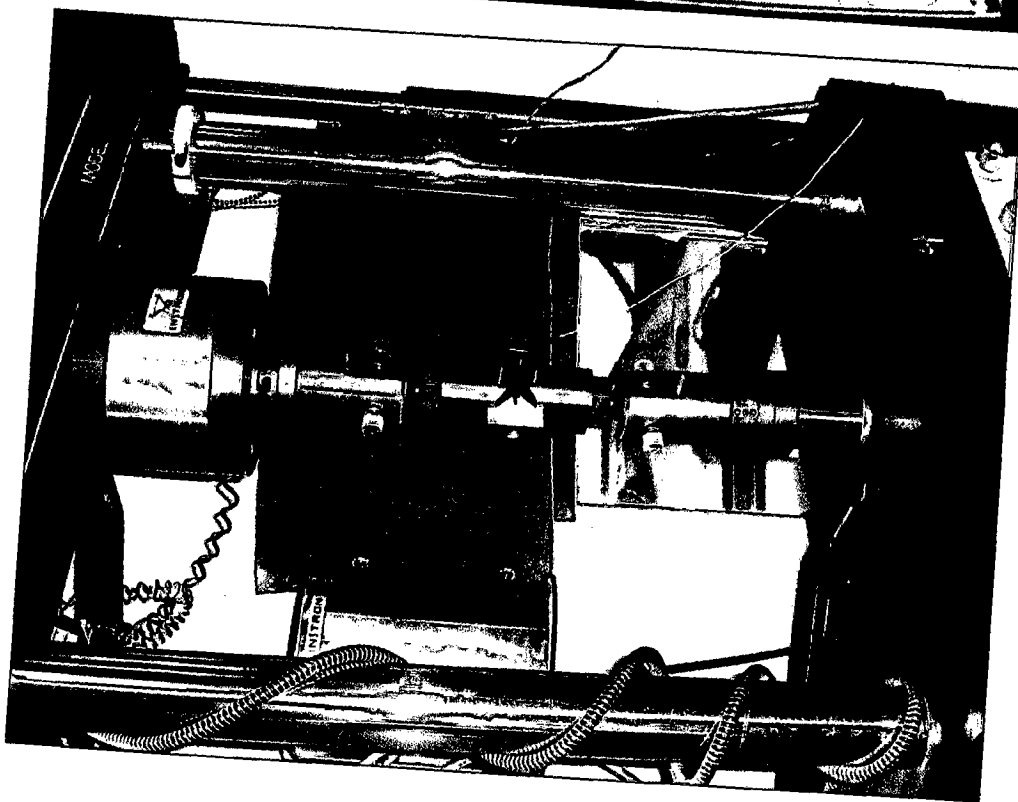
(a)
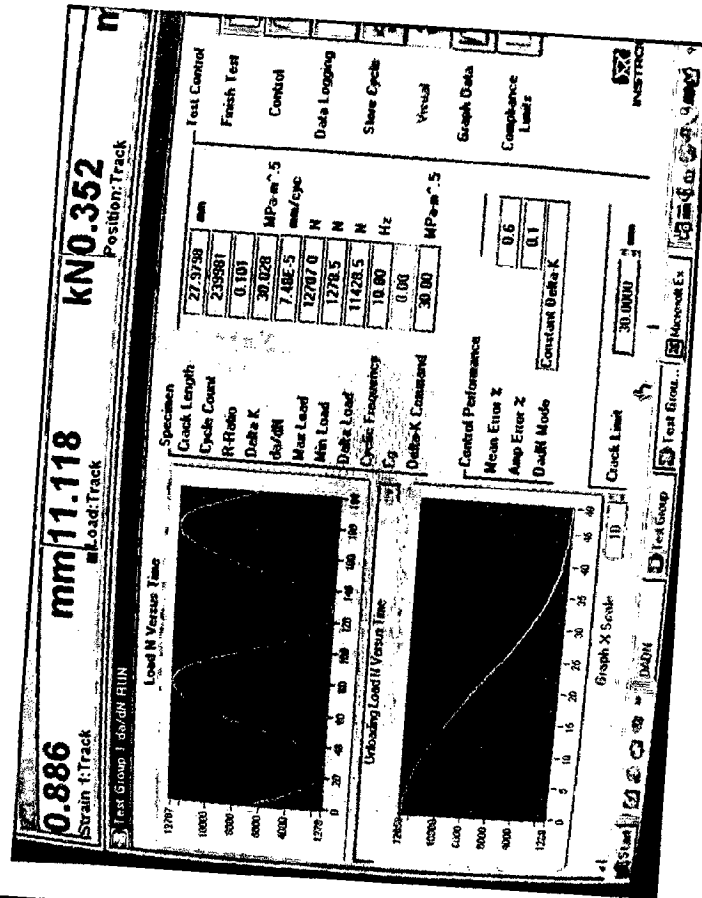
(b)

Fig. 4.16: Photographs showing (a) Instron universal testing machine and (b) a typical software window used for recording and analysing fracture mechanics properties.
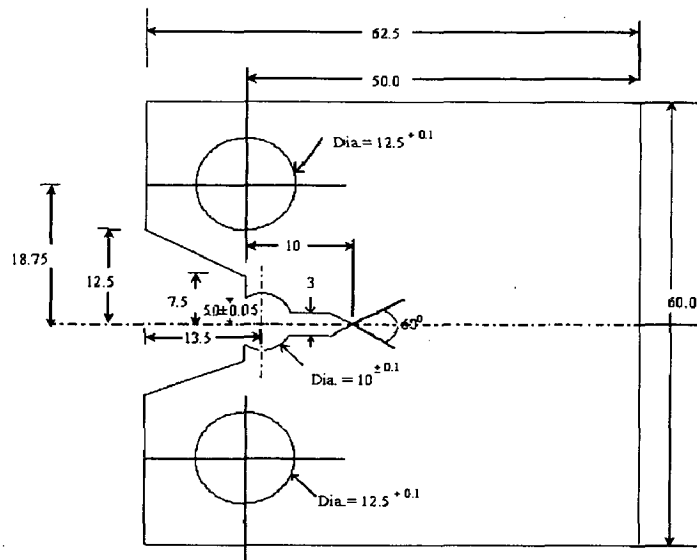
All Dimensions are in mm.
All Dimensions to within ± 0.1 except as indicated.
Root radius of Notch $(r) \leq 0.2$mm

Fig. 4.17: Schematic diagram of C(T) specimen used in Fatigue crack growth test.

The fatigue crack growth tests were also carried out in open-air laboratory environment at room temperature and using a sinusoidal waveform having cyclic frequency of 10 Hz. The test was carried out by constant amplitude method at a given stress ratio (R) of 0.1, where the minimum and maximum stress intensity enhanced with the increase of crack length. The maximum load (P_{max}) was always kept constant for testing of the specimen and it was kept as P_{max} = 14 kN. Here also the crack length was measured by compliance method using high-speed data acquisition and processing system connected to COD gauge. The crack length along with the corresponding minimum and maximum load and cyclic counts (N) were recorded at an interval of 0.25mm of the crack growth. The tabulated data was used for evaluation of crack growth rate (da/dN) and the stress intensity factor range (ΔK). The fatigue crack growth characteristics of various specimens were plotted as log (da/dN) vs. log ΔK and analyzed in the light of the Paris law.

$$(da/dN) = C(\Delta K)^m \tag{4.9}$$

137

The material constants C and m for a crack growth rate were determined by fitting the data points to the power law curve (Eq.4.9). The stress intensity factor range ΔK was estimated as follows.

$$\Delta K = \left| \Delta p / \left(B \sqrt{W} \right) \right| f(a/W) \qquad (4.10)$$

where,

$$f(a/W) = \left[(2 + \beta)/(1 - \beta)^{3/2} \right] \left(0.886 + 4.64\beta - 13.32\beta^2 + 14.72\beta^3 - 5.6\beta^4 \right)$$

$$\beta = (a/W)$$

$$\Delta p = P_{max} - P_{min}$$

The linear regression of log(da/dN) versus log(ΔK) was interpolated to determine the approximate value of fatigue crack growth threshold (ΔK_{th}) corresponding to a growth rate of 10^{-10} m/cycle.

4.7.8 Inter Granular Corrosion Studies

In order to study the acceptability of weld joint with respect to its susceptibility to IGC, a rapid oxalic acid electrolytic etch test was carried out as per ASTM E262 Practice A on the metallographic polished transverse section of weld joint by dipping it into a solution containing 100 g reagent grade oxalic acid ($H_2C_2O_4.2H_2O$) in 900 ml distilled water and using a current density of the order of 1 ± 0.1 A/cm^2. The susceptibility of base metal IGC was also tested by following the same procedure. The inter granular corrosion attack on the weld joints was examined under field emission scanning electron microscope (FE-SEM) having a resolution power of 2nm to reveal more clearly the characteristics of HAZ by evaluation of etched structures developed under the test exposure. In HAZ the evaluation was carried out at two different locations, in heat affected zone just adjacent to fusion line and at a certain distance from the fusion line. The region away from fusion line was identified based on maximum presence of ditches on the matrix. To further confirm the intensity of sensitization, distribution of chromium content across the ditches at few locations was measured by line mapping through EDAX interconnected with FE-SEM.

RESULTS AND DISCUSSIONS

This chapter presents the results of the experiments described in the chapter-4 and analyses these results in order to understand the influence of P-GMA welding process and procedure on joining of nitrogen added austenitic stainless steel. Analysing the characteristics of the weld joints with respect to their mechanical, metallurgical, corrosion and fracture mechanics properties, the necessary control of welding parameters and procedure to improve the weld quality has been established.

5.1 CHARACTERISTICS OF BASE AND FILLER MATERIAL.

5.1.1 Chemical Composition

Chemical compositions of the base metal and filler metals as per ASTM and the test certificate given by the supplier are given in Table-5.1. The chemistry of the base and filler metals as confirmed by analysis using spark emission spectroscopy is also given in Table-5.1. Delta ferrite content estimated on the basis of WRC-92 diagram (Fig. 2.5) for the weld deposits produced by different processes is also shown in Table-5.1. The table primarily depicts that chemical composition of base metal and filler metals given by ASTM and the test certificate is in agreement to the spectroscopy analysis carried out in this investigation. It is further observed that in comparison to SMAW electrode, GMAW filler wire has a relatively lower carbon and higher chromium content resulting in comparatively higher estimated δ-ferrite content which has a beneficial effect in reducing or preventing micro fissuring in austenitic stainless steel weldments.

Table-5.1: Chemical compositions and estimated δ-ferrite content of the base metal and welding filler metals.

Material	Testing method	Chemical analysis (Wt.%)										Equivalents		δ-ferrite content (%)
		C	Cr	Ni	Mn	N	Mo	Si	Cu	S	P	Cr_{eq}	Ni_{eq}	
Base metal (304LN)	ASTM	0.035	18-20	8-11	2.0	0.1-0.16	-	0.75	-	0.03	0.04	-	-	-
	Test certificate	0.024	18.8	9.3	1.7	0.15	-	0.55	-	0.001	0.022	-	-	-
	*	0.023	19.0	9.1	1.8	0.16	0.19	0.57	0.30	0.002	0.021	19.21	13.22	2
GTAW electrode (ER308L)	Test certificate	0.020	19.6	9.6	1.8	-	0.20	0.40	0.1	0.01	0.019	-	-	-
	*	0.020	18.7	11.7	2.0	-	0.20	0.40	0.08	0.01	0.019	18.93	12.40	2-4
SMAW electrode (E308L-15)	Test certificate	0.035	18.3	10.7	2.3	-	0.05	0.37	0.08	0.016	0.018	-	-	-
	*	0.049	18.9	11.9	1.8	-	0.1	0.22	0.12	0.006	0.016	20.07	13.65	2-4
GMAW filler wire (ER308L)	Test certificate	0.022	19.7	9.6	1.3	-	0.10	0.39	0.08	0.007	0.016	-	-	-
	*	0.022	19.9	10.3	2.2	-	0.30	0.39	0.08	0.007	0.016	19.27	11.05	8

* indicates testing by spark emission optical spectroscopy.

5.1.2 Microstructure

Typical microstructure of the SS304LN base material having homogeneously distributed equiaxed grains and twins in the matrix has been shown in Fig. 5.1. The average grain diameter of the matrix lies in the range of 15 ± 5 μm corresponding to ASTM number of 9.5. The base metal contains negligible inclusion and porosity content as shown in Table-5.2.

Fig. 5.1: Typical microstructure of the base metal.

Table-5.2: Inclusion and porosity content of base Metal

Process	Inclusions rating		Inclusion and porosity content, (Vol. %)
	Category	Severity level	
Base Metal	B thin/B thick	0.5-1.5	0.20
	D thin/D thick	3.5-5.0	

5.1.3 Mechanical Properties

5.1.3.1 Tensile properties

Tensile properties of the base pipe in its circumferential and longitudinal directions are shown in Table-5.3. Typical fractograph of the longitudinal tensile specimen has been shown in Fig. 5.2. The dimensionless material constant (α) and strain hardening exponent (n) in Romberg-Osgood equation as given below have been estimated during tensile testing of the specimens.

$$\frac{\varepsilon}{\varepsilon_0} = \frac{\sigma}{\sigma_0} + \alpha \left(\frac{\sigma}{\sigma_0} \right)^n \qquad (5.1)$$

Where, σ is the nominal stress at any instant, ε is the strain at σ, σ_0 is the flow stress estimated as $(\sigma_u + \sigma_y)/2$, and ε_0 is estimated as σ_0/E, wherein E is the modulus of elasticity, σ_u is the ultimate tensile strength and σ_y is the yield strength at 0.2% offset strain. Table-5.3 primarily shows that the base metal is having comparatively higher yield strength in circumferential direction in comparison to that observed in longitudinal direction. However, the ratio of yield strength (σ_y) to ultimate tensile strength (σ_u) of the base metal has not been found to vary significantly with the change in direction from the circumferential to axial one. It has been further observed that in both the directions, base metal has comparatively lower strain hardening exponent (n) (Table-5.3) than most of the commonly used ferrous metals which have the exponent in the range of 5 to 15. The wide spread fine dimples observed on the fractured surface (Fig. 5.2) indicates high ductility of the base metal.

Table 5.3: Tensile properties in base material of different gauge length.

Gauge length (mm)	Orientation	U.T.S. (MPa)		Y.S. (MPa)		YS/UTS Ratio	Elongation (%)		n		α	
25	Circumferential	702	682	350	360	0.53	72.3	71.3	4.22	4.11	38.70	45.39
		676		355			71.4		4.13		43.38	
		668		375			70.2		3.98		54.09	
50	Longitudinal	654	656	336	338	0.52	72.2	70.6	4.10	4.34	45.46	40.91
		654		338			71.6		4.25		42.90	
		660		340			68.0		4.67		34.37	
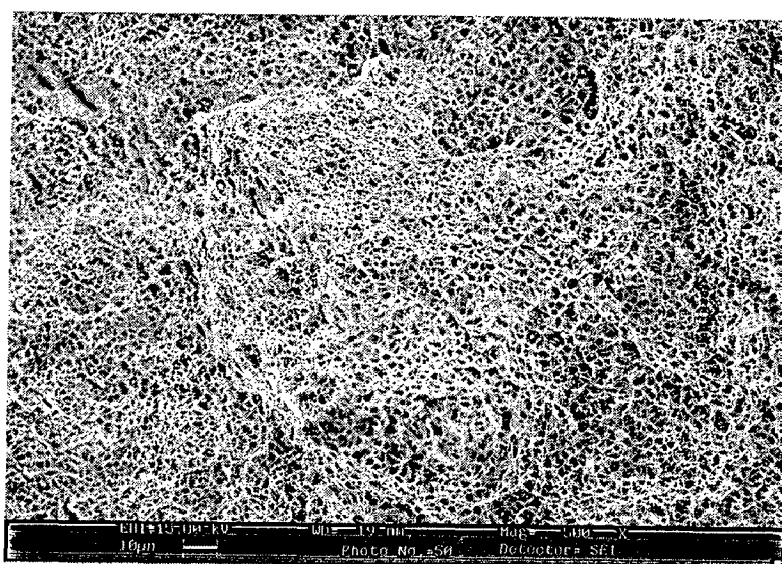
Fig. 5.2: Typical SEM photograph of fractured surface in longitudinal tensile specimen of 304LN austenitic stainless steel.

5.1.3.2 Charpy impact toughness

Charpy impact energy absorbed at room temperature in base metal with notch orientation in radial and circumferential directions (Fig. 4.11) has been given in Table-5.4. Table-5.4 shows that the base metal is having practically similar C_v-impact toughness and lateral expansion in both the radial and circumferential directions and their relatively high values show that the material may not be prone to brittle fracture.

Table 5.4: Energy absorbed in Charpy impact toughness test in base material.

Material	Notch direction							
	Radial				Circumferential			
	Energy absorbed, (J)		Lateral expansion, (mm)		Energy absorbed, (J)		Lateral Expansion, (mm)	
Base material	129	125	2.58	2.58	138	136	2.72	2.76
	120		2.53		131		2.75	
	127		2.62		140		2.82	

142

5.1.3.3 Hardness

Typical indentation of Vickers's micro hardness test in the SS304LN base material has been shown in Fig. 5.3. The indentation does not show any pin cushioning effect resulting from sinking of the metal around the flat faces of the pyramid and hence depicts the true characteristics of the base material. The observed hardness has been found in the range of 230-260 VHN.
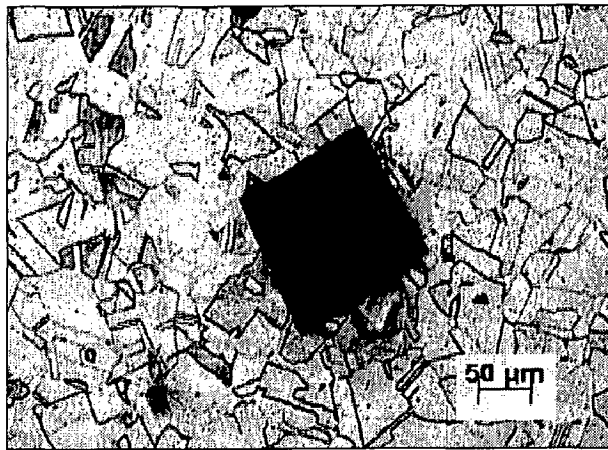
Fig. 5.3:   Typical indentation observed in the base metal.

5.1.4   Fracture Mechanics

5.1.4.1   Fracture toughness

Typical J-R curves observed in longitudinal-circumferential (L-C) and circumferential-longitudinal (C-L) directions have been shown in Fig. 5.4. Various characteristics concerning initiation fracture toughness of the base metal in L-C and C-L directions are given in Table-5.5. The typical load vs. load line displacement (LLD) diagram showing smooth sequence of partial unloading and loading of specimen after regular intervals has been shown in Fig. 5.5.

The comparatively stiffer vertical progress of J-R curve of the base metal (Fig.5.4) along with its higher regression line constants (Table-5.5) indicates high plasticity at crack front in

transverse direction resulting in tunnelling of specimen. This is in agreement to the high ductility of the base metal as given in Table-5.3. The Table-5.5 further depicts that J_Q is comparatively higher in L-C direction than that observed in C-L direction. However, in agreement to an earlier work [Tavassoli 1995], the J_Q values of both the directions of the base material (SS304LN) are not valid J_{IC} values as they do not satisfy the plane strain criterion as thickness B > 25 J_Q/σ_y, where σ_y is the effective yield strength according to the ASTM E813-89 standard.
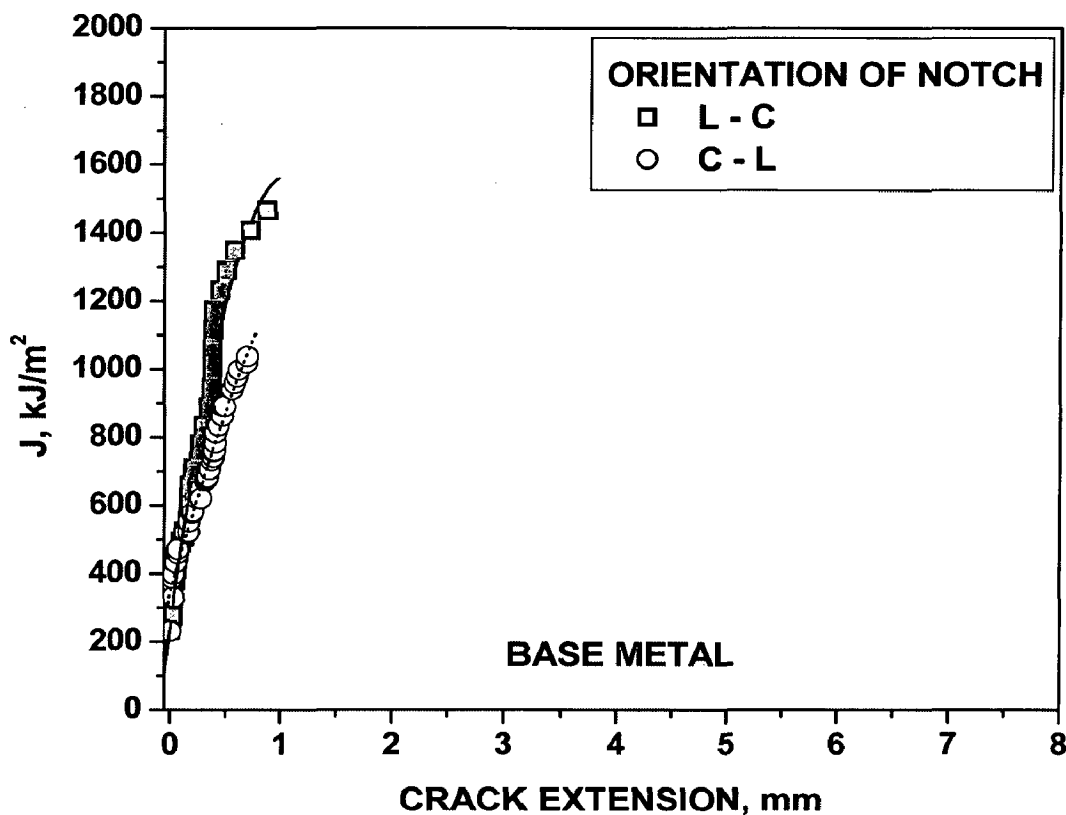
Fig. 5.4: Typical J-R curves of base metal observed in L-C and C-L directions.

Table-5.5: Fracture toughness properties of base metal in longitudinal and circumferential directions.

Location of notch	Orientation	P_{max} (kN)	Δa (mm)	Initiation fracture toughness through mechanical testing				
				Regression line constants			J_Q (kJ/m²)	$J_Q=J_{IC}$ (kJ/m²)
				C_1	C_2	R^*		
Base Metal	L-C	30.37	0.882	1671	313	0.97	1545	No
	C-L	31.23	0.630	1029	356	0.99	1044	No

The estimation of J_{IC} could not be made due to practically vertical progress of the J-R curves (**Fig. 5.4**)
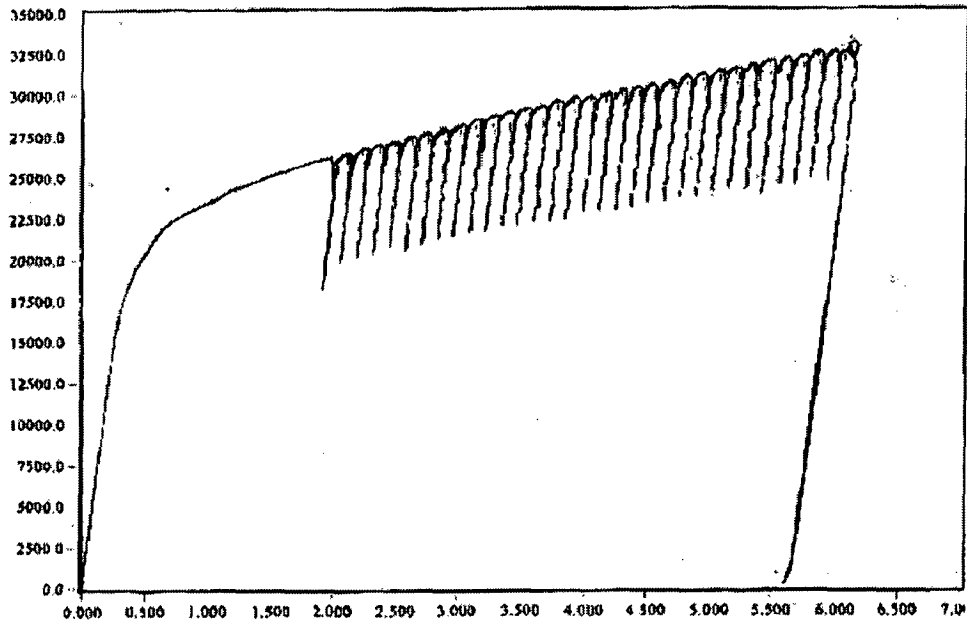
Fig. 5.5: Typical load vs. load line displacement diagram observed in base metal in L-C direction.

5.1.4.2 Fatigue crack growth rate

The fatigue crack growth rate characteristics of base metal with respect to the conditions of testing at two different stress ratios of R=0.1 and 0.5 are given in Table-5.6. The nature of stable fatigue crack growth rate (log(da/dN) vs. log ΔK) of the base metal at different stress ratios of R=0.1 and 0.5 have been shown in Fig.5.6. The table and figure primarily depicts that fatigue crack growth rate of base metal at a given stress ratio (R) of 0.5 is relatively higher than that of R=0.1 as revealed in their values of m and C of the Paris law relationship. It has been further observed that the estimated fatigue crack growth threshold, ΔK$_{TH}$ (Table-5.6), defined as the ΔK value at which growth rates did not exceed 10^{-10}m/cycle, considerably decreases with the increase of stress ratio.

Table-5.6: Fatigue crack growth characteristics of base metal at different stress ratios

Location of notch	Specimen orientation	Stress Ratio (R)	P_{max} (KN)	Paris law constants					ΔK_{TH} MPa$\sqrt{m}$
				m		C (m/cycle)		R*	
Base Metal	L-C	0.1	14	3.09	3.03	4.46×10^{-12}	4.81 x 10^{-12}	0.96	2.72
				2.96		5.16×10^{-12}		0.93	
		0.5	14	2.72	2.74	1.29×10^{-11}	1.25 x $10^{-11.}$	0.98	2.14
				2.76		1.21×10^{-11}		0.97	

R* is Coefficient of corelation
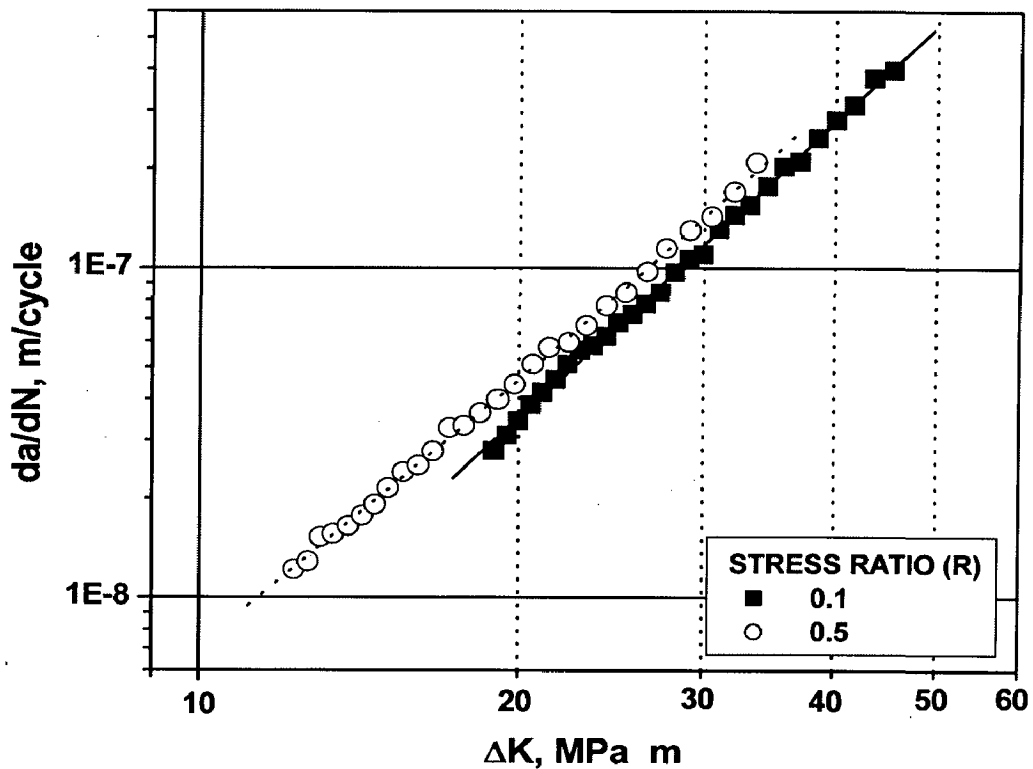
Fig. 5.6: Average FCGR curves observed in base metal at a stress ratio(R) of 0.1 and 0.5.

5.1.5 Inter Granular Corrosion

Typical microstructure of base metal revealed under rapid oxalic acid etch test has been shown in Fig. 5.7. The figure shows few ditches at triple/quadruplet point junction along the grain boundaries. Such ditches may primarily occur either due to locked in stresses in the matrix or carbide formation during hot forming followed by quenching in water or other fast cooling media. In order to confirm this behaviour attracting the chemical attack, the line

mapping of chromium distribution was carried out across the grain boundary (L1), at triple

point junction (L2) and across the twins in equiaxed grains (L3) as shown in Fig. 5.8 (a), (b)

and (c) respectively. In all the cases a significant variation in chromium distribution across

the grain boundary has been observed, but chromium content does not drop markedly below

the required limit of approximately 11.5% to provide enough resistance to corrosion

[Folkhard 1984, Barcik 1983, Shaikh et al 1995]. Thus base metal appears comparatively

free from corrosion attack, but its susceptibility to the sensitization may be more

appropriately analysed on application of weld thermal cycle by different welding processes.

(a)   (b)
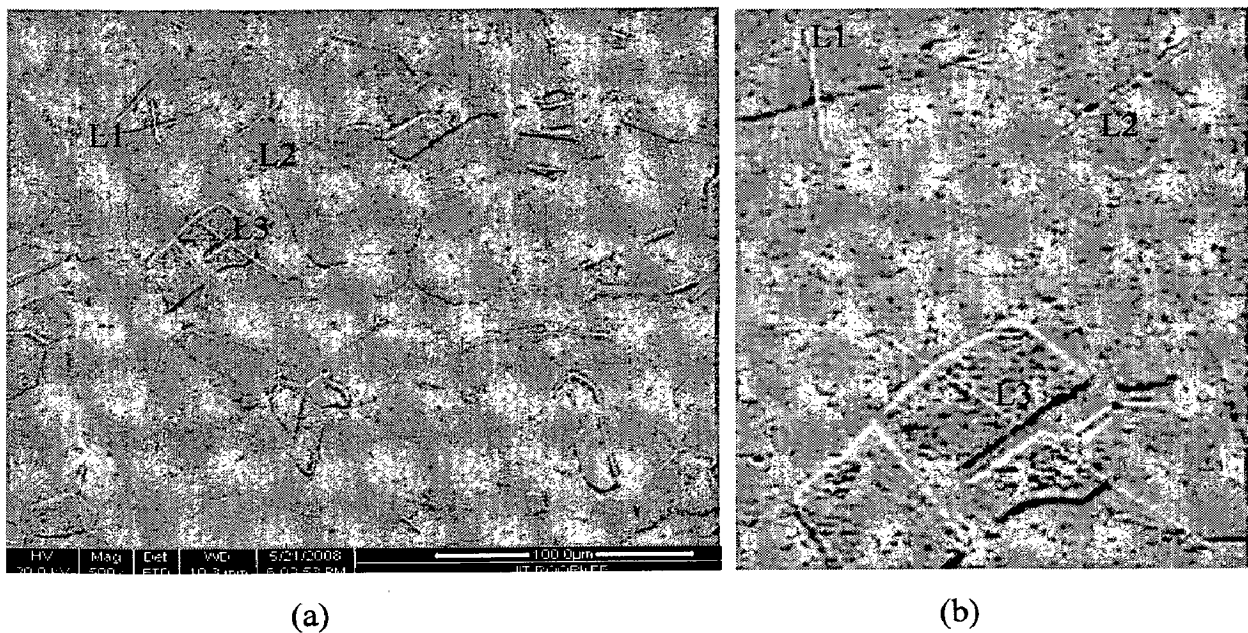
Fig. 5.7: Typical microstructure of base metal showing (a) ditches across the matrix and (b) magnified region wherein chromium distribution was determined by line mapping.
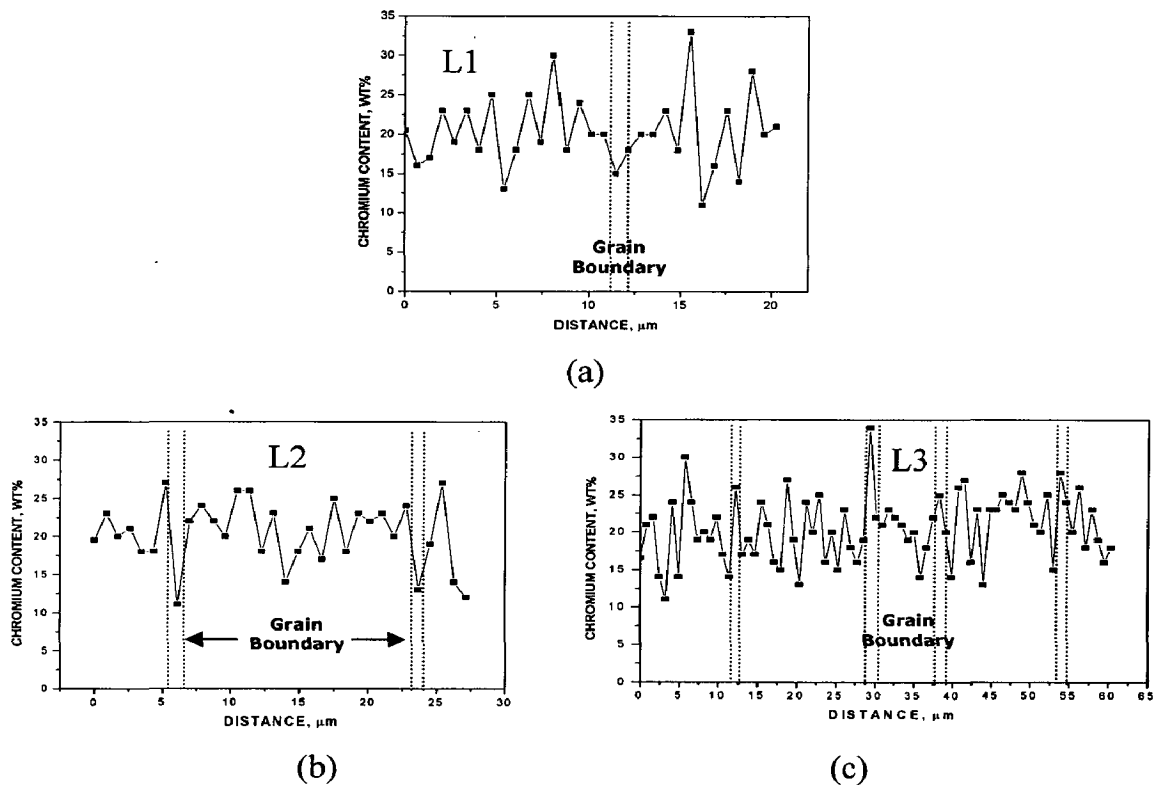
Fig. 5.8: Typical behaviour of chromium distribution across the grain boundary marked in the corresponding micrographs presented in Fig. 5.7 at three different locations of (a) normal grain boundary, (b) grain boundary having few ditches and (c) across the twins.

5.1.6 Summary

The base metal has homogeneously distributed equiaxed grains and twins in the matrix along with negligible inclusion and porosity content. It is also observed that in comparison to commonly used austenitic stainless steel (Section 2.5), the base metal as ASS 304LN has superior mechanical and fracture mechanics properties. However, few ditches have been observed at some locations on the matrix. Thus, thermal influence of welding process and procedure for joining of such steel must be criticality analysed to impart comparable properties to the weld joint. The summarised properties of the base metal are as given in Table- 5.7.

Table-5.7: Summarized properties of the SS304LN base metal

Metallurgical Properties			Mechanical Properties										Fracture mechanics properties			
Inclusion &porosity Content (Vol. %)	Grain size adjacent to F.L		Circumferential Properties			Longitudinal Properties			Charpy impact properties			Hardness VHN	Orientation of notch	Fracture Toughness J_Q (kJ/m^2)	Fatigue crack growth rate test Paris Law Constants	
	Dia. $\pm \sigma$ (µm)	ASTM No.	UTS (MPa)	YS (MPa)	Elongation (%)	UTS (MPa)	YS (MPa)	Elongation (%)	Notch Location	Energy absorbed, (J)	Lateral Expansion, (mm)				m	C (m/cycle)
0.20	15 $\pm$ 5	9.5	682	360	71.3	656	338	70.6	Radial	120	2.56	230-260	L-C	1545	3.03	4.81×10^{-12}
									Circumferential	133	2.73		C-L	1044	2.74	$1.25 \times 10^{-7.7}$

149

5.2 SELECTION OF P-GMA WELDING PARAMETERS THROUGH BEAD ON PLATE DEPOSITION

In welding the acceptability of weld joint is primarily governed by required fusion of base metal through formation of arc crater of sufficient extent in it at an optimum thermal exposure giving rise to a minimum heat affected zone (HAZ) of undesirable microstructure and low residual stresses in weld joint. The control of these aspects can be more conveniently addressed by using P-GMAW process by considering summarized influence of pulse parameters proposed earlier and defined [Ghosh et al 2000] by a hypothetical factor $\phi = [(I_b /$ $I_p)$ f.t_b] where, $t_b = [(1/f) - t_p]$ derived on the basis of energy balance concept of the system. In addition to the hypothetical factor ϕ, the variation of heat input (Ω) to the system as a function of mean current (I_m), arc voltage (V), welding speed (S) and heat transferred to the weld pool (Q_T) also influences the weld characteristics [Palani and Murugan 2006]. Thus, in this section, the nature of variation in characteristics of weld bead as a function of ϕ, Ω and Q_T has been explicitly studied on bead geometry as well as microstructure, corrosion resistance and hardness of different regions of bead on plate deposit. The performance of P-GMAW process with respect to the characteristics of weld bead has been compared with those of the conventional GMAW process. Further, the empirical correlations amongst the ϕ, Ω and Q_T with the various geometrical and metallurgical characteristics of weld bead have been worked out in order to develop a clear understanding on superior use of P-GMAW process in welding of ASS for advanced weld properties.

5.2.1 Thermal behaviour of weld

In P-GMAW and GMAW processes, thermal behaviour of weld largely depends upon heat input of welding process (Ω), which in turn plays a primary role in dictating the geometrical and metallurgical characteristics of weld bead. However, in P-GMAW process of

a given Ω, the variation in ϕ significantly affects the arc characteristics [Ghosh et al 2008] and changes the behaviour of metal transfer thus, consequently governs the heat transfer to weld pool (Q_T). Hence in comparison to GMAW process, the thermal behaviour of weld can be more significantly manoeuvred by using P-GMAW process. But, in order to regulate the P-GMAW process appropriately for desired weld characteristics, it is imperative to know about the correlation amongst the Ω, ϕ and Q_T.

5.2.1.1 Influence of heat input (Ω)

In P-GMAW process at given close range of welding speed, arc voltage and wire feed rate, the pulse parameters significantly vary I_m (Table-5.8) and eventually affects the heat input Ω (eq. (4.1)). Hence at a given welding speed and arc voltage of 20cm/min and 23±2 V respectively the Ω (kJ/cm) as a function of ϕ and V_w (cm/s) (Fig. 5.9), has been worked out as given below.

$$\ln(\Omega) = 0.34 \ln(\phi) + 0.86 \ln(V_w) - 0.08 \ln(\phi) \ln(V_w) + 0.7 \qquad (5.2)$$

The figure indicates that besides the increase of V_w at a given ϕ the increase of ϕ from 0.041 to 0.225 at a given V_w also enhances Ω significantly, which may appreciably affect the characteristics of weld bead. The logarithmic relationship of Ω with the V_w and ϕ depicts (eq. (5.2)) that at its comparatively lower range of about 0.05-0.1, ϕ apparently influences Ω relatively more significantly than that observed at higher ϕ. However, such a variation in Ω at a given V_w and welding speed (Table-5.9) is not possible in GMAW process as there is insignificant change in arc characteristics.

Table 5.8: Typical welding parameters used in P-GMA bead on plate experimentation

Expt No	Wire feed rate, V_W (cm/s)	Heat Input, Ω (kJ/cm)	Q_{AW} kJ/cm	Q_f kJ/cm	Q_T kJ/cm	ϕ	I_m (A)	I_P (A)	I_b (A)	t_P (ms)	t_b (ms)	f (Hz)	Arc Voltage (V)
1	14.2	9.3	8.2	4.8	13	0.047	183	464	30	1.98	5.32	137	24
2		9.9	8.0	4.7	12.7	0.069	191	435	40	1.87	5.38	138	24
3		10.2	7.9	4.7	12.6	0.091	194	420	53	1.99	5.20	139	25
4		10.9	7.8	4.6	12.4	0.141	203	385	76	2.01	5.03	142	25
5		11.1	7.6	4.6	12.2	0.185	206	357	93	2.02	4.92	144	25
6		11.4	7.5	4.6	12.1	0.225	211	331	106	2.07	4.83	145	25
7	12.5	8.1	7.1	4.0	11.1	0.044	166	460	26	2.00	6.47	118	23
8		8.6	7.1	4.0	11.1	0.061	175	437	35	1.95	6.45	119	23
9		8.9	7.1	3.9	11	0.100	178	412	55	2.00	5.87	127	24
10		9.5	7.0	3.9	10.9	0.153	182	378	78	2.01	5.80	128	24
11		9.9	6.9	3.8	10.7	0.193	189	357	94	2.03	5.55	132	25
12		10.2	6.8	3.8	10.6	0.237	190	318	104	2.06	5.46	133	25
13	10.8	6.9	6.3	3.3	9.6	0.042	145	448	24	1.96	7.47	106	22
14		7.2	6.1	3.3	9.4	0.058	151	419	31	1.97	7.55	105	22
15		7.6	6.1	3.3	9.4	0.080	156	400	41	2.02	7.15	109	23
16		8.3	5.9	3.2	9.1	0.147	165	359	69	2.04	6.66	115	24
17		8.6	5.9	3.2	9.1	0.197	171	327	85	2.04	6.43	118	24
18		8.8	5.9	3.2	9.1	0.218	172	300	87	2.05	6.28	120	24
19	9.2	5.7	5.7	2.7	8.4	0.041	125	434	22	1.96	8.24	98	22
20		6.2	5.6	2.7	8.3	0.064	133	409	34	2.03	6.90	112	22
21		6.6	5.3	2.7	8	0.093	140	383	44	2.00	8.00	100	22
22		6.8	4.9	2.7	7.6	0.136	145	343	59	2.01	7.89	101	22
23		7.2	4.9	2.6	7.5	0.189	153	311	74	2.06	7.74	102	22
24		7.6	4.8	2.6	7.4	0.224	156	285	82	2.07	7.36	106	23

Table 5.9 : Typical welding parameters used in GMA bead on plate experimentation

Expt No	V_W (cm/s)	Ω (kJ/cm)	Welding Current (A)	Arc Voltage (V)	W (mm)	H (mm)	P (mm)	A_R (mm^2)	A_P (mm^2)	D_W (%)	H_W	H_{FL}	H_{HAZ}
					Bead Characteristics						Hardness, VHN		
1	12.5	9.7	215	21.5	11.1	4.10	3.60	27.3	20.0	42.3	255	310	330
2	10.8	7.2	190	18.0	8.8	3.42	2.16	18.1	11.4	38.6	245	285	310
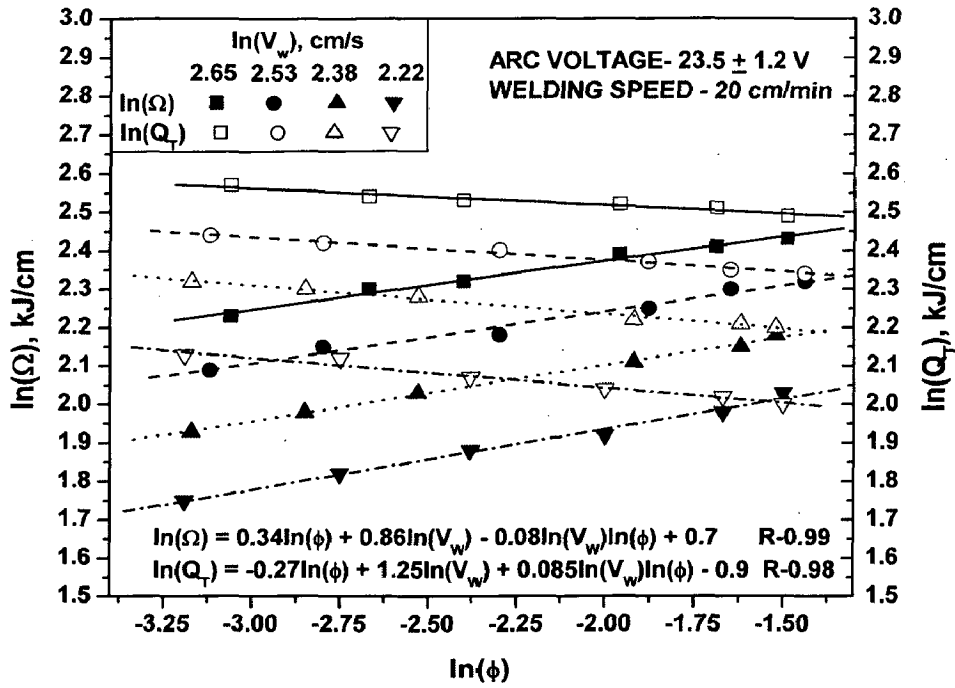
Fig. 5.9: At a given welding speed and arc voltage effect of wire feed rate as well as ϕ on Ω and Q_T in P-GMA welding.

5.2.1.2 Influence of heat transfer (Q_T) to the weld pool

During metal transfer primarily occurring at the peak current (I_P) of P-GMAW process, two heat sources of different nature [Goyal et al 2008] act simultaneously on weld pool. One is continuous heat source (arc heat source) of double ellipsoidal nature acting at the surface of the base plate, which melts and produces an initial weld pool in the base metal. The other one is an interrupted heat source supplying superheated filler metal, considered as a point heat source dictating the size and geometry of weld pool over that initially developed by the arc heating [Goyal et al 2008]. Thus, depending upon the variation of ϕ, total heat transferred to the weld pool (Q_T) is primarily attributed to the initial arc heating (Q_{AW}) followed by the deposition of superheated filler metal (Q_f) affecting the thermal behaviour of the weld metal deposited per pulse [Goyal et al 2008]. Such a variation in Q_T (kJ/cm) has also been shown in Fig. 5.9 as a function of ϕ and V_w and correlated as given below

$$\ln(Q_T) = -0.27 \ln(\phi) + 1.25 \ln(V_w) + 0.085 \ln(\phi) \ln(V_w) - 0.9 \qquad (5.3)$$

The figure further depicts that with the increase of φ from 0.041 to 0.225 at a given V_w, total

heat transferred to the weld pool (Q_T) considerably decreases (eq. 5.3) in spite of significant

enhancement in Ω. Whereas at a given Ω, Q_T significantly decreases with the increase in φ as

shown in Fig. 5.10 and correlated as given below.

$$\ln(Q_T) = 1.36 \ln(\Omega) - 0.46 \ln(\phi) + 0.14 \ln(\phi) \ln(\Omega) - 0.97 \qquad (5.4)$$
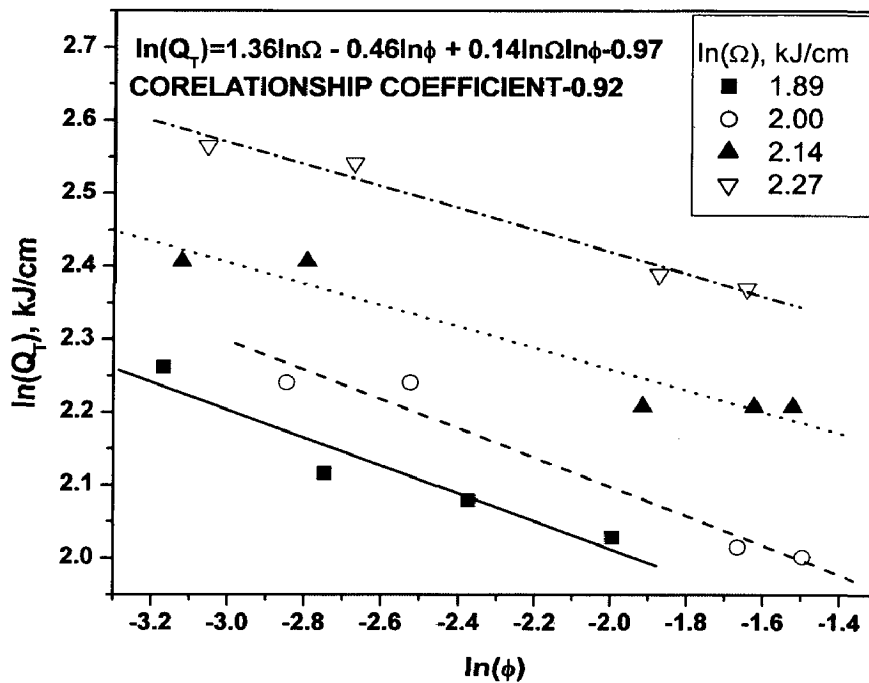
Fig. 5.10: At a given Ω, the effect of φ on Q_T in stable arc P-GMA welding.

The Figs. 5.9 and 5.10 indicate that the increase of φ significantly reduces the energy Q_T

introduced to the welded pool. The enhancement in loss of energy with the increase of φ may be

primarily attributed to the variation in nature of metal transfer and arc characteristics due to

change in I_p and I_b lowering the arc pressure and enhancing the length, root diameter and

projected diameter of the arc [Ghosh et al 2008]. The increase of φ lowers the I_p more

significantly than enhancement of I_b as shown in Table-5.8. However, it is interesting to note that

at a given V_w and φ, Q_T is appreciably more than the Ω especially at lower φ which may be

considered as a great advantage of the P-GMAW process particularly in case of welding of thick sections. These understandings about the influence of ϕ on regulation of heat transfer to weld pool [Ghosh et al 2000] and energy distribution in welding process [Goyal et al 2008] primarily through governance on arc characteristics and behaviour of metal deposition, may help to control the thermal nature of P-GMAW process more precisely by regulation of pulse parameters.

5.2.2 Weld Geometry

5.2.2.1 P-GMA weld bead geometry

At a given heat input of 9.66 ± 0.47 kJ/cm the typical appearance of bead geometry of P-GMA weld deposit made at different ϕ of 0.047, 0.153 and 0.237 has been shown in Fig. 5.11 (a-c) respectively. Similarly at a comparatively lower heat input of 7.1 ± 0.44 kJ/cm the variation in bead geometry at different ϕ of 0.042, 0.136 and 0.224 has been typically shown in Fig. 5.12 (a-c) respectively. The figures indicate that the fusion characteristics of the weld beads are practically free from weld defects like undercut and porosity in agreement with the descriptions on general practice of GMAW for bead on plate deposition of steel as given in ANSI/AWS C5.6-94R (1994). Further the Figs. 5.11 and 5.12 primarily reveal that the width and penetration of weld bead are comparatively more significantly influenced by ϕ and Ω in comparison to bead height. It has been further noticed that at a given heat input, with the increase of ϕ from 0.04 to 0.2, the root reinforcement becomes comparatively flatter as marked by arrows in Figs. 5.11 and 512. Such an influence of variation in ϕ and Ω on bead characteristics has been further studied and compared in Figs. 5.13 and 5.14. The Fig. 5.13(a-c) reveals the characteristics of width (W), penetration (P) and height of reinforcement (H) of weld bead respectively whereas, the Fig. 5.14(a) and (b) show the behaviour of area of reinforcement (A_R) and the base metal fusion (B_F) of weld bead as a function of ϕ and Ω. The W, P and H expressed in (mm) and the area A_R and B_F expressed in (mm^2) of weld bead

are found to be satisfactorily correlated to the ϕ and Ω as stated below with a reasonable coefficient of correlation in the range of 0.87-0.98.

$$W = 0.62\Omega +14.9\phi - 2.08\Omega\phi + 5.62 \tag{5.5}$$

$$P = 0.52\Omega + 5.05\phi - 1.41\Omega\phi - 0.038 \tag{5.6}$$

$$H = 0.2\Omega -1.81\phi - 0.22\Omega\phi + 2.25 \tag{5.7}$$

$$A_R = 4.14\Omega -7.52\phi - 8.39\Omega\phi + 4.59 \tag{5.8}$$

$$B_F = 5.26\Omega + 80.84\phi - 15.15\Omega\phi - 18.45 \tag{5.9}$$

However, the estimated bead dilution (eq. 4.6) has been found to lie in the range of $39 \pm 4\%$ in spite of variation in pulse parameters. This indicates that with proper variation in ϕ and Ω, the area of reinforcement and penetration can be negotiated to achieve almost constant dilution.

(a)

(b)

(c)
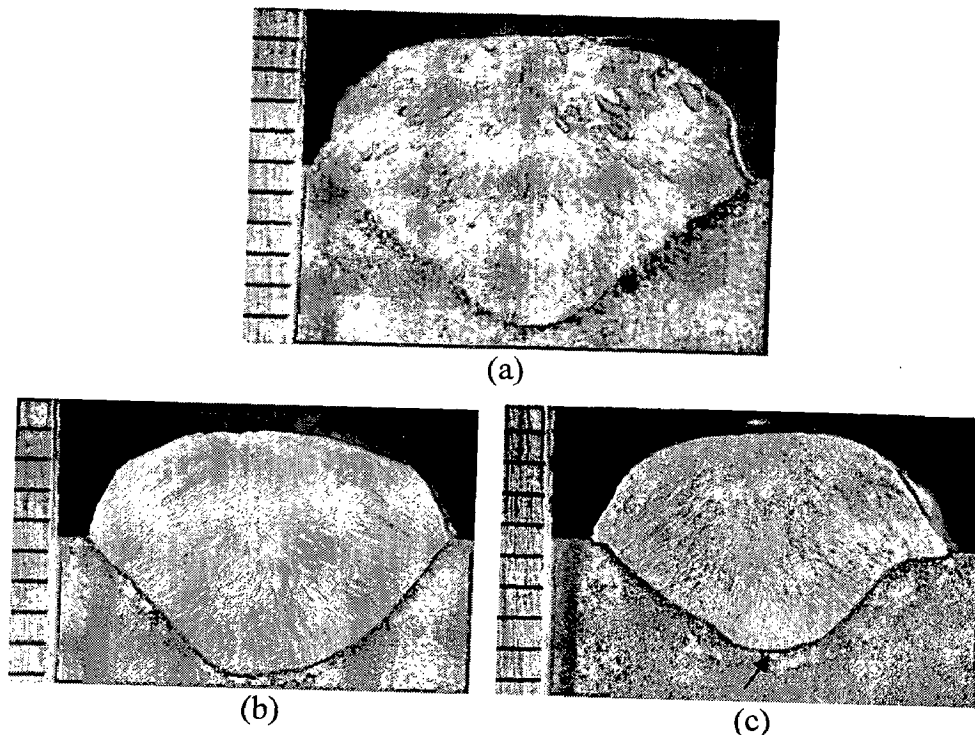
Fig. 5.11: At a given Ω of 9.66 ± 0.47 kJ/cm typical appearance of transverse section of P-GMA weld bead deposited at different ϕ of (a) 0.047 (b) 0.153 and (c) 0.237.

156
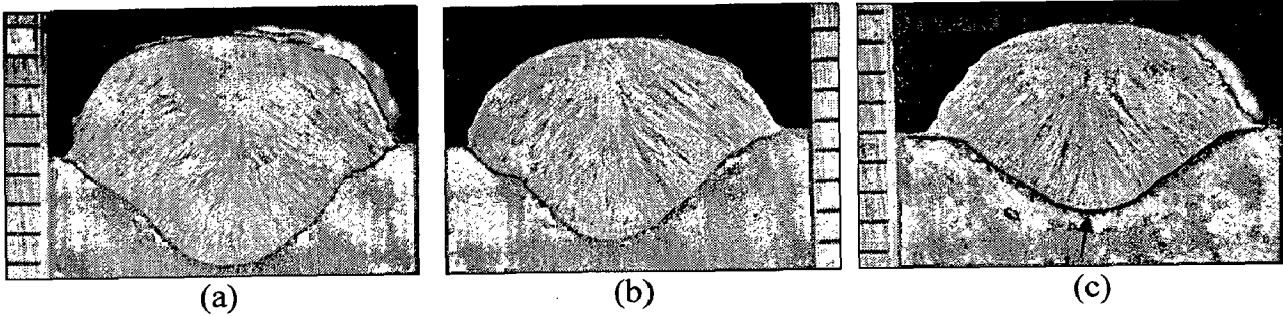
Fig. 5.12: At a given Ω of 7.1 ± 0.44kJ/cm typical appearance of transverse section of P-GMA weld bead deposited at different φ of (a) 0.042 (b) 0.136 and (c) 0.224.

$$W = 0.62\,\Omega + 14.9\phi - 2.08\Omega\phi + 5.62$$

CORELATIONSHIP COEFFICENT - 0.87

(a)

157
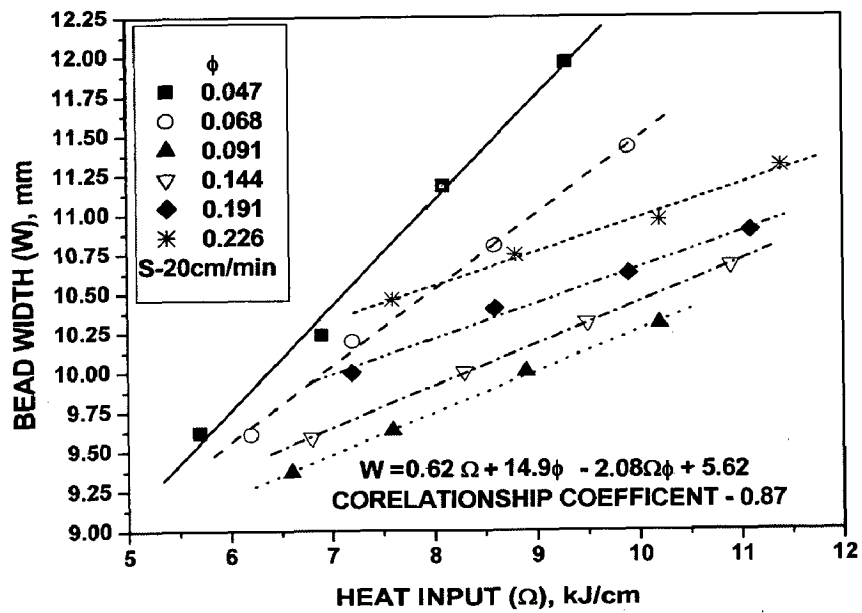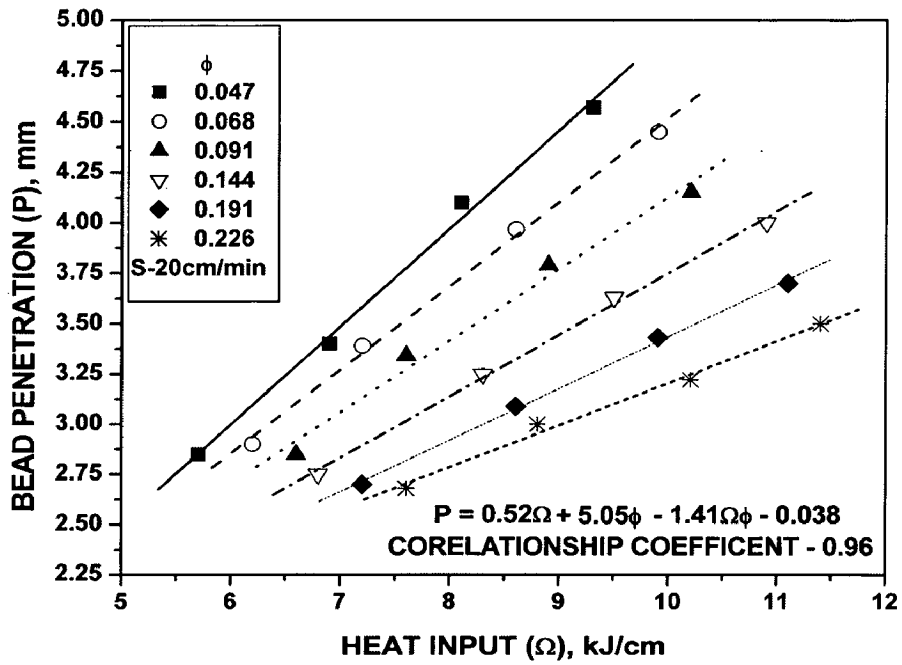
(b)
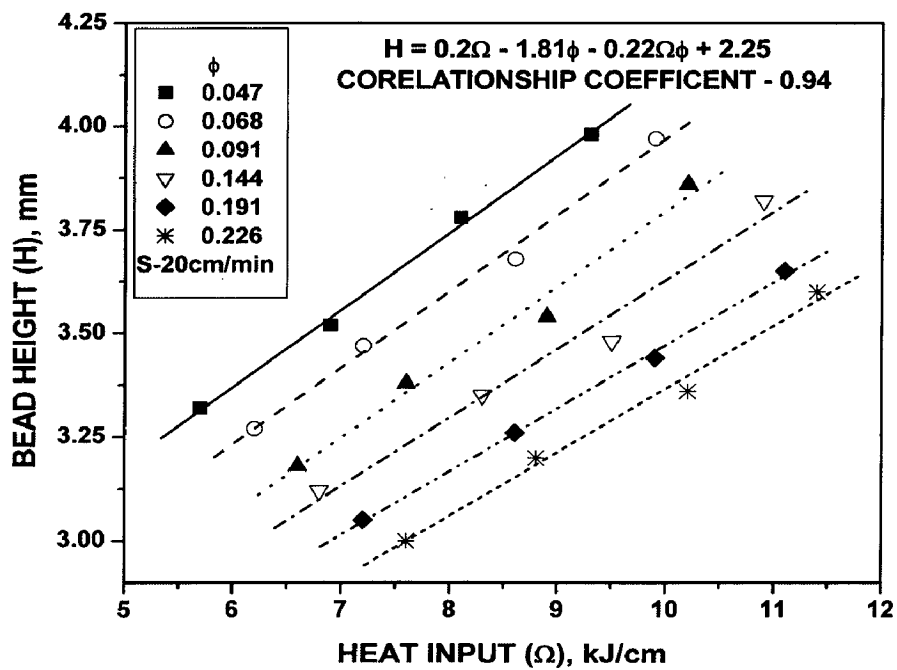
(c)

Fig. 5.13: Influence of variation in ϕ and Ω on (a) width, (b) penetration and (c) height of P-GMA weld beads.
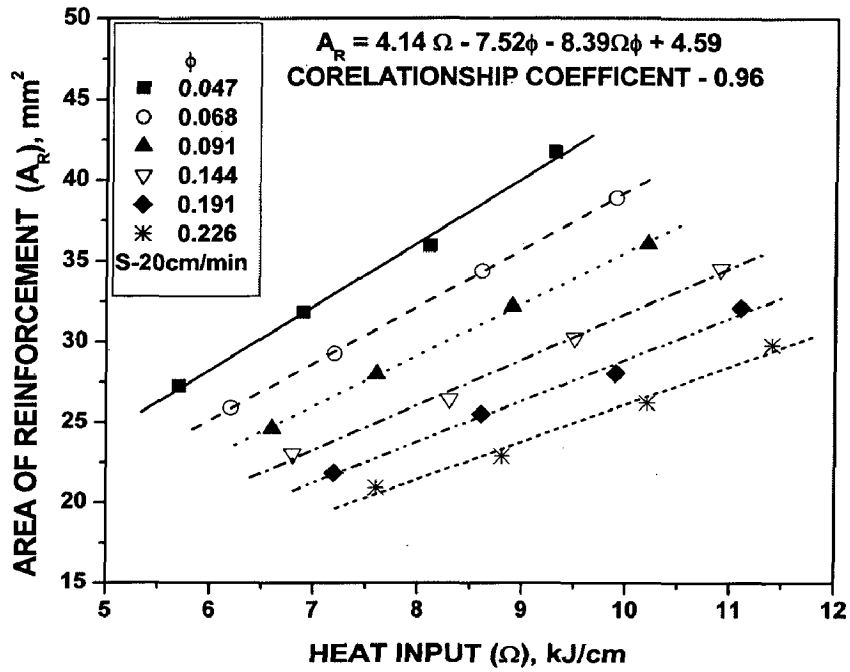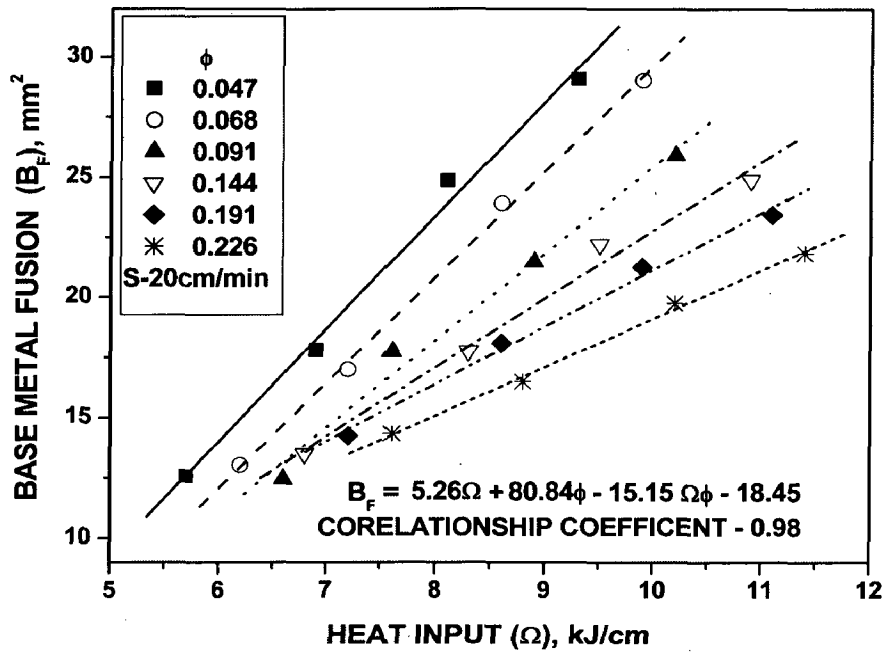
Fig. 5.14: Influence of ϕ and Ω on (a) area of reinforcement and (b) base metal fusion of weld beads.

Figs. 5.11 to 5.14 further show that at a given Ω, the increase of ϕ up to 0.226 significantly reduces the base metal fusion, area of reinforcement, bead height and penetration. At a given ϕ the increase of Ω linearly enhances B_F, being relatively more sensitive at lower ϕ, whereas, at a given Ω the increase of ϕ from 0.04 to 0.225 significantly reduces B_F (Fig. 5.14(b)). But, at a relatively lower Ω of less than about 6.5 kJ/cm, the variation in ϕ practically has insignificant influence on B_F. It has been further observed (Fig. 5.13a) that the increase of ϕ up to 0.091 initially decreases the bead width followed by an increase with a further increase of ϕ up to 0.226. The critical role of ϕ at about 0.1, has also been marked in case of heat input as discussed earlier in Fig. 5.9 and it is in agreement with the observations on weld characteristics reported elsewhere in case of P-GMAW of aluminium [Goyal et al 2007]. In order to further signify the role of ϕ at a given range of Ω, the influence of total heat transferred to the weld pool (Q_T) as a function of pulse parameters on P and B_F was analysed at two different ranges of ϕ of 0.047-0.091 and 0.144-0.226, as shown in Figs. 5.15 and 5.16 respectively.

For the range of ϕ between 0.047-0.091, it is observed that,

$$P = 0.49Q_T + 20.4\phi - 2.3\, Q_T\, \phi - 1.25 \tag{5.10}$$

$$B_F = 4.6Q_T + 171.2\phi - 18\, Q_T\, \phi - 26.6 \tag{5.11}$$

In the range of ϕ between 0.144-0.226, the changed relations are

$$P = 0.39Q_T + 6.65\phi - 0.97Q_T\, \phi - 0.11 \tag{5.12}$$

$$B_F = 3.7Q_T + 76.4\phi - 8.9Q_T\, \phi - 15.1 \tag{5.13}$$

HEAT INPUT (Ω), kJ/cm

6.2±0.5 7.2±0.4 8.5±0.4 9.8±0.5

φ
■ 0.047
● 0.068
▲ 0.091
S-20cm/min

$P = 0.49Q_T + 20.4\phi - 2.3Q_T\phi - 1.25$

CORELATIONSHIP COEFFICIENT-0.98

TOTAL HEAT TRANSFERED TO THE WELD POOL (Q_T), kJ/cm

(a)

HEAT INPUT (Ω), kJ/cm

7.2±0.4 8.6±0.3 9.9±0.4 11.1±0.3

φ
▼ 0.144
◆ 0.191
✶ 0.226
S-20cm/min

$P = 0.39Q_T + 6.65\phi - 0.97Q_T\phi - 0.11$

CORELATIONSHIP COEFFICIENT-0.98

TOTAL HEAT TRANSFERED TO THE WELD POOL (Q_T), kJ/cm
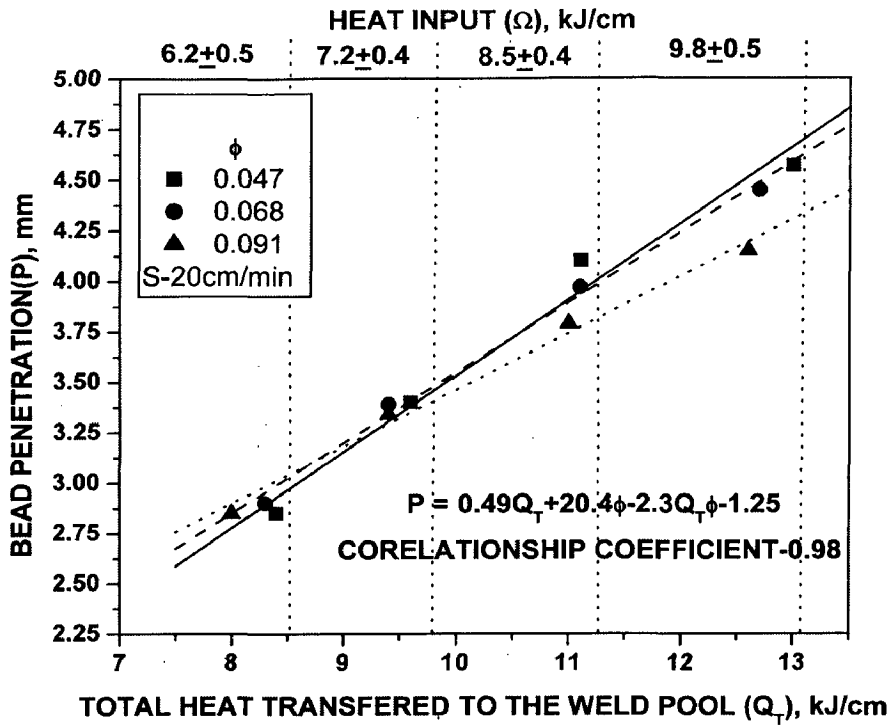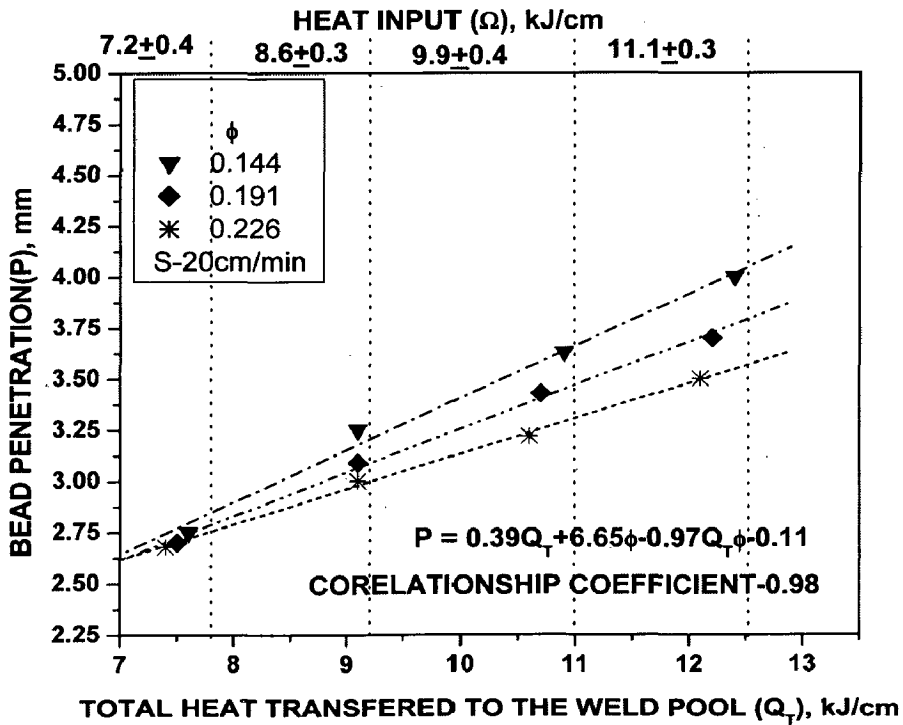
(b)

Fig. 5.15: At varied range of Ω influence of φand Q_T on base penetration at different range of φ of (a) 0.047-0.091 and (b) 0.144-0.226 in P-GMA weld beads.

161

HEAT INPUT (Ω), kJ/cm

6.2±0.5   7.2±0.4   8.5±0.4   9.8±0.5

$B_F = 4.63Q_T + 171.2\phi - 18.01Q_T\phi - 26.63$

CORELATIONSHIP COEFFICIENT-0.86

(a)

HEAT INPUT (Ω), kJ/cm

7.2±0.4   8.6±0.3   9.9±0.4   11.1±0.3

$B_F = 3.66Q_T + 76.4\phi - 8.9Q_T\phi - 15.1$

CORELATIONSHIP COEFFICIENT-0.98
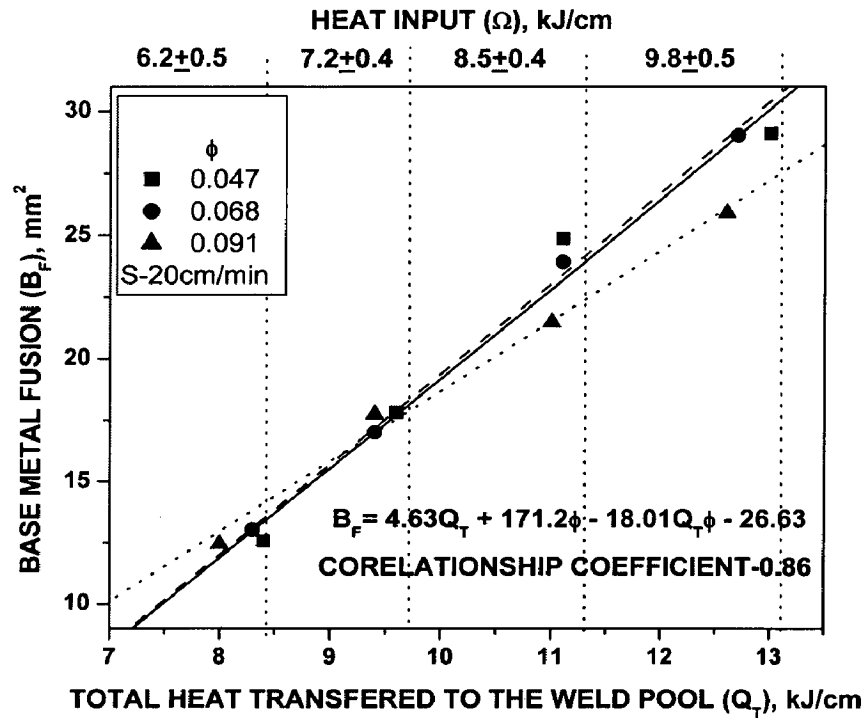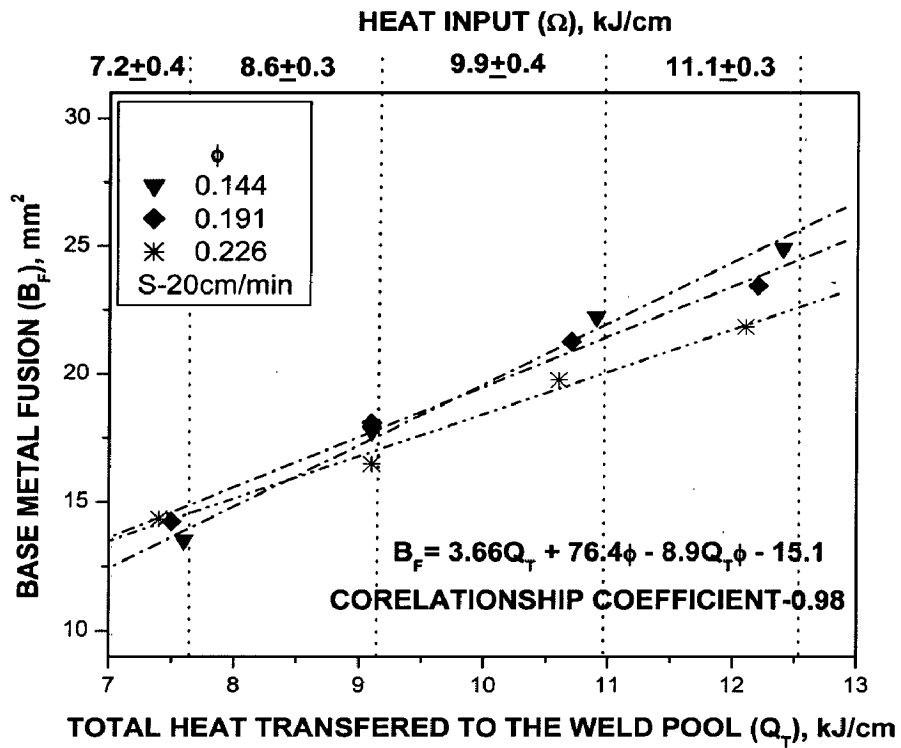
(b)

Fig. 5.16: At varied range of Ω influence of ϕ and Q_T on base metal fusion at different range of ϕ of (a) 0.047-0.091 and (b) 0.144-0.226 in P-GMA weld beads.

Figs. 5.15(a) and 5.16(a) show that ϕ has practically insignificant influence on P and B_F at its relatively lower range of 0.047-0.091 where Q_T and Ω lies within about 10.0 kJ/cm and 7.2±0.4 kJ/cm respectively. However, the effect of increasing ϕ from 0.047 to 0.091 becomes relatively more effective to enhance P and B_F at higher Q_T beyond 10.0 kJ/cm up to about 13.0 kJ/cm, where the Ω also enhances up to about 9.8±0.5 kJ/cm. A similar behaviour of the influence of ϕ on P and B_F is also observed at comparatively higher range of ϕ when increased from 0.144 to 0.226, there is practically insignificant influence on P where Q_T and Ω lies within about 8.0 and 7.2±0.4 kJ/cm respectively (Fig. 5.15(b)) and on B_F, where Q_T lies within about 9.0 and 8.6±0.3 kJ/cm respectively (Fig. 5.16(b)). Here, in Figs. 5.15(b) and 5.16(b), it is interesting to note that the effect of increase in ϕ from 0.144 to 0.226 on enhancement of P and B_F at higher Q_T of about 12.5 kJ/cm becomes quite appreciable of the order of about 15-20% where Ω is also enhanced to about 11.1±0.3 kJ/cm. It is also interestingly observed (Figs. 5.15 and 5.16) that during use of any pulse parameters giving rise to ϕ lying in the range of 0.04 to 0.225, the increase of Q_T up to about 13 kJ/cm almost linearly enhances P and B_F by about 2 times where, Ω varies from about 6.2-11.1 kJ/cm. Although the effect of Q_T on geometrical and metallurgical characteristics of weld bead shows a similar trend, but its degree and rate of influence has been found to vary showing a criticality of ϕ at around 0.1 with different levels of Ω. This may have primarily happened due to onset of certain criticality in the change of thermal and metal transfer behaviour at ϕ below and above 0.1 as shown in earlier works on ferrous and non ferrous metals [Goyal 2008]. This phenomenon should be studied further to develop understanding in order to control P-GMAW process more effectively.

During pulsed current GMAW, the increase of Ω acts as a primary means for basic fusion of base material and maintaining the desired characteristics of weld pool, where Q_T

may subsequently augment the temperature of the molten pool affecting its fluidity to perform various role to keep up weld quality in an arc welding process. Thus, for further manipulation of P and B_F through control of pulse parameters (ϕ) affecting Q_T in P-GMAW process, a minimum Ω is very much necessary. The insignificant influence of ϕ on P and B_F at lower Q_T, as observed in Figs. 5.15 and 5.16 respectively, corroborates this phenomena where a relatively low fluidity of weld pool at a low Ω resist the penetration of droplet up to greater depth. The observations of Figs. 5.15 and 5.16 in this regard may lead one to infer that ϕ and Q_T become effective to vary significantly P and B_F only at Ω beyond about 7.2kJ/cm. The significant flattening of weld bead giving relatively lower B_F and P at a comparatively higher ϕ of the order of 0.2 at different Ω (Figs. 5.11 & 5.12) also appears to be in concurrence with the above discussions. But, an excessive increase of Ω may adversely affect the properties of weld and HAZ. In consideration of these phenomena the conditions of welding as a function of the Ω, ϕ and Q_T has to be designed appropriately in order to uphold desired characteristics of the weld joint.

5.2.2.2 GMA weld bead geometry

Typical appearance of bead geometry of GMA weld deposited at Ω of 7.2 and 9.7kJ/cm has been shown in Fig. 5.17 (a) and (b) respectively and their corresponding bead characteristics have been given in Table-5.9. The figure primarily indicates that the fusion characteristics of the weld beads are also in agreement to those reported in ANSI/AWS C5.6-94R (1994). The figure and table further depicts that at a similar order of Ω, the bead geometry (Fig. 5.17) of GMA weld appears to be appreciably smaller than that of the P-GMA welds prepared at a comparatively lower ϕ of about 0.04-0.05 (Fig. 5.11(a) and 5.12(a)). However, at a comparatively higher ϕ of about 0.22-0.24 (Fig. 5.11(c) and 5.12(c)) the bead geometry of both the GMA and P-GMA welds appears to be almost similar in either of the heat inputs as stated above. Such a variation may have primarily occurred, because the metal deposition in P-GMAW process at a low ϕ of the order of about 0.04-0.05 has taken place by consuming considerably higher rate of wire feed

(Table-5.8 and 5.9) in comparison to that of GMAW process. In addition to the above, the superheated droplet transfers to the weld pool at a comparatively lower velocity in GMAW than the transfer of the same occurs during peak current duration of P-GMAW, resulting in to heat transfer at a shallower depth [Ghosh 2008] inside the weld pool in case of the former one. It may have also caused relatively less penetration and base metal fusion in line with similar discussion in earlier section. Such a phenomenon as an advantage of P-GMAW over the conventional GMAW process has been reported earlier in case of welding of thin austenitic stainless steel sheet with better penetration at low heat input [Goyal 2007].

(a)   (b)
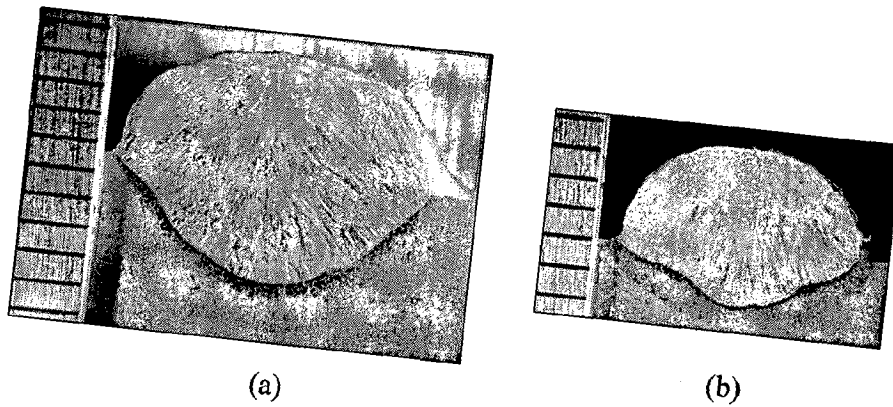
Fig. 5.17: Typical appearance of transverse section of GMA weld bead deposited at different Ω of (a) 9.7 kJ/cm. and (b) 7.2 kJ/cm

5.2.3 Microstructure of Weld

5.2.3.1 P-GMA weld microstructure

The morphology of dendritic cast structure of weld deposit formed during solidification of P-GMA welding largely depends upon locally dominating constitutional and thermal super-cooling [Folkhard 1984] dictated by the heat input and thermal shock exerted by the pulse parameters [Ghosh 2008]. Thus, the weld deposit may have primarily two distinctly different regions of microstructure which can be largely identified as nondirectional cellular dendrite present in upper central part of the reinforcement of weld bead (Figs. 5.18 and 5.19) and co-axial dendrite retained in rest of the matrix (Figs. 5.20 and 5.21). Figs. 5.18 and 5.19 show the

165

morphology of nondirectional cellular dendrite of weld deposit at two different heat inputs of 9.66 ± 0.47 and 7.1 ± 0.44 kJ/cm respectively. In both the figures the effect of variation in ϕ at three different levels of 0.04, 0.14 and 0.23 on the morphology of nondirectional cellular dendrite has been shown in the micrographs denoted as (a), (b) and (c) respectively. Similarly, Figs. 5.20 and 5.21 show the morphology of co-axial dendrite of weld deposit at two different heat inputs of 9.66 ± 0.47 and 7.1 ± 0.44 kJ/cm respectively. Here also, in both the figures the effect of variation in ϕ at three different levels of 0.04, 0.14 and 0.23 on the morphology of co-axial dendrite has been shown in the micrographs marked as (a), (b) and (c) respectively. The micrographs presented in Figs. 5.18-5.21 primarily depict that the variation in ϕ and Ω significantly influences the microstructure of weld bead. At given heat input of 9.66 ± 0.47 and 7.1 ± 0.44 kJ/cm, the increase of ϕ in the range of about 0.042 to 0.237, relatively coarsens the cellular dendrite present in reinforcement part of the weld bead (Figs. 5.18 and 5.19). Similarly, at the same range of heat input, the increase in ϕ coarsens the coaxial dendrite in the rest of the matrix of weld deposit (Figs. 5.20 and 5.21). This has possibly happened due to change in behaviour of metal transfer with the variation of ϕ affecting the cooling characteristics and thermal shock in weld deposit.

(a)

(b)   (c)
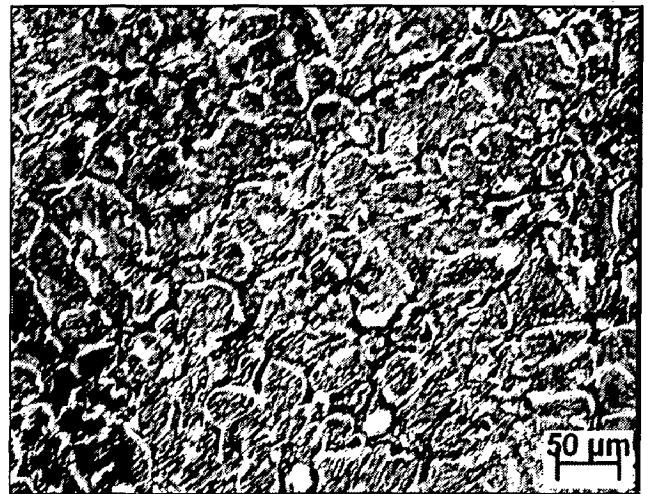
Fig. 5.18:   At a given Ω of 9.66 $\pm$ 0.47kJ/cm the variation in typical microstructure of upper part of the P-GMA weld bead deposited at a different ϕ of (a) 0.047 (b) 0.153 and (c) 0.237.
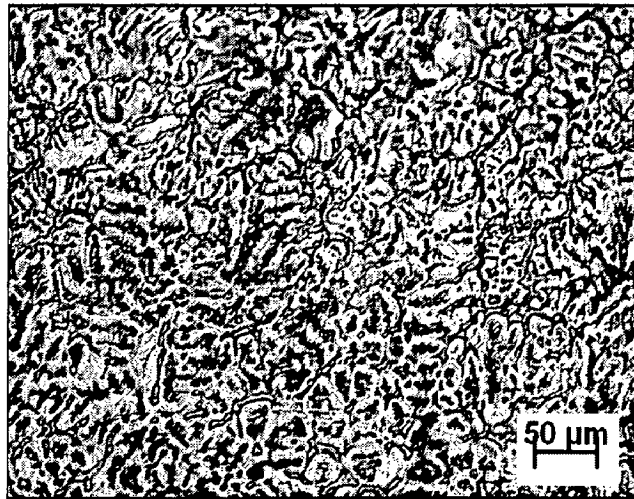
(a)
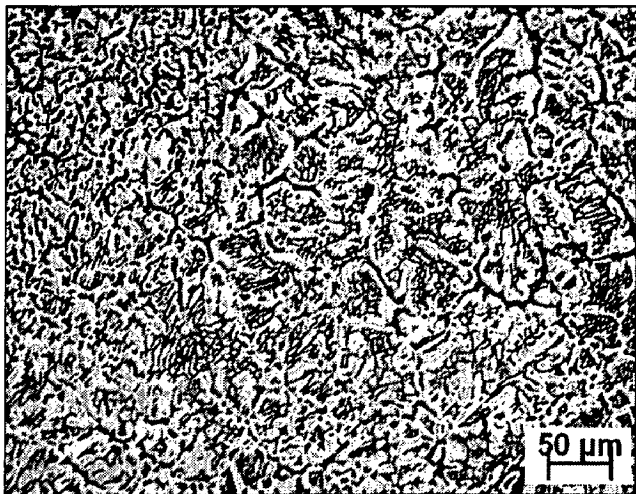
(b)
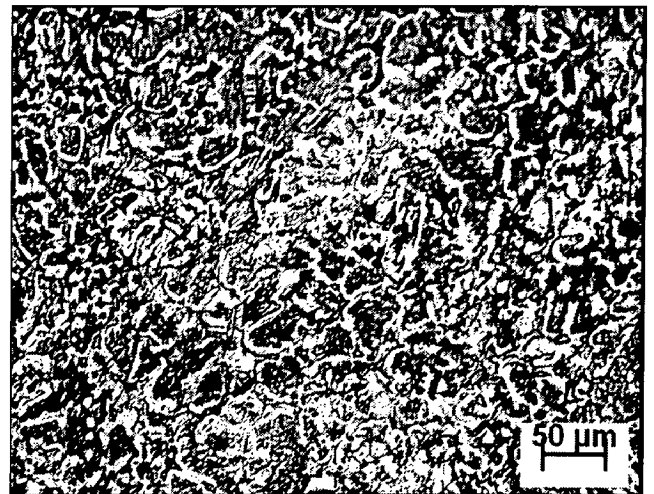
(c)

Fig. 5.19: At a given Ω of 7.1 $\pm$ 0.44kJ/cm the variation in typical microstructure of upper part of the P-GMA weld bead deposited at a different ϕ of (a) 0.042 (b) 0.136 and (c) 0.224.

(a)

(b)

(c)
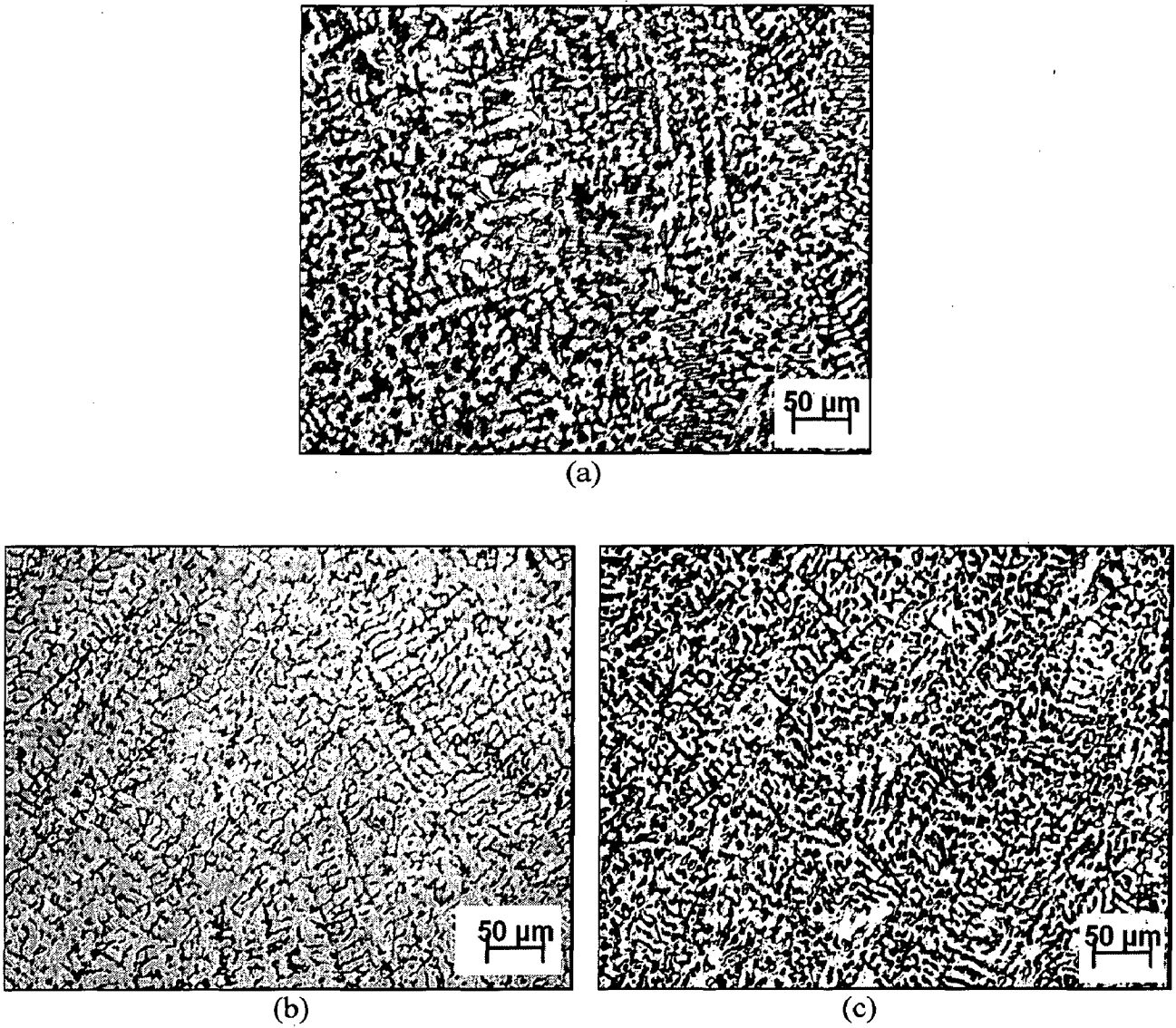
Fig. 5.20: At a given Ω of 9.66 $\pm$ 0.64 kJ/cm the variation in typical microstructure of central part of the weld bead deposited at a different ϕ of (a) 0.047 (b) 0.153 and (c) 0.237.
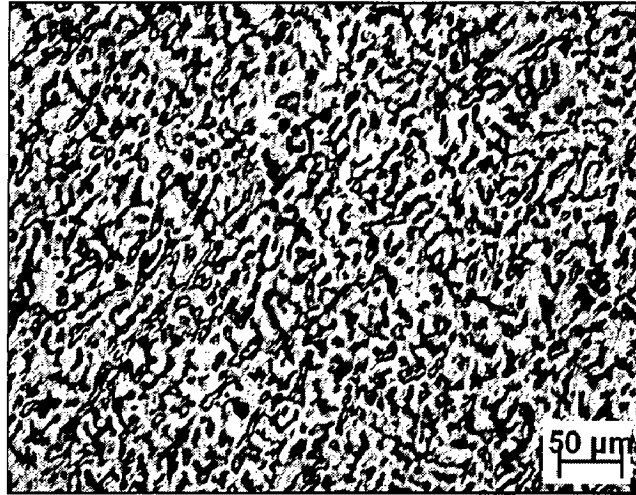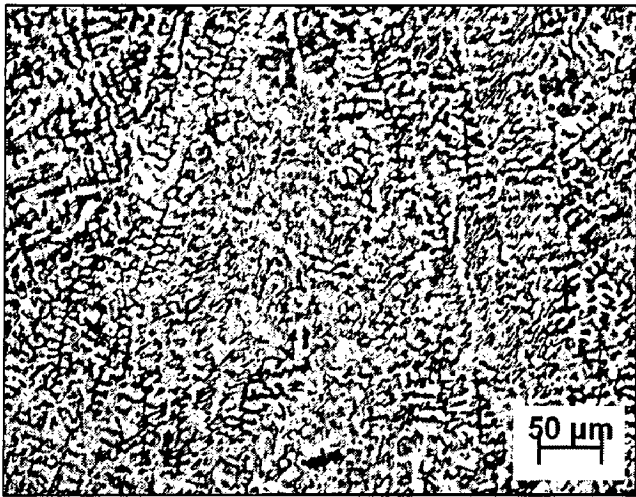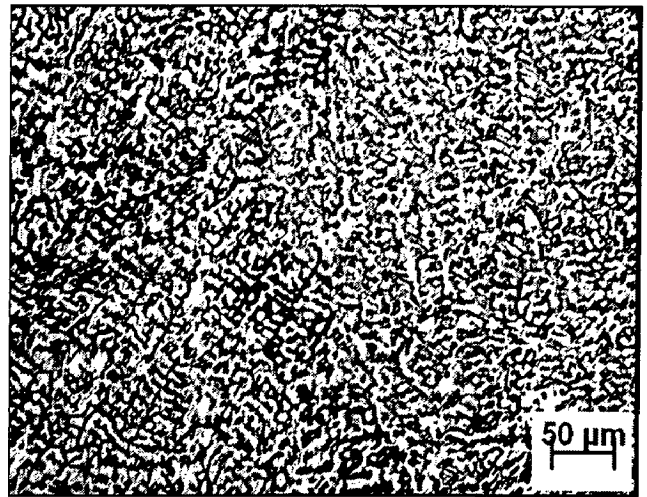
Fig. 5.21: At a given Ω of 7.1 $\pm$ 0.44kJ/cm the variation in typical microstructure of central part of the weld bead deposited at a different ϕ of (a) 0.042 (b) 0.136 and (c) 0.224.

The cellular dendritic region primarily exists in last solidifying central part of reinforcement portion of weld bead because of comparatively slower cooling of this relatively ore solute reach region under comparatively less domination of base metal as the most effective heat sink. The slow cooling allows the growth of large number of primary solids of this region to form cellular structure instead of their coaxial growth to a large extent. As one proceeds towards inner part of weld deposit, the solidification becomes largely dictated by the heat flow to base metal giving rise to a growth of co-axial dendritic structure in the matrix. However, the morphology of both the microstructural regions varies with the change in ϕ as shown in the microstructures presented under (a-c) of the Figs. 5.18-5.21. The refinement of such microstructures primarily depends upon the thermal shock arising out of characteristic interruption in metal deposition during pulse on and pulse off time governed by the variation of ϕ [Ghosh 2008]. During pulse off time the weld metal deposited in pulse on time primarily starts solidifying with coaxial growth of dendrite under a condition of practically no heat gain from outside. It happens because of existence of a comparatively low arc current with practically no or insignificant metal transfer in pulse off period. However, when the subsequent pulsation sets in, the deposition of weld metal on the earlier one causes a localized melting and produces a thermal shock to its adjacent region. The local melting may lead to pinching and breaking of relatively weak solidifying dendrite arms, and the crystallites may get distributed in liquid melt by an agitation, which sets in as a result of development of thermal gradient in it. Many of these crystallites survive from re-melting and grow to result in new randomly oriented crystals leading to a comparatively finer cast structure of the weld by grain multiplication process [Hussain et al 1996].

The presence of practically round shape porosity as a dark spot on the polished unetched matrix of weld bead has been typically shown in Fig. 5.22. It is observed that the P-GMA welds deposited at different ϕ and Ω under the argon gas shielding are having

negligible porosity content of the order of 0.15±0.03 Vol%. Thus, it may be assumed that the contamination of shielding environment and weld deposit becomes practically negligible within the range of pulse parameters used under this investigation.
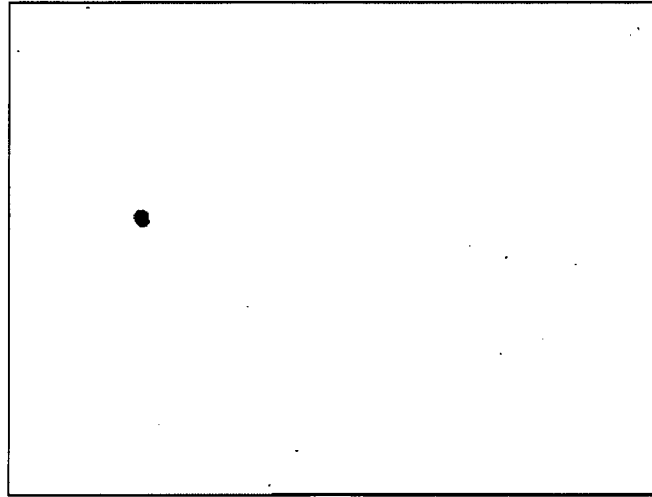
Fig. 5.22:   Typical presence of porosity in the matrix of weld bead.

5.2.3.2 GMA weld microstructure

GMA weld deposit is also having two distinctly different regions of microstructure which can be largely identified as nondirectional cellular dendrite present in upper central part of the reinforcement of weld bead and co-axial dendrite retained in rest of its matrix. At two different Ω of 9.7 and 7.2 kJ/cm, the morphology of nondirectional cellular dendrite present in upper central part of the reinforcement of weld bead is shown in Fig. 5.23 (a) and (b) respectively and the morphology of the co-axial dendrite retained in rest of the matrix of the weld bead is revealed in Fig. 5.24 (a) and (b) respectively. The figures show considerable coarsening of nondirectional cellular dendrite as well as of co-axial growth of dendrites at upper central part and rest of the matrix respectively of the GMA weld deposits in comparison to those of the P-GMA welds (Figs. 5.18-5.21) prepared under similar range of Ω. However, in concurrence with earlier observations in case of P-GMA welds, the coarsening in both the regions marginally reduces with the reduction in severity of weld thermal cycle by lowering of Ω from 9.7 to 7.2kJ/cm.

(a)   (b)
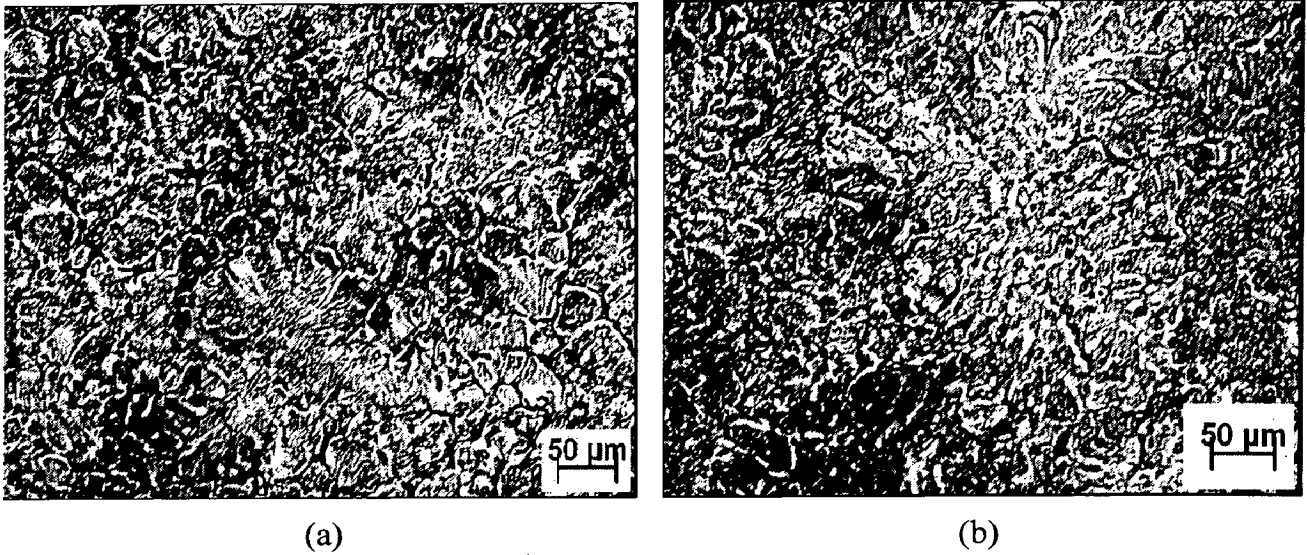
Fig. 5.23: Typical microstructure of upper part of the GMA weld bead deposited at a different Ω of (a) 9.2kJ/cm and (b) 7.1kJ/cm.

(a)   (b)
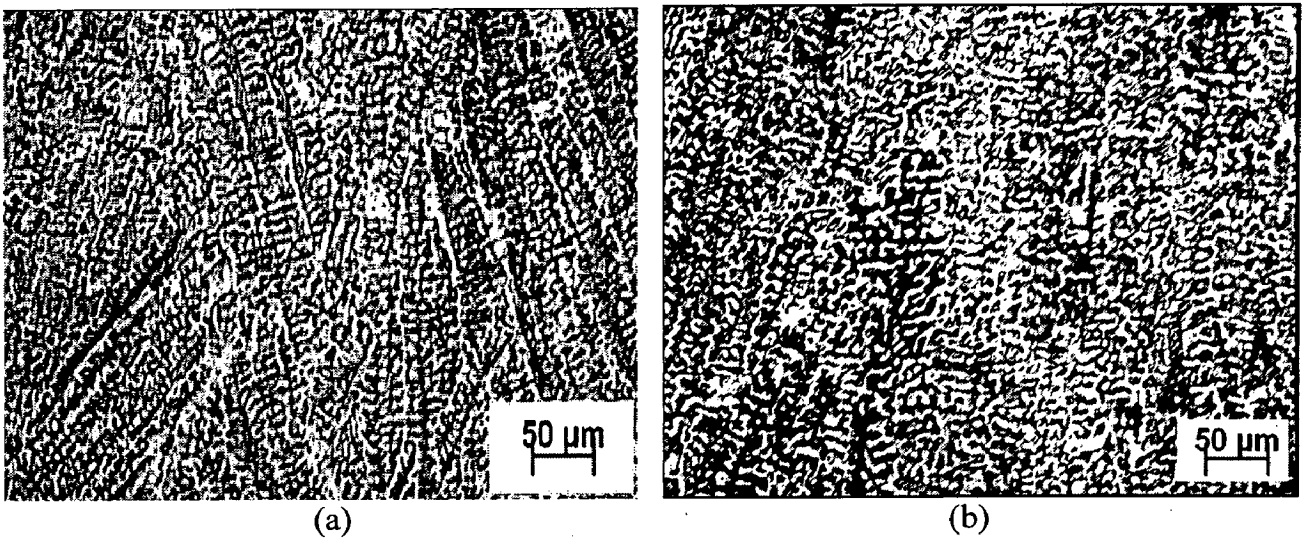
Fig. 5.24: Typical microstructure of central part of the GMA weld bead deposited at a different Ω of (a) 9.2kJ/cm and (b) 7.1kJ/cm.

5.2.4 Microstructure of HAZ

5.2.4.1 HAZ of P-GMA welds

It is observed that the variation in ϕ and Ω also influences the extent of coarse grain region (Z) of HAZ adjacent to fusion line (FL) of weld bead. At a given Ω of 9.66 ± 0.47 kJ/cm, the typical variation of Z at different ϕ of 0.047, 0.153 and 0.237 has been shown in Fig. 5.25 (a-c) respectively. Similarly, at a comparatively lower Ω of 7.1 ± 0.44 kJ/cm the change of Z with the variation of ϕ to 0.041, 0.136 and 0.224 has been typically shown in Fig. 5.26 (a-c) respectively. The nature of variation of Z as a function of Ω and Q_T with the variation in ϕ according to welding parameters as given in Table-5.8 has been compared in Figs. 5.27 and 5.28 respectively. In agreement to the micrographs presented in Figs. 5.25 and 5.26, Fig. 5.27 shows that at a given ϕ, the increase of Ω significantly enhances width of coarse grain region (Z) being comparatively more prominent at a higher ϕ of 0.23. Moreover, at a given Ω, the increase of ϕ from about 0.04 to 0.23 further enhances Z especially at higher Ω. Thus, it appears that the increase of ϕ from 0.047 to 0.226 significantly extends Z by almost two times at a comparatively higher Ω of 9.66kJ/cm, whereas Z almost remains constant at a relatively lower Ω of 7.1kJ/cm. A similar behaviour of enhancement of Z has also been observed with the increase in Q_T in both ranges of variation in ϕ as shown in Fig. 5.28 (a) and (b) respectively. The width of the coarse grain region, Z (mm) as a function of ϕ, Ω (kJ/cm) and Q_T (kJ/cm) has been found to vary following the equations as stated below.

For the range of ϕ of 0.047-0.226;

$$Z = 0.045\Omega - 1.15\phi + 0.22\Omega\phi - 0.094 \qquad (5.14)$$

For the range of ϕ of 0.047-0.091;

$$Z = 0.02Q_T - 1.9\phi + 0.44Q_T\phi - 0.06 \qquad (5.15)$$

For the range of ϕ of 0.144-0.226;

$$Z = 0.06Q_T + 0.85\phi + 0.07Q_T\phi - 0.38 \qquad (5.16)$$

Fig. 5.28 further depicts that at a given Ω and a unit rise in Q_T, Z increases by almost 20% in both the ranges of ϕ. Whereas at a given Q_T and Ω, Z increases by almost 40% with the variation in ϕ. Such a dominant influence of ϕ on Z primarily indicates that thermal behaviour of weld may be significantly altered by varying arc stiffness [Ghosh et al 2008], which in turn must have controlled bulging and elongation of isotherms in transverse and weld direction depending upon the thermal diffusivity of the base metal.
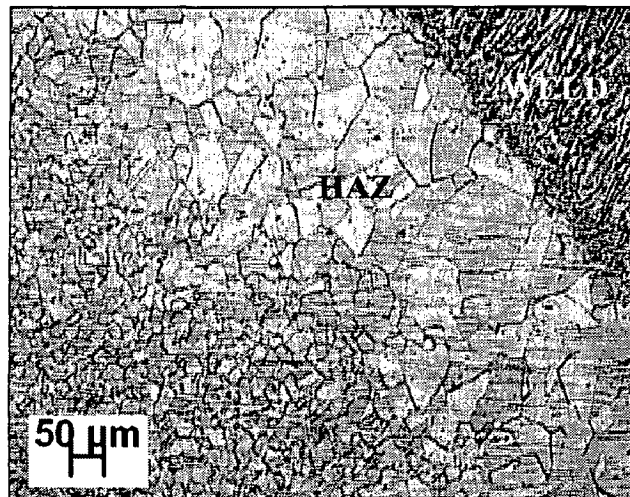
(a)
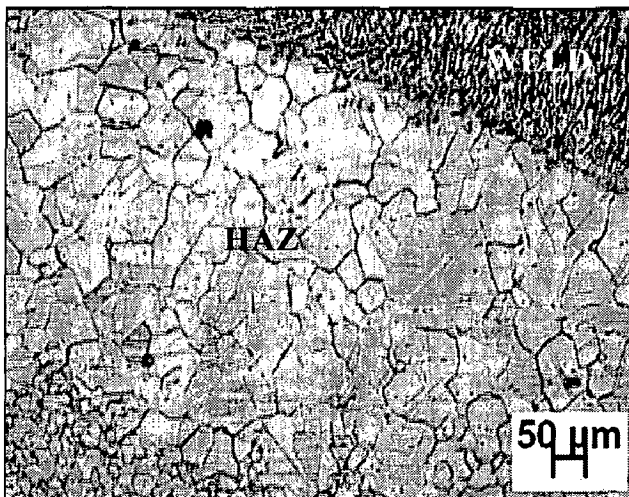
(b)
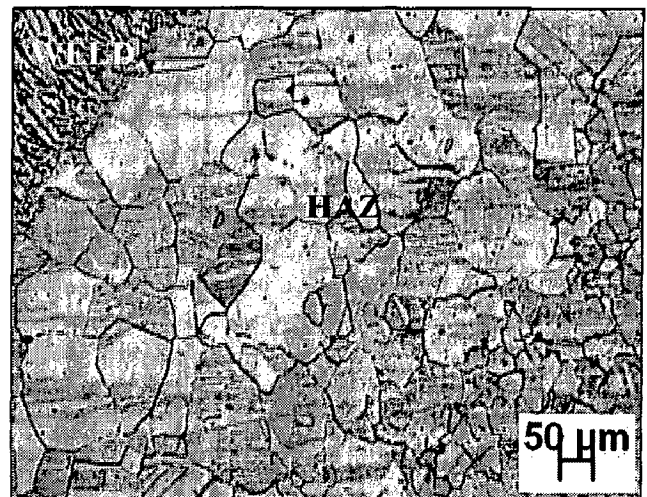
(c)

Fig. 5.25: At a given Ω of 9.66 $\pm$ 0.47kJ/cm the variation in grain growth of HAZ adjacent to fusion line of weld bead deposited at different ϕ of (a) 0.047 (b) 0.153 and (c) 0.237.
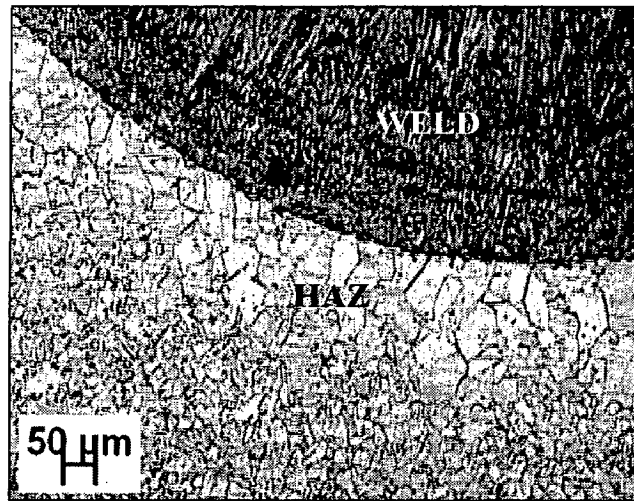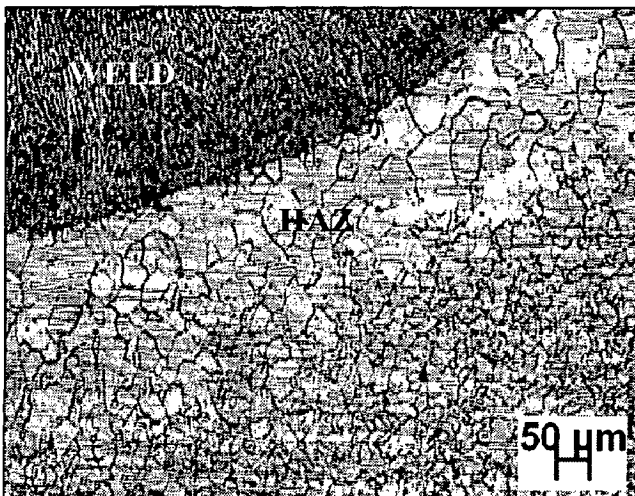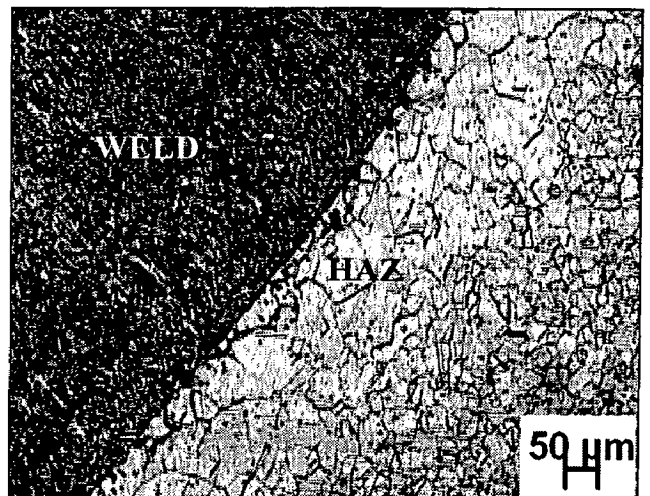
Fig. 5.26: At a given Ω of 7.1 ± 0.44kJ/cm the variation in grain growth of HAZ adjacent to fusion line of weld bead deposited at different φ of (a) 0.042 (b) 0.136 and (c) 0.224.
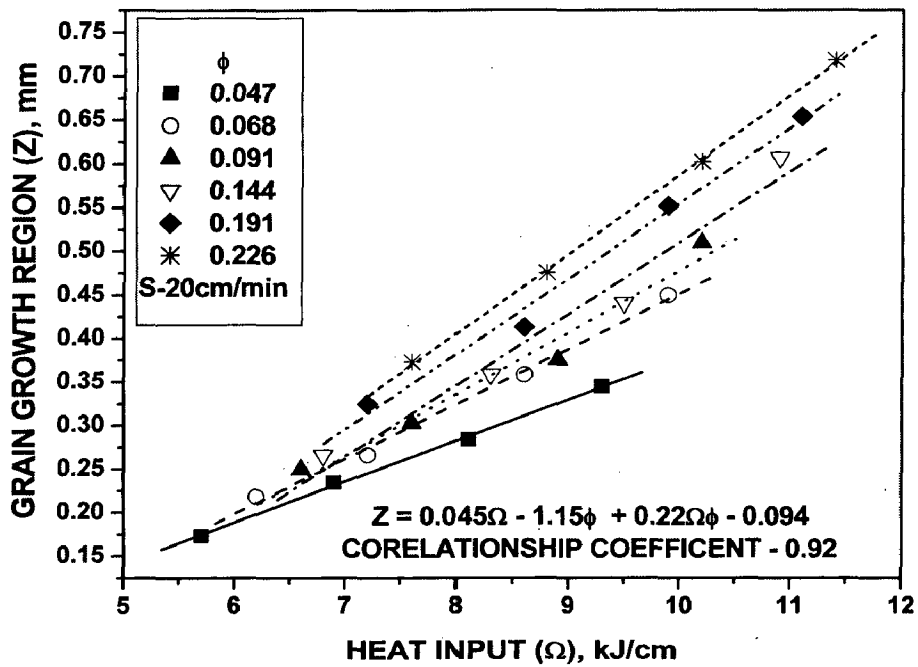
Fig. 5.27: Effect of ϕ and Ω on the width of grain growth region of HAZ adjacent to fusion line of weld bead.

HEAT INPUT (Ω), kJ/cm

6.2±0.5 : 7.2±0.4 : 8.5±0.4 : 9.8±0.5

$Z = 0.02Q_T - 1.9\phi + 0.44Q_T\phi - 0.06$
CORELATIONSHIP COEFFICIENT-0.84

ϕ
■ 0.047
● 0.068
▲ 0.091
S-20cm/min

GRAIN GROWTH REGION(Z), mm

TOTAL HEAT TRANSFERED TO THE WELD POOL (Q$_T$), kJ/cm

(a)

HEAT INPUT (Ω), kJ/cm

7.2±0.4 : 8.6±0.3 : 9.9±0.4 : 11.1±0.3

ϕ
▼ 0.144
◆ 0.191
✱ 0.226
S-20cm/min

$Z = 0.06Q_T + 0.85\phi + 0.07Q_T\phi - 0.38$
CORELATIONSHIP COEFFICIENT-0.98

GRAIN GROWTH REGION(Z), mm

TOTAL HEAT TRANSFERED TO THE WELD POOL (Q$_T$), kJ/cm
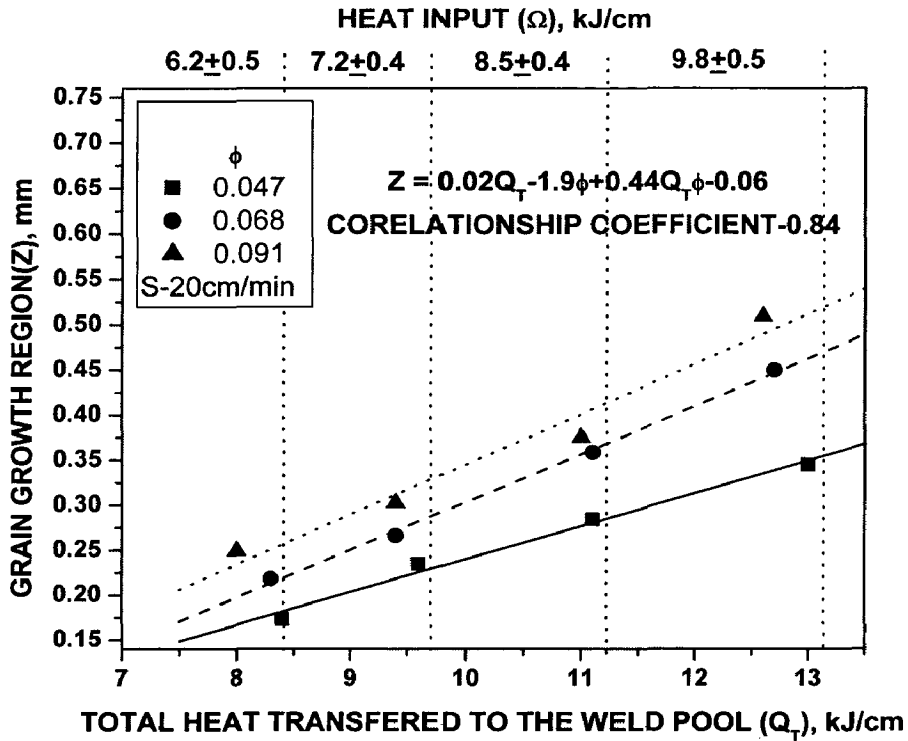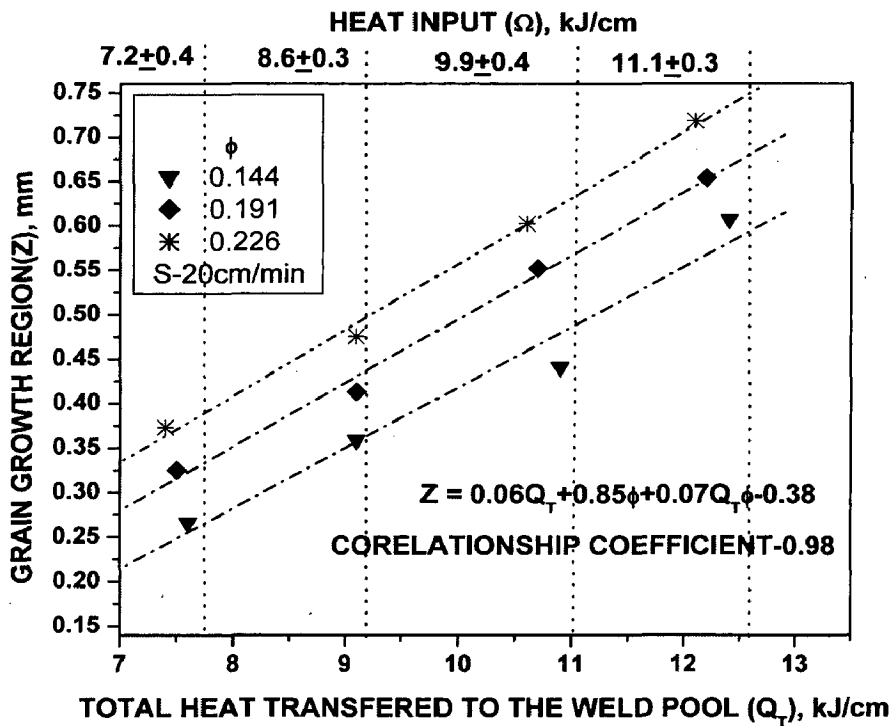
(b)

Fig. 5.28: At varied range of Ω influence of ϕ and Q$_T$ on grain growth region of HAZ adjacent to fusion line at different range of ϕ of (a) 0.047-0.091 and (b) 0.144-0.226 in P-GMA weld beads.

178

In agreement to the eq. (5.14) the average grain size (D) of HAZ adjacent to FL significantly enlarges (Fig.5.29) with the increase of Ω and ϕ following the equation as stated below. Hence it can be assumed that Q_T also influences D in a similar way as observed earlier in case of Z.

$$D = 17.7\phi + 2.02\Omega - 0.71\phi\Omega + 28.6 \qquad (5.17)$$

The extent of grain coarsening (D) and grain growth region (Z) in HAZ for a given material primarily depends upon Ω and Q_T which controls the weld thermal cycle of the matrix adjacent to the FL of HAZ in the range of its temperature for recrystallisation and grain growth in quasi stationary state. However, at a given Ω the appreciable influence of ϕ on Z and D, as observed in Figs. 5.27 and 5.29 respectively, may have primarily happened due to deposition of comparatively larger mass of weld metal in weld pool at a lower ϕ of 0.05 than that of 0.25 (Table-5.8). Further, relatively higher surface area of contact of the weld pool with the base metal at lower ϕ of 0.05 than that at ϕ=0.25 leading to faster rate of heat dissipation from weld pool, may also favour the recrystallisation and grain growth in HAZ in case of the lower ϕ than that for the higher one.
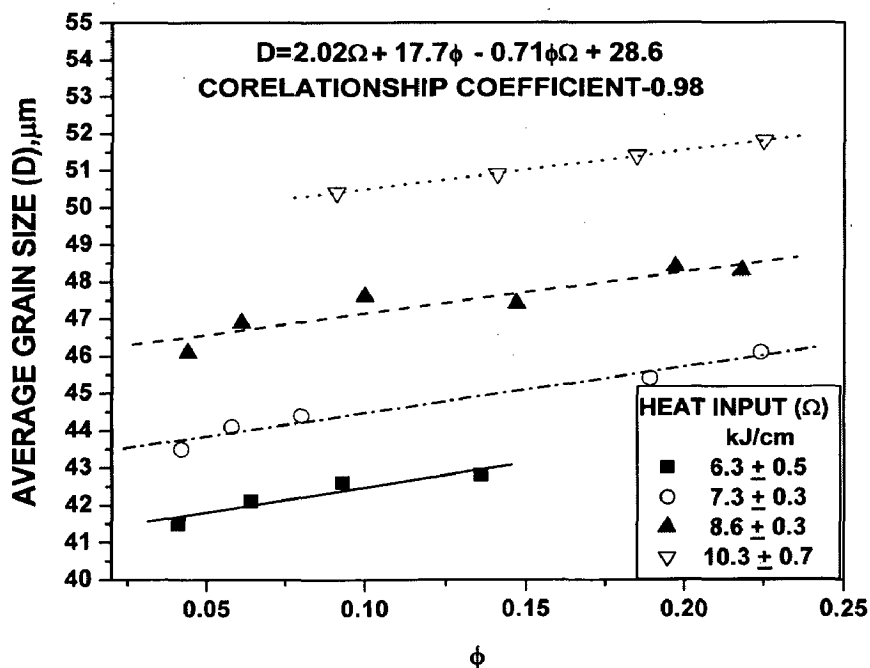
Fig. 5.29: At varied range of Ω, influence of ϕ on average grain size in HAZ adjacent to fusion line of P-GMA weld bead.

5.2.4.2 HAZ of GMA welds

Typical variation of Z at different Ω of 7.2 and 9.7kJ/cm is shown in Fig. 5.30 (a) and

(b) respectively. The grain growth region of GMA welds appears to be similar to that

observed in P-GMA welds of comparatively higher ϕ of 0.22-0.24. However, the average

grain size of HAZ adjacent to FL of GMA welds has been found about 49.6 and 54.7μm at

the Ω of 7.2 and 9.7 kJ/cm respectively. It has been observed that at a given Ω, this grain size

of GMA welds is relatively higher than that observed in similar region of HAZ of the P-GMA

welds (Fig. 5.29). Such a difference in GMA welds with respect to those of the P-GMA

welds may be primarily attributed to the difference in characteristics of weld thermal cycle of

uninterrupted and interrupted nature respectively.

(a)   (b)
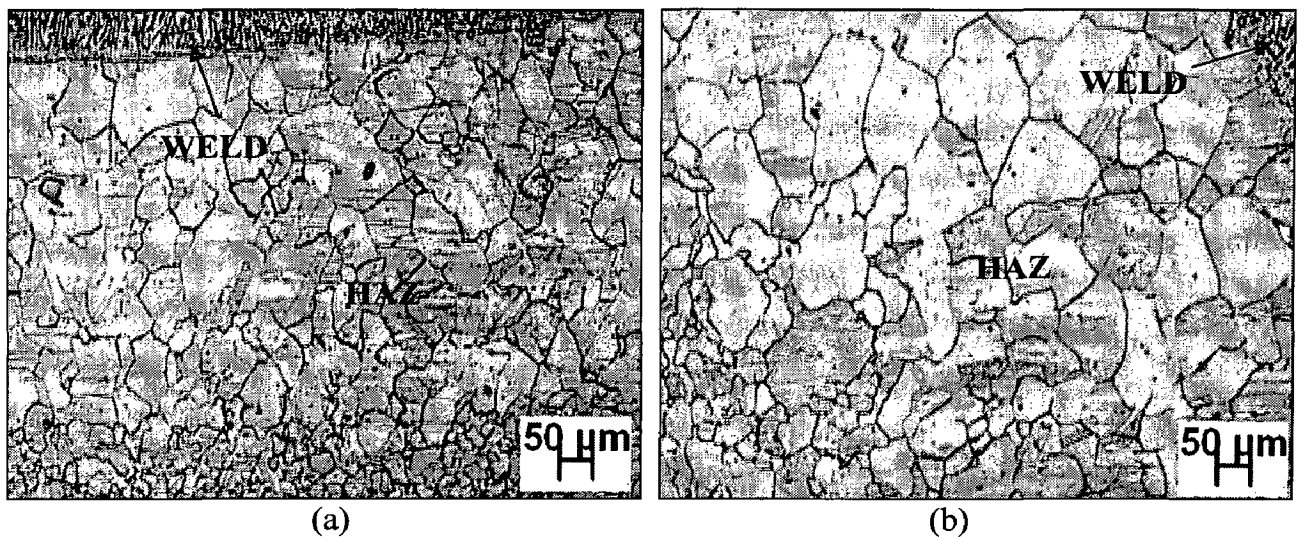
Fig. 5.30:   Grain growth of HAZ adjacent to fusion line observed in GMA weld bead
deposited at different Ω of (a) 7.1kJ/cm and (b) 9.2kJ/cm.

5.2.5 Inter Granular Corrosion

The intergranular corrosion (IGC) susceptibility of the grain growth region in HAZ adjacent to FL has also been studied primarily in P-GMA welds in reference to the summarized influence of pulse parameters ϕ and heat input Ω affecting thermal behaviour of this region. The weld isotherm and thermal cycle as a function of ϕ and Ω influences chromium carbide precipitation at the grain boundary of HAZ giving rise to the formation of a chromium depleted zone in the matrix adjacent to it. Thus, it makes this zone susceptible to corrosion attack appearing as grain boundary thickening which may be considered as a degree of IGC attack to the sensitized grain boundary. This behaviour of HAZ at two different welding conditions of (ϕ=0.225 and Ω=11.4 kJ/cm) and (ϕ=0.041, Ω=5.7 kJ/cm) is shown in Fig. 5.31 (a) and (b) respectively, where the grain boundary thickening is found to lie in the range of about 7.75±0.84µm. Some typical behaviour of variation in chromium concentration in the matrix across the sensitized grain boundary leading to its selective corrosion attack as shown in Fig. 5.31(a) and (b) has been correspondingly shown in Fig. 5.32 (a) and (b). The Fig. 5.32 (a) shows considerably higher concentration of chromium than that in the matrix within the thick corroded region of grain boundary possibly due to presence of chromium carbide in it along with substantially low concentration of chromium with respect to that necessary (11.5wt.%) for corrosion resistance of ASS [Folkhard 1984] in the chromium depleted matrix adjacent to the grain boundary. Although the matrix adjacent to grain boundary shows similar nature of chromium depletion in Fig. 5.32 (b) but, it reveals significantly low chromium concentration within the thick corroded region of grain boundary. This may have happened due to removal of chromium carbide precipitates from this region as corrosion attack around the precipitate help in their detachment and removal resulting in formation of a dark thick ditch at the grain boundary. However, the EDAX analyses presented in Fig. 5.32(a) and (b) clearly reveal that the ASS base material is susceptible to the

181

sensitization which may be more prominent in generally well known sensitized region of HAZ further away from the fusion line. As such, the degree of sensitization of the base material under P-GMAW should be studied as a function of φ and Ω.

(a)   (b)
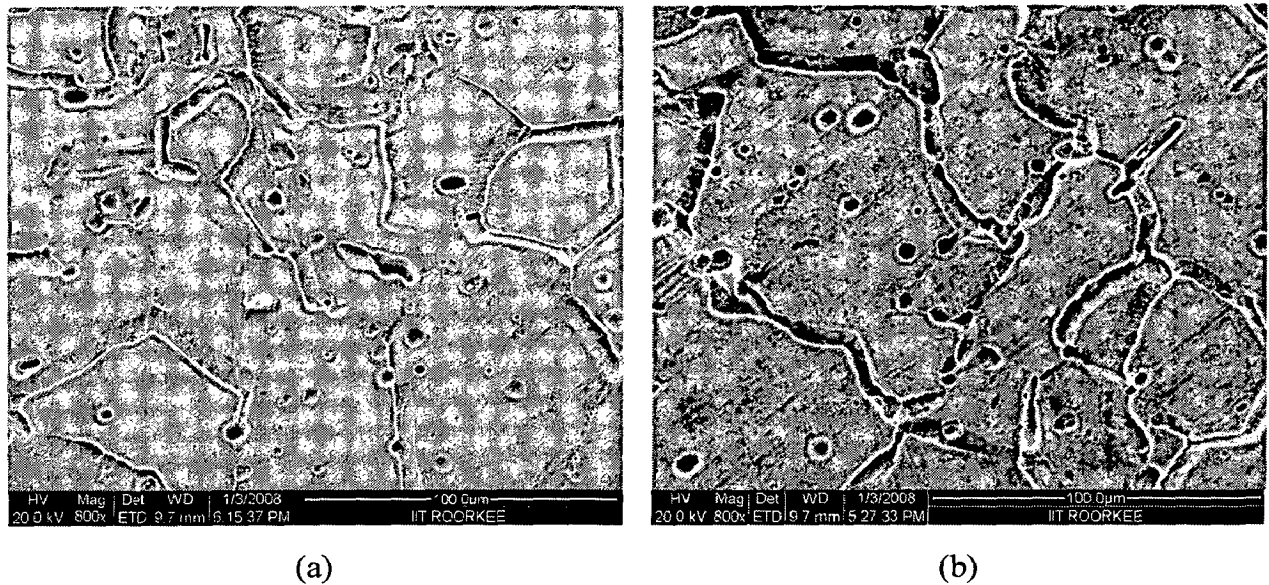
Fig. 5.31: SEM photograph showing typical grain boundary thickening due to IGC attack in grain growth region of HAZ at different welding conditions of (a) φ= 0.225, Ω-11.4kJ/cm and (b) φ= 0.047, Ω-5.7kJ/cm.

(a)   (b)
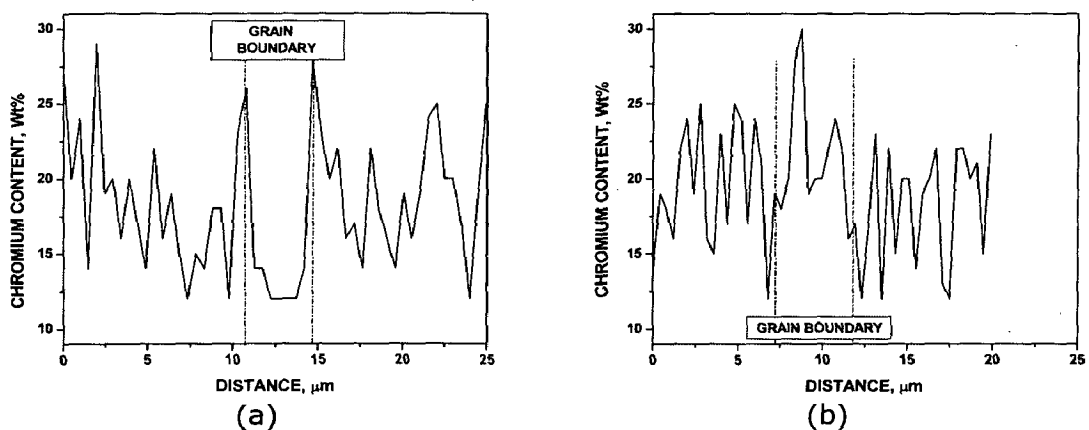
Fig. 5.32: Typical behaviour of chromium distribution across the grain boundary marked in the corresponding micrographs presented in Fig. 24 for different welding conditions of (a) φ= 0.225, Ω-11.4kJ/cm and (b) φ= 0.047, Ω-5.7kJ/cm.

5.2.6 Hardness

5.2.6.1 Hardness of P-GMA weld and HAZ

The influence of variation in ϕ and Ω on hardness (VHN) of central part of weld deposit (H_W) as well as micro-hardness along the fusion line (H_{FL}) and coarse grain region of HAZ (H_{HAZ}) adjacent to FL is shown in Fig. 5.33 (a), (b) and (c) respectively. The figures primarily depicts that at a given ϕ, the increase of Ω almost linearly enhances hardness of weld, FL and coarse grain region of HAZ. It is further observed that at a given Ω, the increase of ϕ from 0.047 to 0.226 also enhances hardness of all these regions as stated above. H_W, H_{FL} and H_{HAZ} as a function of ϕ and Ω can be expressed by the empirical equations as stated below.

$$H_w = 65.28\phi + 9.96\Omega + 23.27\Omega\phi + 116.6 \qquad (5.18)$$

$$H_{FL} = 476\phi + 10.7\Omega - 21.1\Omega\phi + 132.3 \qquad (5.19)$$

$$H_{HAZ} = 232.5\phi + 9.24\Omega + 20.3\Omega\phi + 153.3 \qquad (5.20)$$

At a given close range of variation in dilution of about $39 \pm 4\%$ the increase of H_W with the increase of ϕ and Ω may be attributed primary to increase of severity of weld thermal cycle causing considerable coarsening of microstructure (Figs. 5.20 and 5.21). The grain growth of HAZ close to FL reduces the hardness of this region to lower than that of base metal (230 ± 10 VHN), but the increase of ϕ and Ω enhances it possibly due to a predominant influence of carbide precipitation at the grain boundary as discussed above. The increase in hardness of FL may also be due to happened due to carbide precipitation. The increase of Ω as well as ϕ enhances the width of HAZ (Fig. 5.27) by promoting the severity of thermal effect of weld deposit (Fig. 5.9) and thus, lowers the cooling rate of HAZ favouring the carbide precipitation in it as well as in FL. However, 15-20% higher hardness of HAZ than that of weld may have been caused largely by higher carbon and chromium content of base metal in comparison to that of filler metal used for weld bead deposition (Table-5.8).

(a)

(b)

184
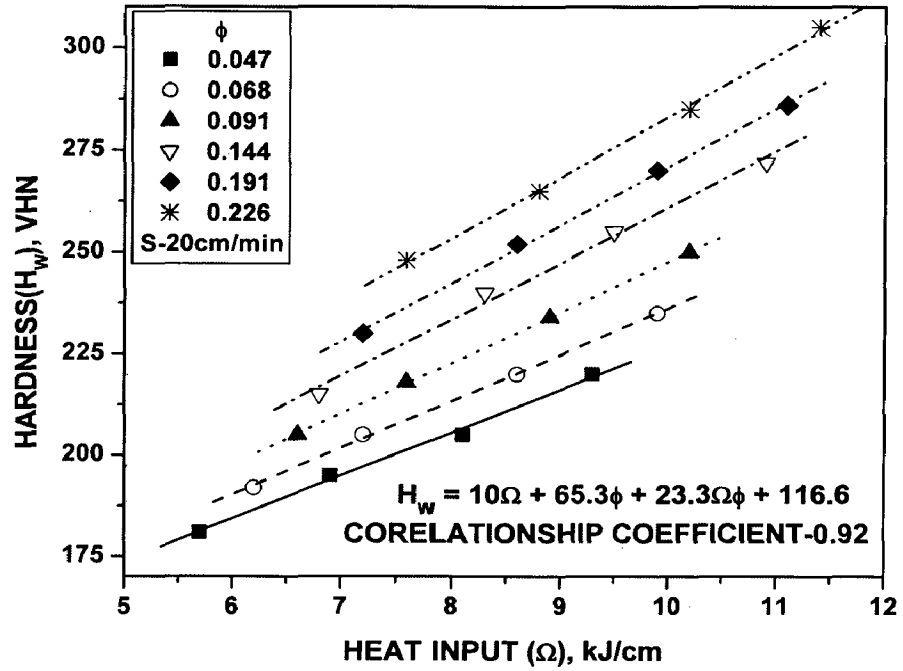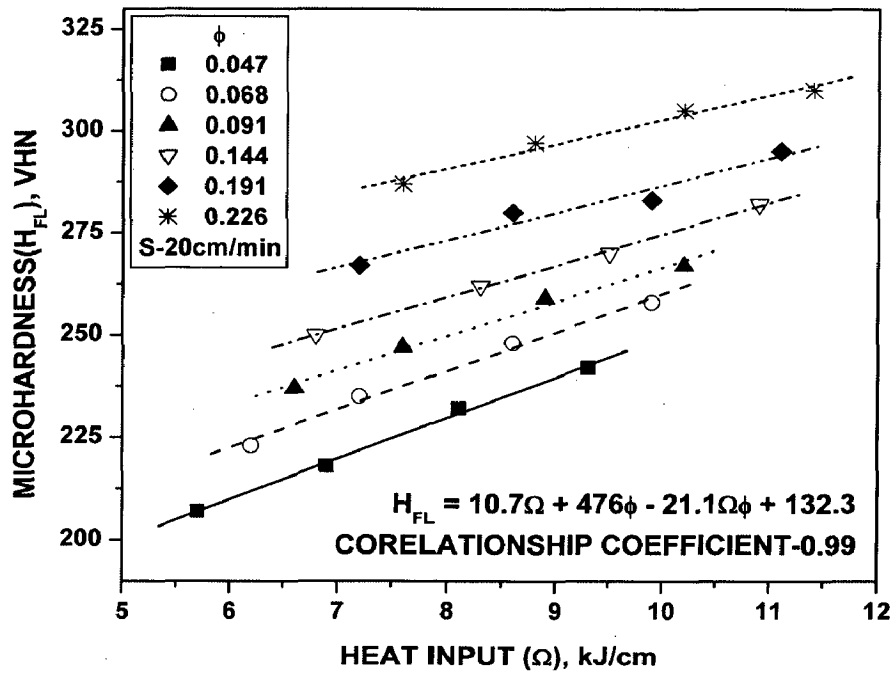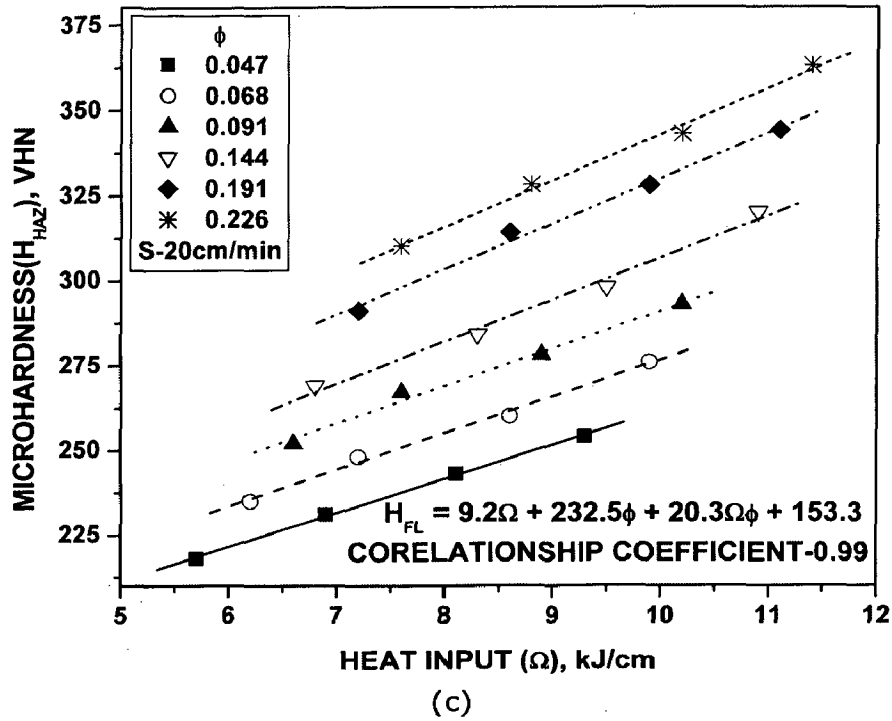
Fig. 5.33: Influence of ϕ and Ω on the hardness of (a) weld deposit (b) along the fusion line and (c) grain growth region of HAZ.

Hardness distribution in grain growth region of HAZ adjacent to fusion line has been further studied at a given Ω by varying Q_T (Fig. 5.34) at two different ranges of ϕ, 0.047-0.091 and 0.144-0.226, and the empirical equations obtained are given below.

For the range of ϕ of 0.047-0.091

$$H_{HAZ} = 7.03Q_T + 650.5\phi + 21.03\ Q_T\phi + 122 \tag{5.21}$$

For the range of ϕ of 0.144-0.226

$$H_{HAZ} = 8.77Q_T + 448\phi + 10.9\ Q_T\phi + 125.3 \tag{5.22}$$

Both equations primarily indicate that hardness increase linearly with the increase in Q_T and ϕ. At a given ϕ and Ω, unit rise in Q_T increases hardness by 4% in both the ranges of ϕ (Fig. 5.34(a) and (b)). But at a given Q_T and Ω, hardness increases by almost 20% with the increase in ϕ in both the above stated ranges. Here also, in confirmity with our earlier discussions, ϕ dominantly influences hardness of the weld within the stated range of Q_T and Ω.

HEAT INPUT (Ω), kJ/cm

| 6.2±0.5 | 7.2±0.4 | 8.5±0.4 | 9.8±0.5 |

$$H_{HAZ} = 7.03Q_T + 650.5\phi + 21.03Q_T\phi + 122$$
CORELATIONSHIP COEFFICIENT-0.84

φ
■ 0.047
● 0.068
▲ 0.091
S-20cm/min

MICROHARDNESS(H_{HAZ}), VHN

TOTAL HEAT TRANSFERED TO THE WELD POOL (Q_T), kJ/cm

(a)

HEAT INPUT (Ω), kJ/cm

| 7.2±0.4 | 8.6±0.3 | 9.9±0.4 | 11.1±0.3 |

$$H_{HAZ} = 8.77Q_T + 448\phi + 10.9Q_T\phi + 125.3$$
CORELATIONSHIP COEFFICIENT-0.98

φ
▼ 0.144
◆ 0.191
✳ 0.226
S-20cm/min

MICROHARDNESS(H_{HAZ}), VHN

TOTAL HEAT TRANSFERED TO THE WELD POOL (Q_T), kJ/cm

(b)

Fig. 5.34: At varied range of Ω influence of φ and Q_T on hardness of grain growth region of HAZ adjacent to fusion line at different range of φ of (a) 0.047-0.091 and (b) 0.144-0.226 in P-GMA weld beads.

186

5.2.6.2 Hardness of GMA weld and HAZ

The influence of Ω on hardness of central part of weld deposit (H_W) as well as micro-hardness along the fusion line (H_{FL}) and coarse grain region of HAZ (H_{HAZ}) adjacent to FL has been given in Table-5.9 (Section 5.2.1.1). The table depicts that increase of Ω marginally reduces H_W primarily due to relative coarsening of microstructure of weld deposit but appreciably enhances H_{FL} and H_{HAZ} possibly due to increase in carbide precipitation. The increase of Ω enhancing the width of HAZ (Fig. 5.30) by promoting the severity of thermal effect on weld deposit lowers the cooling rate of HAZ favouring more carbide precipitation in it as well as in FL. The GMA welds follow the same trend of increase in hardness from weld to HAZ as observed in P-GMA welds and it is interestingly observed that at higher Ω, the GMA welds have similar hardness as observed in P-GMA welds of comparatively higher ϕ of 0.22-0.24.

5.2.7 Summary and Selection of Suitable Parameters for P-GMA Welding of Thick Wall Pipe

The pulse parameters and wire feed rate (V_w) significantly influence the heat input (Ω) and heat transferred to the weld pool (Q_T) in P-GMA welding process. The effect of pulse parameters as indicated by their summarized influence through factor ϕ, provides a good basis to control the P-GMAW process showing significant correlations with the Ω and Q_T in bead on plate weld deposition of austenitic stainless steel. Hence, at an estimated bead dilution of the order of $39 \pm 4\%$ the major geometrical characteristics such as bead penetration (P), base metal fusion (B_F) and metallurgical characteristics such as grain growth region (Z) and hardness of weld bead in HAZ (H_{HAZ}) vary significantly as a function of Ω, ϕ and Q_T as shown in Table-5.10.

187

The table further shows that Ω, ϕ and Q_T are interactive in nature. Hence a combination of these factors should be considered while carrying out welding of thick sections. Thus for carrying out welding of thick sections by multipass welding procedure comparatively lower values of ϕ, Ω and higher Q_T are found mostly suitable considering their minimized adverse influence on various weld bead characteristics.

Table 5.10: Summarized influence of Ω, ϕ and Q_T on weld bead characteristics

	Range of ϕ	P (mm)	B_F (mm^2)	Z (mm)	H_{HAZ} (VHN)
At a given Ω and Q_T influence of ϕ	0.047-0.091	0.075 ▼	0.356 ▼	0.05 ▲	17.42 ▲
	0.144-0.225	0.3 ▼	1.45 ▼	0.13 ▲	47.8 ▲
Within a given range of Ω (6.2-11.1kJ/cm) and ϕ, influence of increase in Q_T by 1kJ/cm	0.047-0.091	0.325 ▲	3.31 ▲	0.05 ▲	8.54 ▲
	0.144-0.225	0.21 ▲	2.04 ▲	0.07 ▲	10.8 ▲
At a given ϕ, within a range of Ω (6.2-11.1kJ/cm) influence of increase in Q_T by 2kJ/cm	0.12 ± 0.04	0.28 ▲	2.16 ▲	0.13 ▲	26.2 ▲
At a given ϕ, within a given range of Q_T (7-13kJ/cm) influence of increase in Ω by 1.25±0.04 kJ/cm	0.12 ± 0.04	0.1 ▲	2.08 ▲	0.03 ▲	15.65 ▲

5.3 CHARACTERISTICS OF CONVENTIONAL GROOVE WELD JOINT UNDER DIFFERENT *WELDING PROCESSES*

The weld joint is a mechanically heterogeneous body composed of base metal, weld metal and heat affected zone (HAZ). These different regions of the weld joint leads to heterogeneous mechanical and metallurgical properties of the material along with considerable development of harmful tensile residual stresses. These difficulties resulting from heterogeneity of weld get further compounded in case of heat-sensitive materials like austenitic stainless steel (ASS), especially of thick sections, due to its lower thermal conductivity and higher coefficient of thermal expansion in comparison to those observed in structural steel [Folkhard 1984, Elmer et al 1982, Timofeev et al 1999, Anderson 2005]. The considerably low thermal conductivity makes the HAZ of arc weld of ASS more prone to sensitization while its significantly high coefficient of thermal expansion develops considerable stresses in the weld. Hence the proper selection of welding process and procedure by considering efficient energy distribution in the welding arc leading to comparatively low heat built-up in the weld pool is imperative to reduce the amount of damage produced in different zones of weld joint due to heterogeneity in their properties.

5.3.1 Weld Quality and Size

The quality and size of weld may significantly vary with the use of different arc welding processes like P-GMA, GMA or SMA welding primarily due to their varying thermal characteristics and process efficiencies. The macro photographs revealed from the transverse sections of the P-GMA weld joints prepared by using two different ϕ values of 0.06 and 0.25 at a given heat input (Ω) of 9.2 ± 0.35 kJ/cm are shown in Fig. 5.35 (a) and (b) respectively. Similarly, at a given relatively lower Ω of 7.8 ± 0.35 kJ/cm, the macro photographs of transverse sections of the P-GMA weld joints prepared at two different ϕ values of 0.05 and 0.25 are shown in Fig. 5.36 (a) and (b) respectively. The macro photographs of the GMA and SMA weld joints as revealed in

their transverse sections are shown in Fig. 5.37 (a) and (b) respectively. Based on the data recorded as shown in Annexure-I, the total number of passes, average Ω in filling passes, area of the weld deposit and overall cumulative transverse shrinkage observed in the conventional groove P-GMA, GMA and SMA weld joints are shown in Table-5.11. In case of P-GMA weld joints heat transferred to the weld pool (Q_T) has also been estimated (section 4.3.1) and compared in Table-5.11.

(a)   (b)
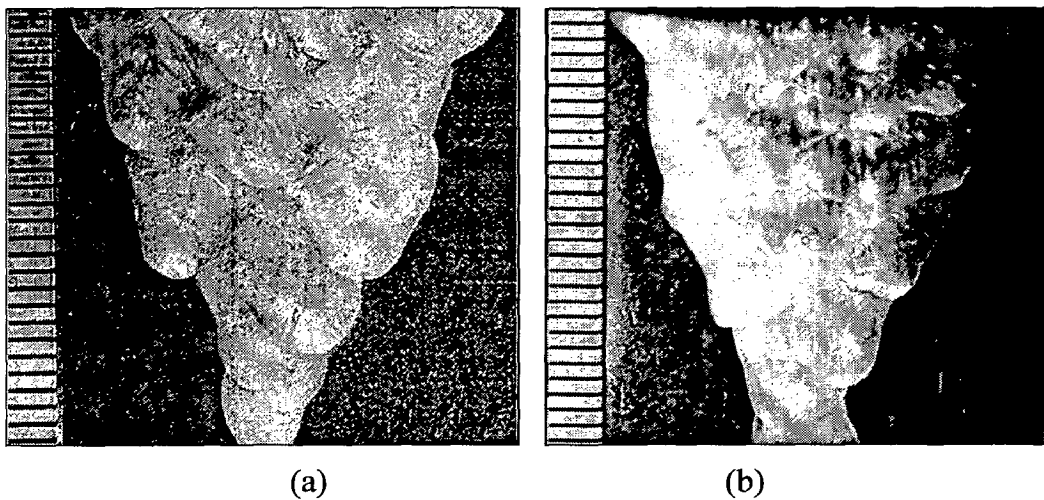
Fig. 5.35:   Typical macro photograph of conventional V-groove weld joint at a given Ω of 9.2 ± 0.35 kJ/cm with the variation in ϕ of (a) 0.06 and (b) 0.25 prepared by using P-GMAW process.

(a)   (b)
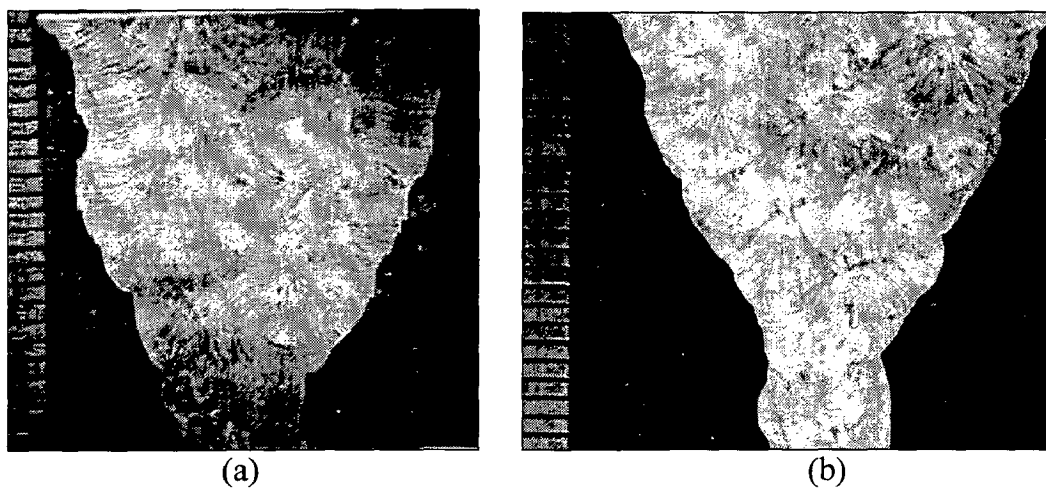
Fig. 5.36:   Typical macro photograph of conventional V-groove weld joint at a given Ω of 7.8 ± 0.35 kJ/cm with the variation in ϕ of (a) 0.05 and (b) 0.25 prepared by using P-GMAW process.

(a)   (b)
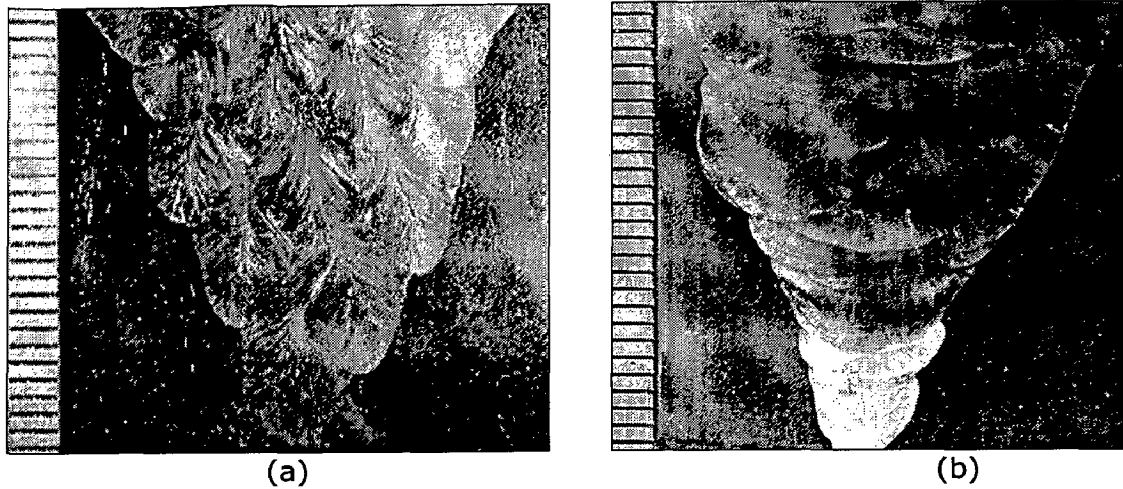
Fig. 5.37: Typical macro photograph of conventional V-groove weld joint prepared by using (a) GMAW and (b) SMAW processes.

Table-5.11: Summarised influence of weld data on type and average proportion of defects discarded from conventional P-GMA, GMA and SMA weld joints.

Process	Weld width (mm)	ϕ	Total number of passes	Average Ω in filling passes, (kJ/cm)	Average Q_T in filling passes, (kJ/cm)	Area of weld deposit (mm^2)	Overall cumulative transverse shrinkage (mm)	Fractional length of LOF of total weld (%)	Type of defects
P-GMAW	23	0.06	14	9.1	11.4	345	5.68± 0.22	4.8	Lack of sidewall/ interpass fusion
	23	0.25	16	9.4	10.5	353	6.04± 0.34	8.3	
	24	0.05	15	7.7	11.1	347	5.30± 0.17	3.9	
	23.5	0.25	16	8.0	9.9	357	5.44± 0.45	9.8	
GMAW	24	-	17	10.7	--	347	6.32± 0.41	10.1	
SMAW	21	-	16	17.1	--	343	6.80± 0.48	7.6	Slag line

Figs. 5.35-5.37 primarily depict that the welds are practically free from any defects such as lack of welding or root fusion. The characteristics of weld joints shown in Table-5.11 reveals that in order to produce a sound weld with almost constant area of weld deposit, the average Ω, number of passes and overall cumulative transverse shrinkage can be considerably reduced by using P-GMAW process in comparison to those found in case of using GMAW and SMAW processes and it clearly demonstrates distinct advantage of P-GMAW process over the other two processes. In P-GMAW process, superheated droplets are transferred to the weld pool during peak current duration at a high velocity, resulting in heat transfer at

certain depth [Goyal et al 2007] of cavity in the weld pool. Thus the corresponding energy released by the droplet at that depth provides better base metal fusion at a comparatively lower Ω. Such a variation in P-GMAW process is primarily achieved through energy distribution across pulse on and off time by controlling pulse parameters through combined influence of Ω, ϕ and Q_T. These factors primarily control mass, velocity and heat content of the droplet transferred at a given set of pulse parameters.

Table-5.11 also reveals that during P-GMA welding the cumulative shrinkage of the weld joint further reduces with the lowering of ϕ from 0.25 to 0.05 and Ω from 9.2 to 7.8 kJ/cm. At a given ϕ, lowering of I_m reduces (Annexure-I) the Ω. Thus, the corresponding reduction in metal deposition must have abridged the volumetric expansion, resulting in contraction of the weld, leading to lowering of shrinkage. At a given Ω, with the decrease of ϕ, the relative rise in Q_T (Table-5.11) may reduce shrinkage by improving heat dissipation through generation of relatively higher surface area of contact of the weld pool with the base metal (Figs. 5.35 and 5.36). Hence, it may be assumed that the use of P-GMA welding with a lower ϕ of 0.05 and Ω of 7.8kJ/cm may reduce the induction of strain especially at the root of the pipe weld in comparison to that obtained in case of the GMA and SMA welding of pipe. This may also consequently minimise residual stresses in the weld joint. Further, Table-5.11 shows that the fractional length of lack of fusion (LOF) of total weld observed in semi-automated GMA weld is relatively higher in comparison to that of P-GMA weld joints and manually prepared SMA weld. Such a variation may have primarily happened due to considerable deviation in transverse shrinkage (Table-5.11) across the eight equally divided quadrants (Annexure-I) of circumferential locations. Prior to weld pass, the location of torch has been fixed with respect to groove wall in semi automation technique followed during preparation of GMA and P-GMA weld joints. During welding in 1GR position, non-uniform temperature field at different circumferential locations must have occurred due to pipe

movement causing interactions between heat transfer, metallurgical transformations and mechanical fields applied during the welding process. Thus non uniformity in transverse shrinkage may have largely occurred producing deformation in the welded structures [Sattari-Far and Javadi 2008]. These deformations must have either shifted the torch towards or away from the groove wall resulting in insufficient melting of initially deposited bead or groove wall respectively. Thus, lack of interpass or sidewall fusion must have occurred in GMA and P-GMA welds.

In P-GMA welds at both the Ω levels, lack of interpass/sidewall fusion is relatively more at $\phi = 0.25$ due to two reasons. Firstly, as explained above, the shifting of torch location with respect to groove wall takes place. Secondly, considerable variation in arc characteristics occurs depending upon pulse parameters employed during welding [Ghosh.et al 2008]. Arc characteristics depending upon its stiffness considerably influences arc deflection. It has been observed that arc deflection considerably increases with the variation in ϕ from 0.05 to 0.25 [Ghosh et al 2008] due to lowering of arc pressure. Thus, metal transfer to the weld pool must have got deflected depending upon arc characteristics, leading finally to insufficient arc crater depth causing lack of fusion. The defective areas revealed under X-ray radiography of pipe weld have been removed and the corresponding sound weld area has been used for further studies.

5.3.2 Chemical Composition and δ-ferrite Content

Chemical compositions of the weld are given in Table-5.12. Delta ferrite content estimated as per WRC-92 diagram [Siewert et al 1988] and measured by ferrite scope across the filler passes in transverse section of various weld deposits are also shown in Table-5.12. The table depicts that irrespective of welding processes used for weld deposition, dilution of base metal introduces nitrogen of the order of 0.1 wt% to the weld and thus, reduces its δ-

ferrite content by stabilizing the austenite phase as per WRC-92 diagram [Siewert et al 1988]. It has been further observed that filler regions of the P-GMA and GMA weld deposits have 6-8% of δ-ferrite content indicating ferrite-austenite (FA) mode of solidification in contrast to austenite-ferrite (AF) mode of solidification observed in case of SMA weld deposits in presence of practically negligible quantity of δ-ferrite in it (Table-5.12). However, in the root pass of all the weld joints carried out by GTAW process, δ-ferrite content has been found to lie in the range of 2.5-4%. In SMA weld, AF mode of solidification also results in considerable loss of chromium caused by oxidation during metal transfer along with base metal dilution. Hence, it may be inferred that P-GMA and GMA welds prepared at relatively lower Ω (Table-5.11) having 6-8% δ-ferrite content (Table-5.12) are comparatively less prone to solidification cracking [Shankar et. al. 2003b, Braint and Andresen 1988, Erve et al 1997] in comparison to SMA weld joint.

Table-5.12: Chemical composition and δ-ferrite content of the weld deposits prepared by using P-GMAW, GMAW and SMAW processes.

Process	Weld width (mm)	φ	Ω kJ/cm	Chemical analysis of weld metal (Wt.%)										Equivalents		Estimated		δ-ferrite content (%)	
				C	Cr	Ni	Mn	N	Mo	Si	Cu	S	P	Cr_{eq}	Ni_{eq}	δ-ferrite content (%)	Solid-ification mode	Root passes	Filler passes
P-GMAW	23.5	0.06	9.1	0.023	18.95	9.46	1.62	0.10	0.12	0.58	0.25	0.01	0.07.7	19.07	12.33	4-5	FA	2.90	6.85
	23	0.25	9.4	0.026	19.30	9.41	1.4	0.10	0.10	0.49	0.18	0.006	0.016	19.51	12.40	6-8	FA	3.20	7.45
	24	0.05	7.7	0.029	19.1	9.35	1.56	0.10	0.14	0.46	0.20	0.012	0.01	19.3	12.4	6-8	FA	3.60	7.45
	23	0.25	8.0	0.024	19.37	9.51	1.71	0.10	0.14	0.49	0.21	0.01	0.012	19.40	12.24	6-8	FA	4.00	7.95
GMAW	24	-	10.7	0.024	19.12	9.40	1.6	0.10	0.14	0.38	0.14	0.013	0.020	19.26	12.28	4	FA	3.80	7.65
SMAW	21	-	17.0	0.027	18.13	7.7.1	2.28	0.10	0.04	0.37	0.14	0.013	0.020	18.17	14.04	-	AF	2.50	0

5.3.3 Microstructure

The typical weld microstructures prepared at a given Ω of 9.2$\pm$0.35 kJ/cm by using P-GMAW process at two different levels of ϕ of 0.06 and 0.25 have been compared in Fig. 5.38 (a) and (b) respectively. Similarly, at a given Ω of 7.7$\pm$0.35 kJ/cm, the typical microstructures of weld deposits at two different levels of ϕ of 0.05 and 0.25 have been compared in Fig. 5.39 (a) and (b) respectively. GMA and SMA weld microstructures have been compared in Fig. 5.40 (a) and (b) respectively. The microstructures presented in Fig. 5.38 to 5.40 depict that the P-GMA, GMA and SMA welds are having different morphology of multipass weld deposit. The P-GMA weld deposit primarily shows considerable refinement in microstructure along with scarcely distributed coaxial dendritic structure, whereas the GMA and SMA welds largely show conventional behaviour of multipass weld that significantly consists of both coaxial dendritic and reheat refined regions. It has been further observed that in P-GMA welds, the refinement of microstructure increases with the lowering of ϕ and Ω from 0.25 to 0.05 and 9.2 to 7.8kJ/cm respectively (Fig. 5.38 and 5.40) primarily due to variation in thermal shock during solidification through interruption in metal deposition imparted by the pulse (Section 2.5.2.1) along with the usual reheat refinement by the subsequent weld pass. However, in the case of conventional GMA and SMA weld deposits, the refined region primarily results from partial reheat refinement of coaxial dendrite of earlier deposited weld bead due to severity of weld thermal cycle imparted by the subsequent weld passes. Such a difference observed in weld microstructure has been further characterized by analyzing the distribution of coaxial dendritic and refined region in P-GMA, GMA and SMA weld deposits as shown in Table-5.13. In agreement to the above mentioned observations, table shows that the use of GMAW and more effectively P-GMAW significantly reduces the coaxial dendritic region in the weld with respect to that observed in SMA weld.

196

The typical microstructures of the HAZ of the weld joint prepared at a given Ω of 9.2$\pm$0.35 kJ/cm by using P-GMAW process at two different levels of ϕ of 0.06 and 0.25, have been compared in Fig. 5.41 (a) and (b) respectively. Similarly, at a given Ω of 7.7$\pm$0.35 kJ/cm the typical microstructures of weld HAZ at two different levels of ϕ of 0.05 and 0.25 have been compared in Fig. 5.42 (a) and (b) respectively. The typical microstructures observed in the HAZ of GMA and SMA welds have been compared in Fig. 5.43 (a) and (b) respectively. The microstructure of HAZ adjacent to fusion line (Figs.5.41-5.43) of the P-GMA, GMA and SMA welds shows certain extent of grain coarsening. The grain size of this region has been compared in Table-5.14. The table shows that P-GMA and GMA weld joints have comparatively less grain coarsening than that observed in case of SMA weld joint. This may have happened primarily due to considerable reduction in severity of weld isotherm arising out of the heat of weld deposition adjacent to the groove wall. However, in P-GMA welds, marginal grain coarsening over base metal grain size (Section-5.1.2) has been found at both the levels of ϕ and Ω. Thus, such a characteristic of HAZ may improve the resistance to stress corrosion cracking susceptibility of P-GMA and GMA weld joints in comparison to that of SMA weld joint.

Table-5.13: Dendrite measurement at various locations in P-GMA, GMA and SMA weld deposit.

Process	ϕ	Ω kJ/cm	Coaxial dendritic region (%)	Refined region (%)
P-GMAW	0.06	9.0	41.3	58.7
	0.25	9.5	47.8	52.2
	0.05	7.8	23.4	76.6
	0.25	8.1	31.7	68.3
GMAW	-	10.7	81.4	18.6
SMAW	-	17.0	83.8	16.2

Table- 5.14: Grain size measured in HAZ adjacent to fusion line in various weld joints.

Process	Weld width (mm)	ϕ	Ω kJ/cm	Avg. Grain dia. $\pm$ S.D (μm)			ASTM No		
				A	B	Avg. of A & B	A	B	Avg.of A & B
P-GMAW	23	0.06	9.1	18± 4	17± 5	18± 7	8.5	9.0	9.0
	24	0.25	9.4	19± 3	18± 7	19± 5	8.5	8.5	8.5
	23.5	0.05	7.7	17± 3	18± 3	17± 6	9.0	9.0	9.0
	24	0.25	8.0	18± 3	17± 6	18± 6	9.0	9.0	9.0
GMAW	24	-	10.7	19± 3	19± 3	19± 3	8.5	8.5	8.5
SMAW	21	-	17.0	29± 6	27± 4	28± 5	7.5	7.5	7.5

S.D. is Standard deviation, A and B are either side of weld joint.
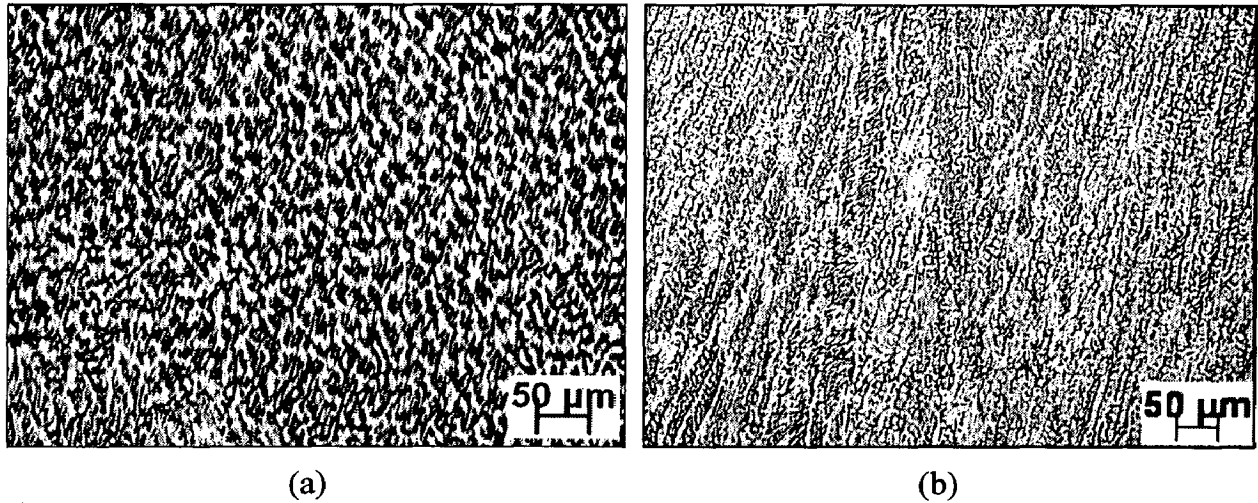
(a)

(b)

Fig. 5.38: At a given Ω of 9.2±0.35 kJ/cm typical microstructure of P-GMA weld deposits at different ϕ of (a) 0.06 and (b) 0.25.
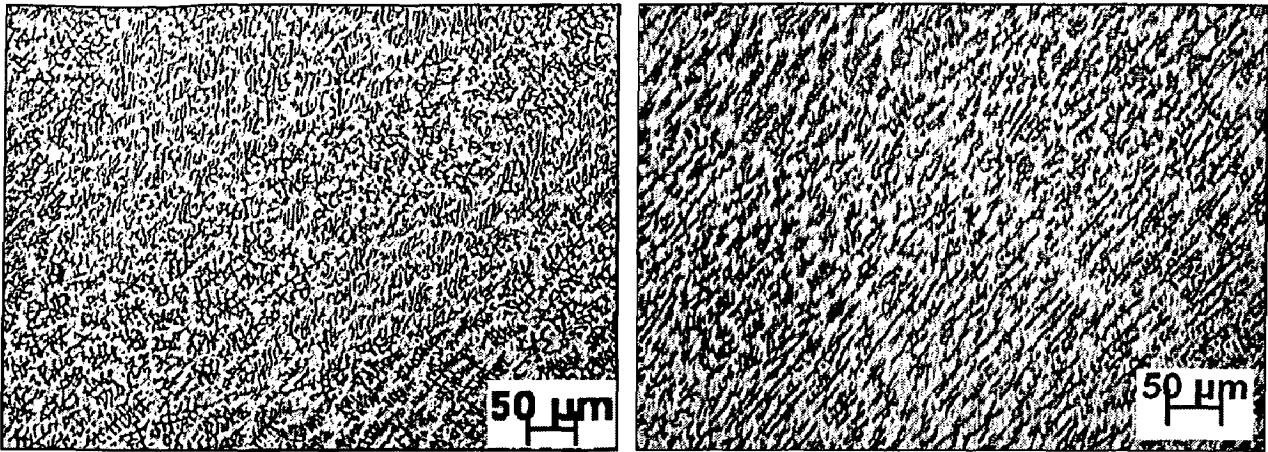
(a)   (b)

Fig. 5.39:   At a given Ω of 7.7 ± 0.5 kJ/cm typical microstructure of P-GMA weld deposits at different ϕ of (a) 0.05 and (b) 0.25.
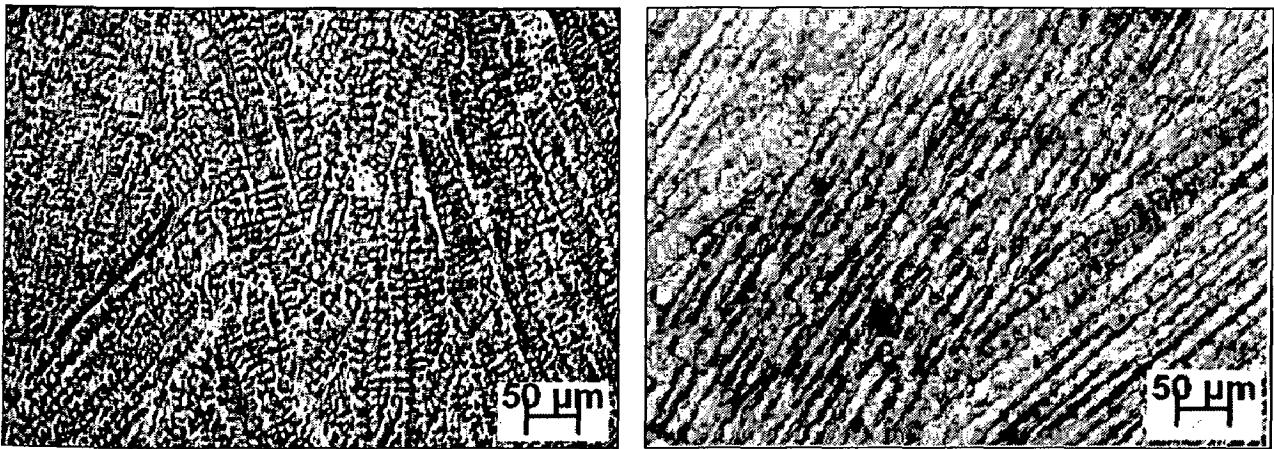
(a)   (b)

Fig. 5.40:   Typical microstructures observed in (a) GMA and (b) SMA weld deposits
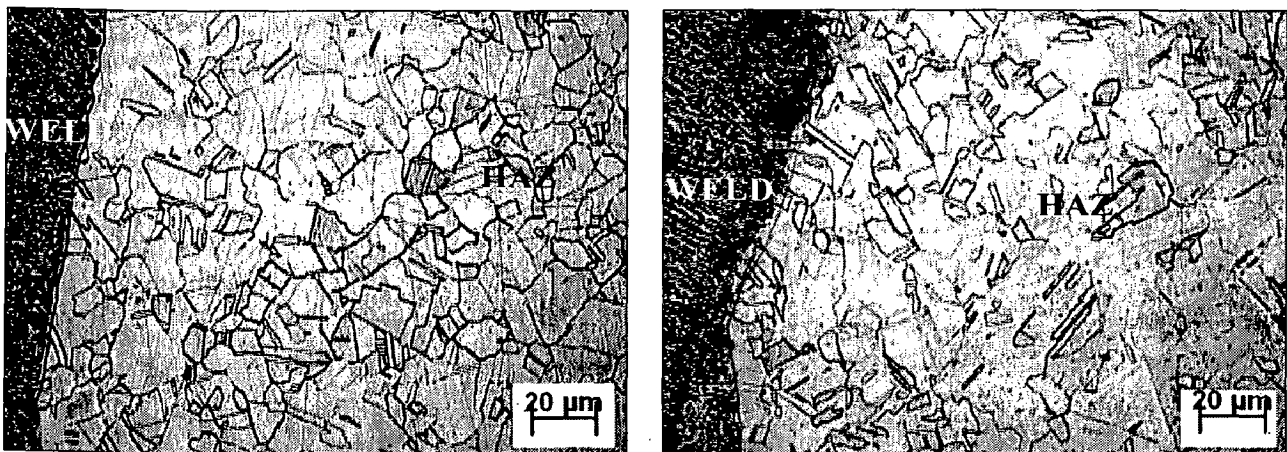
(a)   (b)

Fig. 5.41:   At a given Ω of 9.2 ± 0.35 kJ/cm typical microstructures of heat affected zone adjacent to fusion line of P-GMA weld joints at different ϕ of (a) 0.06 and (b) 0.25.

199

Fig. 5.42: At a given Ω of 7.7 ± 0.5 kJ/cm typical microstructure of heat affected zone adjacent to fusion line of P-GMA weld joints at different ϕ of (a) 0.05 and (b) 0.25.
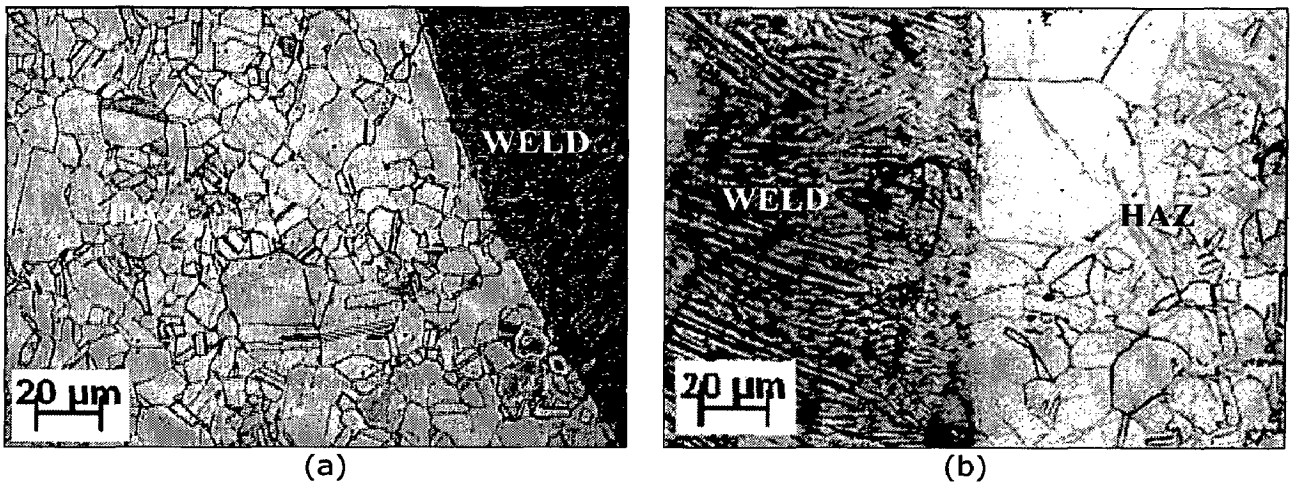
Fig. 5.43: Typical microstructures of heat affected zone adjacent to fusion line of (a) GMA and (b) SMA weld joints

5.3.4 Porosity and Inclusion Content

Depending upon shielding medium of gas or flux in GMAW and SMAW process respectively, the porosity and inclusion content primarily occurs due to atmospheric contamination and slag entrapment. Atmospheric contamination generally happens during GMAW and P-GMAW processes due to inadequate shielding of arc and solidifying weld

pool. Whereas, during SMAW process inclusions due to entrapment of slag occurs generally at intricate locations such as interpass region, where proper cleaning is difficult. The typical presence of inclusions in the matrix of SMA weld deposit has been shown in the micrograph presented in Fig. 5.44. The estimated inclusion and porosity content in the weld deposits of the P-GMA, GMA and SMA weld joints have been shown in Table-5.15. It has been primarily observed that P-GMA and GMA weld joints prepared under the comparatively cleaner environment of argon gas shielding are having 75-80% lower inclusion or porosity content in comparison to that of SMA weld joint. The increase in inclusion content of SMA welds may have primarily happened due to slag entrapment. However, in respect of the inclusion content of base metal, the inclusion or porosity content of the P-GMA and GMA welds has often been found marginally higher indicating the tampering of protection from atmospheric contamination upto certain extent. In P-GMA welds with the reduction in ϕ from 0.25 to 0.05, porosity content drops by almost 25% at both the Ω levels of 9.2 and 7.8kJ/cm. Whereas, at a given ϕ, the porosity content of the weld considerably reduces by almost 50% with the reduction in Ω from 9.2 to 7.8kJ/cm. With the decrease in ϕ, arc turbulence decreases due to enhancement of arc pressure [Ghosh et al 2008] and hence, reduces atmospheric contamination. On the other hand at a given ϕ, the reduction in Ω resulting from considerable decrease in I_m (Annexure-I) consequently decreases the arc length [Ghosh et al 2008] causing lowering of atmospheric contamination.

Table-5.15: Inclusion and porosity content of P-GMA, GMA and SMA weld joints

Process	Weld width (mm)	φ	Ω kJ/cm	Inclusions rating		Inclusion and porosity content, (Vol. %)
				Category	Severity level	
P-GMAW	23	0.06	9.1	D thin/D thick	2.0-5.0	0.43
	23	0.25	9.4	D thin/D thick	2.5-4.5	0.57
	23.5	0.05	7.7	D thin/D thick	3.0-4.5	0.18
	24	0.25	8.0	D thin/D thick	3.0-4.5	0.33
GMAW	24	-	10.7	B thin/B thick	1.0-2.5	0.75
SMAW	21	-	17.0	B thin/B thick	0.5-1.5	2.34
				D thin/D thick	2.5-4.0	
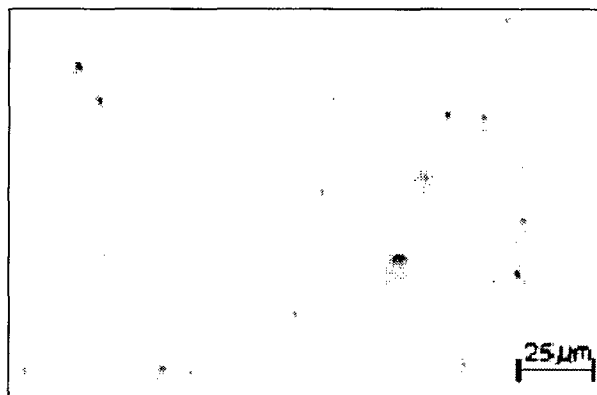
Fig. 5.44: Typical presence of inclusions observed in the matrix of conventional groove SMA weld deposit

5.3.5 Mechanical Properties

5.3.5.1 Tensile properties

The tensile properties of P-GMA, GMA and SMA weld joints of the pipes along their longitudinal (axial weld having joint at centre of the specimen) and circumferential (all weld metal) directions are shown in Table-5.16 and Table-5.17 respectively. The tables also show the corresponding dimensionless material constant (α) and strain hardening exponent (n) of the tensile properties estimated by using Romberg Osgood equation (eq.(5.1)). The fractographs of P-GMA axial welds prepared at a comparatively low Ω of 7.8 ± 0.35kJ/cm by

using ϕ of 0.05 and 0.25 have been shown in Fig. 5.45 (a) and (b) respectively. Similarly, the fractographs of GMA and SMA axial weld joints have been shown in Fig. 5.46 (a) and (b) respectively.

Tables-5.16 and 5.17 primarily reveal that the weld deposit (circumferential direction) is always having comparatively higher yield strength and elongation with lower ultimate tensile strength than that of the longitudinal weld joints fracturing from the weld. Whereas in comparison to base metal (Table-5.3), the ratio of yield strength (σ_y) to ultimate tensile strength (σ_u) of weld joints significantly increases from 0.5 to 0.76 with a considerable sacrifice in elongation, resulting in relatively higher value of strain hardening exponent (n). The tables further interestingly depicts that, irrespective of variation in ϕ and Ω, P-GMA welds have significantly higher tensile properties than those of GMA and SMA weld joints in both longitudinal and circumferential directions. This may have happened primarily due to relatively more wide spread ductile fracture behaviour of P-GMA weld relatively with fine dimples (Figs. 5.45 and 5.46) along with considerably lower inclusion and porosity content (Table-5.15) than those observed in GMA and SMA weld. It is also observed that the poor tensile properties of SMA weld primarily result from the presence of generally round impurity particles of different sizes (Fig. 5.46(b)) in the matrix which give rise to formation of large voids during fracture. This may lead one to believe that void nucleation occurred by debonding at impurity particle/matrix interface, controlled by the plastic flow of the austenite matrix. However, in P-GMA welds the tensile properties marginally improve with the lowering of ϕ and Ω (Table-5.16 and 5.17) in both the longitudinal and circumferential directions due to almost similar chemical composition of weld deposit (Table-5.12) with the variation in pulse parameters.

Table-5.16: Tensile properties in conventional V-groove P-GMA, GMA and SMA weld joints in longitudinal direction.

Process	Weld width (mm)	φ	Ω kJ/cm	UTS (MPa)	YS (MPa)	YS/UTS Ratio	Elongation (%)	n		a		Failure region
P-GMAW	23	0.06	9.1	646	404		42.1	6.89		22.7.7		Weld
				652 (651)	380 (367)	0.56	44.2 (44.6)	6.72	6.77	20.12	20.1	
				656	369		47.1	6.64		18.09		
	23	0.25	9.4	636	370		38.1	6.89		22.7.7		Weld
				646 (641)	355 (362)	0.56	37.1 (37.6)	6.64	6.77	18.09	20.12	
				640	360		37.6	6.71		20.15		
	23.5	0.05	7.7	656	401		41.8	6.79		21.59		Weld
				670 (654)	395 (395)	0.60	42.4 (42.5)	6.65	6.57	21.80	21.89	
				652	390		43.2	6.35		22.18		
	24	0.25	8.0	632	394		40.9	6.53		23.97		Weld
				635 (632)	391 (389)	0.62	41.3 (41.4)	6.34	6.35	23.80	23.79	
				632	384		41.8	6.16		23.61		
GMAW	24	-	10.7	613	383		33.2	6.32		21.94		Weld
				620 (619)	380 (379)	0.61	34.3 (34.2)	6.31	6.30	21.98	21.99	
				625	374		35.1	6.28		22.05		
SMAW	21	-	17.0	565	335		16.8	5.00		10.73		Weld
				545 (555)	360 (353)	0.64	15.1 (16.0)	6.49	5.75	16.73	16.03	
				560	345		16.1	5.78		16.05		

Table-5.17: Tensile properties in conventional V-groove P-GMA, GMA and SMA weld joints in circumferential direction.

Process	Weld width (mm)	φ	Ω kJ/cm	UTS (MPa)	YS (MPa)	YS/UTS Ratio	Elongation (%)	n		a	
P-GMAW	23	0.06	9.1	615	447		40	7.14		32.68	
				605 (608)	443 (438)	0.72	43.4 (42.4)	7.09	6.99	35.50	36.49
				604	424		43.8	6.74		41.29	
	23	0.25	9.4	579	418		43.3	7.25		32.84	
				578 (582)	425 (424)	0.73	43.5 (44.0)	7.10	7.7.7	37.00	38.1
				589	429		45.2	6.98		44.46	
	23.5	0.05	7.7	612	435		44.8	6.93		33.45	
				619 (617)	442 (442)	0.70	43.9 (44.0)	6.74	6.79	39.18	39.27
				620	449		43.3	6.70		45.18	
	24	0.25	8.0	614	443		41.0	7.14		31.68	
				606 (608)	447 (438)	0.72	42.8 (42.4)	6.98	6.99	35.78	35.91
				604	424		43.4	6.84		40.29	
GMAW	24	-	10.7	569	418		47.8	7.19		37.23	
				574 (575)	428 (426)	0.74	41.5 (43.4)	6.98	6.99	30.83	30.82
				582	432		40.9	6.80		24.40	
SMAW	21	-	17.0	599	370		33.0	6.94		37.06	
				568 (569)	365 (365)	0.64	37.9 (37.9)	7.08	7.07	34.28	34.28
				540	360		42.8	7.19		31.50	

Note: - n & a are Strain hardening exponent & Dimensionless material constant as given in Ramberg Osgood expression (Eq. xxi).
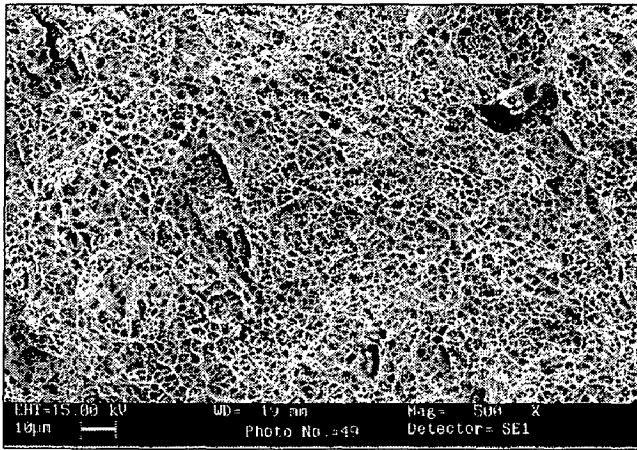
(a)   (b)
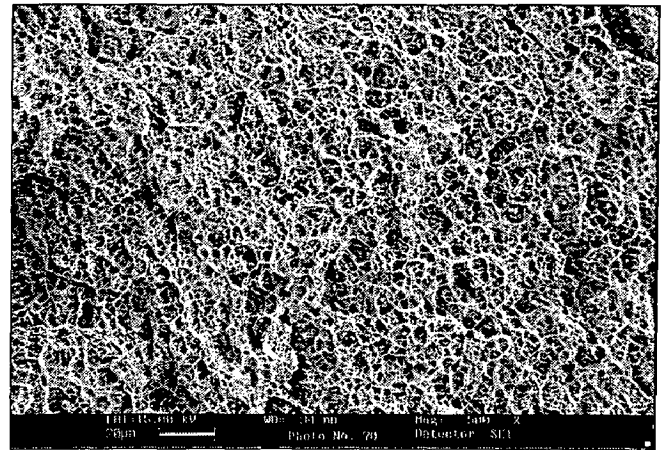
Fig. 5.45:   At a given Ω of 7.7$\pm$0.5 kJ/cm, typical SEM photographs of fractured surface in axial tensile specimens observed in conventional groove P-GMA welds at different ϕ of (a) 0.05 and (b) 0.25.
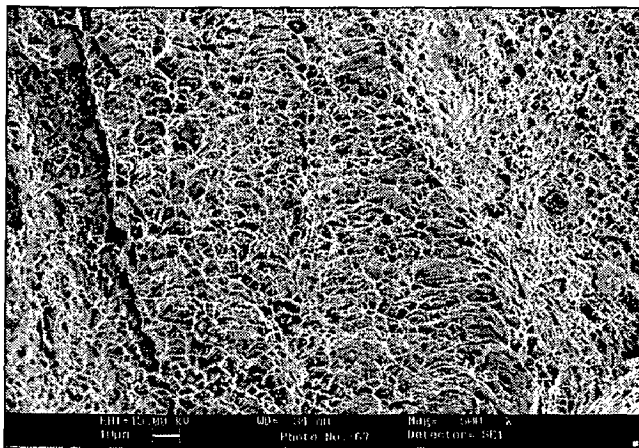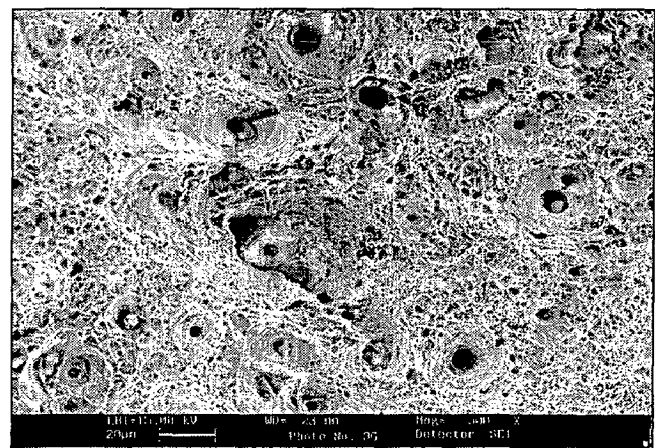
(a)   (b)

Fig. 5.46:   Typical SEM photographs of fractured surface in axial tensile specimens observed in conventional groove welds prepared by using (a) GMAW and (b) SMAW processes.

205

5.3.5.2 *Charpy impact toughness*

Impact properties do not figure in the conventional design criteria for ductile materials, such as the austenitic stainless steels. However, acceptance tests include specifications by keeping minimum value of 120 J for C_v-impact toughness in the as-received state for base metal and 70 J in the as-welded state for weld metal [Tavassoli 1995] of austenitic stainless steel at ambient temperature. Charpy impact energy absorbed at room temperature (RT) in P-GMA, GMA and SMA weld joints with notch orientation in circumferential direction (Fig. 4.11) has been given in Table-5.18. The table primarily depicts that all the weld joints have passed the acceptance criterion as mentioned above. It is further noted that P-GMA and GMA welds are having considerably higher C_v-impact toughness and lateral expansion in comparison to those observed in SMA weld joint. However in comparison to base metal (Table-5.4) both P-GMA and GMA welds show almost equivalent C_v-impact toughness.

The weld metal impact toughness primarily depends upon chemical composition, porosity content and refinement in microstructure [Dieter 1988]. The chemical compositions of filler metal used for P-GMA and GMA welds have significantly higher Mn/C ratio along with considerable nickel content in comparison to that of SMA weld. Also, both P-GMA and GMA welds have significantly lower porosity content (Table-5.15) than that of SMA weld. Moreover, P-GMA welds are having considerably refined dendritic microstructure (Figs. 5.38 and 5.39) especially with the lowering of ϕ and Ω in comparison to that of the GMA and SMA welds (Fig. 5.40). These aspects may have been primarily responsible for comparatively higher impact properties in P-GMA welds than those observed in GMA and SMA welds.

Table-5.18: Energy absorbed in Charpy impact toughness test at RT in conventional groove P-GMA, GMA and SMA weld joints.

Process	Weld width (mm)	φ	Ω kJ/cm	Charpy impact properties			
				Energy absorbed, (J)		Lateral Expansion, (mm)	
P-GMAW	23	0.06	9.1	133	128	2.66	2.59
				126		2.57	
				125		2.54	
	23	0.25	9.4	135	132	2.68	2.63
				132		2.62	
				130		2.60	
	23.5	0.05	7.7	137	133	2.70	2.63
				132		2.61	
				130		2.59	
	24	0.25	8.0	138	135	2.74	2.69
				134		2.65	
				134		2.67	
GMAW	24	-	10.7	127	120	2.54	2.47
				7.78		2.45	
				7.75		2.42	
SMAW	21	-	17.0	103	98	2.01	1.86
				97		1.85	
				95		1.72	

5.3.5.3 Hardness

The influence of variation in Ω and ϕ on hardness across P-GMA welds has been shown in Fig. 5.47. Similarly, the hardness distribution across the GMA and SMA welds is shown in Fig. 5.48. The hardness of both the weld deposit and HAZ of P-GMA and GMA weld joints is significantly higher than the hardness of weld and HAZ of SMA weld joint. The relatively higher hardness of P-GMA and GMA weld may have primarily resulted from their comparatively higher chromium and lower nickel content (Table-5.12). However, in case of GMA weld deposit the scatter in hardness distribution (Fig. 5.48) is relatively higher than that observed for SMA weld deposit. This may attributed primarily be to the presence of comparatively larger number of different kinds of zones of microstructure having dendrite and refined dendritic region (Table-5.13) in GMA than in SMA weld deposit. The variation

207

in microstructure may have affected the hardness distribution in weld deposit due to its influence on the size and distribution of carbide precipitation [David et.al. 1987] in the matrix. But, P-GMA weld joints prepared at a relatively lower Ω of 7.7 kJ/cm show relatively low scatter in hardness distribution in weld deposit in comparison to that in GMA weld, primarily due to large scale refinement of dendritic microstructure in the former type of weld joints (Table-5.13).
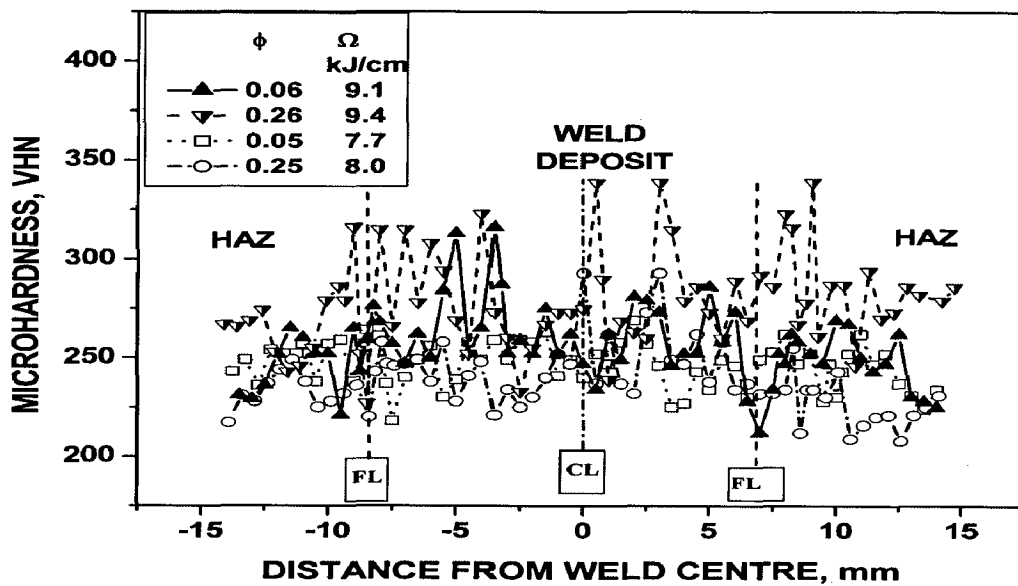
Fig. 5.47:   Variation in hardness observed across the P-GMA welds at two different levels of ϕ and Ω.
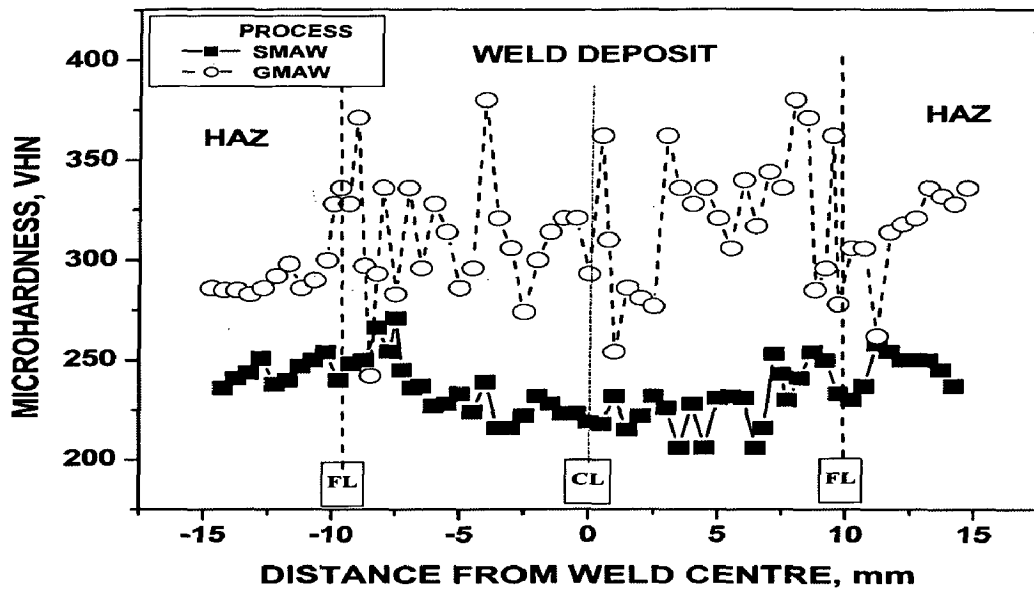
Fig. 5.48: Variation in hardness observed across the weld prepared by using GMAW and SMAW processes.

5.3.6 Residual stresses

The longitudinal and transverse residual stresses present at different locations on the top of the weld, as compared to the centre and fusion lines of the P-GMA, GMA and SMA weld joints are shown in Fig. 5.49 (a) and (b) respectively. Similarly, longitudinal and transverse residual stresses in different locations at the root of the weld as compared to that at the centre and fusion lines of the said weld joints are shown in Fig. 5.50 (a) and (b) respectively. The figures show that at the top and root of weld, longitudinal residual stress reduces by 30-40% and 20-30% respectively for P-GMA and GMA welds in comparison to that observed in case of SMA weld. The transverse residual stress also follows a similar trend but having a magnitude comparatively lower than the longitudinal residual stress of the weld joint as it is commonly observed [Murugan et al 2001, Webster et al 2002, Radaj 1992, Brickstad and Josefson 1998] in earlier works.

In comparison to SMAW the use of GMAW and especially P-GMAW process is advantageous for the reduction of residual stresses in ASS pipe joint primarily due to its

relatively less severity of thermal effect (Table-5.11). The magnitude of residual stress distribution lowers further marginally with the variation in pulse parameters reducing the factor ϕ from 0.25 to 0.05 at a comparatively lower Ω of 7.8kJ/cm, indicating thereby a further control on reduction in severity of weld thermal cycle. Except that observed in Fig. 5.49(a), the longitudinal residual stresses at the top and the root of the GMA and P-GMA welds (Figs. 5.49 and 5.50) are considerably lower in general than the corresponding residual stresses in SMA weld. At the root of different kinds of welds investigated (Fig. 5.50) both the longitudinal and transverse residual stresses reduce from its maximum at weld centre to a minimum level beyond the fusion line. However, the distribution of residual stresses is different at the top of the welds (Fig. 5.49). Here, the distribution of longitudinal residual stresses in P-GMA weld behaves in a fashion similar to that of weld root (Fig. 5.50). But, the distribution of longitudinal residual stresses in GMA and SMA welds and the transverse residual stresses in P-GMA, GMA and SMA welds behave in different manner showing maximum at certain locations in between the weld centre and fusion line of the joint. However, the maximum intensity of residual stress depends upon welding process as it relatively lower in case of P-GMAW and GMAW than SMAW. The dual peak of residual stresses with a depression of stress at weld centre has been observed at the top of the weld, but not at the root, possibly due to its narrowness causing difficulties in multiple spot analyses within it. The presence of dual peak of residual stresses distributed in either side of weld centre line in weld joint of austenitic stainless steel arising out of interactions of shrinkage and quenching stresses has also been reported by earlier workers [Murugan et al 2001, Webster et al 2002, Fricke et al 2001, Deng et al 2008]. However, in almost all the cases investigated, the residual stresses at the weld centre are relatively higher at the root than at the top of the weld.
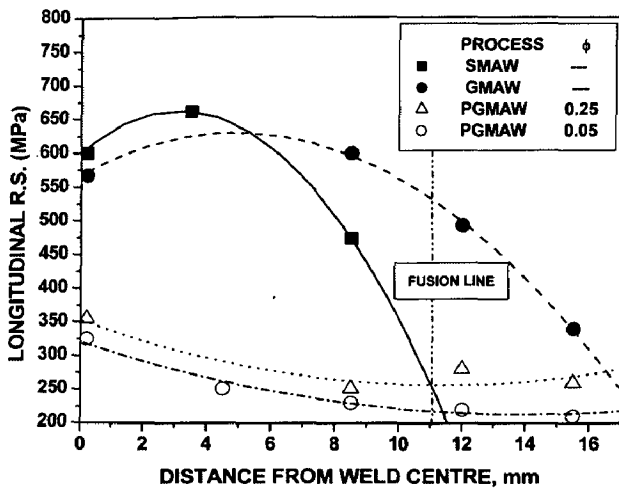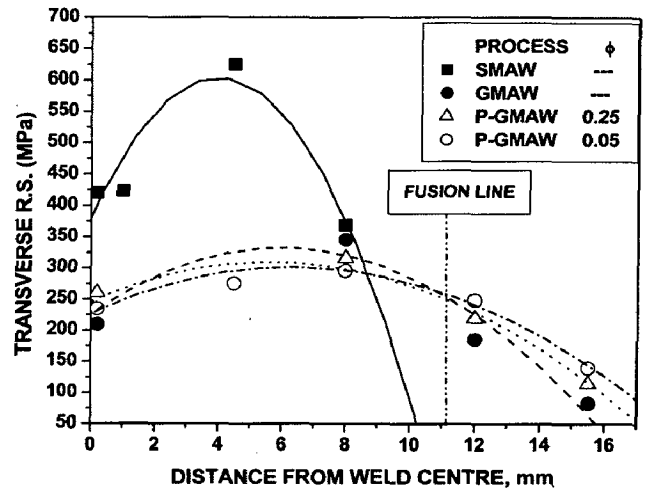
Fig. 5.49: Distribution of (a) longitudinal and (b) transverse residual stresses at the top in the P-GMA, GMA and SMA weld joints.
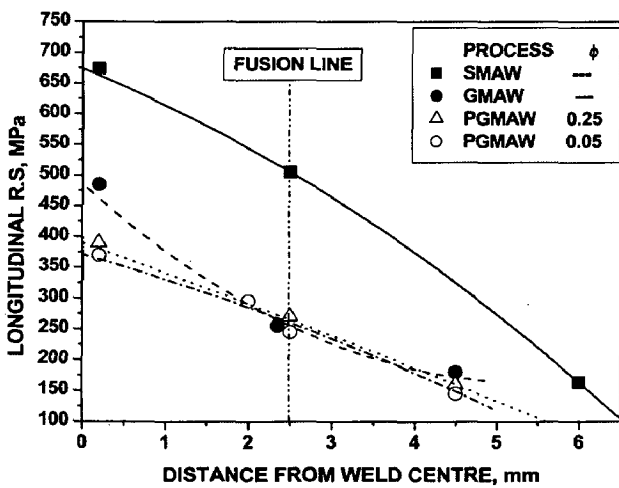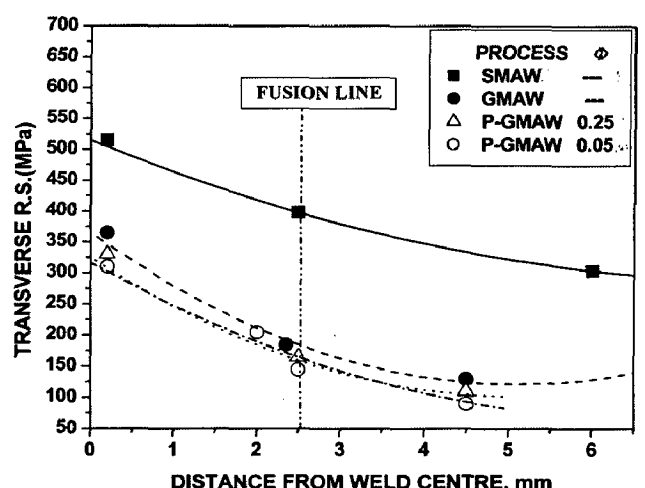
Fig. 5.50 : Distribution of (a) longitudinal and (b) transverse residual stresses at the root in the P-GMA, GMA and SMA weld joints.

211

5.3.7 Fracture Mechanics

Weld joint is a mechanically heterogeneous body composed of base metal, weld metal and HAZ. Weld metal generally forms the weakest zone having least strength and toughness due to presence of micro-crack, porosity, non-metallic inclusion and undesirable micro structural transformations. Under these circumstances it always becomes necessary to examine critically the response of the matrix to propagation of microcrack leading to complete fracture under a given stress. The fracture mechanics concepts, such as fracture toughness, crack growth rate etc., thus, provide a quantitative knowledge for evaluation of structural safety and reliability in terms of applied stress on the flaws present in the matrix.

5.3.7.1 Fracture toughness

The initiation fracture toughness properties of the appreciably ductile P-GMA, GMA and SMA weld deposits in L-C direction are given in Table-5.19. The J-R curves of the P-GMA weld deposits in L-C direction have been compared with the same of the GMA and SMA weld deposits as shown in Fig. 5.51. The figure shows that the P-GMA welds are having significantly higher J_Q value (Table-5.19) in comparison to those observed in GMA and SMA weld joints as marked by its comparatively stiffer progress of J-R curve. The corresponding maximum load (P_{max}) and physical crack extension (Δa) in P-GMA welds (Table-5.19) are also considerably greater than those observed in GMA and SMA weld joints. Accordingly, P-GMA welds prepared at any parameters show considerably superior initiation fracture toughness (J_Q) to that observed in case of GMA and SMA weld. The J_Q observed in GMA and SMA welds are valid J_{1C} value as they satisfy the plain strain criterion of thickness $B > 25 \ J_Q/\sigma_y$ according to the ASTM E813-89 standard, where σ_y is the effective yield strength. Whereas, the valid initiation fracture toughness (J_{1C}) of P-GMA welds cannot be obtained by elastic-plastic fracture mechanics concepts as they do not satisfy the plain strain

criterion due to their significant ductility. However, all the weld joints exhibit a quasi initiation fracture toughness (J_Q) value less than about 50% of that of base metal (Table- 5.5) except in case of the P-GMA weld prepared at a ϕ and Ω of 0.05 and 7.8 kJ/cm respectively. Such an influence of welding processes on J-R curve primarily indicates the variation in total energy absorbed during the fracture process. The total energy absorbed primarily depends upon contribution from the crack deflection and propagation energy required for local crack extension [Dieter 1988]. In P-GMA welds due to significantly lower porosity content (Table-5.15) and refined dendritic microstructure (Fig.5.38 and 5.39) than that observed in GMA and SMA welds, the local crack deflection and the propagation energy required for initiation of fracture due to homogeneity in the matrix may have considerably increased. Whereas, unlike P-GMA weld, a comparatively closely spaced inclusions in SMA weld (Fig.5.46 (b)) may have produced a weak bond with the interface and consequently magnified the heterogeneity in local stresses [Anderson 2005]. Thus, the local crack extension may have occurred at considerably lower propagation energy in SMA weld and hence it shows significantly lower fracture toughness (J_{1C}) [Tavassoli 2005].

It has been further observed that in P-GMA weld joints the J_Q value significantly increases (Table- 5.19) with the decrease of ϕ from about 0.25 to 0.05 at a given Ω lying in relatively high and low ranges of about 9 and 8 kJ/cm respectively. It is further noted that at a given ϕ of about 0.05 or 0.25, a decrease of Ω from the order of about 9 to 8 kJ/cm also enhances J_Q significantly. Such a variation may have been primarily achieved through reduced porosity content (Table-5.15) and refinement of co-axial dendrite microstructure as stated above (Fig. 5.38 and 5.39).

Table-5.19: Fracture toughness properties of conventional groove P-GMA, GMA and SMA weld joints.

Process	ϕ	Ω (kJ/cm)	P_{max} (kN)	Δa (mm)		J_Q (kJ/m^2)		$J_Q = J_{1c}$ (kJ/m^2)
P-GMAW	0.06	9.1	34.1 35.3 36.4	0.51 0.41	0.46	679 723	701	No
	0.25	9.4	35.0 34.0 33.1	0.43 0.66	0.55	588 532	560	No
	0.05	7.7	36.3 37.8 39.2	0.95 0.90	0.93	1010 1060	1035	No
	0.25	8.0	36.8 35.3 33.8	0.96 0.83	0.90	930 667	799	No
GMAW	-	10.7	33.7 30.7 35.3	0.68 0.58	0.76	524 552	538	Yes
SMAW	-	17.0	30.3 28.9 27.4	0.24 0.20	0.22	320 280	300	Yes

Coefficient of corelationship

Fig. 5.51: Typical J-R curves observed in weld deposits of P-GMA, GMA and SMA weld joints in L-C direction.

5.3.7.2 Fatigue crack growth rate

The resistance to crack propagation under any kind of loading basically determines the life of a component. Thus, it is interesting to know the fatigue crack growth rate (FCGR) characteristics of weld under dynamic loading. The FCGR properties of P-GMA welds studied in L-C direction have been compared with the same for GMA and SMA welds as given in Table-5.20. The typical plots of stable FCGR ($\log(da/dN)$ vs. $\log\Delta K$) of the P-GMA as well as the GMA and SMA welds at a stress ratio of R=0.1 and 0.5 are shown in Fig. 5.52 (a) and (b) respectively.

Table-5.20: FCGR characteristics of the P-GMA, GMA and SMA welds.

Process	ϕ	Ω (kJ/cm)	Stress Ratio (R)	m		C (m/cycle)		R*		Estimated ΔK_{TH} (MPa√m)
P-GMAW	0.05	7.7	0.1	4.12	4.24	2.78×10^{-14}	2.82×10^{-14}	0.98	0.985	6.9
				4.36		2.86×10^{-14}		0.99		
			0.5	3.96	3.97	2.78×10^{-13}	2.84×10^{-13}	0.97	0.96	4.4
				3.98		2.90×10^{-13}		0.95		
	0.25	8.0	0.1	3.91	3.95	8.41×10^{-14}	8.47×10^{-14}	0.97	0.965	6.0
				4.01		8.53×10^{-14}		0.96		
			0.5	3.95	3.93	2.92×10^{-13}	2.89×10^{-13}	0.99	0.99	4.4
				3.91		2.86×10^{-13}		0.99		
GMAW	-	10.7	0.1	3.87	3.80	1.43×10^{-13}	1.39×10^{-13}	0.96	0.94	5.7
				3.73		1.35×10^{-13}		0.92		
			0.5	3.10	3.08	4.76×10^{-12}	4.67×10^{-12}	0.93	0.96	2.7
				3.06		4.58×10^{-12}		0.99		
SMAW	-	17.0	0.1	3.62	3.56	3.33×10^{-13}	3.23×10^{-13}	0.94	0.93	5.0
				3.50		3.13×10^{-13}		0.92		
			0.5	3.05	3.00	5.12×10^{-12}	5.26×10^{-12}	0.95	0.93	2.6
				2.95		5.40×10^{-12}		0.91		

R* is Coefficient of co relationship
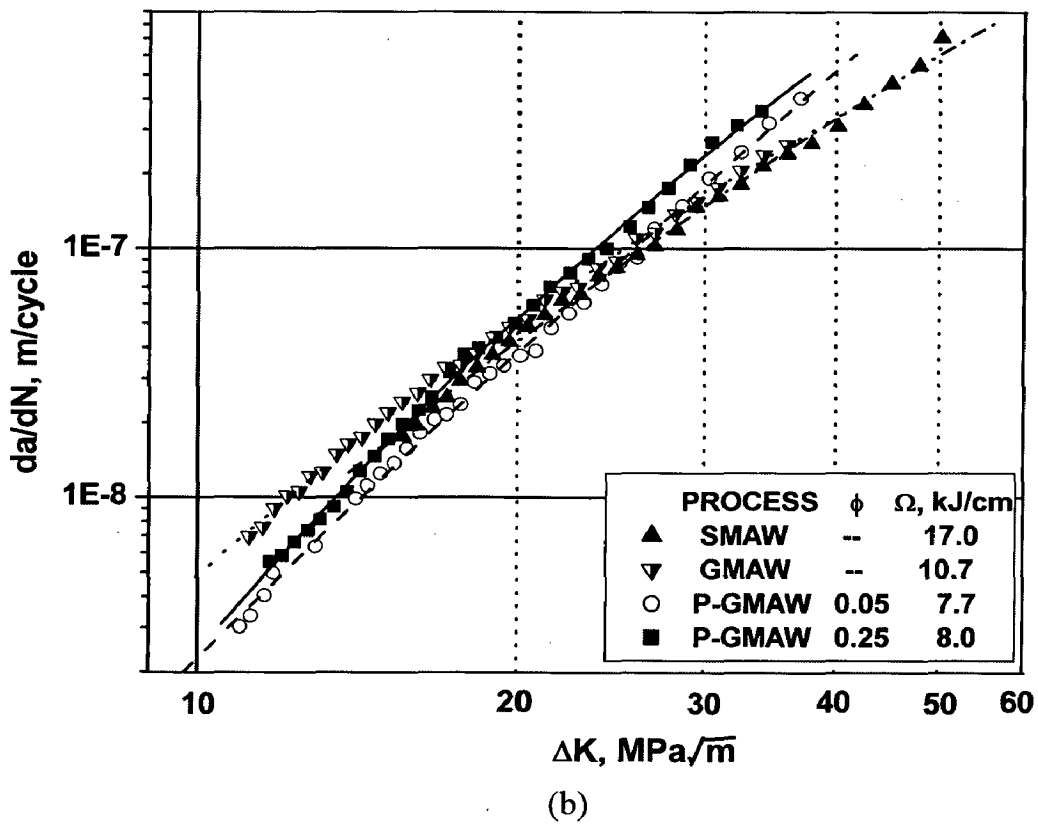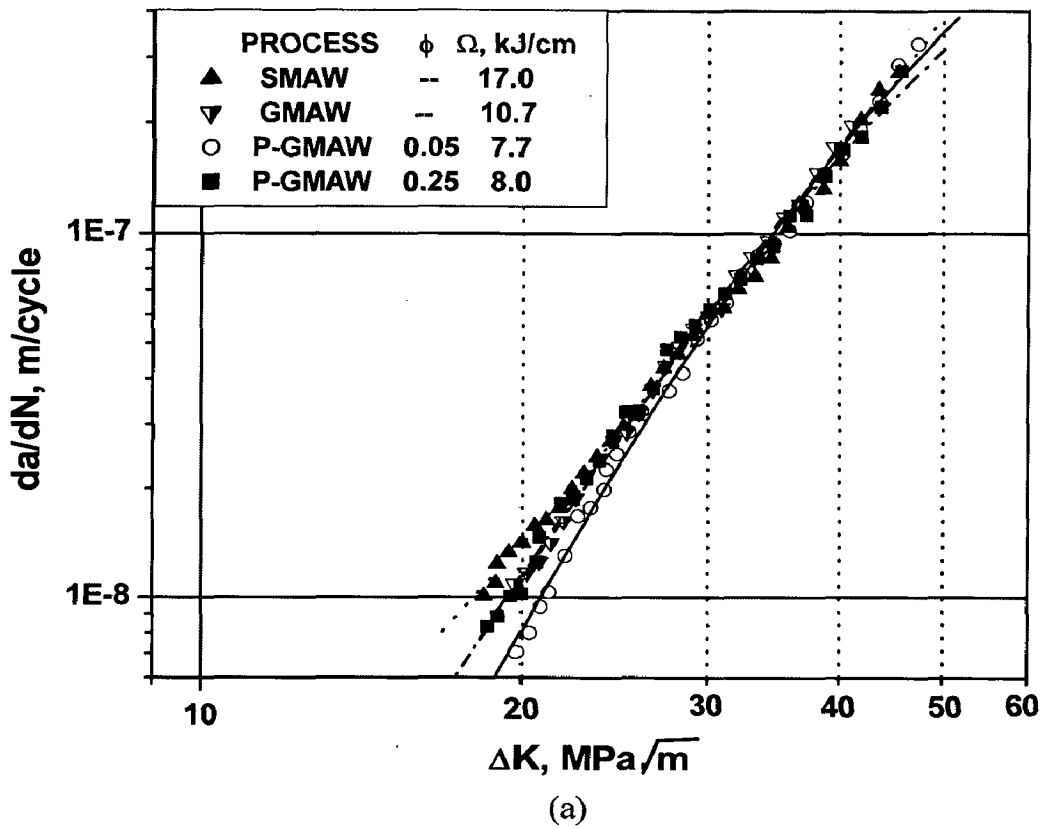
Fig. 5.52: FCGR curves observed in conventional V-groove P-GMA, GMA and SMA weld deposit at a stress ratio(R) of (a) 0.1 and (b) 0.5.

The table and Fig. 5.52 (a) and (b) demonstrates that at both the stress ratio(R) of 0.1 and 0.5, the fatigue crack growth rate properties of P-GMA welds are superior to those observed in GMA and SMA welds in the all-important early part of life as reflected by its relatively higher value of ΔK_{TH}. However, at a comparatively higher ΔK at around 40 $MPa\sqrt{m}$, crack growth rate observed at both the stress ratio of 0.1 and 0.5 shows a different trend. At a comparatively lower stress ratio of 0.1 (Fig. 5.52(a)), crack growth rate appears to be almost constant in all the welds. Whereas, at a stress ratio of 0.5, SMA weld shows better FCGR properties than those observed for P-GMA and GMA welds as evident from considerably lower crack growth rate in SMA weld. In P-GMA welds at a given Ω, FCGR properties improve with lowering of ϕ from 0.25 to 0.05.

Fatigue crack growth rate properties of weld metal largely depend upon residual stress distribution, microstructural refinement, inclusion and porosity content. Fatigue cracks propagate under effectively higher stress ratios than applied due to additive nature of tensile residual stresses in the weld. On the contrary, crack closure occurs if compressive residual stresses exist in the weld [Niemi and Koshimaki 1997]. Whereas, energy required for crack growth considerably increase if the matrix provides resistance to the path of fracture through refined microstructure with negligible inclusion and porosity content [Ghosh et al 1990]. Hence P-GMA welds having comparatively higher ΔK_{TH} value than GMA and SMA welds, are superior in respect to all the aspects as stated above. However, superior FCGR properties of SMA weld at a comparatively higher ΔK at around 40 $MPa\sqrt{m}$ than other welds may have occurred due to fully austenitic structure as marked by its negligible δ-ferrite content (Table-5.12). It has been observed in the literature that δ-ferrite [S'anchez-Cabrera 2007, Rho et al 2000] generally shows lower resistance to fatigue crack growth.

217

5.3.8 Inter Granular Corrosion

Chromium rich carbides ($M_{23}C_6$), which contains two to four times higher amount of chromium than that in the base material, precipitate at the grain boundaries of austenitic stainless steel [Padilha and Rios 2002]. These high-energy grain boundaries are more chemically reactive than the grains. Depending upon severity of weld thermal cycle, carbon rapidly diffuses to the finely precipitated chromium carbide-matrix interface and promotes growth of carbide there but chromium diffuses much more slowly being drawn from the bulk of the material around the grain boundary. This process may lead to depletion of chromium content markedly below the required limit of approximately 11.5% to provide resistance to corrosion along the grain boundaries. Under such condition the ASS is often referred to as being sensitised. These chromium deficient regions then corrode because of local galvanic action, and the grains literally loosen out of the matrix [Folkhard 1984, Covert and Tuthill 2000, Padilha and Rios, 2002, Shankar et.al 2003b].

Nitrogen added ASS are generally less susceptible to intergranular corrosion (IGC) attack associated with grain boundary precipitation of chromium carbide. It primarily happens due to lowering of chromium diffusivity in the matrix in presence of nitrogen and thus retards of nucleation and growth of carbides improving the passivity [Covert and Tuthill 2000, Hertzman 2001, Woo and Kikuchi 2002, Shankar et al 2003a]. During welding, this phenomenon is largely dictated by the weld thermal cycle depending upon welding process, procedure and parameters. The influence of P-GMAW process at a given Ω of 7.8kJ/cm on the FE-SEM microstructures of HAZ adjacent to fusion line as revealed through rapid oxalic acid etch test at two different ϕ of 0.05 and 0.25 are as shown in Fig. 5.53 (a) and (b) respectively. Similarly, influence of GMAW and SMAW processes at a given Ω of 10.7 and

17.1 kJ/cm on microstructures of HAZ adjacent to fusion line after rapid oxalic etch test are

shown in Fig. 5.54 (a) and (b) respectively.
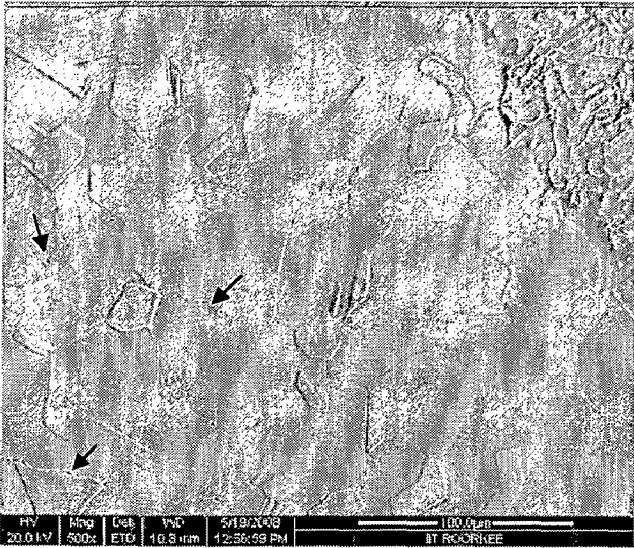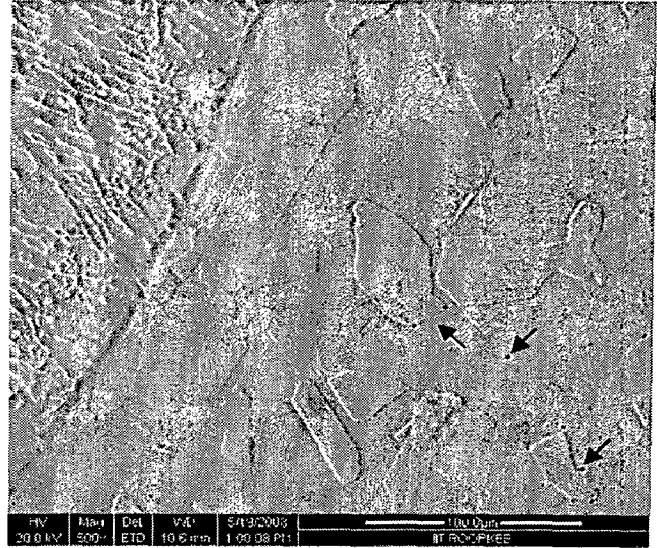
(a)   (b)

Fig. 5.53: At a given Ω of 7.8 $\pm$ 0.5kJ/cm, typical microstructures of HAZ adjacent to fusion line observed after rapid oxalic acid test in P-GMA weld joints at different ϕ of (a) 0.05 and (b) 0.25.
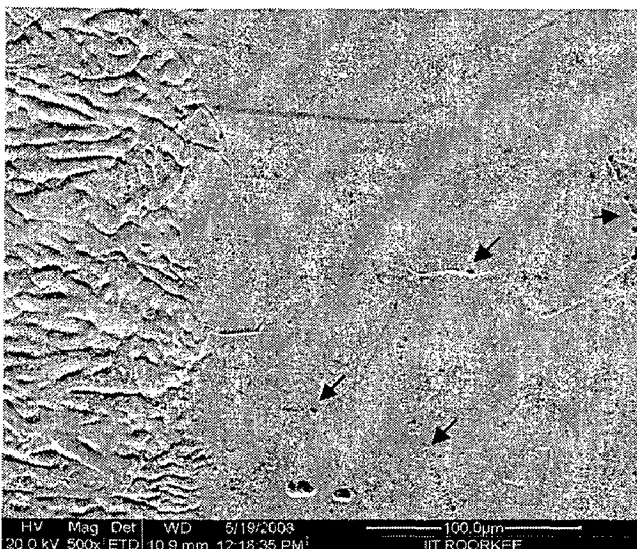
(a)   (b)
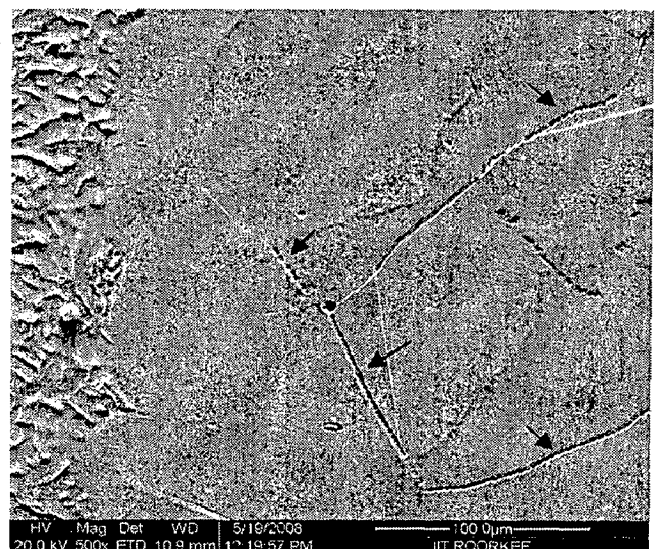
Fig. 5.54: At a given Ω of 17.1 and 10.7kJ/cm, typical microstructures of HAZ adjacent to fusion line observed after rapid oxalic acid test in (a) GMA and (b) SMA weld deposits respectively.

Figs. 5.53 and 5.54 reveal that carbide precipitation in HAZ always occurs during welding but its extent varies in joints made using P-GMA, GMA and SMA welding processes. The influence of welding on carbide precipitation is considerably lower in P-GMA welds, when compared to those observed in case of GMA and SMA weld joints. Carbide precipitation in HAZ primarily occurs at certain location away from the fusion line [Herbsleb 1980, Krishnan and Rao 1991, Nishimoto et.al 1995] depending upon its temperature in the sensitisation temperature range (450^0C-850^0C) prevailing for a required duration (section-2.2.1.1) for a given weld pass. In case of welding of the 25 mm thick wall pipe by multi-layered deposition, wherein almost two to four parallel passes are deposited (Annexure-I) adjacent to both the groove wall, such a sensitised region can be extended upto a region close to the fusion line depending upon distribution of isotherm of the weld passes. This phenomenon of sensitisation may become comparatively more prominent during larger number of weld passes and thus, it justifies the sensitized region observed near fusion line in all the weld joints of comparatively wider conventional V-groove design (Fig. 5.53 and 5.54).

Sensitisation behaviour in HAZ of all the weld joints has been further studied by analysing variation in chromium concentration in the matrix across the prominent ditches in the revealed microstructure. It has been interestingly observed that prominent density of ditches occurs approximately at a distance of 1mm away from the fusion line in all the weld joints shown in Fig. 5.55 and 5.56 respectively. However, the density and size of ditches vary with the process used. P-GMA welds show considerable reduction in density and size of ditches (Figs. 5.55 and 5.56) across the matrix compared to that in GMA and SMA welds. In P-GMA welds, at a given Ω, density of ditches (Fig. 5.55 (a) and (b)) further reduces with the lowering of ϕ. But in all the cases, variation in chromium concentration across the ditches measured at different locations marked as A-D in the figs mentioned above shows almost similar trend of chromium distribution as shown in Fig. 5.57. The figure shows considerably lower concentration of chromium adjacent to thick corroded region of ditch boundary and also at few locations near the boundary. Excessively low concentration of chromium with respect to that necessary (11.5wt.%) for corrosion resistance of ASS [Folkhard 1984] indicates that all the weld joints are prone to sensitisation.
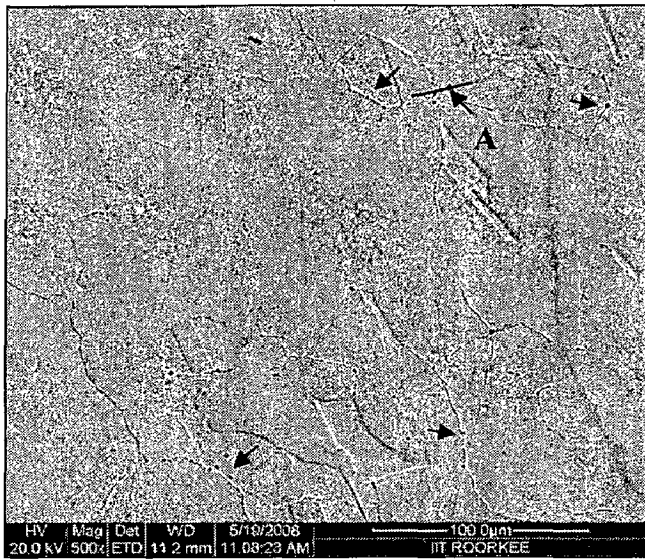
(a) (b)
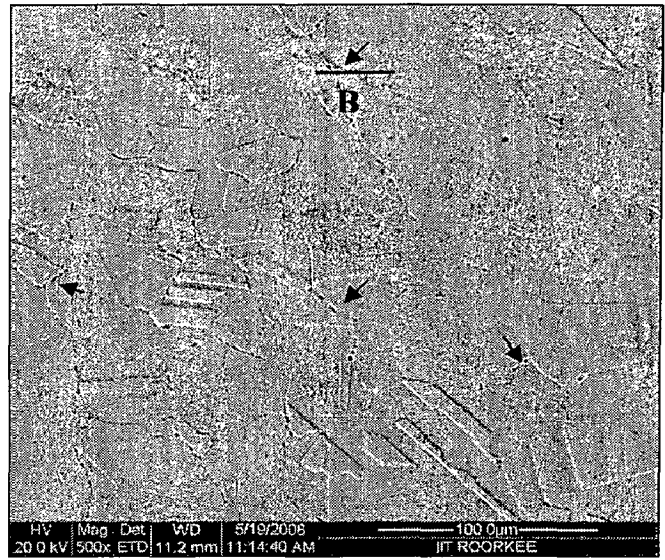
Fig. 5.55: At a given Ω of 7.8 ± 0.5kJ/cm, typical microstructures of HAZ observed approximately 1mm away from the fusion line after rapid oxalic acid test in P-GMA weld joints at different φ of (a) 0.05 and (b) 0.25.
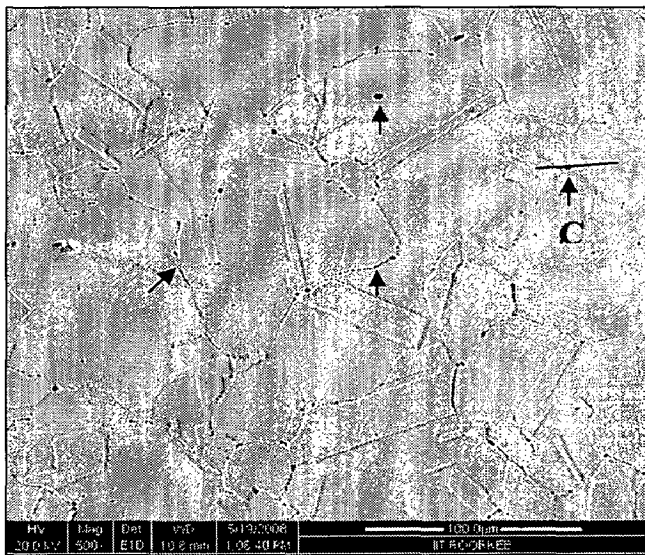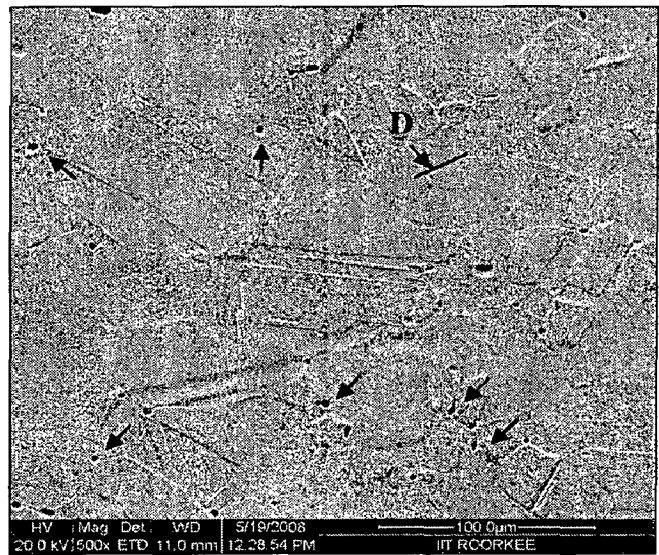
(a) (b)

Fig. 5.56: Typical microstructures of HAZ observed approximately 1mm away from the fusion line after rapid oxalic acid test in (a) GMA and (b) SMA weld deposits.
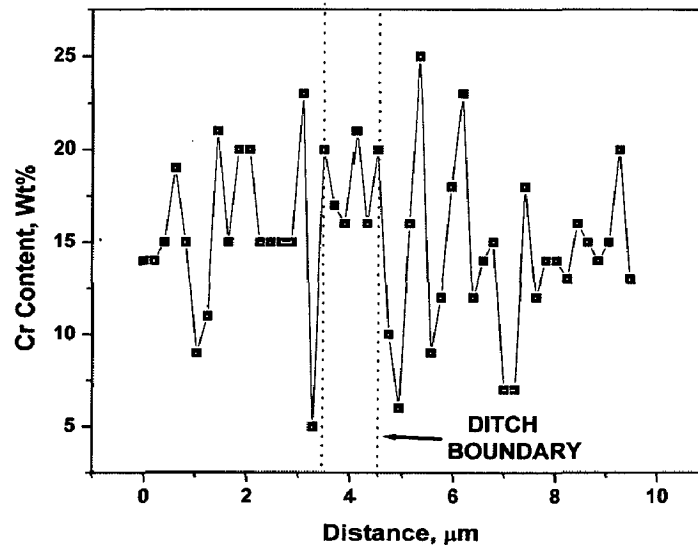
Fig. 5.57: Typical behaviour of chromium distribution across the ditch boundary in HAZ of all the welds presented in Figs.5.55 and 5.56.

Intensity of corrosion attack primarily depends on chemical composition, influence of severity of weld thermal cycle exerted during each pass on isotherms in HAZ and the number of thermal cycles undergone in a weld joint. Since all the weld joints have been prepared with same base material, influence of chemical composition in all the cases will be similar. Severity of weld thermal cycle of the matrix in HAZ primarily depends on average heat input (Ω) employed in the filling passes during the welding process. Since P-GMA welds have been prepared at a comparatively lower Ω than that of GMA and SMA welds (Table-5.11), it may be assumed that weld thermal cycle has been comparatively less severe in P-GMA welds than the other ones. As the number of thermal cycles is equal to number of weld passes, which are similar in number in all the weld joints, cumulative influence of thermal cycle may reduce further in P-GMA welds than that of GMA and SMA welds. In P-GMA welds at a given Ω, comparatively higher amount of mass deposition (Annexure-I) with larger Q_T (Table-5.11), takes place at a relatively lower ϕ of 0.05 than that of 0.25. Thus, the higher surface area of contact of weld pool with the adjoining base metal generated, may have led to faster rate of heat dissipation. Hence, improvement in corrosion properties may have resulted due to considerable reduction in severity of weld thermal cycle. However, corrosion properties of weld should be further analysed by reducing number of passes through narrow gap welding technique.

5.3.9 Summary

P-GMAW process has the capacity to control the amount of heat transferred to the weld pool (Q_T) by varying mass, velocity and heat content of the droplet resulting into achieving equivalent amount of metal deposition at a significantly lower heat input (Ω) in comparison to that in GMAW and SMAW processes. Thus, in P-GMA welds, considerable reduction in residual stresses along with refined microstructure in multi-pass deposit have been observed in comparison to that in GMA and SMA weld joints. In addition to above, the reduction in inclusion and porosity content in P-GMA welds by almost 30% and 90% than those in GMA and SMA weld joints respectively, have further improved the fracture mechanics and mechanical properties of the weld significantly. It has been further interestingly observed that the P-GMA welds prepared at ϕ of 0.05 in comparison to 0.25 develops considerably lower residual stresses at the top and the root of the weld, as well as improves fracture toughness and tensile properties of the weld along with significant reduction in inclusion and porosity content. Susceptibility to corrosion attack also considerably reduces in P-GMA welds especially with the lowering of ϕ, than that observed in GMA and SMA welds as marked by the reduction in density and size of ditches in HAZ. The summarised properties of P-GMA, GMA and SMA weld joints are as given in Table-5.21.

Table-5.21: The summarized influence of welding parameters on various properties of the conventional groove P-GMA, GMA and SMA weld joints.

Process	Ω (kJ/cm)	φ	I (A)	I_m (A)	I_P (A)	I_b (A)	t_P (ms)	f (Hz)	Arc Voltage (V)	Welding Speed (cm/min)	Q_T (kJ/cm)	Total number of passes	Overall Cumulative Transverse shrinkage (mm)	Cr_{eq}	Ni_{eq}	δ-ferrite Root passes	δ-ferrite Filler passes	Solidification mode	Area of weld deposit (mm²)	Inclusion & porosity Content (Vol. %)	Grain size Dia. ($\mu m \pm \sigma$)	ASTM No.
SMAW	17.1	-	140	-	-	-	-	-	28	9.1	--	16	6.80±0.48	18.17	14.04	2.50	0	AF	343	2.34	28±5	7.5
GMAW	10.7	-	225	-	-	-	-	-	22.7	20	--	17	6.32±0.41	19.26	12.28	3.80	7.65	FA	347	0.75	19±3	8.5
P-GMAW	9.1	0.06	-	196	410	34	2.03	105	22.4	20	11.4	14	5.68±0.22	19.07	12.33	2.90	6.85	FA	345	0.43	18±7	9.0
P-GMAW	9.4	0.25	-	182	321	105	1.97	120	24.2	20	10.5	16	6.04±0.34	19.51	12.40	3.20	7.45	FA	353	0.57	19±5	8.5
P-GMAW	7.7	0.05	-	160	450	28	2.03	114	22.5	20	11.1	15	5.30±0.17	19.3	12.4	3.60	7.45	FA	347	0.18	17±6	9.0
P-GMAW	8.0	0.25	-	176	313	106	2.03	126	21.8	20	9.9	16	5.44±0.45	19.40	12.24	4.00	7.95	FA	357	0.33	18±6	9.0

Mechanical Properties

Process	Ω (kJ/cm)	φ	Axial Tensile UTS (MPa)	Axial Tensile YS (MPa)	Axial Tensile Elongation (%)	All Weld Tensile UTS (MPa)	All Weld Tensile YS (MPa)	All Weld Tensile Elongation (%)	Charpy Energy absorbed (J)	Charpy Lateral expansion (mm)	Fracture toughness J_Q (kJ/m²)
SMAW	17.1	-	555	353	16.0	569	365	37.9	98	1.86	300
GMAW	10.7	-	619	379	34.2	575	426	43.4	120	2.47	538
P-GMAW	9.1	0.06	651	367	44.6	608	438	42.4	128	2.59	701
P-GMAW	9.4	0.25	641	362	37.6	582	424	44.0	132	2.63	560
P-GMAW	7.7	0.05	654	395	42.5	617	442	44.0	133	2.63	1035
P-GMAW	8.0	0.25	632	389	41.4	608	438	42.4	135	2.69	799

Fracture mechanics properties — Fatigue crack growth rate test

	Stress ratio(R)=0.1 m	Stress ratio(R)=0.1 C (m/cycle)	ΔK_{TH} MPa√m	Stress ratio(R)=0.5 m	Stress ratio(R)=0.5 C (m/cycle)	ΔK_{TH} MPa√m
SMAW	3.56	3.23×10^{-13}	5.0	3.00	5.26×10^{-12}	2.6
GMAW	3.80	1.39×10^{-13}	5.7	3.08	4.67×10^{-12}	2.7
P-GMAW	-	-	-	-	-	-
P-GMAW	-	-	-	-	-	-
P-GMAW	4.24	2.82×10^{-14}	6.9	3.97	2.84×10^{-13}	4.4
P-GMAW	3.95	8.47×10^{-14}	6.0	3.93	2.89×10^{-13}	4.4

224

5.4 INFLUENCE OF NARROW GROOVE P-GMA AND SMA WELDING ON CHARACTERISTICS OF WELD JOINT

During welding of austenitic stainless steels in which $\gamma \rightarrow \alpha$ transformation does not take place, the metallurgical transformations occurring during solidification often have a much stronger impact on the properties of weld metal than in case of low alloyed or unalloyed steels [Folkhard 1984]. During multi-pass welding of thick sections, the heat affected zone of base metal and weld deposit undergoes repeated heat treatment by the multiple passes of weld deposition. However, the extent of this treatment primarily depends upon amount of heat transferred to the weld pool per pass (Q_T) through metal deposition and the number of passes layed down to fill the weld groove. This phenomenon dictates the reheat refinement of weld deposit as well as recrystallization and grain growth in HAZ.

The thermal behaviour of P-GMA welding affecting the characteristics of weld joint has been analysed in the previous section and compared to those of GMA and SMA welding in case of conventional V-groove butt weld wherein the weld area and number of passes are kept almost constant. In this section, major emphasis has been laid on welding procedure by reducing the amount of heat transferred to the weld pool (Q_T) and also, through reduction in weld area with narrow groove design. To achieve this, P-GMAW process has been primarily used in narrow grove welds, considering its flexibility in metal deposition with suitable selection of ϕ, Ω and Q_T based on the discussion in bead on plate studies (secton-5.2). In addition to above, narrow groove has a distinct advantage over conventional V-groove. In narrow groove due to low angle of attack with groove wall, surface area exposed to arc will considerably increase in comparison to that in conventional V-groove as shown schematically in Fig. 5.58. Thus, the heat density in the groove wall surface beneath the arc will considerably reduce the thermal severity at this location.
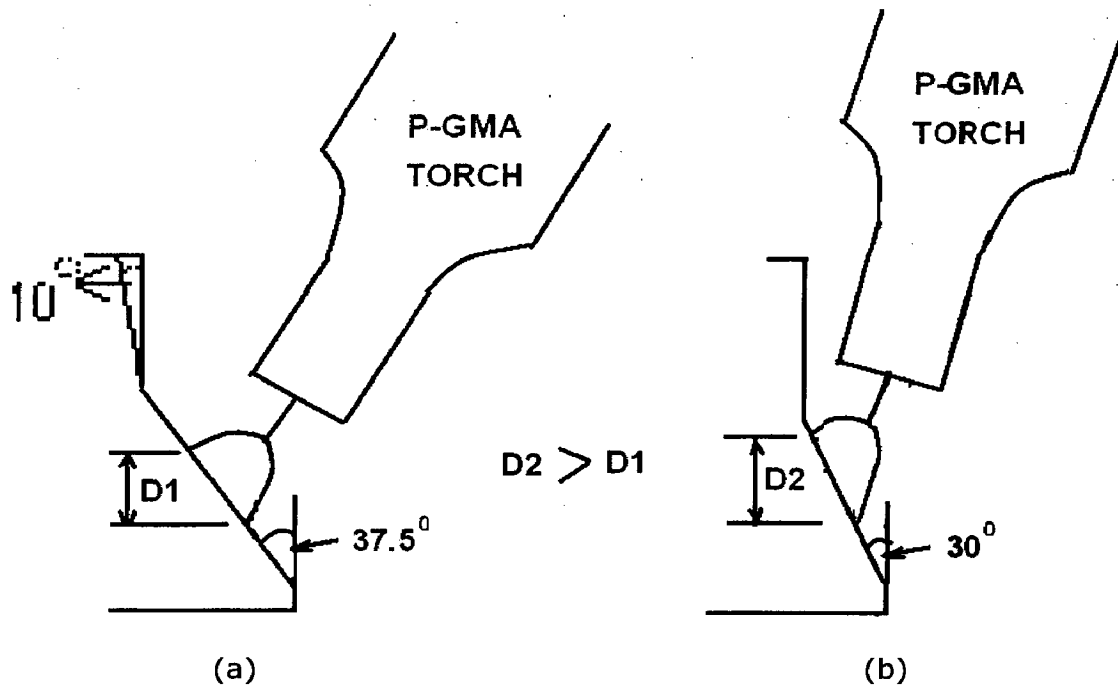
Fig. 5.58   Schematic diagram showing surface area exposed to arc marked by its cross-section in (a) Conventional V-groove and (b) typical narrow groove design.

The suitability of P-GMAW process in narrow gap welding has been justified by comparing its properties with narrow groove SMA welds at almost similar area of weld deposit. However, narrow gap welding with GMAW process has been avoided considering the fact that controlled spray mode of metal deposition is achieved at higher deposition rate leading to a comparatively severe weld thermal cycle. Further, for carrying out weld deposition at a significantly low angle of attack to groove wall generally requires higher heat input to achieve side wall fusion. Such a variation in GMAW can only be achieved by increasing the welding current further much above the transition level leading to further severity of weld thermal cycle.

5.4.1 Weld Quality and Size

The macro photographs revealed from the transverse sections of the narrow groove P-GMA welds with the weld width of 17mm, 15mm and 11mm at a given ϕ of 0.05 are shown in Fig. 5.59 (a), (b) and (c) respectively. At a relatively higher ϕ of 0.25, the macro photographs of the narrow groove P-GMA welds revealed in their transverse sections with the weld width of 15 mm and 11 mm are shown in Fig. 5.60 (a) and (b) respectively. Similarly the macro photographs of the narrow groove SMA weld joints with the weld width of 14 mm and 11 mm as revealed in their transverse sections are shown in Fig. 5.61 (a) and (b) respectively. Based on the data recorded as shown in Annexure-I, the summarized data of total number of passes, average Ω in filling passes, area of the weld deposit and overall cumulative transverse shrinkage observed in narrow groove SMA and P-GMA weld joints are shown in Table 5.22. In case of P-GMA welds the influence of ϕ and Q_T on the above parameters have also been compared in Table 5.22.

| (a) | (b) | (c) |
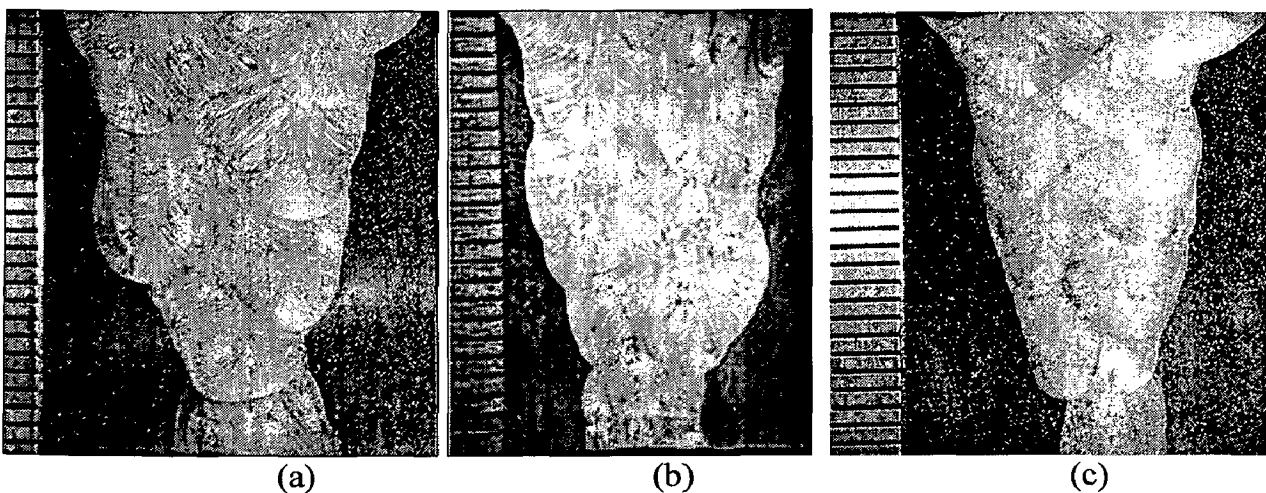
Fig. 5.59 Typical macro photographs showing narrow groove P-GMA weld joints prepared at a given ϕ of 0.05 and Ω with weld width of (a) 17mm (b) 15mm and (c) 11.5mm.
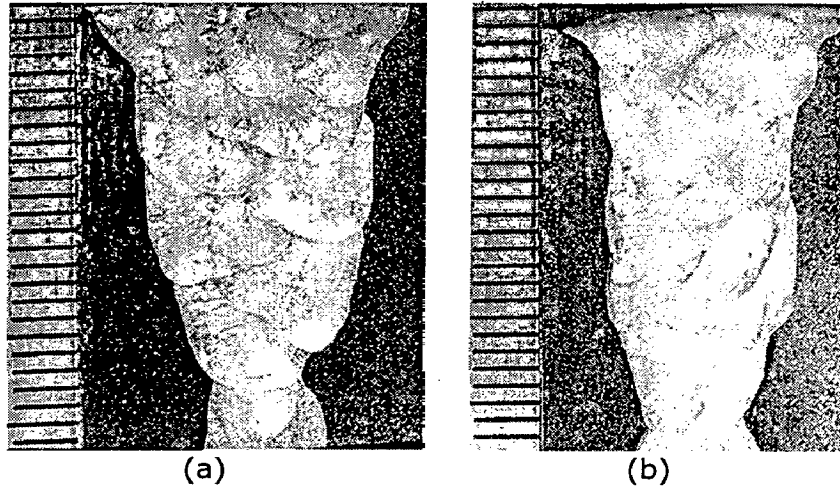
Fig. 5.60 Typical macro photographs showing narrow groove P-GMA weld joints prepared at a given φ of 0.25 and Ω with weld width of (a) 15mm and (c) 11.5mm.
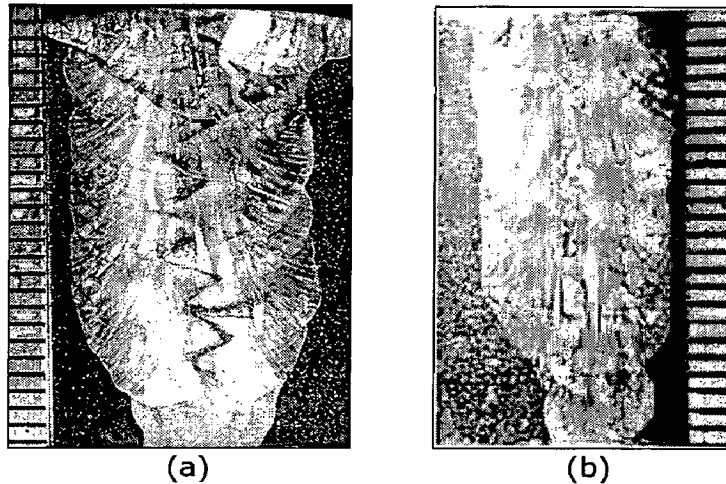
Fig. 5.61: Typical macro photographs showing narrow groove SMA weld joints prepared with weld width of (a) 14mm and (b) 11mm.

Table 5.22: Summarised influence of weld data on type and average proportion of defects discarded from narrow groove P-GMA and SMA weld joints.

Process	Groove width (mm)	Weld width (mm)	φ	Total number of passes	Average Ω in filling passes, (kJ/cm)	Average Q_T in filling passes, (kJ/cm)	Area of machined groove (mm²)	Area of weld deposit (mm²)	Overall cumulative transverse shrinkage (mm)	Fractional length of LOF of total weld (%)	Type of defects
P-GMAW	20	17	0.06	12	9.4	11.4	340	267	5.0± 0.35	1.0	Lack of fusion
	17	15	0.05	12	7.5	11.1	300	239	4.25± 0.31	8.0	
			0.25	15	8.0	9.9		242	4.43± 0.40	10.2	
	15	11.5	0.05	10	7.5	11.1	270	215	4.04± 0.16	11.5	
			0.25	11	7.9	9.9		225	4.20± 0.28	24.0	
SMAW	16	14	-	19	9.9	--	368	274	4.76± 0.68	5.3	Slag line & Lack of fusion
	13	11	-	17	7.4	--	275	220	3.90± 0.37	7.0	

Figs. 5.59-5.61 primarily depict that the welds are practically free from any defects as lack of welding or root fusion. The characteristics of weld joints shown in Table 5.22 reveals that at a given area of narrow groove and Ω, the number of passes required in P-GMAW process have considerably reduced by 30-35% in comparison to conventionally used SMAW process. This has happened due to characteristic feature of higher deposition rate achieved [ASM handbook 1984, Ghosh et al 1991b, Suban and Tusek 2001] with P-GMA welding process. However, the use of narrow groove welding procedure considerably reduces the area of weld deposit by about 35-40 vol% in comparison to that of conventional groove weld (Table 5.11) in both P-GMAW and SMAW processes. The table further reveals that by varying welding process, cumulative shrinkage reduces by narrowing the weld groove and lowering of Ω and ϕ. It indicates a possibility of reduction in strain especially at the root of the narrow groove pipe weld [Murugan et al 2001] in comparison to that observed in conventional V-groove pipe weld (Table 5.11), consequently minimising the residual stresses. The radiographs of the welds depict that there exists some defects in P-GMA welds primarily as lack of fusion, while in SMA welds, the defects largely develops as slag-line leading to lack of fusion. Table 5.22 shows that the semi-automated P-GMA weld joints develop relatively higher proportion of lack of fusion in comparison to manually prepared SMA weld at similar weld width. However, the lack of fusion occurs in small patches of 10-15 mm at few locations in total weld length as measured on radiographs of P-GMA weld except where relatively higher ϕ and Ω of 0.25 and 7.8 kJ/cm respectively have been used. The larger amount of lack of fusion at relatively higher ϕ and, lower Ω and Q_T (Table 5.22) may be attributed to comparatively lower heat introduced (Fig.5.9) in the process.

In P-GMA weld joints, lack of inter pass and side wall fusion at different locations primarily occurr due to similar reasons observed in conventional groove weld (section 5.3.1). Whereas, in SMA weld joints, the slag inclusion may primarily occur due to sticking of slag on weld deposit which becomes difficult to remove during interpass cleaning due to an increase in magnitude of wedging effect [Shtrikman and Grinin 1979], especially in case of narrow gap welding. The defects revealed have been analyzed and correspondingly marked in proper location of the pipe welds in reference to the starting sector of the weld pass (Fig. 4.7).

5.4.2   Chemical Composition and δ-ferrite Content

Chemical compositions of weld are given in Table 5.23. Delta ferrite content estimated as per WRC-92 diagram [Siewert et al 1988] and measured by ferrite scope across the filler passes in transverse section of various weld deposits are also shown in Table 5.23. The table depicts that irrespective of the welding process and procedure used for narrow groove weld deposition, the dilution of base metal introduces nitrogen of the order of 0.1 wt% to the weld and thus, reduces its δ-ferrite content by stabilizing the austenite phase as per WRC-92 diagram [Siewert et al 1988]. It has been further observed that filler regions of P-GMA weld deposits have 4-7% of δ-ferrite content indicating ferrite-austenite (FA) mode of solidification. In contrast to that, the austenite-ferrite (AF) mode of solidification is observed in case of SMA weld deposits containing practically negligible δ-ferrite in it (Table 5.23). Whereas, in the root pass carried out by GTAW process the δ-ferrite is considerably higher in P-GMA welds compared to that observed in SMA welds. This indicates that root region gets diluted more by P-GMAW filler metal having comparatively higher estimated δ-ferrite content (Table 5.1) in comparison to that in SMA weld. The narrow groove SMA weld in concurrence to the earlier observations on conventional groove (Table 5.12) also shows AF mode of solidification

indicating a considerable loss of chromium caused by oxidation during metal transfer along with base metal dilution. Table 5.23 further depicts that with the variation in ϕ and Ω in P-GMA welds, chemical composition of welds with different groove design (Table 5.12) have shown insignificant deviation primarily due to similar metal deposition procedure. Thus, 4-7% of δ-ferrite content has been observed in all the welds. Whereas, narrow groove SMA weld joint with 11 mm weld width has significantly higher amount of carbon in comparison to that in the narrow groove weld joint with 14 mm weld width and conventional V-groove weld joints (Table 5.12). However, it is observed that the carbon content of the narrow groove weld joints with 11 mm weld width is close to that of the filler metal indicating lower dilution of base metal due to comparatively shallow included angle of attack with the groove wall of the order of 25-30^0 than that used in narrow groove weld joint with 14 mm weld width and conventional V-groove weld joints with angle of attack of the order of 40-45^0 and 70-75^0 respectively. Hence, it may be inferred that narrow groove P-GMA welds prepared at relatively lower Ω (Table 5.22) having 4-7% δ-ferrite content (Table 5.23) are comparatively less prone to solidification cracking [Hunter and Ferry 2002, Koseki and Flemings 1996, Lippold and Savage 1986] in comparison to SMA weld joint.

Table 5.23: Chemical composition and δ-ferrite content of the narrow groove weld deposits prepared by using P-GMAW and SMAW processes.

Process	Weld width (mm)	φ	Ω kJ/cm	Chemical analysis of weld metal (Wt.%)										Equivalents		Estimated		δ-ferrite content (%)	
				C	Cr	Ni	Mn	N	Mo	Si	Cu	S	P	Cr_{eq}	Ni_{eq}	δ-ferrite content (%)	Solid-ification mode	Root passes	Filler passes
P-GMAW	17	0.06	9.4	0.025	19.10	9.37	1.63	0.10	0.16	0.48	0.19	0.01	0.009	19.26	12.29	4	FA	4.06	5.45
	15	0.05	7.5	0.029	19.08	9.35	1.56	0.10	0.14	0.46	0.20	0.012	0.007	19.22	12.42	4-5	FA	4.50	5.65
		0.25	8.0	0.027	18.9	9.42	1.52	0.10	0.15	0.56	0.21	0.008	0.002	19.05	12.42	6-8	FA	4.66	6.94
	11.5	0.05	7.5	0.024	19.2	9.64	1.61	0.10	0.15	0.56	0.20	0.009	0.002	19.35	12.53	4-5	FA	3.00	4.10
		0.25	7.9	0.025	19.1	9.54	1.62	0.10	0.15	0.56	0.21	0.008	0.002	19.25	12.47	4-5	FA	3.00	5.70
SMAW	14	-	9.9	0.029	18.45	11.1	2.34	0.10	0.05	0.50	0.12	0.006	0.013	18.50	14.15	-	AF	1.50	0
	11		7.4	0.042	18.35	11.0	2.41	0.10	0.08	0.58	0.15	0.012	0.018	18.43	14.55	-	AF	1.50	0

5.4.3 Microstructure

During welding, the crystallization process is primarily controlled by dissipation of heat into solid metal, with comparatively insignificant amount of heat being dissipated into the surrounding atmosphere. This process of heat transfer has a decisive influence on the type, size and orientation of the crystals being formed in weld and HAZ [Folkhard 1984, Padilha and Rios 2002]. Hence micro structural studies in narrow groove have been carried out in order to analyse the influence of thermal conditions prevailing in P-GMA weld during deposition and compare it to that in commonly used SMA weld deposition. At a given Ω and weld width of 7.7 ± 0.35 kJ/cm and 14 mm respectively, the influence of variation in ϕ at two different levels of 0.06 and 0.25 on the microstructures of weld prepared by using P-GMAW process are as shown in Fig. 5.62 (a) and (b) respectively. Similarly, at a given Ω and weld width of 7.7 ± 0.35 kJ/cm and 11 mm respectively, the typical microstructures observed at two different levels of ϕ of 0.05 and 0.25 are compared respectively in Fig. 5.63 (a) and (b). The typical microstructures observed in narrow groove SMA welds deposited with weld width of 14 mm and 11 mm have been shown in Fig. 5.64 (a) and (b) respectively.

The microstructures presented in Fig. 5.61 to 5.63 primarily depict that the narrow groove welds of both P-GMA and SMA processes show similar features of multipass weld deposition as those observed in corresponding conventional groove welds (Figs. 5.39-5.40). However, the narrow groove P-GMA weld deposit shows more refinement of microstructure along with scarcely distributed coaxial dendritic structure with the lowering of ϕ from 0.25 to 0.05 as compared to that observed in case of conventional groove P-GMA welds. The considerable refinement of microstructure with the lowering of ϕ to 0.05, and it may have primarily happened

due to variation in thermal shock during solidification through interruption in metal deposition imparted by the pulse parameters along with a comparatively less severity of weld thermal cycle of multipass deposition in case of the narrow groove weld resulting in a lower amount of weld deposit compared to that in conventional groove weld. Whereas, in comparison to conventional groove weld (Fig.5.40(b)) the narrow groove SMA welds show further increase in reheat refined regions (Fig.5.64) with the reduction in weld width from 14 mm to 11 mm. This may be attributed primarily to comparatively higher fraction of interpass region resulting from partial reheat refinement of coaxial dendrite of earlier deposited weld bead due to severity of weld thermal cycle imparted by the subsequent passes. Such a difference observed in weld microstructure has been further characterized by analyzing the distribution of coaxial dendritic and refined region in P-GMA and SMA weld deposits as shown in Table 5.24. In agreement with the above mentioned observations, the table shows that the use of P-GMAW significantly reduces the coaxial dendritic region in the welds in comparison to those observed in SMA welds.

At a given Ω of 7.7 ± 0.35kJ/cm, the influence of practically narrowest P-GMA weld on the weld HAZ microstructures at different ϕ of 0.05 and 0.25 are compared in Fig. 5.65 (a) and (b) respectively. The typical microstructures observed in the HAZ adjacent to fusion line of narrow groove SMA welds of weld width of 14 mm and 11 mm have been shown in Fig. 5.66 (a) and (b) respectively. The microstructure of HAZ adjacent to fusion line (Figs.5.65 & 5.66) of the narrow groove P-GMA and SMA welds also show, certain extent of grain coarsening as it is observed in the case of their conventional groove welds (Fig. 5.41 and 5.42). The grain size of HAZ of various P-GMA and SMA weld joints has been compared in Table 5.25. The table shows that the narrow groove joints of both P-GMA and SMA welding processes have comparatively less grain coarsening than those observed in conventional groove weld joints

(Table 5.14). The table further reveals that narrow gap P-GMA weld joints have considerable reduction in grain coarsening in comparison to that in the narrow gap SMA weld joints. This indicates that grain coarsening reduces with the change in welding process and procedure due to considerable reduction in severity of weld thermal cycle arising out of the heat of weld deposition adjacent to the groove wall. However, at a given Ω of P-GMA welds, the increase in ϕ from 0.05 to 0.25 marginally coarsens the grain size adjacent to fusion line in HAZ. Such an advantage of lower ϕ at a given Ω may be beneficial to improve the resistance of HAZ to susceptibility to stress corrosion cracking susceptibility of HAZ in narrow groove P-GMA welds in comparison to that in SMA weld joints.

Table5.24: Area fraction refinement of dendrite in narrow groove P-GMA and SMA weld.

Process	Weld width (mm)	ϕ	Ω kJ/cm	Coaxial dendritic region (%)	Refined region (%)
P-GMAW	17	0.06	9.4	36.3	63.7
	15	0.05	7.5	25.4	74.6
		0.25	8.0	31.8	68.2
	11.5	0.05	7.5	18.8	81.2
		0.25	7.9	25.7	76.3
SMAW	14	-	9.9	56.1	43.9
	11		7.4	69.6	30.4

Table 5.25: Grain size of HAZ adjacent to fusion line in different weld joints.

Process	Weld width (mm)	ϕ	Ω kJ/cm	Avg. Grain dia. $\pm$ S.D (μm)			ASTM No		
				A	B	Avg. of A & B	A	B	Avg.of A & B
P-GMAW	17	0.06	9.4	16 $\pm$ 5	20 $\pm$ 4	17 $\pm$ 5	9.5	8.5	9.0
	15	0.05	7.5	13 $\pm$ 7	13 $\pm$ 4	13 $\pm$ 5	9.5	9.5	9.5
		0.25	8.0	13 $\pm$ 4	13 $\pm$ 2	13 $\pm$ 3	9.5	9.5	9.5
	11.5	0.05	7.5	12 $\pm$ 5	12 $\pm$ 4	12 $\pm$ 5	9.5	9.5	9.5
		0.25	7.9	13 $\pm$ 3	12 $\pm$ 4	13 $\pm$ 3	9.5	9.5	9.5
SMAW	14	-	9.9	20 $\pm$ 3	20 $\pm$ 3	20 $\pm$ 3	8.5	8.5	8.5
	11		7.4	17 $\pm$ 2	18 $\pm$ 2	18 $\pm$ 2	9.0	9.0	9.0

S.D. is Standard deviation, A and B are either side of weld joint.
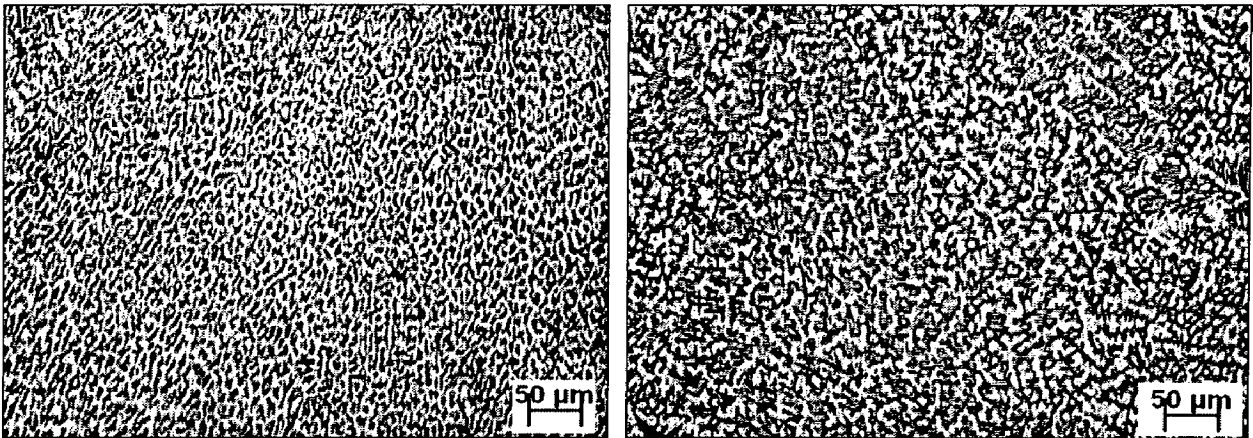
(a)   (b)

Fig. 5.62   At a given Ω of 9.2±0.35 kJ/cm, typical microstructures observed in narrow groove P-GMA weld (14mm weld width) deposited at different ϕ of (a) 0.06 and (b) 0.25.
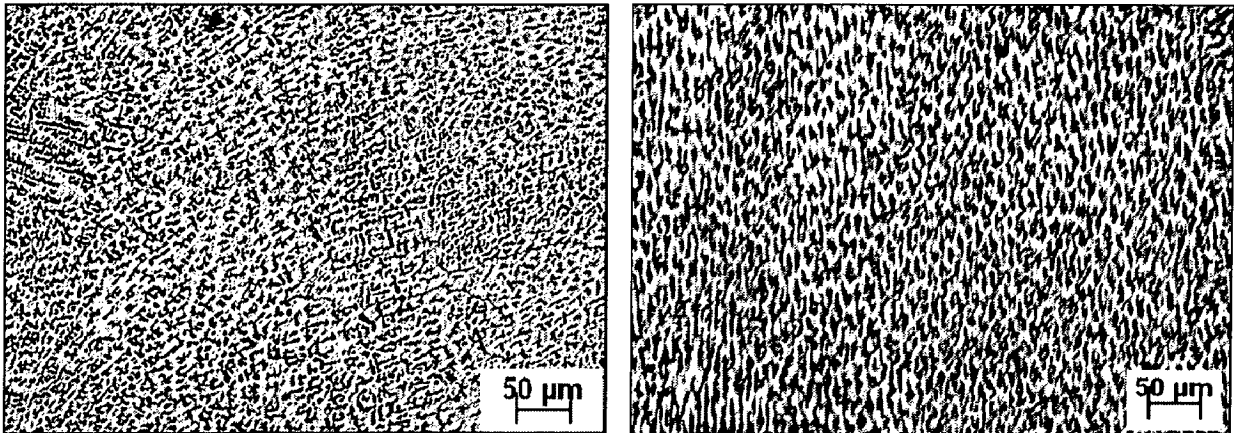
(a)   (b)

Fig. 5.63   At a given Ω of 7.7±0.35 kJ/cm, typical microstructures observed in P-GMA weld (11mm weld width) deposited at different ϕ of (a) 0.05 and (b) 0.25.

(a)   (b)
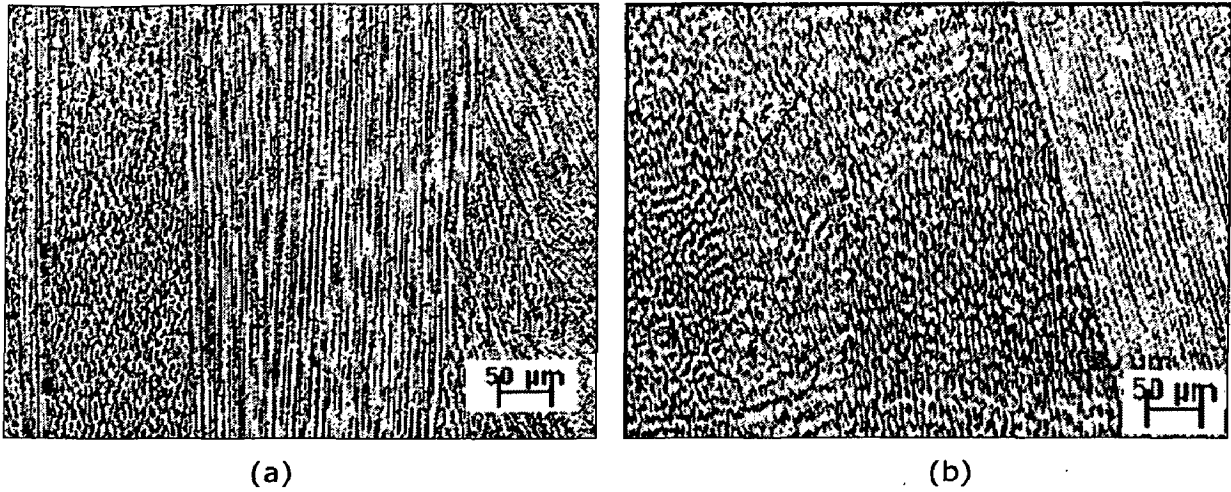
Fig. 5.64   Typical microstructures observed in narrow groove SMA weld deposit prepared with (a) 14mm and (b) 11mm weld width.
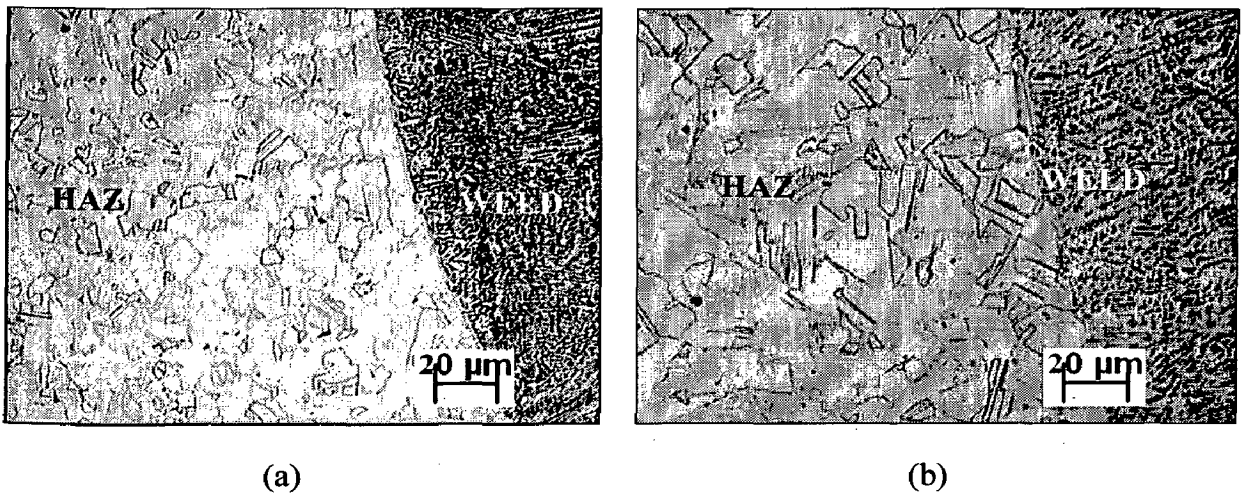
(a)   (b)

Fig. 5.65:   At a given Ω of 7.7 ± 0.35 kJ/cm influence of ϕ on typical microstructures of heat affected zone adjacent to fusion line in narrow groove P-GMA weld with 11mm weld width; (a) $\phi=0.05$ and (b) $\phi=0.25$.

(a)   (b)

Fig. 5.66 Typical microstructures observed in heat affected zone adjacent to fusion line of narrow groove SMA welds at a weld width of (a) 14mm and (b) 11mm.

5.4.4 Porosity and Inclusion Content

The estimated inclusion and porosity content in the narrow groove P-GMA and SMA weld deposits have been shown in Table 5.26. The presence of inclusions observed on fractured surface in the narrow groove P-GMA and SMA welds of weld width of the order of 11 mm has been shown in Fig. 5.67 (a) and (b) respectively. The negligible presence of round facets in the fractographs presented in Fig. 5.67(a) than those observed in 5.67(b) reveal that the P-GMA welds have very less porosity content than that of SMA welds. The table further depicts that the narrow groove P-GMA weld joints prepared under comparatively cleaner environment of argon gas shielding are having 80-90% lower porosity or inclusion content in comparison to that of the narrow groove SMA weld joints. However, in comparison to conventional groove welds (Table 5.15), P-GMA welds have shown marginal increment in porosity content, whereas inclusion and porosity content in the narrow groove SMA welds have increased by almost 30%. In P-GMA welds, at a given ϕ and Ω, the variation in porosity content of P-GMA weld has been found to follow almost similar trend as observed in conventional groove welds (Table 5.15), primarily due to insignificant change in pulse parameters used for weld metal deposition. Inclusion content of SMA welds increase with the reduction in weld width primarily due to greatly impaired

238

detachability of slag as marked by embedded inclusions (Fig. 5.67(b)) in the matrix. This primarily happens due to increase in strength of thick slag layer formed at the approaching edges of the weld groove depending upon cooling conditions provided by the narrow groove [Shtrikman and Grinin 1979]].

Table 5.26: Inclusion and porosity content of P-GMA and SMA weld joints

Process	Weld width (mm)	ϕ	Ω kJ/cm	Inclusions rating		Inclusion and porosity content, (Vol. %)
				Category	Severity level	
P-GMAW	17	0.15	9.2	D thin/D thick	3.0-4.5	0.32
	15	0.05	7.4	D thin/D thick	3.0-4.5	0.19
		0.25	8.0	B thin/B thick	1.0-2.0	0.56
				D thin/D thick	3.0-4.5	
	11.5	0.05	7.4	B thin/B thick	1.0-2.5	0.23
				D thin/D thick	3.0-5.0	
		0.25	7.2	B thin/B thick	1.0-3.0	0.68
				D thin/D thick	2.5-5.0	
SMAW	14	-	10.6	B thin/B thick	0.5-1.5	2.62
				C thick	1.0-2.5	
				D thin/D thick	2.5-5.0	
	11	-	7.8	B thin/B thick	0.5-1.5	3.19
				C thick	1.0-4.0	
				D thin/D thick	2.5-5.0	
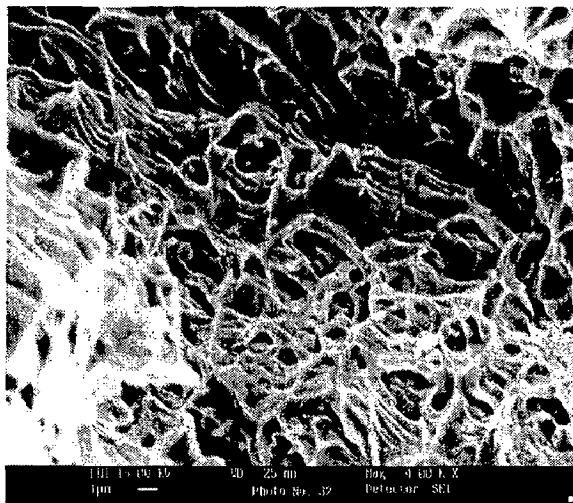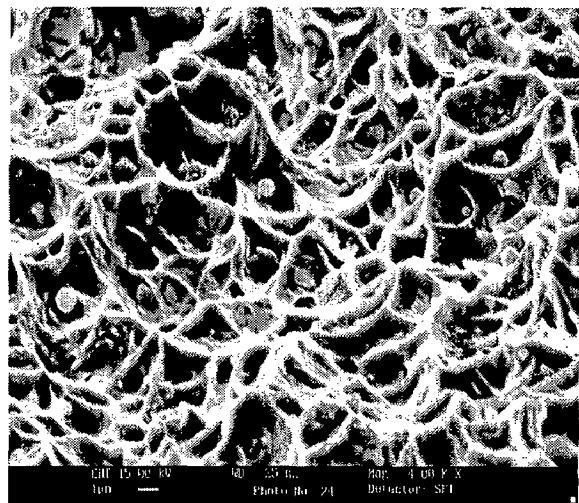
(a)   (b)

Fig. 5.67 Typical presence of porosity and embedded inclusions inside the pores revealed in the fractograph of narrow groove (a) P-GMA and (b) SMA welds of 11mm weld width.

5.4.5 Mechanical Properties

5.4.5.1 Tensile properties

The tensile properties along longitudinal (axial weld having joint at centre of the specimen) and circumferential (all weld metal) directions of narrow groove pipe welds prepared by using P-GMA and SMA welding processes are shown in Table 5.27 and Table 5.28 respectively. The corresponding dimensionless material constant (α) and strain hardening exponent (n) of the tensile properties estimated by using Romberg Osgood expression (eq. 5.1) are also given in the tables in order to characterise primarily the response to fracture of the material. Typical fractographs of P-GMA about 11 mm weld width narrow groove welds with 11 mm weld width, at different ϕ of 0.05 and 0.25 are compared with SMA weld shown in Fig. 5.68 (a), (b) and (c) respectively, where the fracture took place from weld under uniaxial tensile test of longitudinal specimen of weld joint.

Tables-5.27 and 5.28 reveal that weld deposit (circumferential direction) has comparatively higher yield strength and elongation under uniaxial tension in circumferential direction than those observed in longitudinal direction of weld joints fracturing from the weld. It infers that the tensile properties of the weld metal may have been significantly influenced by the microstructural anisotropy primarily resulting from the orientation of coaxial morphology of dendrite in weld deposit in reference to the axis of loading [Dieter 1988]. Whereas, in comparison to base metal (Table 5.3), the ratio of yield strength (σ_y) to ultimate tensile strength (σ_u) of weld significantly increases from 0.5 to 0.76 with a considerable sacrifice in elongation,

240

resulting in relatively higher value of strain hardening exponent (n). The tables further reveal that at a given weld width, the narrow groove P-GMA welds have significantly higher tensile properties in both the longitudinal and circumferential directions than those observed in SMA weld joints. However, in comparison to their respective conventional groove (Tables 5.16 and 5.17), both P-GMA and SMA narrow groove weld joints show marginal improvement in tensile properties primarily due to similar chemical composition of weld deposit (Tables 5.12 and 5.23).

The fractographs of the narrow groove SMA weld of weld width of 11 mm (Fig. 5.68 (c)) show considerably higher inclusion content (Table 5.26) along with fine wavy markings near to the cavity. Whereas narrow groove P-GMA weld (11mm weld width) of different ϕ of 0.05 and 0.25 (Fig. 5.68 (a) and (b)) respectively shows wide spread ductile fracture behaviour with fine dimples along with considerably lower porosity content (Table 5.26) than that observed in SMA weld joints. However, both P-GMA and SMA narrow groove weld joints (Fig. 5.68) show considerably higher plastic flow of the austenite matrix as marked by fine wavy markings near the cavity than those observed in corresponding conventional groove welds (Figs. 5.45 and 5.46) due to considerably higher refined region (Tables 5.24 and 5.13) in the former.

Table 5.27: Tensile properties in longitudinal (axial) direction of narrow groove weld joints.

Process	Weld width (mm)	φ	Ω kJ/cm	UTS (MPa)	YS (MPa)	YS/UTS Ratio	Elongation (%)	n	a	Failure region
P-GMAW	17	0.15	9.4	653	372		48.1	5.80	24.26	Weld
				653 (653)	365 (363)	0.56	44.6 (45.8)	5.67 (5.70)	22.71 (22.91)	
				652	352		44.7	5.64	21.75	
	15	0.05	7.5	649	372		46.7	5.80	22.64	
				653 (654)	369 (368)	0.56	46.0 (45.0)	5.81 (5.82)	21.53 (21.54)	
				660	363		44.3	5.84	20.46	
	15	0.25	8.0	635	354		45.8	5.14	27.53	
				634 (633)	342 (344)	0.54	42.8 (43.8)	5.51 (5.50)	21.73 (22.73)	
				630	336		42.8	5.85	18.93	
	11.5	0.05	7.5	646	366		43.7	5.80	24.26	
				650 (651)	363 (364)	0.56	45.6 (45.8)	5.67 (5.70)	22.71 (22.91)	
				657	362		48.0	5.64	21.75	
	11.5	0.25	7.9	637	348		31	6.32	21.94	
				632 (631)	346 (344)	0.55	34.6 (34.7)	6.28 (6.28)	22.05 (22.27)	
				624	339		38.4	6.24	22.81	
SMAW	14	-	9.9	560	358		22.0	6.20	20.38	Weld
				554 (556)	348 (350)	0.63	21.8 (22.8)	6.24 (6.25)	20.45 (20.54)	
				554	344		24.6	6.31	20.79	
	11	-	7.4	576	362		21.9	6.14	20.34	
				578 (582)	354 (354)	0.61	22.5 (23.4)	5.88 (5.92)	20.33 (21.26)	
				592	347		25.8	5.74	22.11	

Table 5.28: Tensile properties in circumferential (all weld) direction of narrow groove we joints.

Process	Weld width (mm)	φ	Ω kJ/cm	UTS (MPa)	YS (MPa)	YS/UTS Ratio	Elongation (%)	n	a
P-GMAW	17	0.15	9.4	628	476		39.9	6.04	26.76
				614 (616)	465 (466)	0.76	40.0 (40.0)	6.09 (6.10)	28.99 (29.01)
				606	456		40.0	6.16	31.29
	15	0.05	7.5	623	468		39.9	7.19	30.40
				622 (622)	459 (461)	0.74	40.4 (40.5)	6.84 (6.86)	38.62 (38.42)
				620	456		41.2	6.54	46.24
	15	0.25	8.0	626	475		43.0	7.92	32.63
				617 (618)	464 (466)	0.75	39.4 (40.4)	7.23 (7.43)	33.05 (33.44)
				611	459		38.8	7.14	34.64
	11.5	0.05	7.5	667	419		56.6	8.32	28.74
				668 (668)	413 (414)	0.62	55.4 (53.6)	7.92 (7.86)	31.84 (31.3)
				669	411		48.9	7.33	33.36
	11.5	0.25	7.9	624	439		30.9	6.24	39.48
				641 (641)	425 (426)	0.66	31.1 (31.7)	6.42 (6.39)	35.34 (36.01)
				657	414		33.1	6.51	33.23
SMAW	14	-	9.9	598	434		32.2	8.39	26.62
				577 (580)	448 (446)	0.78	27.9 (28.1)	7.53 (7.56)	23.10 (23.2)
				566	455		24.2	6.76	19.88
	11	-	7.4	593	425		44.0	6.38	38.84
				599 (598)	432 (431)	0.72	39.0 (39.7)	6.45 (6.45)	34.43 (35.13)
				602	435		36.0	6.53	32.13

Note: - n & a are Strain hardening exponent & Dimensionless material constant as given in Ramberg Osgood expression (Eq. (5.1)).
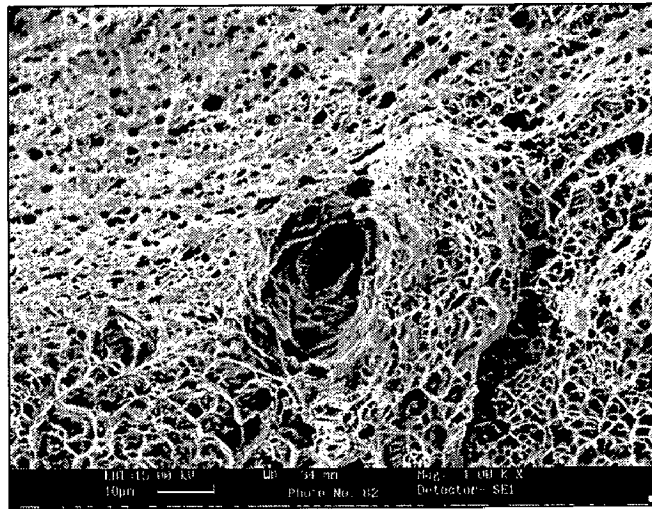
(a)
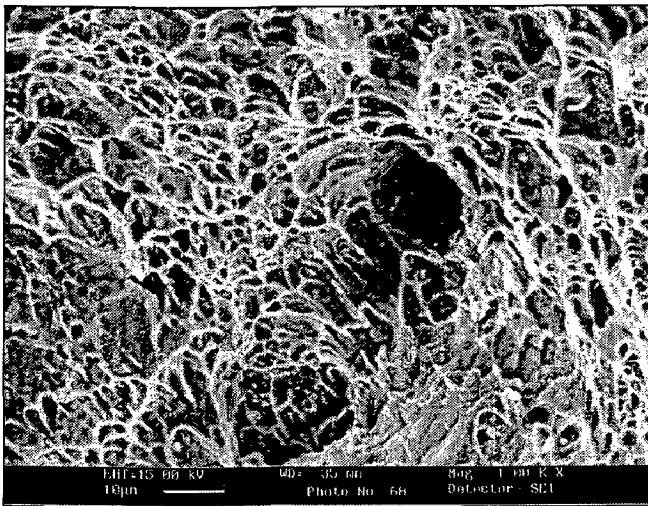
(b)

(c)
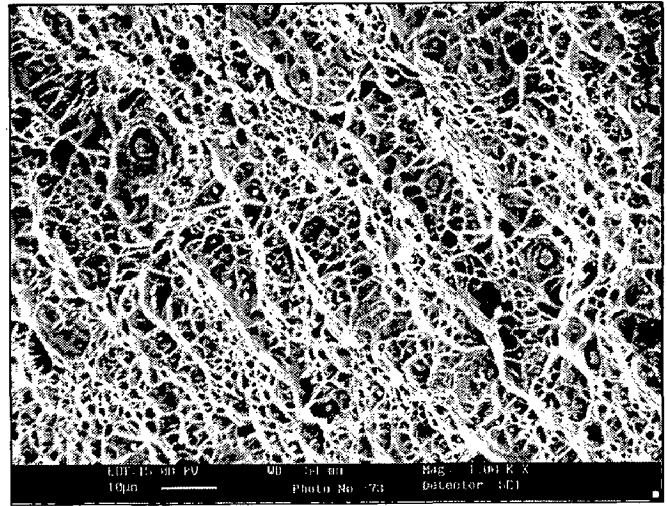
Fig. 5.68: At a given Ω of around 7.7 kJ/cm and weld width of 11mm typical SEM photographs of fractured surface in axial tensile specimens observed in narrow groove P-GMA welds at different ϕ of (a) 0.05, (b) 0.25 and (c) SMA weld.

5.4.5.2 Charpy impact toughness

Charpy impact energy absorbed in P-GMA and SMA weld joints with notch orientation in circumferential direction (Fig. 4.11) has been given in Table 5.29. The table reveals that all the weld joints have passed the acceptance criterion of 70 J in the as-welded state for weld metal [Tavassoli, 1995]. It has been further observed that narrow groove P-GMA welds have appreciably better C_v-impact toughness and lateral expansion in comparison to that observed in SMA weld joint. However, in comparison with base metal (Table 5.4) and conventional groove welds (Table 5.18), narrow groove P-GMA welds show almost equivalent C_v-impact toughness in spite of variation in ϕ .

The weld metal impact toughness primarily depends upon chemical composition, porosity content and refinement in microstructure [Dieter 1988]. The chemical composition of filler metal used in P-GMA welds has significantly higher Mn/C ratio along with considerable nickel content in comparison to that used in SMA weld. Further, P-GMA welds have significantly lower porosity content (Table 5.26) than that observed in SMA weld. P-GMA welds have also considerably higher refined dendritic microstructure (Table 5.24) especially with the lowering of ϕ in comparison to SMA weld joints at a given Ω. Thus, in spite of higher δ-ferrite content which generally tends to decrease the toughness, these various positive aspects may have primarily contributed to comparatively higher impact properties in P-GMA welds than those observed in SMA weld joints.

Table 5.29: Energy absorbed in Charpy impact toughness test in narrow groove P-GMA and SMA weld joints.

Process	Weld width (mm)	φ	Ω kJ/cm	Charpy impact properties		Lateral Expansion, (mm)	
				Energy absorbed, (J)		Lateral Expansion, (mm)	
P-GMAW	17	0.06	9.4	136	132	2.66	2.59
				133		2.61	
				127		2.50	
	15	0.05	7.5	133	132	2.61	2.59
				132		2.59	
				131		2.57	
		0.25	8.0	131	128	2.64	2.60
				128		2.62	
				125		2.54	
	11.5	0.05	7.5	137	134	2.67	2.63
				135		2.64	
				129		2.59	
		0.25	7.9	128	126	2.54	2.50
				126		2.51	
				124		2.46	
SMAW	14	-	9.9	97	94	1.84	1.78
				94		1.78	
				91		1.72	
	11	-	7.4	88	91	1.44	2.47
				92		1.53	
				93		1.65	

5.4.5.3 Hardness

The hardness distribution across the narrow groove P-GMA and SMA weld joints at a given weld width of 14-15 mm have been shown in Fig. 5.69. Similarly, at a given weld width of 11 mm the hardness distribution across P-GMA and SMA weld joints has been compared in Fig.5.70. At a given weld width of 14 mm and 11 mm, the hardness distribution in weld deposit and HAZ of both P-GMA and SMA weld joints are of similar magnitude across the region. It is further observed that both P-GMA and SMA welds with 11 mm weld width have marginally lower hardness than those observed in corresponding welds with 14 mm width. Whereas, at a relatively lower Ω of 7.7±0.35 kJ/cm, influence of φ on hardness distribution appears to be practically negligible in weld and HAZ

of both conventional and narrow groove P-GMA weld joints. However, in comparison to conventional groove SMA weld (Fig. 5.48), relatively higher hardness distribution in weld region along with considerable scattering across the weld and HAZ region are observed in narrow groove SMA weld joints.

In P-GMA welds, comparatively less scatter in hardness across weld and HAZ at both the Ω and ϕ levels, indicates uniformity in microstructure due to large scale refinement of dendritic microstructure (Figs. 5.62 and 5.63) than that observed in conventional groove welds (Figs. 5.41 and 5.42). Whereas considerable amount of scatter in hardness may have occurred due to presence of comparatively larger number of different kinds of zones of microstructure having coaxial dendrite and refined dendritic region (Table 5.24) in the SMA weld deposit.
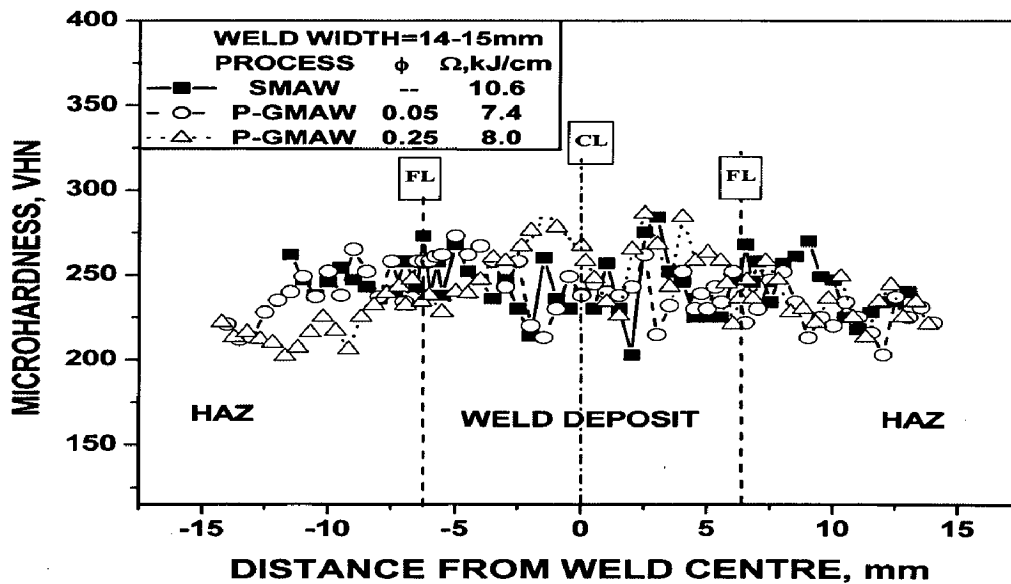
Fig. 5.69: At a given weld width of 14mm, hardness distribution observed across the narrow groove P-GMA and SMA welds with the variation in ϕ and Ω.

246
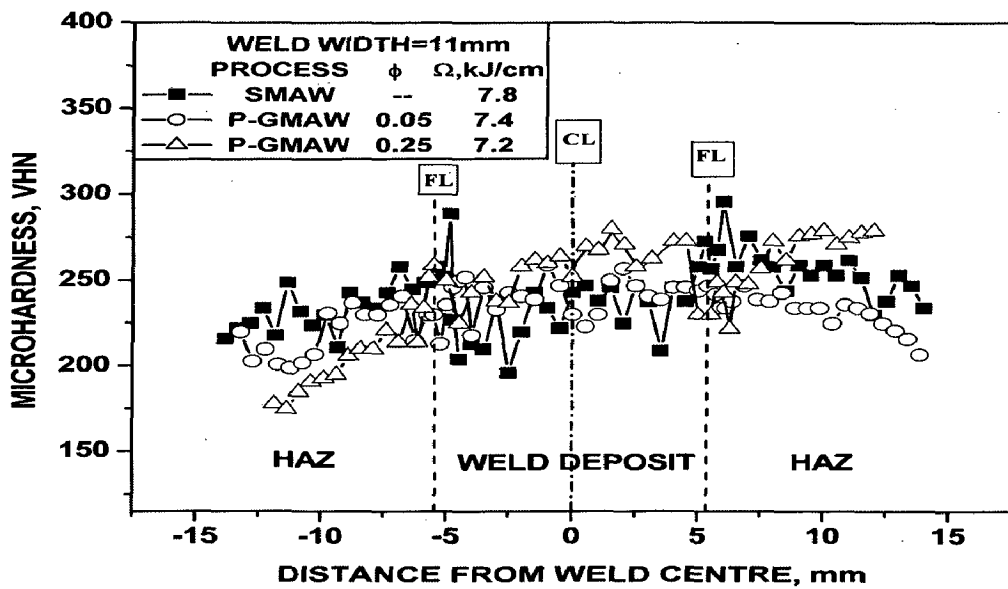
Fig. 5.70: At a given weld width of 11mm, hardness distribution observed across the narrow groove P-GMA and SMA welds with the variation in ϕ and Ω.

5.4.6 Residual Stresses

The longitudinal and transverse residual stresses present at different locations on top of the weld in reference to the centre and fusion lines of the narrow groove P-GMA and SMA weld joints at a given weld width of 14-15 mm are shown in Fig. 5.71 (a) and (b) respectively. Whereas at a given weld width of 11 mm the longitudinal and transverse residual stresses present at different locations on top of the weld in reference to the centre and fusion lines of the narrow groove P-GMA and SMA weld joints are shown in Fig. 5.72 (a) and (b) respectively. Similarly, at root of the weld, the longitudinal and transverse residual stresses in different locations, in reference to the centre and fusion lines at a given weld width of 14 mm and 11 mm are shown in Figs. 5.73 and 5.74 respectively. The figures show that for similar groove width at the top and the root of the weld, longitudinal residual stress reduces by 25-45% with the use of P-GMAW process in comparison to that obtained using SMAW process. Narrow gap welding technique further reduces harmful tensile longitudinal residual stresses with respect to those observed in case of the conventional V-groove weld joint. The transverse residual stress has also been found to follow a similar trend but having a magnitude comparatively lower than the longitudinal

247

residual stress of the weld joint as it is commonly observed [Murugan et al 2001, Webster et al 2002, Fricke et al 2001, Deng et al 2008].

P-GMAW process is found to be advantageous in respect of reduction in residual stress distribution in ASS pipe joint, primarily due to the use of relatively less severe weld thermal cycle along with reduction in number of weld passes (Table 5.22) for similar groove design in comparison to those for SMAW process. Whereas a considerable difference in the development of residual stresses in the conventional and narrow gap welds may be attributed primarily to the severity of thermo mechanical characteristics arising out of differential expansion and contraction stresses resulting from multipass deposition, which becomes comparatively milder in case of the narrow gap weld holding appreciably lower amount of weld deposit [Radaij 1992]. However, Figs. 5.72 to 5.75 show that there is considerable variation in distribution of residual stresses across the weld and its nature changes significantly with narrowing down of the weld groove. It appears that the top of the narrow groove SMA weld is having a dual peak of residual stresses with a depression of stress at the weld centre, which could not be so well identified at the root of the weld as its narrowness causing difficulties in multiple spot analyses within it. The presence of dual peak of residual stresses distributed in either side of weld centre line in weld joint of austenitic stainless steel has also been reported by earlier workers arising out of interactions of shrinkage and quenching stresses [Murugan et al 2001, Webster et al 2002, Radaj 1992, Brickstad and Josefson 1998]. But it is interesting to note that the dual peak behaviour of residual stress of the weld vanishes in P-GMA weld groove showing a relatively higher order of stresses at weld centre and it gradually reduces as we move towards HAZ. However, in P-GMA welds at different ϕ of 0.05 to 0.25, the residual stress distribution in both longitudinal and transverse direction varies negligibly at the top and the root of weld. The significance of this nature of distribution of residual stresses in P-GMA and SMA narrow groove welds may be carefully considered in the context of the influence of residual stresses on kinetics of sensitization in weld and heat affected zone near to the fusion line.
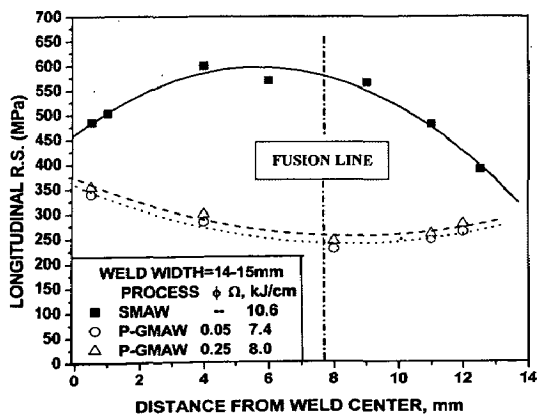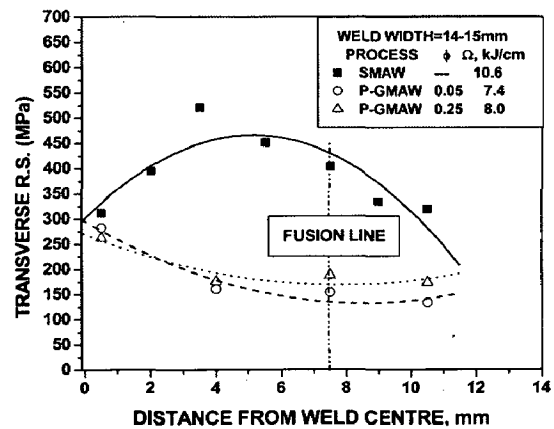
Fig. 5.71 At a given weld width of 14mm distribution of (a) longitudinal and (b) transverse residual stresses at the top in narrow groove P-GMA and SMA welds.
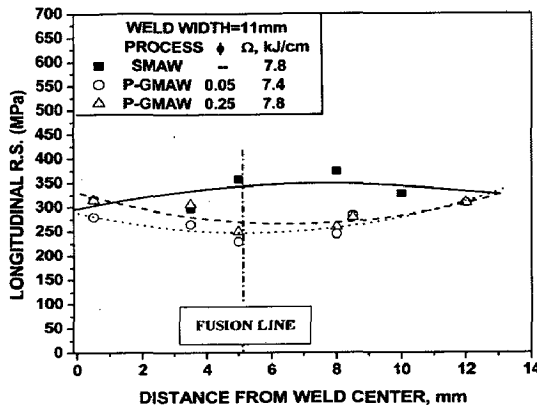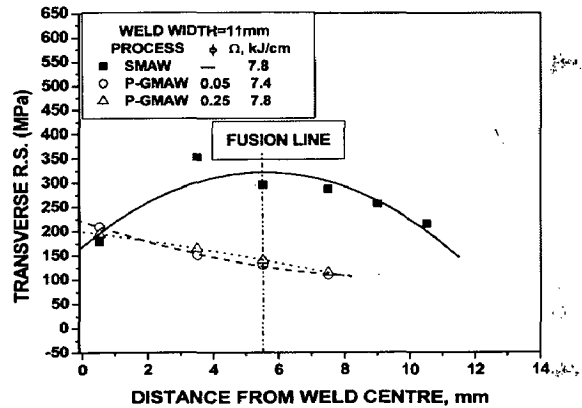
Fig. 5.72 At a given weld width of 11mm distribution of (a) longitudinal and (b) transverse residual stresses at the top in narrow groove P-GMA and SMA welds.
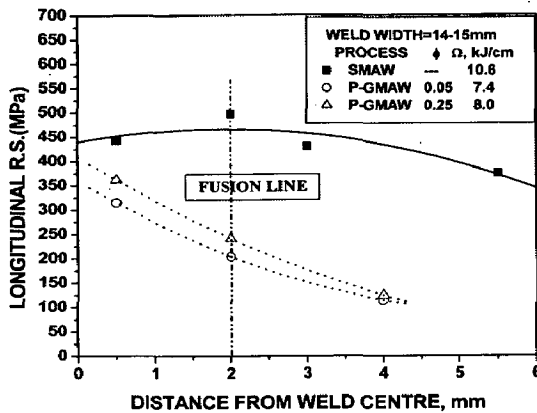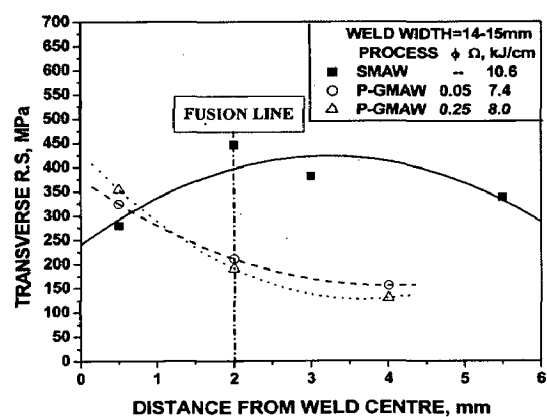
Fig. 5.73: At a given weld width of 14mm distribution of (a) longitudinal and (b) transverse residual stresses at the root in narrow groove P-GMA and SMA welds.

249
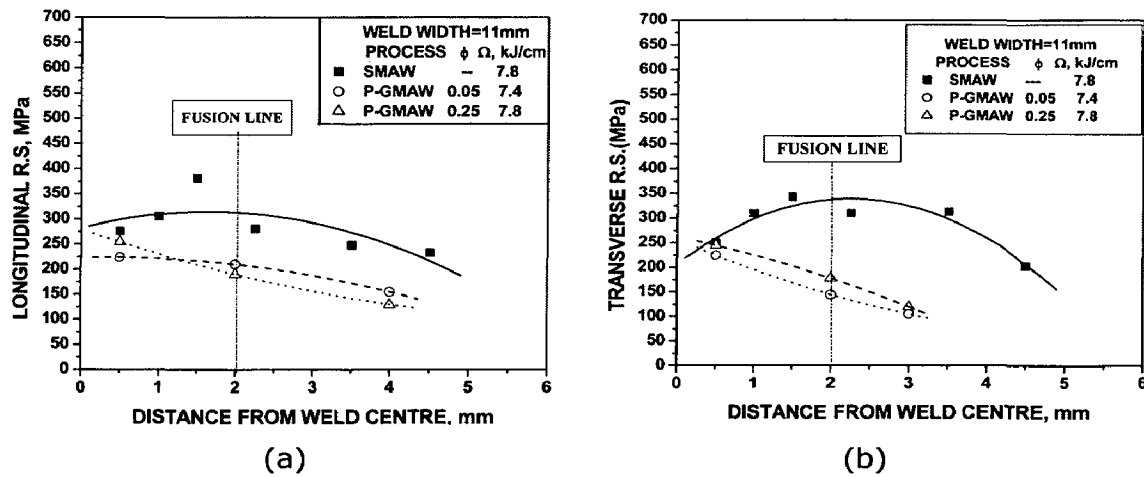
Fig. 5.74: At a given weld width of 11mm distribution of (a) longitudinal and (b) transverse residual stresses at the root in narrow groove P-GMA and SMA welds.

5.4.7 Fracture Mechanics

5.4.7.1 Fracture toughness

The initiation fracture toughness properties of the narrow groove P-GMA and SMA weld deposits in L-C direction are given in Table 5.30. The typical J-R curves of the P-GMA and SMA welds deposits in L-C direction are compared in Fig.5.75. The figure shows that the narrow groove P-GMA welds are having 2-5 times higher J_Q value (Table 5.30) compared to those observed in narrow groove SMA weld joints marked by comparatively stiffer progress of J-R curve. The corresponding maximum load (P_{max}) and physical crack extension (Δa) in P-GMA welds (Table 5.30) are also considerably greater than those observed in narrow groove SMA weld joints. It is further observed that at a given Ω of 7.7±0.35kJ/cm, by narrowing down the groove in P-GMA weld joints, J_Q increases significantly with the decrease of ϕ from 0.25 and 0.05. However, in case of the P-GMA welds, J_Q observed are not valid J_{1C} value as they do not

250

satisfy the plain strain criterion of thickness B > 25 J_Q/σ_y, where σ_y is the effective yield strength according to the ASTM E813-89 standard. Whereas, J_Q values observed in SMA welds are valid J_{1C} as they satisfy the plain strain criterion. At a given Ω of 7.7$\pm$0.35kJ/cm by narrowing down the groove of P-GMA welds, fracture resistance of the weld increases from 50-90% of that of base metal with the decrease of ϕ from 0.25 and 0.05, signifying improvement in fracture mechanics properties. Whereas, the comparatively lower J_Q value of 15-20% of that of base metal (Table 5.5) exhibits very poor fracture resistance of narrow groove SMA weld joints.

Narrow groove P-GMA and SMA weld joints show different trend of fracture resistance in comparison to their corresponding conventional V-groove welds (Table 5.19). In P-GMA welds at a given ϕ and Ω, fracture toughness improves significantly by narrowing down the weld width. Whereas fracture resistance initially improves marginally and then, considerably decreases by narrowing down the SMA weld groove from 14 mm to 11 mm weld width. In SMA weld joints, such a trend may have occurred due to increase in closely spaced inclusion content (Table 5.26 and Fig. 5.67(c)), which must have intensified the stress locally [Anderson 2005] leading to poor fracture resistance. However with narrowing down the groove in P-GMA welds at a given ϕ and Ω, the microstructure further refines (Figs. 5.62 and 5.63) with negligible rise in porosity content (Table 5.26). This may have resulted in comparatively higher amount of energy absorption before crack initiation leading to fracture. Hence, with the lowering of Ω and ϕ, the increase in the amount of energy absorbed may have given rise to comparatively stiffer progress of J-R curve.

251

Table 5.30: Fracture toughness properties of narrow groove P-GMA and SMA weld joints.

Process	Weld Width (mm)	φ	Ω (kJ/cm)	P_max (kN)	Δa (mm)	J_Q (kJ/m²)	J_Q = J_1c (kJ/m²)
* P-GMAW	15.0	0.05	7.5	37.4 / 36.5 → 37.0	0.44 / 0.56 → 0.50	742 / 732 → 737	No
		0.25	8.0	34.6 / 35.5 → 35.1	0.79 / 0.65 → 0.72	713 / 648 → 680	No
	11.5	0.05	7.5	46.0 / 44.1 → 45.1	0.63 / 0.71 → 0.67	1527 / 1492 → 1510	No
		0.25	7.9	36.4 / 37.3 → 36.9	0.81 / 0.88 → 0.85	890 / 866 → 878	No
SMAW	13.5	-	9.9	28.9 / 30.6 → 29.8	0.30 / 0.39 → 0.35	362 / 334 → 348	Yes
	11.5	-	7.4	29 / 28.7 → 28.9	0.23 / 0.30 → 0.27	256 / 230 → 243	Yes

* The estimation of J_{1c} in P-GMA welds could not be made due to vertical progress of the J-R curves (Fig. 5.75)
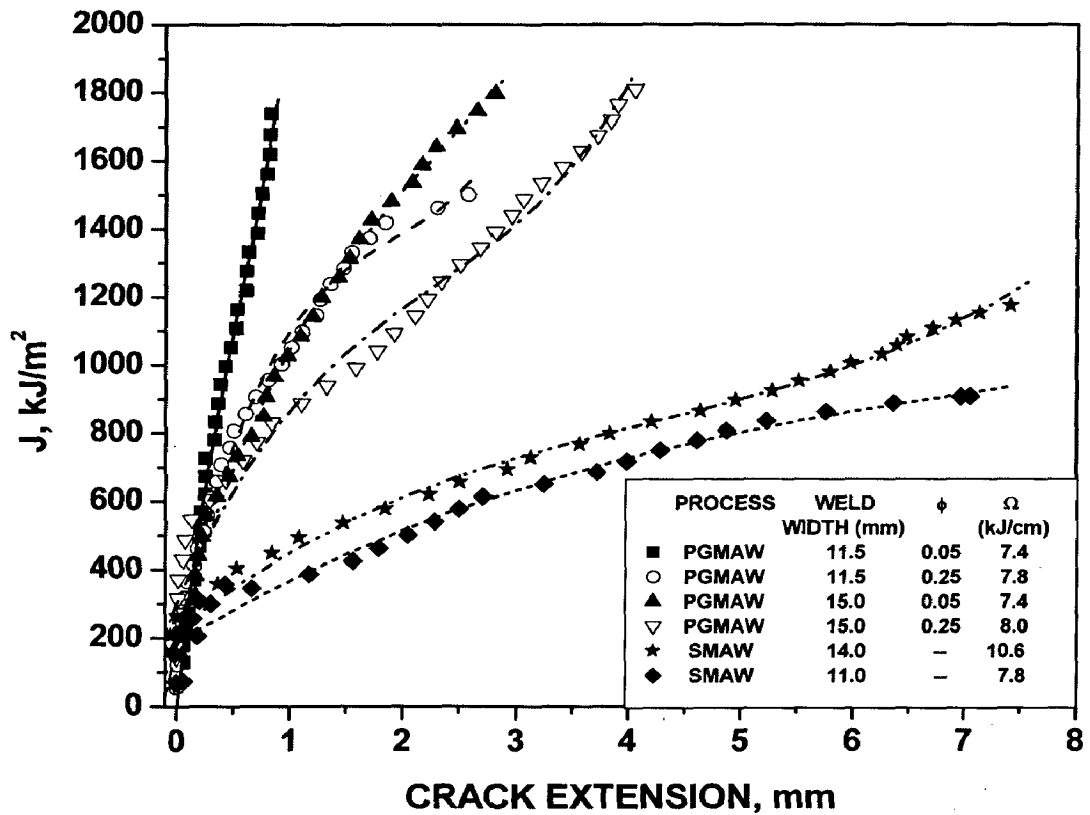
Fig. 5.75: Typical J-R curves observed in narrow groove weld deposits of P-GMA and SMA weld joints in L-C direction.

5.4.7.2 Fatigue crack growth rate

FCGR properties in L-C direction of the practically narrowest groove P-GMA and SMA welds at a stress ratio (R) of 0.1 and 0.5 are given in Table 5.31. The typical plots of stable FCGR (log(da/dN) vs. logΔK) of the narrow groove P-GMA and SMA welds at a stress ratio of R=0.1 and 0.5 are shown in Fig. 5.76 (a) and (b) respectively. At a given stress ratio of 0.5, macro photograph of fractured surface of base metal have been compared with that observed in narrow groove P-GMA and SMA weld (φ=0.05) as shown in Fig. 5.77 (a), (b) and (c) respectively.

Table 5.31: FCGR characteristics of practically narrowest groove P-GMA and SMA welds.

Process	Weld width (mm)	φ	Ω (kJ/cm)	Stress Ratio	Paris law constants m		C (m/cycle)		R*		ΔK$_{TH}$ MPa√m
P-GMAW	11.5	0.05	7.5	0.1	4.28 / 4.42	4.35	1.85×10^{-14} / 1.75×10^{-14}	1.8×10^{-14}	0.98 / 0.96	0.97	7.25
				0.5	4.05 / 4.41	4.23	1.28×10^{-13} / 1.22×10^{-13}	1.25×10^{-13}	0.97 / 0.98	0.97	4.85
	11.5	0.25	7.9	0.1	4.09 / 3.71	3.90	3.8×10^{-14} / 4.2×10^{-14}	3.8×10^{-14}	0.98 / 0.93	0.96	7.53
				0.5	3.14 / 3.20	3.17	3.4×10^{-12} / 3.1×10^{-12}	3.25×10^{-12}	0.94 / 0.95	0.95	2.94
SMAW	11	--	7.4	0.1	3.52 / 3.78	3.65	2.41×10^{-13} / 1.99×10^{-13}	2.2×10^{-13}	0.94 / 0.96	0.95	5.34
				0.5	2.98 / 3.18	3.08	3.85×10^{-12} / 3.65×10^{-12}	3.75×10^{-12}	0.96 / 0.95	0.96	2.90

R* is Coefficient of co relationship

Fig. 5.76: FCGR curves observed in conventional V-groove P-GMA and SMA weld deposit at a stress ratio(R) of (a) 0.1 and (b) 0.5.
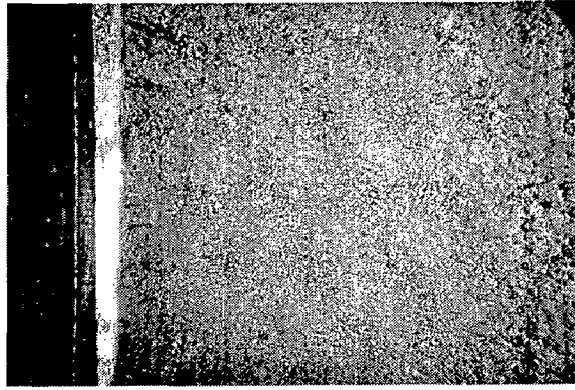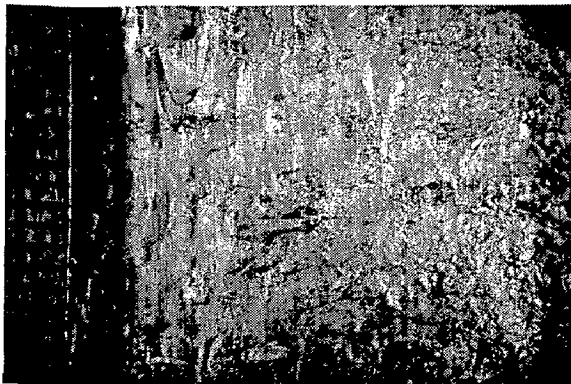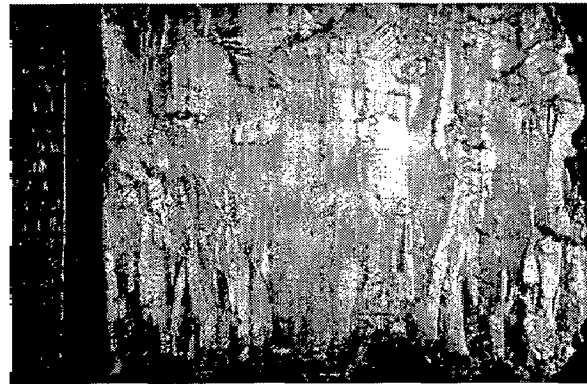
Fig. 5.77: At a given stress ratio of 0.5, macro photograph of fractured surface observed in (a) base metal, practically narrowest groove (b) P-GMA and (c) SMA weld deposits.

The table 5.31 and Fig. 5.76(a) and (b) primarily depicts that at almost constant Ω, with both the stress ratio(R) of 0.1 and 0.5, the fatigue crack growth rate of narrow groove P-GMA welds are superior to those observed in similar SMA welds with 11 mm weld width in the all-important early part of the life as reflected by its relatively higher value of ΔK_{TH}. Similar trend of higher ΔK_{TH} in P-GMA welds than that of SMA weld have also been observed in conventional groove welds (Table 5.20). But narrow groove welds (Table 5.31) show a significantly higher ΔK_{TH} in comparison

255

to conventional groove welds, except in P-GMA weld at higher ϕ of 0.25 with stress ratio of 0.5. Such a lower ΔK_{TH} observed in P-GMA weld at higher ϕ of 0.25 with stress ratio of 0.5 may have occurred due to its comparatively higher propensity to lack of fusion (Table 5.22). However, in all the other narrow groove welds a comparatively higher ΔK_{TH} may have resulted due to its superiority over conventional groove welds in respect of residual stress distribution and refinement in microstructure (section-5.4.6 and 5.4.3) for a given chemical composition of weld metal. Whereas, at a higher ΔK at around $40\, MPa\sqrt{m}$ (Fig 5.76), narrow groove SMA welds also show better FCGR properties than those of P-GMA and GMA welds in concurrence with the observations of conventional groove welds (section 5.3.7.2).

The influence of residual stresses on FCGR has also been analysed by observing the fracture surface of the specimen as per ASTM E647. Irregular crack growth, namely excessive crack front curvature or out-of-plane crack growth generally indicates that residual stresses are affecting the measured da/dN versus ΔK relationship. Irregular crack growth as indicated by comparatively rough surface can be clearly observed in welds in comparison to that in base metal as shown in Fig. 5.77. However, the P-GMA weld has comparatively less irregular crack growth as reflected by its relatively scanty rough surface in comparison to SMA weld joint, indicating considerable reduction in residual stresses [ASTM E-647-88a].

5.4.8   Inter Granular Corrosion

The influence of P-GMAW and SMAW processes on narrowest groove welds at almost constant Ω of 7.8 kJ/cm on the FE-SEM microstructures of HAZ adjacent to fusion line revealed through rapid oxalic acid etch test are shown in Fig. 5.78. Similarly at almost constant Ω of 7.8

kJ/cm, the influence of P-GMAW and SMAW processes on their microstructures of HAZ, 1 mm away from the fusion line are shown in Fig. 5.79. In both the cases the influence of ϕ at two different levels of 0.05 and 0.25 in P-GMA welds are compared in Figs. 5.78 (a) and (b) and 5.79(a) and (b) respectively.

Figs. 5.78 and 5.79 reveal that at a given Ω, P-GMA welds are practically free from carbide precipitation in HAZ as marked by insignificant ditches across the matrix, at different ϕ. However, with the increase in ϕ from 0.05 to 0.25, the density of ditches marginally increases. Whereas, prominent ditches are still observed in SMA welds (Figs. 5.78(c) and 5.79(c)) at both the locations of HAZ near fusion line and 1 mm away from it. This indicates that due to comparatively higher number of weld passes (Table 5.17) in SMA welds than that in P-GMA welds, the cumulative effect of weld thermal cycle exerted during each pass on isotherms in HAZ appears to have prevailed in the sensitisation temperature range (450^0C-850^0C) for the required duration. Thus, chromium distribution across the ditch shown in Fig. 5.79 (a) and (b) observed in P-GMA weld at a ϕ of 0.25 are compared with that for SMA weld at a distance of 1mm away from the fusion line respectively. The location at which chromium distribution has been analysed, is correspondingly marked in Fig. 5.80. The chromium distribution clearly reveals that chromium content in P-GMA weld (Fig. 5.80(a)) have crossed the corrosion resistance limit of 11.5% across the ditch rendering the joint free from susceptibility to corrosion attack. However, considerably lower concentration of chromium adjacent to thick corroded region of the ditch boundary and also at few locations near the boundary indicates that narrow groove SMA welds (Fig. 5.80(b)) are susceptible to corrosion attack.
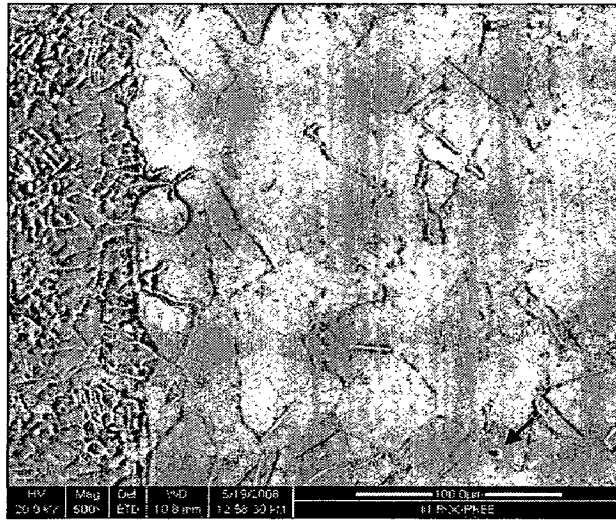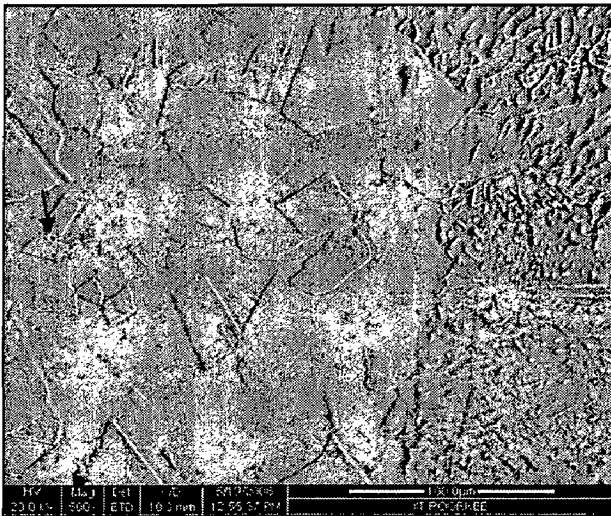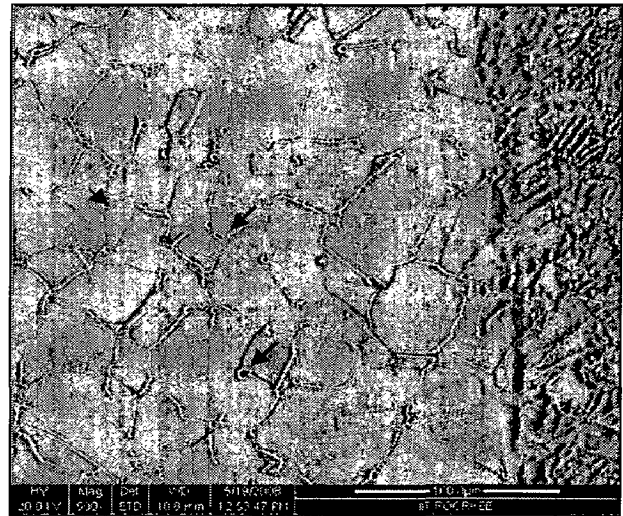
Fig. 5.78: At almost constant Ω of 7.8kJ/cm, typical microstructures of HAZ adjacent to fusion line observed after rapid oxalic acid test in narrowest groove P-GMA welds at (a) ϕ=0.05, (b) ϕ=0.25 and in (c) narrowest groove SMA welds.
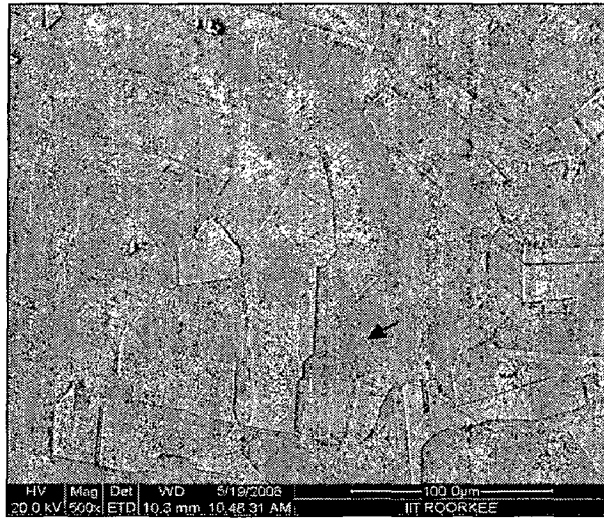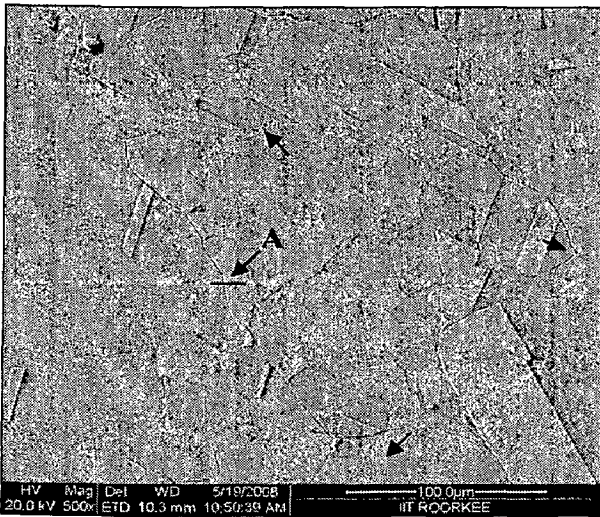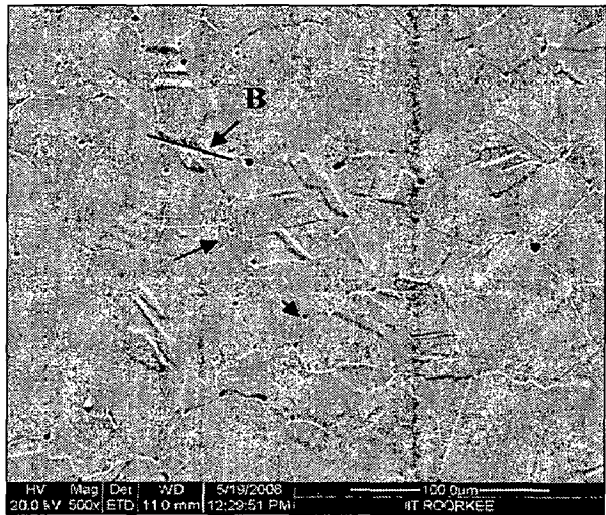
Fig. 5.79 At almost constant Ω of 7.8kJ/cm, typical microstructures of HAZ observed approximately 1mm from the fusion line after rapid oxalic acid test in narrowest groove P-GMA welds at (a) ϕ=0.05, (b) ϕ=0.25 and in (c) narrowest groove SMA welds.
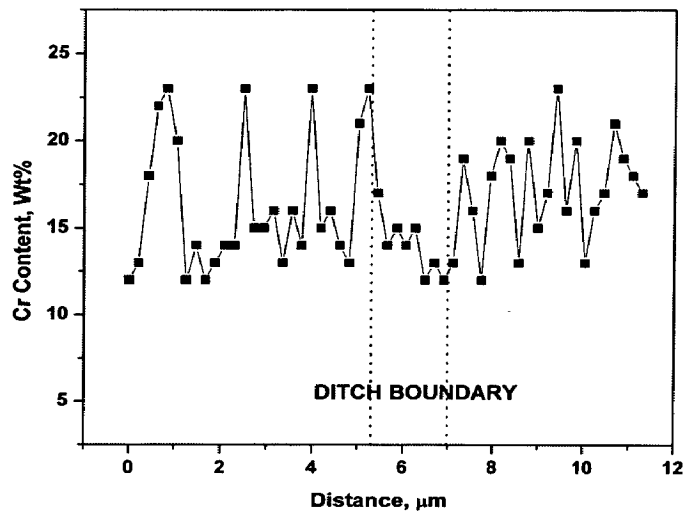
(a)
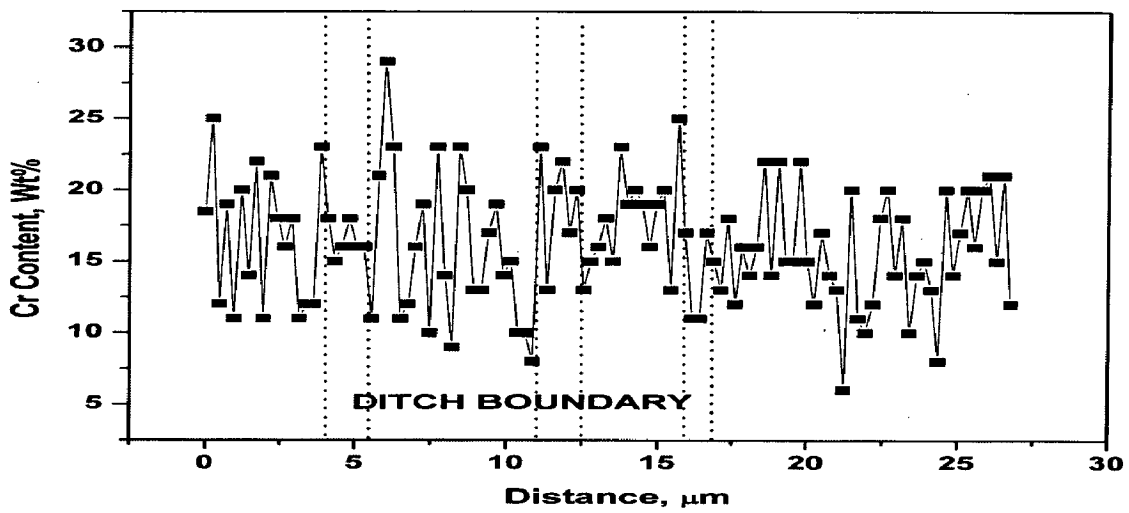
(b)

Fig. 5.80: Typical behaviour of chromium distribution across the ditch boundary in HAZ of narrowest groove (a) P-GMA weld at ϕ of 0.25 and (b) SMA weld.

5.4.9 Summary

This section has been summarised into two parts. In the first part the advantages of narrow groove P-GMA welds over the conventional one have been pointed out considering the fact that in narrow groove, heat density in the groove wall surface beneath the arc considerably reduces the severity of weld thermal cycle. The other part highlights the advantage of narrow groove P-GMA welds over the narrow groove SMA welds.

Part-A

The use of narrow groove welding considerably reduces the area of weld deposit by about 35-40 vol% in comparison to that observed in the conventional groove weld. Such a reduction in area have primarily reduced severity of weld thermal cycle resulting in considerable reduction in residual stresses, coaxial dendrite in weld and grain coarsening near FL in HAZ by around 15-25% than that observed in conventional groove at a given Ω and ϕ. Thus, the combined effect of the above aspects has improved the tensile properties, fracture toughness and FCGR properties. Narrow groove welds are also observed to be free from corrosion attack in contrast to the susceptibility of conventional groove welds to corrosion.

Part-B

Significant improvement observed in narrow gap P-GMA weld characteristics over those of SMA welds occurs due to three principal reasons; firstly, the cleaner argon shielded P-GMA welds have 80-90% less inclusion content than their counterparts of SMA weld. Secondly, ϕ controls the amount of heat transferred to the weld pool (Q_T) by varying mass, velocity and heat content of the droplet achieving equivalent amount of metal deposition at a significantly lower heat input (Ω) in comparison to that in SMAW process. Lastly, the control of pulse parameters has considerably reduced the number of weld passes and hence the cumulative effect of weld thermal cycle. These three aspects have improved all the properties of P-GMA welds with respect to SMA welds as shown in the summarized Table 5.32.

Table 5.32: Summarized influence of welding parameters on various properties of the narrow groove P-GMA and SMA weld joints

Process	Ω (kJ/cm)	φ	I (A)	I_m (A)	I_p (A)	I_b (A)	t_p (ms)	f (Hz)	Arc Voltage (V)	Welding Speed (cm/min)	Q_T (kJ/cm)	Total number of passes	Overall Cumulative Transverse shrinkage (mm)	Cr_{eq}	Ni_{eq}	δ-ferrite content (%) Root passes	δ-ferrite content (%) Filler passes	Solidification mode	Area of weld deposit (mm²)	Inclusion &porosity Content (Vol. %)	Grain size adjacent to F.L. Dia. (μm ± σ)	ASTM No.
SMAW	10.6	-	160	-	-	-	-	-	28	17.6	--	19	4.76±0.68	18.50	14.15	-	AF	1.50	274	2.62	20±3	8.5
	7.8	-	140	-	-	-	-	-	23	16.7	--	17	3.90±0.37	18.43	14.55	-	AF	1.50	220	3.19	18±2	9.0
P-GMAW	9.2	0.06	-	196	410	34	2.03	105	22.4	20		12	5.0±0.35	19.26	12.29	4	FA	4.06	267	0.32	17±5	9.0
	7.4	0.05	-	160	450	28	2.03	114	22.5	20	11.4	12	4.25±0.31	19.22	12.42	4-5	FA	4.50	239	0.19	13±5	9.5
	8.0	0.25	-	176	313	106	2.03	126	21.8	20	11.1	15	4.33±0.40	19.05	12.42	6-8	FA	4.66	242	0.56	13±3	9.5
	7.4	0.05	-	160	450	28	2.03	114	22.5	20	9.9	10	4.04±0.16	19.35	12.53	4-5	FA	3.00	215	0.23	12±5	9.5
	7.8	0.25	-	176	313	106	2.03	126	21.8	20	11.1	11	4.20±0.28	19.25	12.47	4-5	FA	3.00	225	0.68	13±3	9.5

Process	Ω (kJ/cm)	φ	Axial Tensile UTS (MPa)	Axial Tensile YS (MPa)	Axial Tensile Elongation (%)	All Weld Tensile UTS (MPa)	All Weld Tensile YS (MPa)	All Weld Tensile Elongation (%)	Charpy Energy absorbed (J)	Charpy Lateral expansion (mm)	Fracture toughness J_Q (kJ/m²)	R=0.1 m	R=0.1 C (m/cycle)	ΔK_{TH} MPa√m (R=0.1)	R=0.5 m	R=0.5 C (m/cycle)	ΔK_{TH} MPa√m (R=0.5)
SMAW	10.6	-	556	350	22.8	580	446	28.1	94	1.78	348	-	-	-	-	-	-
	7.8	-	582	354	23.4	598	431	39.7	91	2.47	243	3.65	2.2×10^{-13}	5.34	3.08	3.75×10^{-12}	2.90
P-GMAW	9.2	0.06	653	363	45.8	616	466	40.0	132	2.59	-	-	-	-	-	-	-
	7.4	0.05	654	368	45.0	622	461	40.5	132	2.59	737	-	-	-	-	-	-
	8.0	0.25	633	344	43.8	618	466	40.4	128	2.60	680	-	-	-	-	-	-
	7.4	0.05	651	364	45.8	668	414	53.6	134	2.63	1510	4.35	1.8×10^{-14}	7.25	4.23	1.25×10^{-13}	4.85
	7.8	0.25	631	344	34.7	641	426	31.7	126	2.50	878	3.90	3.8×10^{-14}	7.53	3.17	3.25×10^{-12}	2.94

The specific conclusions drawn from different facets of the present work have already been given in the corresponding chapters. However, finally the generic conclusions drawn from the present work can be summarized as follows.

Designing and Development of Narrow GMAW Torch Nozzle Device

1. A narrow torch nozzle device of rectangular face (12x24 mm) and 32 mm extension works satisfactorily with appropriate cooling system to facilitate narrow gap P-GMA welding of thick wall stainless steel pipe.

2. The newly developed narrow torch nozzle device performs satisfactorily in conventional GMA and pulse current GMA welding showing comparable arc stability and gas shielding as observed through oxidation characteristic of weld deposit to those observed in case of using the conventional GMAW torch nozzle device.

P-GMA Weld Bead on Plate Studies

1. Geometrical characteristics of weld bead with respect to its penetration, width and height as well as area of reinforcement and base metal fusion vary with welding parameters showing good correlations with the heat input (Ω), summarized influence of pulse parameters (ϕ) and total heat transferred to the weld pool (Q_T) at an estimated bead dilution of the order of $39 \pm 4\%$.

2. Lowering of Ω, ϕ and Q_T refines microstructure of weld deposit by minimizing the amount of coaxial dendrite in the matrix.

3. Microstructure of HAZ studied as extent of grain growth region and grain size adjacent to fusion line linearly increases with the increase of Ω, ϕ and Q_T.

4. Hardness linearly increases in weld deposit, along fusion line and in coarse grain region of HAZ with the increase of Ω, ϕ and Q_T.

Conventional Groove Weld Characteristics

5. At a given Ω of 7.8$\pm$ 0.3 kJ/cm the decrease of ϕ from 0.25 to 0.05 reduces the residual stresses at the top and root of the P-GMA weld.

6. In comparison to GMA and SMA welding the P-GMA welding can produce sound weld at a comparatively lower Ω of 7.8$\pm$ 0.3 kJ/cm with a low ϕ of 0.05. Thus, the use of P-GMA welding reduces residual stresses of weld by almost 15-20% than GMA weld and 30-40% than SMA weld.

7. The Ω and ϕ lying in the range of 7.7-9.4 kJ/cm and 0.05-0.25 respectively, insignificantly influence the porosity content in P-GMA weld.

8. The use of P-GMA welding reduces porosity and inclusion content of weld by almost 25-30% than GMA weld and about 90% than SMA weld.

9. Lowering of Ω and ϕ refines microstructure of multipass weld deposit by minimizing the amount of coaxial dendrite in the matrix.

10. The use of P-GMA welding reduces amount of coaxial dendrite of weld by almost 60-80% than GMA and SMA welds.

11. Tensile properties of P-GMA weld decreases with the increase of Ω and ϕ in the range of 7.7$\pm$0.35 to 9.3$\pm$0.35 kJ/cm and 0.05 to 0.25 respectively.

12. The use of P-GMA welding increases tensile properties of the weld by almost 5-10% than GMA weld and about 15-20% than SMA weld.

13. Initiation fracture toughness of the P-GMA weld decreases with the increase in Ω and ϕ in the range of 7.7$\pm$0.35 to 9.3$\pm$0.3kJ/cm and 0.05 to 0.25 respectively.

14. The use of P-GMA welding increases initiation fracture toughness (J_Q) by almost 50-80% than GMA weld and about 200-250% than SMA weld.

15. P-GMA weld becomes comparatively more susceptible to corrosion attack with the increase in Ω and ϕ in the range of 7.7±0.35 to 9.3±0.35 kJ/cm and 0.05 to 0.25 respectively.

16. The use of P-GMA welding reduces susceptibility to corrosion attack in comparison to GMA and SMA welds.

Narrow Groove Weld Characteristics

17. Use of pulse current GMAW with newly developed narrow torch nozzle device can successfully produce narrow groove weld of 25 mm thick wall 300 NB austenitic stainless steel pipe having weld width of 13-14mm.

18. Newly developed narrow gap welding procedure using P-GMAW process reduces area of weld deposit by about 35-40 vol%.

19. In similar narrow groove design, use of P-GMAW process reduces number of passes by 25-30% than SMAW process at almost constant Ω.

20. The use of P-GMAW process reduces residual stresses by 20-35% than SMAW in similar narrow groove design at almost constant Ω.

21. The use of P-GMAW process with narrow gap welding procedure reduces amount of coaxial dendrite of weld by almost 10-15% than conventional groove welds.

22. Change from conventional to narrow gap welding procedure insignificantly influences the tensile properties of P-GMA welds

23. Initiation fracture toughness of the narrow groove P-GMA welds decreases with the increase in Ω and ϕ in the range of 7.7 ± 0.35 to 9.3 ± 0.3 kJ/cm and 0.05 to 0.25 respectively.

24. The use of narrow groove P-GMA welding increases initiation fracture toughness (J_Q) by about 250-300% than narrow groove SMA weld.

25. P-GMA weld prepared with narrow gap welding procedure appears free from corrosion attack at Ω and ϕ of 7.7 ± 0.35 kJ/cm and 0.05 respectively.

26. SMA weld prepared with narrow gap welding procedure shows susceptibility to corrosion attack at Ω of 7.5 ± 0.35 kJ/cm.

In the light of the understanding on the work presented in this report it is realised that following studies should be carried out further to improve the reliability of performance of narrow groove P-GMAW of thick wall stainless steel pipe.

1. The weld quality and its properties as a function of Ω, ϕ and Q_T should be studied more in detail with wider range of their variations.

2. The narrow gap P-GMA welding technique with narrow torch nozzle should be tried in higher thick wall stainless steel pipe.

3. The use of narrow gap P-GMA welding technique with narrow torch nozzle should be explored further to produce narrower weld than that obtained (weld width 11-12mm) in this work.

REFERENCES

1. **Allum, C. J.** and Quintino, L., [1985(a)] "Control of fusion characteristics in pulsed current MIG welding – Part I. Dependence of Fusion Characteristics of process parameters", *Metal Construction*, Vol. 17(4), pp. 242R-245R.

2. **Allum, C. J.** and Quintino, L., [1985(b)], "Control of fusion characteristics in pulsed current MIG welding – Part II, Simple model of fusion characteristics", *Metal construction*, Vol. 17, pp 314R -317R.

3. **Allum, C. J.**, [1983], 'MIG welding – Time for a reassessment", *Metal construction*, Vol. 15(6), pp 347-353.

4. **Amin, M.** and Ahmed, N., [1987], "Synergic control in MIG welding", *Metal Construction*, Vol. 19(1), pp 22-28.

5. **Amin, M.**, [1981], "Synergic pulsed MIG welding" *Metal Construction*, Vol. 13(6), pp349-353.

6. **Amin, M.**, [1983], "Pulse current parameters for arc stability and controlled metal transfer in arc welding", *Metal Construction*, Vol. 15(5), pp 272-287.

7. **Amin, M.**, [1986], "Microstructure control of synergic pulsed MIG welding", *Metal construction*, Vol. 18(4), pp 216-221.

8. **Anderson, T.L**, [2005], "Fracture Mechanics-Fundamentals and applications", Taylor & Francis, 3rd edition, USA

9. **Andren, H.O.**, Henjered, A. and Norden, H., [1980], "Composition of MC Precipitates in a Titanium Stabilized Austenitic Stainless Steel", *Journal of Material Science*, Vol.15, pp.2365-2368

10. **ASM Handbook**, [1992], "Phase Diagrams", Vol. 3, ASM International, Materials Park, OH.

11. **ASM handbook**, [1994], "Welding, Brazing and Soldering", Vol. 6, ASM International, Materials Park, OH.

12. **Baldev Raj**, Mudali, K., Vasudevan, M. and Shankar, P, [2002], "Current status on AISI types 304 LN and 316 LN austenitic stainless steels", Special Issue on High Nitrogen Steels Part A, *Trans. Ind. Inst. for Metals*, Vol.55 (4), pp.131-147.

13. **Barcik, J.**, [1983], "The kinetics of sigma phase precipitation in AISI 310 and AISI 316 steels", *Metallurgical and Materials Transactions A*, 14A, pp.635-641.

14. **Basak, A,** Roy,D.K. and **Dutta, G.L.,** [1995], "Adhesive wear characteristics of cast nitrogenated stainless steel", *Wear* , Vol.184, pp. 241-244.

15. **Basavaraju, C.,** [2000], "Simplified analysis of shrinkage in pipe to pipe butt welds", *Nuclear Engineering and Design,* Vol.197, pp.239-247.

16. **Bayley, C.,** Glinka, G. and Porter, J., [2000], "Fatigue crack initiation and growth in A517 submerged arc welds under variable amplitude loading", *International Journal of Fatigue,* Vol.22, pp.799-808.

17. **Braint, C.L.,** Andresen, P.L., [1988], "Grain boundary segregation in austenitic stainless steels and its effect on intergranular corrosion and stress corrosion cracking", *Metallurgical and Materials transactions A,* Vol.19A, pp. 495- 504.

18. **Briant, C.L.,** [1987], "Grain boundary segregation of phosphorus and sulfur in type 304L & 316L stainless steel and its effect on intergranular corrosion in the huey test", *Metallurgical and Materials transactions A,* Vol.18A, pp. 691-699.

19. **Brickstad, B.** and Josefson, B.L., [1998], "A parametric study of residual stresses in multi-pass butt-welded stainless steel pipes", *International Journal of Pressure Vessels and Piping,* Vol.75, pp.11-25.

20. **Brooks, J.A.,** Williams, J.C. and Thompson, A.W., [1983], "Microstructural origin of the skeletal ferrite morphology of austenitic stainless steel welds", *Metallurgical and Materials transactions A,* 14A, pp.1271-1284.

21. **Cai, G.J.,** Andren, H.O. and Svensson, L.E., [1997], "Effect of cooling after welding on microstructure and mechanical properties of 12pct Cr steel weld metals", *Metallurgical and Materials Transactions A,* Vol.28A, pp.1417-1428.

22. **Çam, G.,** Erim, S., Yeni, Ç. and Koçak, M., [1999], "Determination of mechanical and fracture properties of laser beam welded steel joints", *Welding Journal,* Vol.78 (6), pp.193s-201s.

23. **Cerjak, H.,** Nagel. G. and Prader, R., [1999], "Quantification of the toughness distribution in a heavy section submerged arc multilayer reactor pressure vessel weldment", *Nuclear Engineering and Design,* Vol.190, pp.29–39

24. **Chang, P.H.,** Teng, T.L., [2004], "Numerical and experimental investigations on the residual stresses of the butt-welded joints", *Computational Materials Science,* Vol.29, pp.511-522.

25. **Choi, S. K.,** Yoo, C.D. and Kim, Y.S., [1998a], "Dynamic simulation of metal transfer, part I: Globular and spray transfer modes", *Welding journal,* Vol. 77(1), pp 38-s-44-s.

26. **Cieslak, M.J** and Savage, W.F., [1980], "Weldability and solidification phenomena of cast stainless steel", *Welding Journal*, Vol.59 (5), pp.136s-146s.

27. **Cieslak, M.J.** and Ritter, A.M., [1985], "Precipitate formation in austenitic stainless steel welds", *Scripta Metallurgica*, Vol.19, pp.165-168.

28. **Cieslak, M.J.**, Ritter, A.M. and Savage, W.F., [1984], "Chi-Phase formation during solidification and cooling of CF-8M weld metal", *Welding Journal*, Vol.63(4), pp.133s – 139s.

29. **Clark, D.E.**, Buhrmaster, C. L. and Smartt, H.B., [1989], " Drop transfer mechanisms in GMAW", Recent trends in welding science and technology, 2nd international conference of welding research, Gatlinburg, USA, 14-18 May, 1989, pp. 371-375.

30. **Clark, J.** and **Goswami, T.**, [2002], "Life prediction of stainless steels used in nuclear reactors", *Mechanical Behavior of Materials*, Vol. 13(5-6), p 273-282.

31. **Collard, J.E.**, [1988], "Adaptive pulsed GMAW control: The digipulse system", *Welding Journal*, Vol. 67(11), pp.35-38.

32. **Colombieer, L.** and Hochmann, L., [1967], "Stainless heat resisting steels", Edward Arnold Publishers Ltd., pp 68-69.

33. **Cook, G.E.** and Levick, P.C., [1985], "Narrow gap welding with hot wire GTA process", Welding Journal, Vol. 64(8), pp. 27-31

34. **Cornu**, Jean, [1988], "Advanced welding system" Vol. 2, *IFS Publication Ltd. UK*, pp. 127-165.

35. **Covert, R.A.** and Tuthill, A.H., [2000], "Stainless steels: An introduction to their metallurgy and corrosion resistance", *Dairy, Food and Environmental Sanitation*, Vol. 20(7), pp. 506-517.

36. **Craig, E.F**, [1987a], "A unique mode of GMAW transfer", *Welding Journal*, Vol. 66(9), pp51-55.

37. **Craig, E.F.**, [1987b], "Pulsed spray welding- A mode of weld metal transfer that should revolutionize the GMAW process", *Welding Journal*, Vol. 66(9), pp79.

38. **Cui, Y.**, Lundin, C.D. and Hariharan, V., [2005], "Mechanical behavior of austenitic stainless steel weld metals with microfissures", *Journal of Material Processing Technology*, Article in press.

39. **Cui, Y.**, Lundin, C.D., [2005], "Effect of microfissures on mechanical properties of 3081 austenitic stainless steel weld metals", *Journal of Material Science*, Vol. 40, pp.1281 – 1283.

40. **Cui, Y.,** Phd. Thesis [August 2004], "Effect of Microfissures on Corrosion Performance and Mechanical Properties of Austenitic Stainless Steel Weld Metals", The University of Tennessee, Knoxville.

41. **David, S.A.,** Vitek, J.M., Keiser, J.R. and Oliver, W.C., [1987], "Use of a mechanical properties microprobe in the study of weld transformations", *Metallurgical Transactions A*, Vol.18A, pp.1996-1999.

42. **Davies, A.C.,** "The science and practice of welding- Volume 1-Welding science and technology, Ninth edition", Cambridge University Press, pp. 36-37.

43. **Delong, W.T.,** [1974], "Ferrite in austenitic stainless steel weld metal", *Welding Journal*, Vol. (7), pp. 273-S to 286-S.

44. **Deng,D.,** Murakawa, H. and Liang,W., [2008], "Numerical and experimental investigations on welding residual stress in multi-pass butt-welded austenitic stainless steel pipe", *Computational Materials Science*, Vol. 42, pp. 234–244.

45. **Dieter, G.E.,** [1988], "Mechanical Metallurgy", McGraw-Hill book company, UK

46. **Dillenbeck V.R.** and Castagno, L., [1987], "The effect of various shielding gases and associated mixtures in GMA welding of mild steel", *Welding Journal*, Vol. 66, pp. 45 to 49.

47. **Dong, P.,** [2001], "Residual stress analyses of a multi-pass girth weld: 3-D special shell versus axisymmetric models", *Journal of Pressure Vessel Technology*, Vol.123, pp.207-213.

48. **Dorling, D.V.,** [1992], "Applying pulsed GMA welding to pipeline construction", *Welding Journal*, Vol. 71(10), pp. 39-46.

49. **Elmer, J.W.,** Allen, S. M. and Eagar, T. W., [1989], "Microstructural development during solidification of stainless steel alloys", *Metallurgical and Materials Transactions A,* Vol. 20A, pp. 2117-2134.

50. **Elmer, J.W.,** Olson, D.L. and Matlock, D.K., [1982], "Thermal expansion characteristics of. austenitic stainless steel filler metals", Welding Journal, Vol. 61 (9), pp. 293s–301s.

51. **Erve M.,** Wesseling, U., Kilian, R., Hardt, R., Brtimmer, G., Maier, V. and Ilg, U., [1997], "Cracking in stabilized austenitic stainless steel piping of German boiling water reactors characteristic features and root cause", *Nuclear Engineering and Design*, Vol. 171, pp. 113-123.

52. **Fan, F.G** and Kovacevic. R., [2004], "A unified model of transport phenomena in gas metal arc welding including electrode, arc plasma and molten pool", *Journal of Physics D: Applied Physics,* Vol. 37, pp 2531–2544.

53. **Farrar, R. A.,** [1987], "Microstructure and phase transformations in duplex 316 manual metal arc weld metals: the role of carbon", *Journal of Materials Science,* Vol. 22, pp. 363-373.

54. **Folkhard, E.,** [1984], "Welding Metallurgy of Stainless Steels", Springer-Verlag, Wien.

55. **Fonseca E.M.M.,** de Melo F.J.M.Q. and Oliveira, C.A.M., [2005], "The thermal and mechanical behaviour of structural steel piping systems", *International Journal of Pressure Vessels and Piping,* Vol. 82, pp 145-153.

56. **Francis, J.A.,** Bhadeshia, H.K.D.H. and Withers, P.J., [2007], "Welding residual stresses in ferritic power plant steels", *Materials Science and Technology,* Vol. 23(9), pp. 1009-1020.

57. **Fricke, S.,** Keim, E. and Schmidt, J., [2001], "Numerical weld modelling-amethod for calculating weld-induced residual stresses", *Nuclear Engineering and Design,* Vol. 206, pp.139-150.

58. **Futamura, K.,** [1978], "Application of narrow gap automatic welding process to heavy steel structures of building", *Australian Welding Journal,* pp.37-40

59. **Gery, D.,** Long, H. and Maropoulos, P., [2005], "Effect of welding speed, energy input and heat source distribution on temperature variations in butt joint welding", Journal of Materials Processing Technology, Vol. 167, pp. 393-401.

60. **Ghosh, P. K.** and Gupta, P.C., [1996], "Use of pulse current MIG welding improves the weld charachteristics of Al-Zn-Mg alloy", Indian Welding Journal, Vol. 29(2), pp 24-32.

61. **Ghosh, P. K.,** [1999], "Decide pulse parameters for desired properties of pulsed current GMAW weld", international Welding Conference (IWC 99) on Welding and Allied Technology" Challenges in 21st century" at New Delhi, Feb. 15-17, 1999, pp 18-28.

62. **Ghosh, P.K.** and Dorn, L., [1993], "Thermal behaviour of pulsed MIG Al-Zn-Mg weld – An analytical model analysis", *International Journal on Joining of Materials,* Vol. 5(4), pp 143-150.

63. **Ghosh, P.K.** and Rai, B.K., [1998], "Correlations of pulse parameters and bead characteristics in pulsed current flux cored GMAW process", *Indian Welding Journal,* Vol. 31(4), pp.30-39

64. **Ghosh, P.K.** and Sharma, V., [1991], "Weld bead chemistry and its characteristics in pulsed MIG welded Al-Zn-Mg alloy", *Materials Transactions JIM*, Vol. 32(2), pp.145-150.

65. **Ghosh, P.K.**, [1996], "An analysis of weld characteristics as a function of pulse current MIG welding parameters", *International Journal on Joining of Materials*, Vol. 8(4), pp. 157-161

66. **Ghosh, P.K.**, [1999], "Decide pulse parameters for desired properties of pulsed current GMA weld", Procd. Int. Weld. Conf. (IWC'99), Welding and Allied Technology Challenges in 21st Century, New Delhi, 15-17 Feb., Vol. I, pp.18

67. **Ghosh, P.K.**, and Rai, B.K., [1996], "Characteristics of pulsed current bead on plate deposit in flux cored GMAW process", *ISIJ International*, Vol. 36(8), pp.1036-1045

68. **Ghosh, P.K.**, Dorn, L. and Issler, L., [1994], "Fatigue crack growth behaviour of pulsed current MIG weld of Al-Zn-Mg alloy", *International Journal on Joining of Materials*, Vol. 6(4), pp. 163-168.

69. **Ghosh, P.K.**, Dorn, L., and Goecke, S.F. [2001], "Universality of corelationships among pulse parameters for different MIG welding power sources", *International Journal on Joining of Materials*, Vol. 13(2), pp. 40-47

70. **Ghosh, P.K.**, Dorn, L., Hubner, M. and Goyal, V.K., [2007a], "Arc characteristics and behaviour of metal transfer in pulsed current GMA welding of aluminium alloy", *Journal of Materials Processing Technology*, Vol. 194, pp. 163-175.

71. **Ghosh, P.K.**, Dorn, L., Kulkarni, S. and Hoffmann, F., [2008], "Arc Characteristics and Behaviour of Metal Transfer in Pulsed Current GMA Welding of Stainless Steel", *Journal of Material Processing Technology*, In press

72. **Ghosh, P.K.**, Gupta, P.C. and Goyal, V.K., [1998], "Stainless steel cladding of structural steel plate using pulsed current GMAW process", *Welding Journal*, Vol.77(7), 307s-312s.

73. **Ghosh, P.K.**, Gupta, P.C. and Jain, N.K., [1989], "Studies on the properties of weld deposit at various pulse frequencies in MIG welding of Al-Zn-Mg alloy", *Indian Welding Journal*, Vol. 68(10), pp 550-558

74. **Ghosh, P.K.**, Gupta, P.C. and Somani, R., [1991a], "Influence of pulse parameters on bead geometry and HAZ during bead on plate deposition by MIG welding process", *Z. Metallkde.*, Vol. 82(10), pp. 756-762

75. **Ghosh, P.K.,** Gupta, P.C. and Somani, R., [1991b], "Influence of pulse parameters on the porosity formation in pulsed MIG weld deposit of aluminium alloy", *International Journal of Joining of Materials*, Vol. 3(2), pp.49-54

76. **Ghosh, P.K.,** Gupta, S.R. and Randhawa, H.S., [1999], "Characteristics and criticality of bead on plate deposition in pulsed current vertical-up GMAW of steel", *International Journal for Joining of Materials*, Vol. 11(4), pp. 99-110

77. **Ghosh, P.K.,** Gupta, S.R. and Randhawa, H.S., [2000], "Characteristics of a pulsed-current, vertical up gas metal arc weld in steel", *Metallurgical Transactions A*, Vol. 31A, pp.2247-2259.

78. **Ghosh, P.K.,** Gupta, S.R., Gupta, P.C. and Rathi, R., [1990], "Influence of pulsed MIG welding on the microstructure and porosity content of Al-Zn-Mg alloy weldment", *Practical Metallography*, Vol.27, pp. 613-626.

79. **Ghosh, P.K.,** Gupta, S.R., Gupta, P.C. and Rathi, R., [1990], "Pulsed MIG welding of Al-Zn-Mg alloy", *Material Transactions of JIM*, Vol. 31(8), pp. 723-729.

80. **Ghosh, P.K.,** Gupta, S.R., Gupta, P.C. and Rathi, R., [1991(c)], "Fatigue characteristics of pulsed MIG welded Al-Zn-Mg alloy", *J. Mat. Science*, Vol. 26, pp 6161-6170.

81. **Ghosh, P.K.,** Gupta. S.R. and Jain. N.K., [1989], "Studies on the properties of weld metal deposited at various pulse frequencies in MIG-Welding of Al-Zn-Mg alloy", *Indian Welding Journal*, Vol. Oct., pp.550-558.

82. **Ghosh, P.K.,** Gupta. S.R., Gupta. P.C. and Rathi, R., [1990], "Pulsed MIG-Welding of Al-Zn-Mg alloy", *Metallurgical Transactions. JIM*, Vol. 31(8), pp. 723 – 729.

83. **Ghosh, P.K.,** Kulkarni, S.G., Kumar, M. and Dhiman,H.K., [2007b], "Pulsed current GMAW for superior weld quality of austenitic stainless steel sheet", *ISIJ International,* Vol. 47(1), pp. 138–45.

84. **Ghosh, P.K.,** Randhawa, H.S. and Gupta, S.R., [2000], "Characteristics of pulsed current vertical-up GMA weld of steel", *Metallurgical and Materials Transactions A*, Vol. 31A(12), pp.2247-2259.

85. **Gill, T.P.S.,** Gnanamoorthy, J. B. [1982], "A method for quantitative analysis of delta-ferrite, sigma and $M_{23}C_6$ carbide phases in heat treated type 316 stainless steel weldments", *Journal of Material Science*, Vol. 17, pp. 1513-1518.

86. **Gill, T.P.S.,** Vijayalakshmi, M., Rodriguez, P. and Padmanabhan, K.A., [1989], "On microstructure- property correlation of thermally aged type 316L stainless steel weld metal", *Metallurgical and Materials Transactions A*, Vol. 20A, pp. 1115- 1124.

87. **Gill, T.P.S.**, Vijayalakshmi, M., Rodriguez, P. and Padmanabhan, K.A., [1986], "Transformation of delta-ferrite during the postweld heat treatment of type 316L stainless steel weld metal", *Welding Journal*, Vol. (5), pp. 122s-136s.

88. **Goswami, T.**, [2003], "Fatigue crack growth behavior of Ti-6Al-4V alloy forging", *Materials and Design*, Vol.24, pp. 423-433.

89. **Goyal,V.K.**, Ghosh, P.K. and Saini, J.S., [2007], "Process controlled microstructure and cast morphology of dendrite in pulsed current gas metal arc weld deposits of Aluminium and Al-Mg Alloy", *Metallurgical and Materials Transactions A*, Vol.38(8), pp. 1794-1805.

90. **Goyal,V.K.**, Ghosh, P.K. and Saini, J.S., [2008], "Analytical studies on thermal behaviour and geometry of weld pool in pulsed current gas metal arc welding", *Journal of Material Processing Technology*, In Press, Corrected Proof.

91. **Guha, B.**, [1993], "Fatigue characteristics of 'bead-on–plate' of aluminium and Al-Zn-Mg alloy", *Theoretical and Applied Fracture Mechanics*, Vol. 19, pp. 151-156.

92. **Hafele,P.**, [1994], "A numerical calculation of the energy release rate for non-self-similar crack growth for mixed mode fracture", *International Journal of Fracture*, Vol. 66, pp. R25-R32.

93. **Han, H.Y.** and Sun, Z., [1999], "Development of Welding Wire for High-Purity Austenitic Stainless Steels", *Welding Journal*, Vol.78 (2), pp. 38s-44s.

94. **Harris, S.D.** and Nag, N.R., [1975], "Kinetics of niobium carbide precipitation in a low carbon austenitic steel", *Journal of Material Science*, Vol.10, pp. 1137-1148.

95. **Heald, P.R.**, Maidigan, R.B., Siewert, T.A. and Lin, S., [1994], "Mapping the droplet transfer modes for an ER-1000 S-1 GMAW electrode", *Welding Journal*, Vol. 73(2), pp 38-s-43-s.

96. **Herbsleb, G.**, [1980], "The stress corrosion cracking of sensitized austenitic stainless steels and nickel-base alloys", *Corrosion Science*, Vol.20, pp. 243–268.

97. **Hertzman, S.**, [2001], "The influence of nitrogen on microstructure and properties of highly alloyed stainless steel welds", *ISIJ International*, Vol.41(6), pp. 580–589.

98. **Hull, F.C.**, [1952], "Effects of composition on embrittlement of Austenitic Stainless Steel", *Welding Journal*, Vol. 52, pp. 104-S to 113-S.

99. **Hunt, C.** and Ortega, P., [1997], "Helium- a light weight gas with heavy weight performance", *Welding and metal fabrication*, Vol. 65, pp. 10-14.

100. **Hunter, A.** and Ferry, M., [2002], "Phase formation during solidification of AISI 304 austenitic stainless steel", *Scripta Materialia*, Vol.46, pp. 253–258.

101. **Hussain, H.M.**, Ghosh, P.K., Gupta, P.C. and Potluri, N.B., [1996], "Properties of Pulsed Current multipass GMA welded Al-Zn-Mg alloy", *Welding Journal*, Vol. 75(7), pp. 210-s-215-s.

102. **Iamboliev, T.**, Katayama, S. and Matsunawa, A., [2003], "Interpretation of phase formation in austenitic stainless steel welds", *Welding Journal*, Vol. (12), pp. 337s-347s.

103. **Innyi, T.**, [1975], "Narrow gap welding for corner joint in box grinder made of heavy high tensile strength (80 Kg/mm class) steel", *Advanced Welding Technology*, Japan Welding Society, pp. 387-390.

104. **Inoue, H.**, Koseki, T., Ohkita, S., Tanaka, T., [1995], "Effect of solidification on subsequent ferrite-to-austenite massive transformation in an austenitic stainless steel weld metal", *ISIJ International*, Vol. 35(10), pp. 1248-1257.

105. **Irving, B.**, [1994], "Trying to make some sense out of shielding gases", *Welding Journal*, Vol.63, pp. 65-70.

106. **Jacobsen, N.**, [1992], "Monopulse investigation of drop detachment in pulsed gas metal arc welding", *Phys. D, Appl. Phys.*, Vol. 25, pp 783-797.

107. **Jahromi S.A.J.**, Javadpour, S. and Kh. Gheisari, [2005], "Failure analysis of welded joints in a power plant exhaust flue", *Engineering Failure Analysis*, Vol. 13(4),pp. 527-536.

108. **Jilong, Ma** and Apps, R.L., [1982], "MIG transfer discovery of importance to industry", *Welding & Metal Fabrication*, Vol. 14, No. 9, pp 307-316.

109. **Jilong, Ma** and Apps, R.L., [1983], "Analysing metal transfer during MIG welding", *Welding and Metal Fabrication*, Vol. 15(4), pp 119-128.

110. **Johnson, J. A.**, Carision, N. M. and Smart, H.B., [1989], "Detection of metal transfer mode in GMAW", Recent trends in welding science and technology, 2nd international conference of welding research, Gatlinburg, USA, 14-18 May, 1989, pp. 377-381.

111. **Johnson,P.G.**, Szekely, R.B., Madigan and Quinn, T.P., [1995], "Power characteristics in GMAW: experimental and numerical investigations". *Welding Journal*, Vol. 74(3), pp 93-s-102-s.

112. **Jones D.F.**, U.S. Patent 6,744,013, "Welding Torch for Use in Gas Metal Arc Welding", (Parweld Limited) 1 June 2004.

113. **Jonsson, P.G.**, Eagar, T.W. and Szekely, J., [1995], "Heat and metal transfer in gas metal arc welding using argon and helium", *Metallurgical and Materials Transactions B*, Vol. 26B, pp. 383-395.

114.   **Joseph, A.,** Harwig, D., Farson, D. F. and Richardson, R., [2003], "Measurement and calculation of arc power and heat transfer efficiency in pulsed gas metal arc welding", *Science and Technology of Welding and Joining,* Vol. 8(6), pp. 400-406.

115.   **Kamiya,O.,** Chen, Z. W. and Kikuchi, Y., [2002], "Micro porosity formation in partially melted zone during welding of high nitrogen austenitic stainless steels", *Journal of Materials Science,* Vol. 37, pp. 2475 – 2481.

116.   **Kang, Y.H.** and Na, S.J., [2003], "Characteristics of welding and arc signal in narrow groove gas metal arc welding using electromagnetic arc oscillation", *Welding Journal,* Vol.82(5), pp. 93s-99s.

117.   **Kanjilal, P,** Pal, T.K. and Majumdar, S.K., [2007], "Prediction of Element Transfer in Submerged Arc Welding", *Welding Journal,* Vol. 86(5), pp. 135s-146s.

118.   **Karimiyan, A,** Farhangi, H and Allahyari, A.A, "Investigation of the effects of aging on the room and high temperature tensile properties and fracture of stainless steel 316l weld metal", Proceedings of 8th International Fracture Conference 7 – 9 November 2007, Istanbul/TURKEY, pp.518-526.

119.   **Kazannov, Y.L.,** Stepankov, V.N. and Protsenko, L.N., [1982], "Recrystallisation and fine structure of weld zone metal of welded joints in thin sheets of an austenitic steel", *Svar. Proiz,* Vol. (5), pp. 7-9.

120.   **Kearns, L.P.,** [1978], "Welding Handbook", American welding society, Vol. II, pp.131 to 137

121.   **Kim, Y.S.** and Eagar, T.W., [1993a], "Analysis of metal transfer on gas metal arc welding", *Welding Journal,* Vol. 72(6), pp. 269-s-278-s.

122.   **Kim, Y.S.** and Eagar, T.W., [1993b], "Metal transfer in pulsed current gas metal arc welding", *Welding Journal,* Vol. 7, pp. 279s-287s.

123.   **Kim, Y.S.,** D.M. and Eagar, T.W., [1991], "Analysis of electrode heat transfer in gas metal arc welding", *welding Journal,* Vol. 70(1), pp. 20s-31s.

124.   **Kimura, S.,** Ichihara, I., and Nagai, Y., [1979], "Narrow gap, gas metal arc welding process in flat position", *Welding Journal,* Vol. 58(7), pp. 44–52.

125.   **Koseki, T.** and Flemings, M.C., [1996], "Solidification of undercooled Fe–Cr–Ni alloys part II – microstructural evolution", *Metallurgical and Materials Transactions A,* Vol. 27A, pp. 3226–3240.

126.   **Krishnan, K. N.** and Rao, K.P., [1991], "Effect of microstructure on stress corrosion cracking behaviour of austenitic stainless steel weld metals", *Materials Science and Engineering A,* Vol. 142, pp. 79-85.

127. **Kusko, C. S.,** Dupont, J. N. and Marder, A. R., [2004], "Influence of stress ratio on fatigue crack propagation behavior of stainless steel welds", *Welding Journal*, Vol. 83, pp.59s-64s.

128. **Lai, J. K. L.,** [1983], "A study of precipitation in AISI type 316 stainless steel", *Material Science and Engineering*, Vol. 58, pp. 195-209.

129. **Laing, B.,** Heid, R. and Pollack, A., [1985], "Narrow gap welding of HY-100 plate using close loop, adaptive feedback, through-the-arc tracking technology", *Welding Journal*, Vol.64 (11), pp. 38s.

130. **Lambentt, J.A.,** [1989], "Assessment of the pulsed GMA technique for tube attachment welding" *Welding Journal*, Vol. 68(2), pp 35-43.

131. **Lancaster, J. F.,** [1984], "The Physics of welding", Pergamon Press, New York, USA.

132. **Lenivkin, V.A.,** [1981], "The continuity of current in pulsed-arc welding with pulses of varying shape", *Welding Production*, Vol. 28(2), pp. 12-14.

133. **Liao, M.T** and Chen, W.J., [1999], "A comparison of gas metal arc welding with flux-cored wires and solid wires using shielding gas", *International Journal of Advanced Manufacturing Technology*, Vol. 15, pp. 49-53.

134. **Liao, M.T.** and Chen, W., [1998], "The effect of shielding-gas compositions on the microstructure and mechanical properties of stainless steel weldments", *Materials Chemistry and Physics*, Vol. 55, pp. 145-151.

135. **Lima, A. S.,** Nascimento, A. M., Abreu, H. F. G., De Lima-Neto, P., [2005], "Sensitization evaluation of the austenitic stainless steel AISI 304L, 316L, 321 and 347", *Journal of Material Science*, Vol. 40, pp. 139–144.

136. **Lin, Y.C.** and Chen, P.Y., [2001], "Effect of nitrogen content and retained ferrite on the residual stress in austenitic stainless steel weldments", *Materials Science and Engineering A*, Vol. 307, pp. 165-171.

137. **Lin, Y.C.** and Chen, P.Y., [2001], "Effect of nitrogen content and retained ferrite on the residual stress in austenitic stainless steel weldments", *Material Science and Engineering A*, Vol.307, pp.165-171.

138. **Lippold, J.C.** and Savage, W.F., [1986], "Solidification of austenitic stainless steel weldments-Part III. The effect of solidification behaviour on hot cracking susceptibility", *Welding Journal*, Vol. 62, pp. 204s-209s.

139. **Lippold, J.C.,** [1983], "An investigation of heat affected zone hot cracking in alloy 800", *Welding Journal*, Vol. 62, pp. 1s-11s.

140. **Liu, S.** and Siewert, T.A., [1989], "Metal transfer in gas metal arc welding: Droplet rate", W*elding Journal*, Vol. 68(2), pp. 52s-58s.

141. **Loh, P.C.**, Loper, C.R. and Gregory, J.T., [1991], "Gas metal arc welding of HK 40 steel", *Welding Journal*, Vol. 70(11), pp. 31-36.

142. **Lowke, J.J.**, Morrow,R., Haider, J. and Murphy,A.B., [1997], "Prediction of gas tungsten arc welding properties in mixtures of argon and hydrogen", *IEEE Transaction on Plasma Science*, Vol. 25, pp. 925-930.

143. **Lucus, W.**, [1992], "Choosing a shielding gases -part II", *Welding and Metal Fabrication*, Vol. 60, pp. 269 to 276.

144. **Lucus, W.**, [1992], "Shielding gases for arc welding-part I", *Welding and Metal Fabrication*, Vol. 60, pp. 218 to 225.

145. **Lundin, C.D.** and Savage, F., [1980], "Hot cracking resistance of austenitic stainless steel weld metal", *Welding Journal*, Vol. 59, pp. 226s to 232s.

146. **Lundin, C.D.**, Lefand, C.H. and Qiao,C., [1993], "Evaluation of backfilled solidification cracks in austenitic stainless welds in relationship to evaluation of hot cracking", *Welding Journal*, Vol. 72, pp. 321s- 328s.

147. **Lyttle, K.A.**, [1983], "GMAW-a versatile process on the move", *Welding Journal*, Vol. 62(3), pp. 15-23.

148. **Malin, V.Y.**, [1983a], "The state-of-the-art of narrow gap welding", Part I, *Welding Journal*, Vol.62(4), pp. 22-36.

149. **Malin, V.Y.**, [1983b], "The state-of-the-art of Narrow Gap welding", Part II, *Welding Journal*, Vol.62(6), pp.37-46.

150. **Malone, M.D.**, [1967], "Sigma and 885^0K (475^0C) embrittlement of chromium-nickel stainless steel weld metal", *Welding Journal*, Vol. 46( ), pp. 241s-253s.

151. **Mandiang, Y.** and Cizeron, G., [1996], "Phosphorus effects on microstructural evolution and phase stability in type 316 Ti stainless steels", *Material Science and Engineering A*, Vol.206, pp.233-240

152. **Maruo, H.** and Hirata, Y., [1984] " Study of pulsed MIG welding", IIW Doc. SG 212-258-84, Welding Department , Osaka University, Japan, July 1984.

153. **Matthews, J.R.**, Lassaline, E.E., Porter, J.F. and Leewis, K.G., [1992], "Evaluating frequency modulated GMA welding of HY 80 steel", *Welding Journal*, Vol. 71(9), pp. 49-53.

154. **Metals Handbook**, [1979], "Properties and selection : Nonferrous alloys and pure metals", Vol. 2, 10th ed., ASM International, Metal Park, Ohio.

155. **Mozhi, T.A.,** Juhas, M.C. and Wilde, B.E., [1987], "Modeling low temperature sensitization of austenitic stainless steels", *Scripta Metallurgica,* Vol. 21, pp.1547-1552.

156. **Murugan, N.** and **Parmar, R.S.,** [1994], "Effect of MIG process parameters on the geometry of the bead in the automatic surfacing of stainless steel", *Journal of Material Processing Technology,* Vol. 41, pp. 381-398.

157. **Murugan, N.** and **Parmar, R.S.,** [1995], "Mathematical models for bead geometry prediction in automatic stainless steel surfacing by MIG welding", *International Journal for Joining of Materials,* Vol. 7(2/3), pp.71-80.

158. **Murugan, S.,** Rai, S.K., Kumar, P.V., Jayakumar, J., Baldev Raj, and Bose, M.S.C., [2001], "Temperature distribution and residual stresses due to multipass welding in type 304 stainless steel and low carbon steel weld pads", *Inernational Journal of Pressure Vessals and Piping,* Vol. 78, pp. 307-317.

159. **Nage, D.D.,** Raja, V.S., Raman, R., [2006], "Effect of nitrogen addition on the microstructure and mechanical behavior of 317L and 904L austenitic stainless steel welds", *Journal of Material Science,* Vol. 41, pp. 2097–2112.

160. **Nakayama, H.,** [1976], "Application of narrow gap automatic CO_2 arc weaving horizontal position welding process to heavy steel structures of building", IIW Doc. XII-632-76, XII-B-193-76, p34

161. **Needham, J.C.,** [1965], "Pulse controlled consumable electrode welding arcs", *British welding Journal,* Vol. 12(4), pp. 191-197.

162. **Nemchinsky, V.A.,** [1997], "Electrode evaporation in an arc with pulsing current", *Journal of Physics D: Applied Physics,* Vol. 30, pp. 2895–2899.

163. **Newman, J.C.** and Raju, J.S., [1980], "Stress intensity factors for internal surface cracks in cylindrical pressure vessels", Trans ASME, Journal of Pressure Vessel Technology, Vol. 102, pp.342-346.

164. **Niemi, E.** and Koshimaki, M., [1997] "Fatigue strength of welded joints in three types of stainless steel", *Welding in the World,* Vol.39 (2), pp. 65-73.

165. **Nishimoto, K. H.,** Morland, and Nakao, Y., [1995], "Low temperature sensitization in the weld metal of type 308 stainless steel and its improvement by laser surface melting treatment, *ISIJ International,* Vol.35(10), pp. 1265-1271.

166. **Nomura, H.** and Sugitani, Y., [1984], "Further improvements of narrow gap welding techniques", *Joining of Metals,* pp. 73-85.

167. **Nosse J.R.,** U.S. Patent 6,211,490, Nozzle for Shielded Arc Welding Gun, (to Lincoln Global, Inc.) 3 April 2001.

168. **Ogawa, K.,** Sawaragi, Y., Otsuka, N., Hirata, H., Natori, A. and Matsumoto, S., [1995], "Mechanical and corrosion properties of high strength 18%Cr austenitic stainless steel weldment for boiler", ISIJ International, Vol. 35(10), pp. 1258-1264.

169. **Ogawa, M.,** Hiraoka, K., Katada, Y., Sagara, M. and Tsukamoto, S., [2002], "Chromium nitride precipitation behavior in weld heat affected zone of high nitrogen steel", *ISIJ International*, Vol. 42(12), pp. 1391-1398.

170. **Ogawa, T.,** Suzuki, K. and Zaizen, T., [1984], "The weldability of nitrogen-containing austenitic stainless steel:part II – porosity, cracking and creep properties", *Welding Journal*, Vol. 64, pp. 213s–223s.

171. **Okagawa, R.D.,** Dixon, R.D. and Olson, D.L., [1983], "The influence of nitrogen from welding on stainless steel weld metal microstructures", *Welding Journal*, Vol. 62, pp. 204s-209s.

172. **Padilha, A. F.** and Rios, P.R., [2002], "Decomposition of austenite in austenitic stainless steels", *ISIJ International*, Vol. 42(4), pp. 325–337.

173. **Palani, P.K.** and Murugan, N., [2006], "Selection of parameters of pulsed current gas metal arc welding", *Journal of Materials Processing Technology*, Vol. 172, pp. 1–10.

174. **Pan, J.L.,** Zhang, R.H., Ou, Z.M., Wu, Z.Q. and Chen, Q, [1989], "Adaptive control GMA welding- A New technique for quality control", *Welding Journal*, Vol. 68(3), pp. 73-76.

175. **Parvathavarthini, N.** and Dayal, R.K., [2002], "Influence of chemical composition, prior deformation and prolonged thermal aging on the sensitization characteristics of austenitic stainless steels", *Journal of Nuclear Materials*, Vol. 305, pp. 209–219.

176. **Peckner,D** and Bernstein, I.M., [1977], "Handbook of stainless steels", Mc-Graw-Hill Book Company, USA

177. **Piatti, G.** and Vedani, M., [1990], "Relation between tensile properties and microstructure in type 316 stainless steel SA weld metal", *Journal Of Materials Science*, Vol.25, pp. 4285-4297.

178. **Praveen, P.,** Yarlagadda, P.K.D.V. and Kang, M.J., [2005], "Advancements in pulse gas metal arc welding", *Journal of Materials Processing Technology*, Vol. 164–165, pp. 1113–1119.

179. **Pujar, M.G.,** Dayal, R.K., Gill, T.P.S. and Malhotra, S.N., [1998], "Microstructural evaluation of molybdenum containing stainless steel weld metals by a potentiostatic etching technique", *Journal of Material Science*, Vol. 33, pp. 2691-2700.

180. **Quinn, T.P.**, Maidgan, R.B. and Siewert, T.A., [1994], "An electrode extension model for gas metal arc welding", *Welding Journal*, Vol. 73(10), pp. 241s-247s.

181. **Quintino, L.** and Alllum, C.J., [1984], "Pulsed GMAW: Interactions between process parameters, Part I", *Welding and Metal Fabrication*, Vol. 16(4), pp. 126-129.

182. **Radaij, D.**, [1992], "Heat effects on welding", Springer-Verlag, USA, 1992, p.45.

183. **Rajasekaran, S.**, Kulkarni, S.D., Mallya, U.D. and Chaturvedi, R.C., [1998], "Droplet detachment and plate fusion characteristics in pulsed current gas metal arc welding", *Welding Journal*, Vol. 6, pp. 254s-268s.

184. **Rajashekhar, K.**, Harendranath, C.S., Raman, R. and Kulkarni, S.D., [1997], "Microstructural evolution during solidification of austenitic stainless steel weld metals: A color metallographic and electron microprobe analysis study", *Materials Characterization*, Vol. 38, pp. 53-65.

185. **Randhawa, H.S.**, Ghosh., P.K., and Gupta, S.R., [2000], "Some basic aspects of geometrical characteristics of pulsed current vertical-up GMA weld", *ISIJ International*, Vol. 40 (1), pp. 71-76.

186. **Randhawa, H.S.**, Ghosh., P.K., and S.R. Gupta, [1998], "Geometric characteristics of pulsed current positional GMA weld", *ISIJ Int.*, Vol. 38(4), pp. 276-284.

187. **Redding, C.J.**, [2002], "Fume model for gas metal arc welding", Welding Journal, Vol. (6), pp.95s-103s.

188. **Reddy, G. M.** and Mohandas, T., [2001], "Explorative studies on grain refinement of ferritic stainless steel welds", *Journal of Materials Science Letters*, Vol. 20, pp.721–723

189. **Rho, B.S.**, Hong, H.U. and Nam, S.W., [2000], "The effect of δ-ferrite on fatigue cracks in 304L steels", *International Journal of Fatigue*, Vol. 22, pp.683-690

190. **Ritter, A.M.**, Cieslak, M.J. and Savage, W.F., [1983], "Precipitation in CF-8M duplex stainless steel welds", Metallurgical and Materials Transactions A, Vol.14A, pp.37.

191. **Ritter, A.M.**, Henry, M.F. and Savage, W.F., [1984], "High temperature phase chemistries and solidification mode prediction in nitrogen strengthened austenitic stainless steels", Metallurgical Transactions A, Vol.15A, pp.1339-1351.

192. **Ronda, J.** and Oliver, G.J., "Comparison of applicability of various thermo-viscoplastic constitutive models in modelling of welding", *Computer Methods in Applied Mechanics and Engineering*, Vol.153, pp.195-221

193. S'anchez-Cabrera, V.M., Rubio-Gonz'alez, C., Ru'iz-Velab, J.I. and Ram'irez-Baltazar, C. , [2007], "Effect of preheating temperature and filler metal type on the microstructure, fracture toughness and fatigue crack growth of stainless steel welded joints", *Materials Science and Engineering A,* Vol.452–453, pp. 235–243

194. **Sarafianos, N.,** [1992], "Structure morphology effect of Ti and Nb stabilized austenitic stainless steel welds on corrosion properties", *Journal of Material Science,* Vol.27, pp. 226-232.

195. **Sarkani, S.,** Tritchkov, V. and Michaelov, G., [2000], "An efficient approach for computing residual stresses in welded joints", *Finite Elements in Analysis and Design,* Vol.35, pp.247-268

196. **Sasmal, B.,** [1997], "Mechanism of the formation of $M_{23}C_6$ plates around undissolved NbC particles in a stabilized austenitic stainless steel", *Journal of Material Science,* Vol.32, pp. 5439 – 5444

197. **Shaikh, H.,** Khatak, H.S., Sahadri, S.K. and Gnanamoorthy, J.B., [1995], " Effect of ferrite transformation on the tensile and stress corrosion properties of type 316 L stainless steel weld metal thermally aged at 873^0 K ", *Metallurgical and Materials transactions A,* Vol.26A, pp. 1859- 1868

198. **Shankar, V.,** Gill, T.P.S., Mannan, S.L. and Sundaresan, S., [2003a], "Effect of nitrogen addition on microstructure and fusion zone cracking in type 316L stainless steel weld metals", Material Science and Engineering A, Vol. 343, pp. 170-181

199. **Shankar, V.,** Gill, T.P.S., Mannan, S.L. and Sundaresan, S., [2003b], "Solidification cracking in austenitic stainless steel welds", *S_adhan_a ,* Vol. 28(3/4), pp.359–382.

200. **Shanker, V.,** Gill, T.P.S., Terrance, A.L.E., Mannan, S.L., and Sundaresan, S., [2000], "Relation between microstructure, composition, and hot cracking in Ti-stabilized austenitic stainless steel weldments", *Metallurgical and Materials Transactions A,* Vol. 31A, pp. 3109-3122.

201. **Shanmugam, A.,** Raja, A., Santhakumari, A., Rohira, K.L. and Murti, K.G.K., [1997], "Process stability criterion for MIG welding", *Indian Welding Journal,*Vol. (1), pp. 32 to 36.

202. **Shtrikman, M.M.** and Grinin, V.V., [1977], "The automatic narrow gap welding of high strength steels and titanium alloys", Welding Production, Vol.24(1), pp.19-23.

203. **Shtrikman, M.M.** and Grinin, V.V., [1979], "On stability of the gap width in the argon shielded narrow-gap welding of short workpieces", Welding Production, Vol. 26(3), pp.19-23.

204. **Sierdzinski, M.S.** and Ferree, S.E., [1999], "New low hydrogen flux cored wires for welding high strength steels", Proceedings of International welding conference, New Delhi, 15-17 Feb., Vol. 1, p.381

205. **Siewert, T.A.**, McCowan, C.N. and Olson, D.L., [1988], "Ferrite number prediction to 100 FN in stainless steel weld metal", *Welding Journal*, Vol.67( ), pp.289s–298s

206. **Simmons, J.W.**, [1995], "Mechanical properties of isothermally aged high nitrogen stainless steel", *Metallurgical and Materials Transactions A*, Vol.26A, pp. 2085-2101.

207. **Slemon, G.R.** and Straughen, A., [1980], "Electric machines", Addison-wesley publishing company, pp. 326 to 338

208. **Smati, Z.**, [1986], "Automatic pulsed MIG welding", *Welding Journal*, Vol. 65(1), pp 38s-44s.

209. **Song, Y.**, Baker, T.N. and McPherson, N.A., [1996], "A study of precipitation in as welded 316LN plate using 316L/317L weld metal", *Materials Science and Engineering*, Vol.A212, pp.228-234

210. **Song, Y.**, McPherson, N.A. and Baker, T.N., [1996], "The effect of welding process on the chi phase precipitation in as-welded 317L weld metals", *ISIJ International*, Vol. 36(11), pp. 1392 1396

211. **Sourmail, T.**, [2001], "Precipitation in creep resistant austenitic stainless steels", *Materials Science and Technology*, Vol.17, pp. 1-14

212. **Sourmail, T.**, Too, C.H. and Bhadeshia, H.K.D.H., [2003], "Sensitisation and evolution of chromium-depleted zones in Fe–Cr–Ni–C Systems", *ISIJ International*, Vol.43(11), pp.1814–1820

213. **Stenbacka, N.** and Person, K.A.,[1989], " Shielding gases for gas metal arc welding", Welding Journal, Vol. 68, No. 11, pp 41-47.

214. **Stuart K.**, Longhofer R.L., U.S. Patent 6,847,009, Welding Contact Tip and Diffuser, (Tweco Products, Inc) 25 January 2005.

215. **Suban, M.** and Tusek, J., [2001], "Dependence of melting rate in MIG/MAG welding on the type of shielding gas used", *Journal of Material Processing Technology*, Vol.119, pp. 185 to 192.

216. **Suban, M.**, Tusek, J. and Uran, M., [2001], "Use of hydrogen in welding engineering in former times and today", *Journal of Material Processing Technology*, Vol.119, pp.193 to 198

217. **Subramaniam, S.,** White, D.R., Jones, J.E. and Lyons, D.W., [1998], "Droplet transfer in pulsed gas metal arc welding of aluminium", Welding Journal, Vol. (11), pp.458s-464s

218. **Suutala, N.,** [1983], "Effect of solidification conditions on the solidification mode in austenitic stainless steels", *Metallurgical and Materials Transactions A*, Vol.14A, pp.191–197

219. **Swada, S.,** Hori, K., Kawahara, M., Takao, M. and Asano, I., [1979], "Application of narrow gap process" Welding Journal, Vol. 59(9), pp.17-25.

220. **Talonen, J.** and Hanninen, H., [2007], "Formation of shear bands and strain-induced martensite during plastic deformation of metastable austenitic stainless steels", *Acta Materialia*, Vol.55, pp.6108-6118

221. **Tavassoli, A.A.,** [1995], "Assessment of austenitic stainless steels", *Fusion Engineering and Design*, Vol.29, pp. 371-390.

222. **Tekriwal, P.** and Mazmuder, J.,[1988], " Finite element analysis of 3-dimensional transient heat transfer in GMA welding", Welding Journal, Vol. 67, pp 150s-156s.

223. **Teng, T.L.** and Chang, P.H., [1998], "Three-dimensional thermo mechanical analysis of circumferentially welded thin-walled pipes", *International Journal of Pressure Vessels and Piping*, Vol.75, pp.237-247

224. **Teng, T.L.,** Chang, P.H. and Tseng, W.C., [2003], "Effect of welding sequences on residual stresses", *Computers and Structures*, Vol.81, pp.273-286

225. **Teng, T.L.,** Fung, C.P. and Chang, P.H., [2002], "Effect of weld geometry and residual stresses on fatigue in butt-welded joints", *International Journal of Pressure Vessels and Piping*, Vol. 79, pp. 467–482.

226. **Terumi, N.** and Kazuo, H., [2002], "Wire melting behaviour by non-steady heat conduction numerical analysis in gas metal arc welding", *Quarterly Journal of the Japan Welding Society*, Vol. 20(1), pp. 53-62

227. **Thamodharan, M.,** Beck, H.P. and Wolf, A., [1999], "Steady and pulsed direct current welding with single convertor", *Welding Journal*, Vol. 78(3), pp. 75s to 79s

228. **Timofeev, B.T.,** Karzov, G.P., Blumin, A.A. and Anikovsky, V.V., [1999], "Fracture toughness of austenitic welded joints", *International Journal of Pressure Vessels and Piping*, Vol.76, pp.393-400

229. **Trindade, F.M.** and Allum, C.J., [1984], "Characteristics in steady and pulsed current GMAW", *Welding and Metal Fabrication*, Vol. 16(9), pp 264-271.

230. **Tseng, K.H.** and Chou, C.P., [2002], "The effect of pulsed GTA welding on the residual stress of a stainless steel weldment", Journal of Material Processing Technology, Vol.123, pp. 346-353.

231. **Tujsek, J.**, [2000], "Experimental investigation of gas tungsten arc welding and comparison with theoretical predictions", *IEEE Transactions on Plasma Science*, Vol. 28, pp. 1688 to 1693

232. **Tusek, J.** and Suban, M., [2000], "Experimental research of the effect of hydrogen in argon as a shielding gas in arc welding of high-alloy stainless steel", *International Journal of Hydrogen Energy*, Vol.25, pp. 369 to 376

233. **Tyagi V.**, U.S. Patent 6,060,690, Welding Nozzle for Improved Gas Coverage, (to Caterpillar Inc.) 9 May 2000.

234. **Ueguri, S.**, Hara, K. and Komura, H.,[1985], "Study of metal transfer in pulsed GMA Welding", *Welding Journal*, Vol. 64(8), pp 242s-250s.

235. **Vanderschaeve, F.**, Taillard, R. and Foct, J., [1995], "Discontinuous precipitation of Cr_2N in a high nitrogen, chromium-manganese austenitic stainless steel", *Journal of Material Science*, Vol.30, pp. 6035-6046

236. **Varin, R. A.**, [1979], "Effect of extrinsic grain-boundary dislocations on $M_{23}C_6$ precipitate nucleation in an austenitic stainless steel", *Journal of Material Science*, Vol.14, pp. 811-816

237. **Villafuerte, J.C.** and Kerr, H.W., [1990], "Grain structures in gas tungsten-arc welds of austenitic stainless steels with ferrite primary phase", *Metallurgical and Material Transactions A*, Vol.21A, pp.979-986

238. **Vitek, J.M.** and David, S.A., [1984], "The solidification and aging behaviour of types 308 and 308CRE stainless steel welds", *Welding Journal*, Vol. 63(8), pp. 246s-253s.

239. **Vitek, J.M.** and David, S.A., [1986], "The sigma phase transformation in austenitic stainless steel", *Welding Journal*, Vol. 65 (4), pp. 106s to 111s

240. **Vitek, J.M.**, DasGupta, A. and David, S.A., [1983], "Microstructural modification of austenitic stainless steels by rapid solidification", *Metallurgical and Material Transactions A*, Vol.14A, pp.1833-1841

241. **Vornovitskii, L.V.**, Gelpern, S.A., Tureshskii, A.V., [1977], "The manual narrow gap arc welding of non-rotating joints in pipelines", Welding Production, Vol. 24(6), pp.18-20.

242. **Wang, F.**, Hou, W.K., Hu, S.J., Asibu, S.K., Schultz, W.W. and Wang, P.C., [2003], "Modelling and analysis of metal transfer in gas metal arc welding", *Journal of Physics D: Applied Physics*, Vol. 36, pp. 1143–1152

243. **Wang, G.**, Huang, P.G. and Zhang, Y.M., [2004], "Numerical analysis of metal transfer in gas metal arc welding under modified pulsed current conditions", *Metallurgical and Materials Transactions B*, Vol. 35B, pp.857-866.

244. **Waszink, J.H.** and Piena, M.J., [1986], "Experimental Investigation of drop detachment and drop velocity in GMAW", *Welding Journal*, Vol. 65(11), pp 289s-298s.

245. **Waszink, J.H.** and Van, Den Heuvel G.J.P.M.,[1982], "Heat generation and heat flow in the filler wire in GMAW welding", *Welding Journal*, Vol. 61(8). pp 269s-282s.

246. **Weber, J.**, [1982], "Pulsed GMAW- A pulse for mild western metalworker", *Welding Journal*, Vol 61(11), pp 51-52.

247. **Webster, P.J.**, Ananthaviravakumar, N., Hughes, D.J., Mills, G., Preston, R.V., Shercliff, H.R. and Withers, P.J., [2002], "Measurement and modelling of residual stresses in a TIG weld", *Applied Physics A Materials Science & Processing*, Vol. A74 [Suppl.], pp. S1421–S1423

248. **Woo, I.** and Kikuchi, Y., [2002], "Weldability of high nitrogen stainless steel", *ISIJ International*, Vol.42(12), pp.1334–1343.

249. **Yaghi, A.H.**, Hyde, T.H., Becker, A.A., Williams, J.A. and Sun, W., [2005], "Residual stress simulation in welded sections of P91 pipes", *Journal of Materials Processing Technology*, Vol.167, pp.480-487.

250. **Zhong, Y.**, Shan, Y., Xiao, F. and Yang, K., [2005], "Effect of toughness on low cycle fatigue behavior of pipeline steels", *Materials letters*, Vol.59, pp.1780-1784.

LIST OF PUBLICATIONS BASED ON THESIS

1. SHRIRANG KULKARNI, P.K.GHOSH AND S.RAY, "IMPROVEMENT OF WELD CHARACTERISTICS BY VARIATION IN WELDING PROCESSES AND PARAMETERS IN JOINING OF THICK WALL 304LN STAINLESS STEEL PIPE", ISIJ International, Accepted.

2. SHRIRANG KULKARNI, P.K.GHOSH AND S.RAY, "SOME CRITICAL ASPECTS OF PULSE CURRENT GMA WELD BEAD ON PLATE DEPOSIT-PART-I:INFLUENCE ON BEAD GEOMETRY", Metallurgical and Materials Transactions A, Communicated.

3. SHRIRANG KULKARNI, P.K.GHOSH AND S.RAY, "SOME CRITICAL ASPECTS OF PULSE CURRENT GMA WELD BEAD ON PLATE DEPOSIT-PART-II:INFLUENCE ON WELDING METALLURGY", Metallurgical and Materials Transactions A, Communicated.

WELDING PROCEDURES

Welding sequence followed in P-GMA, GMA and SMA conventional V-groove weld joints is as schematically shown in figure below.
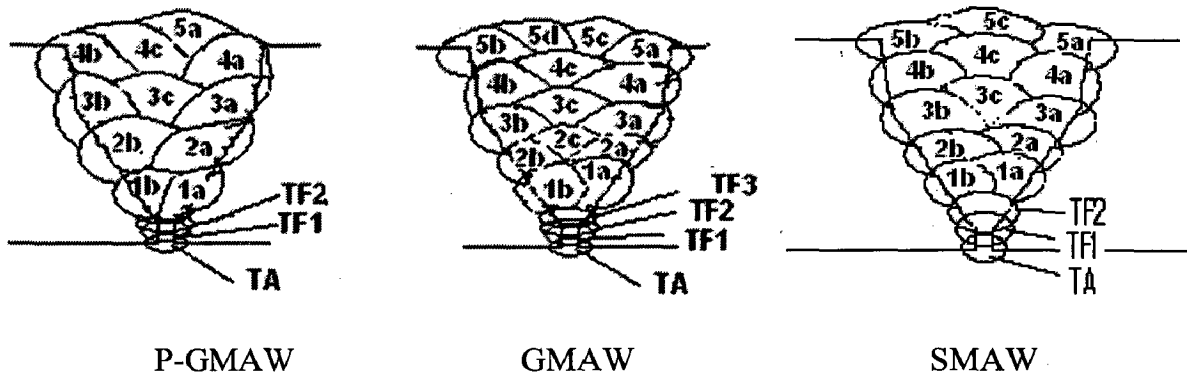
P-GMAW   GMAW   SMAW

The corresponding welding parameters used for preparation of P-GMA, GMA and SMA weld joints is as shown in table below:

Process	Pass No	Wire Feed Rate (cm/s)	Ω (kJ/cm)	ϕ	Welding Current (A)	Pulse Parameters					Arc Voltage (V)	Welding Speed (cm/min)	Technique/ Angle of Attack
						Mean current $I_{m,}$ (A)	Peak current $I_{p,}$ (A)	Base current $I_{b,}$ (A)	Peak duration $t_{p,}$ (ms)	Pulse frequency $f,$ (Hz)			
GTAW	TA	-	7.7	-	90	-	-	-	-	-	8.2	4.0	By weaving
	TF1	-	8.5	-	120	-	-	-	-	-	10.0	5.9	
	TF2/3	-	12.9	-	130	-	-	-	-	-	10.4	4.4	
P-GMAW	1a, b	12.5	9.0	0.06	-	174	419	31	1.97	105	21.5	20	55
	Upto 4a,b,c				-	196	410	34	2.03	105	22.4	20	55
	5a				-	200	414	32	2.03	105	22.5	20	60
	1a, b	10.8	9.5	0.25	-	175	315	92	2.02	118	23.8	20	55
	Upto 4a,b,c				-	182	321	105	1.97	120	24.2	20	55
	5a,b,c				-	170	312	98	1.92	118	24.7	20	55
	1a, b	10.8	7.8	0.05	-	130	439	27	2.03	106	23.0	20	55
	Upto 4a,b,c				-	160	450	28	2.03	114	22.5	20	55
	5a,b				-	158	448	28	2.03	110	22.5	20	70
	1a, b	9.2	8.1	0.25	-	177	314	104	2.03	122	22.3	20	55
	Upto 4a,b,c				-	176	313	106	2.03	126	21.8	20	60
	5a,b,c				-	174	315	107	2.03	125	21.2	20	70
GMAW	1a, b	12.5	10.7	-	221	-	-	-	-	-	22.5	20	55⁰
	Upto 4a,b,c				225	-	-	-	-	-	22.7	20	55⁰
	5a,b,c,d				235	-	-	-	-	-	23.4	20	55⁰
SMAW	1a, b	-	17.1	-	100	-	-	-	-	-	26	8.5	By weaving
	Upto 4a,b,c				140	-	-	-	-	-	28	9.1	
	5a,b,c				140	-	-	-	-	-	28	9.8	

Cumulative transverse shrinkage was measured after each pass at eight circumferential segments during multipass deposition as schematically shown in figure below:
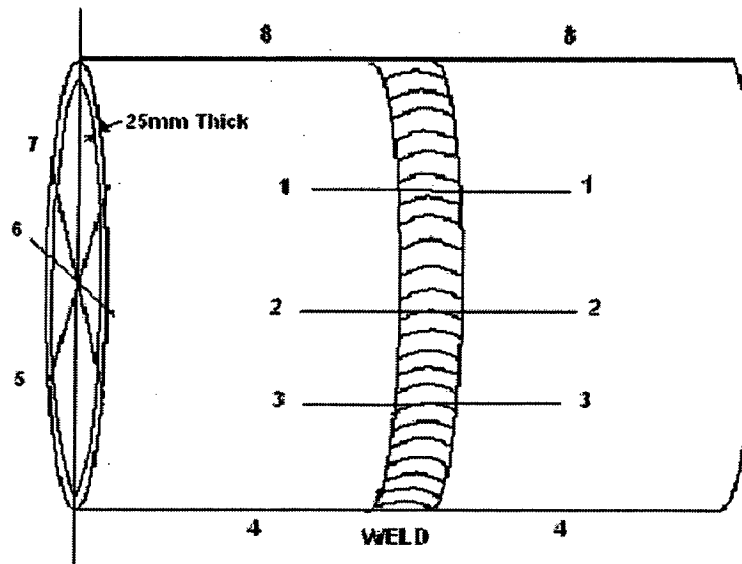
The overall transverse shrinkage in eight circumferential segments of multipass P-GMA, GMA and SMA welds of pipe is as shown in table below

Process	Ω (kJ/cm)	φ	Cumulative shrinkage at different locations on pipe, (mm)								Average shrinkage (mm)
			1-1	2-2	3-3	4-4	5-5	6-6	7-7	8-8	
P-GMAW	9.0	0.06	5.64	6.06	5.69	5.96	5.52	5.59	5.56	5.41	5.68 ± 0.22
	9.5	0.25	5.60	5.89	5.91	6.67	6.23	5.75	6.02	6.25	6.04 ± 0.34
	7.8	0.05	5.45	5.23	5.25	5.09	5.11	5.25	5.44	5.56	5.30 ± 0.17
	8.1	0.25	5.25	5.09	5.18	5.23	5.68	4.94	6.02	6.15	5.44 ± 0.45
GMAW	10.7	-	6.58	6.56	5.70	6.26	6.64	6.88	5.98	5.95	6.32 + 0.42
SMAW	17.1	-	6.80	6.99	6.91	7.37	7.23	6.95	6.02	6.15	6.80 ± 0.48

Welding sequence followed in narrow groove P-GMA weld joints is as schematically shown in figure below.
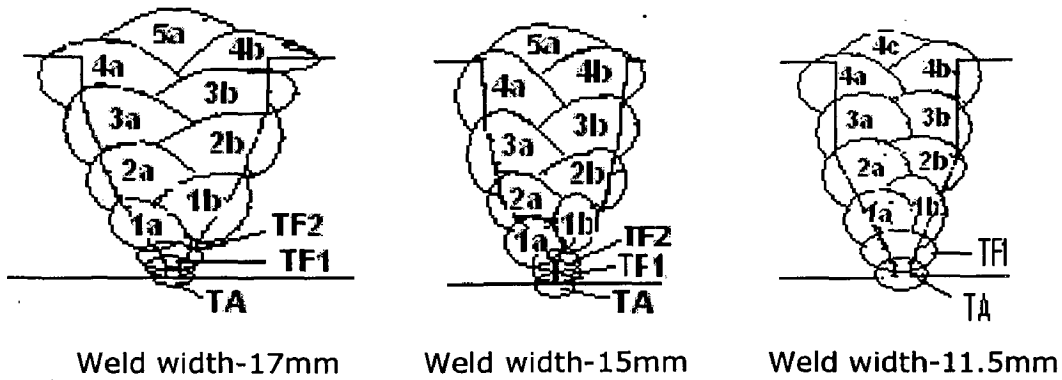
Weld width-17mm   Weld width-15mm   Weld width-11.5mm

Welding sequence followed in narrow groove SMA weld joints is as schematically shown in figure below.

Weld width-14mm   Weld width-11mm
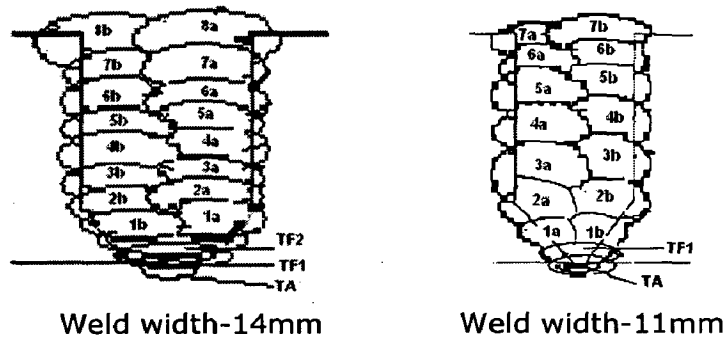
The corresponding welding parameters used for preparation of P-GMA weld joints are as shown in table below

Process	Weld Width (mm)	Pass No	Wire Feed Rate (cm/s)	Ω (kJ/cm)	φ	Pulse Parameters					Arc Voltage (V)	Welding Speed (cm/min)	Technique/ Angle of Attack
						Mean current I_m, (A)	Peak current I_p, (A)	Base current I_b, (A)	Peak duration t_p, (ms)	Pulse frequency f, (Hz)			
GTAW	--	TA	-	7.7	-	-	-	-	-	-	8.2	4.0	By weaving
		TF1	-	8.5	-	-	-	-	-	-	10.0	5.9	
		TF2	-	12.9	-	-	-	-	-	-	10.4	4.4	
GMAW P-GMAW	17	1a, b	12.5	9.4	0.06	164	409	28	1.97	106	21.5	20	55
		Upto 4a,b				196	410	34	2.03	105	22.4	20	55
		5a,b,c,d				200	414	32	2.03	105	22.5	20	60
	15	1a, b	10.8	7.5	0.06	130	439	27	2.03	106	23.0	20	55
		Upto 4a,b				160	450	28	2.03	114	22.5	20	55
		5a				158	448	28	2.03	110	22.5	20	60
		1a, b	9.2	8.0	0.25	177	314	104	2.03	122	22.3	20	55
		Upto 4a,b				176	313	106	2.03	126	21.8	20	55
		5a,b				174	315	107	2.03	125	21.2	20	55
	11.5	1a, b	10.8	7.5	0.05	130	439	27	2.03	106	23.0	20	55
		Upto 3a,b				160	450	28	2.03	114	22.5	20	55
		4a,b				158	448	28	2.03	110	22.5	20	70
		1a, b	9.2	7.9	0.25	177	314	104	2.03	122	22.3	20	55
		Upto 4a,b				176	313	106	2.03	126	21.8	20	60
		5a				174	315	107	2.03	125	21.2	20	70

The corresponding welding parameters used for preparation of SMA weld joints are as shown in table below

Process	Weld Width (mm)	Pass No	Ω (kJ/cm)	Welding Current (A)	Arc Voltage (V)	Welding Speed (cm/min)	Technique/ Angle of Attack
GTAW	--	TA	7.7	90	8.2	4.0	By weaving
		TF1	8.5	120	10.0	5.9	
		TF2	12.9	130	10.4	4.4	
SMAW	14	1a, b	9.9	110	24	18.9	By weaving
		Upto 7a,b		160	28	17.6	
		8a,b		160	28	17.8	
	11	1a, b	7.4	95	21	18.8	By weaving
		Upto 6a,b		140	23	16.7	
		7a,b		140	23	17.7	

In narrow groove welds cumulative transverse shrinkage was measured after each pass at eight circumferential segments during multipass deposition by following the same procedure mentioned above in conventional groove welds

The overall transverse shrinkage in eight circumferential segments of multipass P-GMA and SMA welds of pipe is as shown in table below

Process	Weld Width (mm)	Ω (kJ/cm)	φ	Cumulative shrinkage at different locations on pipe, (mm)								Average shrinkage (mm)
				1-1	2-2	3-3	4-4	5-5	6-6	7-7	8-8	
P-GMAW	17	9.4	0.06	5.39	5.46	5.30	4.88	5.03	4.67	4.62	4.64	5.0 ± 0.35
	15	7.5	0.05	4.34	3.78	4.12	4.17	4.09	4.82	4.20	4.50	4.25 ± 0.31
		8.0	0.25	4.08	3.99	4.25	3.94	4.04	5.00	4.54	4.80	4.33 ± 0.40
	11.5	7.5	0.05	4.11	4.03	3.75	3.85	4.18	4.06	4.20	4.12	4.04 ± 0.16
		7.9	0.25	4.08	4.48	4.36	4.56	4.06	4.24	4.13	3.66	4.20 ± 0.28
SMAW	14	17.1	-	5.14	4.92	5.56	4.74	5.5	3.78	4.56	3.84	4.76 ± 0.68
	11	10.7	-	3.25	3.70	3.80	3.80	3.95	4.20	3.98	4.51	3.90 ± 0.37

DYE PENETRANT TEST PROCEDURE

1.   **Scope:** Dye penetrant examination of circumferential butt weld joint in 300mm NB pipe using solvent removal colour contrast (visible) penetrant and non-aqueous wet developer.

2.   **Type of materials used in test procedure:**

a)   **Penetrant:** Solvent removal colour contrast (Visible) penetrant. Brand Name PP-15A of P-Met Co., Baroda.

b)   **Penetrant Remover:** Solvent remover or cleaner. Brand Name PC-21A of P-Met Co., Baroda.

c)   **Developer:** Non-aqueous wet developer. Brand Name PD-31A of P-Met Co., Baroda.

3.   **Pre examination cleaning, material for cleaning and minimum time allowed for drying** : Prior to each liquid penetrant examination, the surface to be examined and all adjacent areas within at least 1" have been made dry and free from all dirt, grease, lint, scale, welding flux, weld spatter, oil, paint and other extraneous matter that could obscure surface openings or otherwise interfere with the examinations. Surface preparation by grinding, machining or other methods was avoided, where the surface irregularities could mask indications of unacceptable discontinuities. Solvent removers or cleaning was used for cleaning. After cleaning and before application of penetrant, drying of the surfaces was accomplished by normal evaporation.

4. **Application of penetrant**: the penetrant was applied by spraying. Dwell time was kept as 5 minimum minutes. Temperature of the surface was held at room temperature varying in between 10^0 to 45^0C.

5. **Removal of excess Penetrant and Drying**: After the specified penetration time elapsed, any penetrant remaining on the surface was removed by taking care to minimise removal of penetrant from discontinuities.

6. **Application of developer and developing time**: Non-aqueous developer was applied only on the dry surface by spraying. Developing time for final interpretation began after ensuring dry coating.

7. **Interpretation**: Final interpretation was made within 7 to 60 minutes after developing time. A minimum light intensity of 100 watt bulb was used to ensure adequate sensitivity during the examination and evaluation of indications.

8. **Evaluation and acceptance standard**: Evaluation was done as per ASME Section-III NB5350.

9. **Post Examination and Cleaning**: After evaluation, examined surfaces were cleaned with solvent remover or cleaner immediately.

10. **Record**: A report was prepared after each examination.

RADIOGRAPHIC TEST PROCEDURE

1. **Technique**: Single wall single image (Fig. 9) to detect and evaluate internal discontinuities in butt weld.

2. **Source of Radiation and Intensity of Radiation**: Ir-192 Source of source size 3x3mm.

3. **Test Specification No.**: ASME Section III NB and ASME Section V.

4. **Radiography Method**: Ir-192 Source, exposure as per exposure table to attain optical density between 2.5 to 3.5.

5. **Extent of Examination**: 100% circumference.

6. **Maximum un-sharpness allowed**: 0.5mm.

7. **Source to Film Distance (SFD)**: I/D of pipe approximately 275mm.

8. **Film Specification**: NPX-100 of Jindal Photo Films.

9. **Screen Specification**: Lead screen (0.2mm front and 0.2mm back).

10. **Pentrameter**: ASME wire type 1B.

11. **Total Number of films**: 8(size 75x182mm), (Coverage approximately 127mm length)

12. **Image Quality Indicator (I.Q.I) Sensitivity**: ASME 1B, 9 Nos. wires should be visible (3rd thickest wires, IQI on source side).

13. **Density**: 2 to 4

14. **Film Processing**: Standard processing parameters.

15. **Acceptance Standard**: ASME Section III NB 5320.